DOE/PC/79003--T19 Vol. II Vol. 2

OPTICAL PROPERTIES OF FLY ASH

Contract No. DE-AC22-87PC 79903

We have no objection from a patent standpoint to the publication or dissemination of this material.

Office of Intellectual Property Counsel
DOE Field Office, Chicago

9-27-95
Date

FINAL REPORT

Prepared for Pittsburgh Energy Technology Center

Principal Investigator: Professor S. A. Self

December 1994

HIGH TEMPERATURE GASDYNAMICS LABORATORY
Mechanical Engineering Department
Stanford University

Final

DISCLAIMER

DISCLAIMER

Portions of this document may be illegible in electronic image products. Images are produced from the best available original document.

DOE/PC/79003--T19 Vol II Vol.-2

OPTICAL PROPERTIES OF FLY ASH

Contract No. DE-AC22-87PC 79903

We have no objection from a patent standpoint to the publication or dissemination of this material.

Mark P. Dvorscak 9-27-95

Office of Intellectual Property Counsel
DOE Field Office, Chicago

Date

FINAL REPORT

Prepared for Pittsburgh Energy Technology Center

Principal Investigator: Professor S. A. Self

December 1994

HIGH TEMPERATURE GASDYNAMICS LABORATORY
Mechanical Engineering Department
Stanford University

Final

OPTICAL PROPERTIES OF FLY ASH

Contract No. DE-AC22-87PC 79903
(Active during period 15 September 1987 to 31 March 1992)

FINAL REPORT
(Volume II)

Prepared for Pittsburgh Energy Technology Center

Principal Investigator: Professor S. A. Self

December 1994

The High Temperature Gasdynamics Laboratory
Mechanical Engineering Department
Stanford University
Stanford, California 94305

PREFACE

Research performed under this contract was divided into four tasks under the following headings:

Task I	Characterization of Fly Ash
Task II	Measurements of the Optical Constants of Slags
Task III	Calculations of the Radiant Properties of Fly Ash Dispersions
Task IV	Measurements of the Radiant Properties of Fly Ash Dispersions

Tasks I and IV constituted the Ph.D. research topic of Sarbajit Ghosal, while Tasks II and III constituted the Ph.D. research topic of Jon Ebert. Together their doctoral dissertations give a complete account of the work performed.

This final report, issued in two volumes consists of an Executive Summary of the whole program followed by the dissertation of Ghosal (Vol. I) and Ebert (Vol. II). Each volume includes a list of publications and conference presentations resulting from the work.

Sidney A. Self

Stanford December 1994

ACKNOWLEDGEMENTS

It is a pleasure to record my personal satisfaction in advising Drs. Ebert and Ghosal in their graduate studies; their insights, energies and good humor made the direction of this work a rewarding experience.

Together, we should like to thank Mr. James D. Hickerson, PETC program manager, for his support and encouragement. We must also acknowledge the many practical contributions of Mr. Rodman Leach, Research Engineer on this project.

Finally we wish to record our debt to Dr. D. G. Goodwin, who was co-advised by Professors M. Mitchner and S. A. Self, for his pioneering work in this field under an earlier program support by the National Science Foundation.

EXECUTIVE SUMMARY

The overall goal of this project was to provide a fundamental scientific basis for understanding and calculating radiative heat transfer in coal combustion systems, particularly as influenced by the presence of inorganic constituents deriving from the mineral matter in coal.

The calculation of radiative heat transfer requires specification of the spectral absorption and scattering coefficients (a_λ and s_λ) and the scattering phase function (Φ_λ) of the medium. While the contributions to these properties by the infrared-active gases (CO_2 and H_2O) are well-documented, the contribution by the dispersed particulate phase (fly ash) may be large and hitherto was poorly understood. In general, the particulates produce two opposing tendencies on radiation transfer. Scattering impedes the transfer of gas radiation, while particle emission enhances the overall radiation transfer. In addition slag layers on combustor walls, deposited from entrained fly ash, provide a significant barrier to heat transfer.

Calculation of the optical properties of a particulate dispersion rests on the Mie theory for a single particle. This theory is readily available only for a homogeneous, isotropic sphere and requires specification of the size parameter $x \equiv (\pi d/\lambda)$ and the complex refractive index $m \equiv (n+ik)$ of the particle material, a function of composition, wavelength and temperature. The optical properties of the dispersion is then obtained by convolving the Mie theory for a single sphere with the size and refractive index distributions of the polydispersion.

In practice, it is not possible to invert measurements of the optical properties of a particulate dispersion to infer the size and refractive index distributions of the particulates. Even if one knows the size distribution from independent measurements, one can infer, at best, only some effective average refractive index. Because of the impracticality of obtaining fundamental data on the complex refractive index of particulates from measurements on a polydispersion, and in view of the heterogeneity of composition of fly ash, an alternative strategy was adopted.

The basic approach was to measure the optical constants (i.e. the components, n, k of the complex refractive index) on bulk samples of synthetic slags, for which reliable techniques are available. Such measurements were made over relevant ranges of wavelength, composition and temperature, and constitute the fundamental data base for computing radiation transfer in fly ash laden combustion gases. To utilize such data on the optical constants of slag in calculations of radiation transfer in ash dispersions, it is also

necessary that the ash be characterized with respect to its size and composition distributions. Characterization of a range of representative ashes constituted a second component of the work. It should be recognized that this basic approach rests on the fortunate fact that the vast majority of fly ash particles are closely spherical, optically isotropic (because they are vitreous) and homogeneous, although the composition varies significantly from particle to particle.

The research program consisted of four tasks, as outlined below.

TASK I - CHARACTERIZATION OF FLY ASH

Representative samples of fly ashes were characterized with respect to their size and composition distributions, including correlation of composition with size over ranges of interest for radiation transfer. Ashes from six coals selected for study under the concurrent PETC program on "Transformation of Inorganic Coal Constituents in Combustion Systems" were obtained from electric power plants or from samples produced earlier in the 10^6BTU/hr pilot combustor at Foster-Wheeler.

Size distributions were determined by Coulter counter, while size-composition distributions were obtained from computer-controlled SEM-EDX microprobe analyses.

In addition, techniques were developed for ash separation by both size and density by combined wet sieving and centrifuging in liquids of various specific gravity, as well as separation of the magnetic component (magnetite from the combustion of pyrite). Analysis of the separated fractions yielded further information on the size-composition distributions as well as information on the fraction of cenospheric ash (i.e. particles containing gas bubbles).

TASK II - MEASUREMENTS OF THE OPTICAL CONSTANTS OF SLAGS

Coal slags and fly ash are basically impure calcium-aluminosilicate glasses. The host glass is essentially transparent ($k \leq 10^{-4}$) in the visible and near infrared, with a very strong absorption band ($k \sim 1$) in the range 8-12 μm due to vibration of the Si-O bond. The principal infrared-active impurity is iron (as the ferrous ion) which produces significant absorption ($k \sim 10^{-4}$–10^{-3}) in the range 0.5–5 μm, important for radiation transfer at combustion temperatures.

Synthetic slags of controlled composition were produced by melting appropriate mineral oxides in a furnace at ~1560°C and cooled slowly to produce homogeneous bulk samples. For measurements at low temperatures (to ~800°C) thin wafers (50–500 μm) were cut and optically polished. The optical constants over the wavelength range 0.5–8 μm were

determined by measuring the absorption and surface reflectance and use of the Fresnel relations. For the range 8–13 μm where the absorption is too strong ($k > 10^{-2}$) to allow direct measurements of absorption on thin wafers, n and k were obtained from surface reflectance measurements at normal incidence using the Kramers-Kronig relations.

At high temperatures (≥1600°C) when the slag is liquid, an alternative technique was devised for measuring the absorption of thin liquid layers, by a double pass using reflection from a submerged platinum mirror. The absorption coefficient (and hence k) was determined from the change in signal when the liquid film depth was changed a known amount by raising or lowering the mirror by a micrometer-controlled increment.

For the longer wavelengths ($\lambda \geq 8$ μm), where the absorption is too strong ($k \geq 10^{-2}$) to allow direct absorption measurements on a thin film, n and k were determined solely from surface reflectance measurements on the liquid slag using the Kramers-Kronig technique.

The final outcome of Task II is a set of correlation formulae for the complex refractive index of synthetic slags as a function of composition, wavelength and temperature. These formulae constitute a fundamental data base for the calculation of radiation transfer in ash-laden combustion gases.

TASK III - CALCULATION OF THE RADIANT PROPERTIES OF FLY ASH DISPERSIONS

Sample calculations were made for typical ash loadings, size distributions and compositions for simple geometries, with two main purposes: first, to provide insight and physical understanding of the role of fly ash in radiative heat transfer in combustion systems; second, to indicate the sensitivity of the results to the characteristics of the input data. Such calculations were also used to determine appropriate conditions and to predict the expected measured radiative properties for the experiment of Task IV.

TASK IV - MEASUREMENTS OF THE RADIANT PROPERTIES OF FLY ASH DISPERSIONS

This experiment was intended to validate the overall approach by critically testing our ability to predict the measured spectral absorption and scattering coefficient of hot, gaseous fly ash dispersions under well-controlled laboratory conditions utilizing the ash characteristics and the optical property data developed in Tasks I and II. However, in the event, it proved impossible to generate well-deagglomerated aerosols from ash powder samples, so we settled for a somewhat less stringent but much easier-to-accomplish test using room-temperature dispersions of ash in several infrared transmitting liquids covering the wavelength range 1-

13 μm. Measurements of spectral extinction (by scattering and absorption) showed good agreement with predictions for four ashes when account was taken of the presence of cenospheres in the ash. The effect of cenospheres is greatly enhanced in liquid dispersions compared with gaseous dispersions, for which it is essentially negligible.

In summary, the overall goal of the research was accomplished; a new, general method for realistically incorporating the effects of fly ash in radiative transfer computations in coal combustion systems has been established. With the use of the correlation formulae for the dependence of the complex refractive index of fly ash on composition, wavelength and temperature, resulting from this work, all that is required to calculate heat transfer in the radiant section of a particular coal combustor is specification of the geometry and boundary conditions, plus data from standard microanalytical techniques of the size and composition distributions of a sample of ash from the particular coal of interest. The correlation formulae are also directly applicable for calculating radiation transfer through slag deposits on combustor walls.

PUBLICATIONS AND CONFERENCE PRESENTATIONS

1. D. G. Goodwin and J. L. Ebert, "Rigorous Bounds on the Radiative Interaction between Real Gases and Scattering Particles," Journal of Quantitative Spectroscopy and Radiative Transfer 37, no. 5, pp. 501-508, 1987.

2. Sidney A. Self, Comment on "Rigorous Bounds on the Radiative Interaction between Real Gases and Scattering Particles," by D. G. Goodwin and J. L. Ebert, Journal of Quantitative Spectroscopy and Radiative Transfer 37, no. 5, pp. 513-514, 1987.

3. J. L. Ebert and S. A. Self, "Radiation Heat Transfer in a Dispersion of Flyash," in R. W. Bryers and K. S. Vorres (eds), Engineering Foundation Conference on Mineral Matter and Ash Deposition from Coal, Santa Barbara, CA, Feb. 22-26, pp. 599-611, 1988.

4. J. L. Ebert and S. A. Self, "The Optical Properties of Molten Coal Slag," Proc. 26th National Heat Transfer Conference, Philadelphia, PA, August 1989.

5. S. Ghosal and S. A. Self, "Optical Characterization of Coal Fly Ash," *Radiative Transfer - Theory and Applications*, Ed. A. M. Smith and S. H. Chan, American Society of Mechanical Engineerings, HTD-Vol. 244, pp. 105-115, 1993.

6. S. Ghosal, J. L. Ebert and S. A. Self, "Size Distributions of Fly Ashes by Coulter Multisizer: Use of Multiple Orifices and Fitting to Truncated Lognormal Function," Particle and Particle Systems Characterization, Vol. 10, pp. 11-18, 1993.

7. S. Ghosal and S. A. Self, "Infrared Extinction Measurements on Fly Ash Dispersions," *General Papers in Radiative Transfer*, Ed. M. F. Modest, I. S. Habib, and M. Sohal, American Society of Mechanical Engineers, HTD-Vol. 257, pp. 51-61, 1993.

8. S. Ghosal, J. L. Ebert and S. A. Self, "The Infrared Refractive Indices of $CHBr_3$, CCl_4, and CS_2," Infrared Physics, Vol. 34, No. 6, pp. 621-628, 1993.

9. S. Ghosal, J. L. Ebert and S. A. Self, "Chemical Composition and Size Distributions for Fly Ashes," Fuel Processing Technology, in press.

10. S. Ghosal and S. A. Self, "Particle Size-Density Relationship and Cenospheric Content of Coal Fly Ashes," Fuel, in press.

INFRARED OPTICAL PROPERTIES OF COAL SLAG AT HIGH TEMPERATURES

A DISSERTATION
SUBMITTED TO THE DEPARTMENT OF MECHANICAL ENGINEERING
AND THE COMMITTEE ON GRADUATE STUDIES
OF STANFORD UNIVERSITY
IN PARTIAL FULFILLMENT OF THE REQUIREMENTS
FOR THE DEGREE OF
DOCTOR OF PHILOSOPHY

Jon Lloyd Ebert
August 1994

Abstract

Radiation heat transfer from the hot combustion products of pulverized-coal combustion (CO_2, H_2O, soot, char, and fly ash) to the cooled walls is the dominant mode of heat transfer in such combustion systems. During this combustion process, inorganic minerals (mostly SiO_2, Al_2O_3, CaO) within the coal melt and coalesce to form droplets of molten slag (fly ash) which subsequently cool to form mostly glassy solid spheres with large particle to particle variations in both diameter and composition. To predict the effects of fly ash on the radiative heat transfer through such a medium, one must know its radiative properties, which depend on the diameter- and composition-averaged scattering and absorption properties.

The approach adopted here recognizes that the optical constants (n, k) of a homogeneous isotropic material such as glassy slags are only a function of composition, temperature, and the wavelength (λ). One can measure (n, k) of bulk materials with compositions similar to those of individual particles and compute the scattering and absorption properties of single homogeneous isotropic particles using Mie theory. When combined with measurements of the composition and diameter distributions for real ashes, the integrated radiative properties of an ash dispersion can be computed, allowing one to systematically investigate the factors that influence the average radiative properties.

Measurements of the optical constants (n, k) for bulk molten slags ($\sim 1600°C$) are reported here for a range of compositions spanning those of most fly ash particles. The measurements were made over the near infrared wavelength range $1 \leq \lambda \leq 13\mu m$ where most thermal radiation occurs at typical coal combustion temperatures ($1000 - 2000K$).

Synthetic slags with well controlled compositions were produced having various amounts of SiO_2, Al_2O_3, CaO, and Fe_2O_3, with the Fe_2O_3 and SiO_2 contents being the most important independent variables affecting the optical constants. The synthetic slags studied here had Fe_2O_3 contents ranging from 0 to 19 wt.% and SiO_2 contents ranging from 10 wt.% to 60 wt.%.

The near-normal reflectance of a pool of molten slag was measured over the wavelength range $1 \leq \lambda \leq 13\mu m$. From this measurement the real refractive index, n, was computed over the entire wavelength range from $1 \leq \lambda \leq 13\mu m$ using the Kramers-Kronig relations. This procedure also yields the absorption index, k, in the range where $k > 0.1$. In the wavelength range from $1 - 5\mu m$, where k is too small to determine from reflectance measurements ($k^2 \ll (n-1)^2$), a technique was developed to measure the transmittance ($\exp(-4\pi kh/\lambda)$) of a thin layer of molten slag. A platinum mirror was submerged below the surface of the molten slag and the thickness of the layer of slag above the mirror (h) was adjusted to provide a direct measurement of k.

In the wavelength range from $1 - 4\mu m$ the absorption index, k, depends on the Fe_2O_3 content (and OH) in the slag. At longer wavelengths ($8 - 13\mu m$) absorption is

due to fundamental vibrational absorption by SiO_2; thus k is strongly dependent on SiO_2 content. In the intermediate wavelength range ($4 < \lambda < 8\mu$m) the absorption is due to multiphonon processes associated with the SiO_2 vibrational absorption mechanisms at longer wavelengths.

Correlations were developed that estimate n and k over the entire wavelength range from 1-13 μm from knowledge of the composition. Results from others studies (Ghosal, 1993) provided compositions of thousands of individual fly ash particles from several representative U.S. coals, along with their size distributions. These composition distributions were used to compute the optical constants distributions and Mie theory was used to compute the size-averaged scattering and absorption properties. Radiative properties for various ash loadings were computed for dispersions of these ashes.

The effects of size and composition distributions and of ash loading on the radiative properties of a dispersion were studied. Ashes with larger particles (i.e., larger volume to area ratio) tend to have smaller extinction coefficients than distributions with smaller particles. However, all ashes studied tend to have reasonably similar average radiative properties, despite significant composition variations. Also, use of the average composition to compute the average radiative properties produces reasonably accurate results.

The effect of fly ash on radiative transfer through a planar layer of uniformly dispersed ash with absorption and emission by CO_2 and H_2O was studied for both an isothermal layer and a layer in radiative equilibrium. Generally the ash increases the emission of the isothermal layer somewhat, but the most significant effect is the strong extinction caused by scattering. A similar effect is seen for a layer in radiative equilibrium where addition of ash to a layer of CO_2 and H_2O causes a significant decrease in the heat flux across the layer.

CONTENTS

Nomenclature

A	mean molar refractivity
A	correlation parameter in two-phonon model for k
A_0,A_1	parameters in two-phonon correlation for k_b
A_i	mean molar refractivity of species i
A_i	Legendre coefficients for expansion of Φ_λ
B	parameter for normal dispersion fit of $n(\lambda)$
$\mathbf{B}$	magnetic induction
B_0,B_1	parameters in two-phonon correlation for k_b
B_i	coefficients for $\delta - P_n$ expansion
C	parameter for normal dispersion fit of $n(\lambda)$
$C_{v,i}$	volume fraction of ash with for optical constants class i
C_v	ash volume fraction in dispersion
$C_{v,x}$	volume fraction of ash with oxide weight fraction x within dx
$\mathbf{D}$, D	electric displacement vector and its magnitude
D	particle diameter
D_{32}	Sauter mean diameter
$\mathbf{E}$, E	electric field intensity vector and its magnitude
E_{loc}	magnitude of local electric field
$\mathbf{H}$	magnetic field intensity
I	radiance, power flux per unit solid angle
$I_{b\lambda}$	Planck blackbody radiance
I_λ	spectral radiance
I_r	measured radiance from reference path
I_s	measured radiance from sample path
$\mathbf{J}$	conduction current density
L	thickness of planar layer
$\mathbf{M}$	magnetization vector
$\hat{M}$	magnitude of electric field vector
N	number density of atoms or molecules
N_m	Avagadro's number, $\simeq 6.02 \times 10^{23}$ atoms/mole
$\mathbf{P}$	electric polarization
P	polarization
P	pressure
Q	normalized radiative power flux
Q_a	absorption efficiency
Q_s	scattering efficiency
R	reflectance of solid interface
R	linear correlation coefficient
R_g	reflectance of gold in infrared ($\simeq 0.992$)
$\mathbf{S}$	Poynting vector
T	temperature

c_0	speed of light in vacuum
f	volume fraction of oxygen in air
f	coefficient in $\delta - P_n$ expansion
f_λ	blackbody fraction in spectral band λ
g	asymmetry parameter
g	integrated radiance or incident radiation
h	submerged reflector depth
k	magnitude of wave vector,$= 2\pi m/\lambda_0$
$\mathbf{k}$	wave vector
k	imaginary part of complex refractive index, or absorption index
$\overline{k}$	average absorption index
k_b	correlation parameter in two-phonon model for k
k_o	correlation parameter in two-phonon model for k
m	complex refractive index, $m = n + ik$
n_∞^2	high frequency limit of dielectric constant
n	real part of complex refractive index, or refractive index
n_i	number of moles of species i
p_i	partial pressure of species i in gas mixture
q	power flux
$\mathbf{q}_\lambda(\mathbf{r})$	spectral heat flux vector
$\mathbf{r}$	position vector
$\tilde{r}$	reflection coefficient
$\tilde{t}$	transmission coefficient
u	logarithm of particle diameter, D
$\overline{u}$	logarithm of number median particle diameter, D_n
x	particle size parameter $(= \pi D/\lambda)$
x	coordinate direction normal to a planar layer
x	oxide weight fraction, $0 \leq x \leq 1$
x_{ash}	ash mass fraction in coal
$\hat{x}_i$	mole fraction of species i
x_i	weight fraction of species i
$x_{m,i}$	mass fraction of species i

Greek

α	absorption coefficient
α	mean polarizability of an atom or molecule
α_λ	spectral absorption coefficient
$\alpha_{P,0-\lambda}$	contribution to Planck mean quantity for wavelengths shorter than λ
β_λ	Spectral extinction coefficient, $= \alpha_\lambda + \sigma_\lambda$
δ	change in submerged reflector depth
$\delta\lambda_o$	empirical correction term for λ_o in mixture rule correlation for n
$\delta(1-\mu)$	delta function in $\delta - P_n$ expansion

$\delta\omega$	frequency shift parameter in two-phonon correlation for k
$\delta\rho$	empirical correction term for ρ in mixture rule correlation for n
γ	damping parameter of harmonic oscillator
ϵ	emittance of planar layer
ϵ	complex dielectric constant, $\epsilon = m^2$
ϵ'	real part of complex dielectric function
ϵ''	imaginary part of complex dielectric function
ε_0	permittivity of free space
ε	permittivity of medium
Θ	phase shift on reflection
λ	wavelength
λ_0	wavelength in vacuum
λ_o	parameter for normal dispersion fit of $n(\lambda)$
μ	direction cosine between two directions
μ	permeability of medium
μ_0	permeability of free space
Ω	solid angle
$\hat{\mathbf{\Omega}}$	direction vector for radiative transport
ω	scattering albedo
ω	angular frequency or frequency in wavenumbers
ω_o	natural frequency of harmonic oscillator
ω_p	plasma frequency of harmonic oscillator
ρ	charge density of unbound electric charges
ρ	reflectance of planar layer
ρ	mass density
ρ_i	mass density of species i
σ	electrical conductivity
σ	Stefan-Boltzmann constant
σ	scattering coefficient
σ_g	geometric standard deviation of log-normal size distribution
σ_λ	spectral scattering coefficient
σ_u	logarithm of σ_g
τ	transmittance of planar layer
τ_0	optical depth of planar layer
$\tau_{0,\text{gas}}$	effective optical depth of planar layer of gas only
Φ_λ	spectral scattering phase function
$\phi(D)$	particle size distribution function
χ	electric susceptibility

subscripts

0	at $x = 0$ in planar layer
0, n	size distribution parameter on a particle number basis
1	at $x = L$ in planar layer

2, a	size distribution parameter on a particle area basis
3, v	size distribution parameter on a particle volume basis
c	complex field
i	species index for mixtures
i	index denoting optical constants class
j	index for multiple oscillator constants
P	Planck mean radiative property
λ	spectral radiative quantity

Chapter I.

Introduction

I.1 Motivation

Radiation is the dominant mode of heat transfer in many coal combustors and gasifiers, and the prediction of heat transfer is a critical factor in combustor design. It is common for a coal combustor to have a radiant section where pulverized coal particles are injected and burned, followed by a convective section where superheat tubes collect thermal power from the hot combustion products. Since the radiant section may have peak temperatures exceeding 1700 K, the heat transfer to its cooled walls is predominantly by radiation. As the hot gases and particles exit the radiant section they enter the convective section in which the flow crosses superheat tubes and other heat transfer surfaces. If the fly ash particles in the convective section are too hot, they are "sticky" or even molten and will collect on the cooler heat transfer surfaces. This "fouling" process reduces the heat transfer by building up an insulating layer of ash and slag on the cooler surfaces. Therefore, a primary design criterion is the exit temperature from the radiant section of the coal combustor, and the radiative properties of the products of coal combustion directly affect this exit temperature. Thus, sizing the radiant section is critical. If it is too small the exit temperature will be too high and fouling of the convective section will occur. If it is too large, then unnecessary cost will be incurred in cooling by radiation transfer at low temperatures, for which it is less efficient than convective transfer.

The radiant section of a pulverized coal combustor contains several constituents that participate in the radiant heat transfer. The infrared active gases, chiefly CO_2 and H_2O, absorb and emit radiation in selective wavelength bands. Carbonaceous particles of char and soot absorb and emit radiation over a broad wavelength range but scatter very little radiation. Fly ash, the inert mineral matter in coal, emits, absorbs, and scatters radiation.

The radiative properties of the combustion gases are well enough known to permit reasonably accurate estimates of radiative transfer. Many measurements in the last 20 to 30 years have resulted in reasonably accurate (5-15%) semi-empirical

gas band models [1-2] that can be used to predict radiation transfer through CO_2 and H_2O at temperatures found in coal combustors. Carbon dioxide has strong vibrational–rotational absorption bands at wavelengths of 2.7 μm, 4.3 μm, and 15 μm in addition to some weaker absorption bands. Water vapor has a broad vibrational absorption band near 6.3 μm and narrower absorption bands near 2.7 μm, 1.87 μm, and 1.38 μm. Between theses gas absorption bands the hot gases are transparent and other constituents, such as soot, char, and fly ash, contribute to emission and absorption.

The radiative properties of carbonaceous particles (soot and char) are also reasonably well known [3-4]. Such particles have high emittance over a broad wavelength range and significantly contribute to emission from the flame region. However, to maintain high carbon conversion efficiencies, reactors are generally large enough that most soot and char is pyrolized in a relatively small volume of the radiant section, leaving CO_2, H_2O, fly ash, and small residual amounts of soot and char responsible for radiative transport throughout much of the furnace.

Several numerical studies [5-10] have shown that fly ash is an important factor in the radiation transfer in coal combustors. Coal may contain from 2% to 25% ash by weight with typical values of 5-15%. Ash is the primary scattering constituent in the furnace environment and can effectively shield the cooler furnace walls from the hotter flame regions. Lowe, et. al. [6] modeled a pulverized coal fired furnace and concluded that fly ash is a dominant participant in radiation transfer in regions of the furnace where combustion is complete. To date, such calculations have lacked accurate data for the optical properties of fly ash.

Accurate measurements of the radiative properties of fly ash were only recently obtained by Goodwin [11] in work at Stanford, supported by NSF. Earlier measurements of the optical constants of fly ash [12-16] showed considerable uncertainty. Goodwin measured the optical constants of bulk synthetic solid slags from which the optical properties of fly ash dispersions can be computed. While most of Goodwin's measurements were for slags at room temperature, he also made measurements of the absorption index, k, up to temperatures of approximately 1200 K. These measurements showed that the spectral absorption index, k, of high iron slags increases with increasing temperature.

The main purpose of the present study was to extend the database on optical properties of slags to higher temperatures, where slag is molten, and to include a wider

range of compositions as revealed in a parallel study by Ghosal [17] of the size and composition distributions of samples of fly ashes from combustion of representative U.S. coals.

I.2 The Formation of Fly Ash

Fly ash is formed from the inert minerals that are released when coal particles burn. Coal particles contains mineral inclusions that vary in composition and size from one coal particle to the next. The mineral inclusions are chiefly kaolinite ($Al_2O_3 \cdot 2SiO_2 \cdot 2H_2O$), pyrites ($FeS_2$), and calcite ($CaCO_3$) with lesser amounts of quartz (SiO_2), rutile (TiO_2), and many other minerals. During the combustion of a coal particle, it typically breaks into fragments and as the carbonaceous materials pyrolize, the mineral inclusions in the coal melt and coalesce to form a fly ash particle. The composition of the final fly ash particle reflects the mixture of inclusions from which it was formed. There are significant variations in composition from one ash particle to another, but because they spend some time in the molten phase, and cool quickly, they tend to be closely spherical, of homogeneous composition and vitreous (glassy) when solid. Recent work by Ghosal [17] has quantified this variation in composition for several ash samples using computer controlled scanning electron microscopy.

The diameter of fly ash particles ranges from sub–micron to 100 μm or more, with a median diameter† typically in the 10–15 μm range. Generally the size distribution is modeled quite accurately by a log-normal curve (i.e., Gaussian in logarithm of diameter) [17].

---

† Median diameter based on volume, i.e., half of the ash volume (or mass) is attributable to particles with diameter less than the median size.

I.3 Relationship of Bulk Slag Properties to Fly Ash Properties

It is observed that the size and composition distributions of fly ash vary from coal to coal [17]. Also, for a specific coal, the ash composition varies from particle to particle. Therefore, measuring the radiative properties of one particular ash will not yield results that are generally applicable to other fly ash dispersions. Moreover, such an approach does not lead to an understanding of the underlying fundamental properties that determine the character of the radiative properties of a dispersion, or help one understand how variation of the ash characteristics affects its radiative properties.

Mie theory provides a fundamental approach to the problem. For a homogeneous and isotropic sphere, Mie theory relates its scattering and absorption characteristics to its size and complex refractive index, $m = n + ik$. If one knows the size and complex refractive index for all the particles in a polydispersion, then the average radiative properties for the polydispersion (e.g., scattering coefficient, scattering phase function, and absorption coefficient) can be computed.

The complex refractive index, $m(\lambda, C, T)$, is a material property that depends only on wavelength, the composition and temperature of the material. It does not depend on the size or shape of the particle. The real part of the complex refractive index n is commonly referred to as the *refractive index*, and is the ratio of the speed of light in vacuum to that in the material. The imaginary part of the refractive index, k, is commonly called the *absorption index* and it describes the attenuation of radiant intensity through the medium according to Beer's Law, $I(s)/I(0) = \exp(-4\pi ks/\lambda)$. Well established techniques can be used to measure n and k for homogeneous bulk materials.

The approach adopted in this study is based on the fact that if correlations for $m = m(\lambda, C, T)$ are available for an appropriate range of wavelengths, λ, compositions, C, and temperatures, T, then to compute the radiative properties for any given dispersion of fly ash, all one needs is data on the size and compostion distributions of a sample of the ash. Fortunately, these distribtuions can be obtained by straightforward microanalytical techniques, as described by Ghosal [17].

The validity of this approach depends largely on the fly ash particles being homogeneous and isotropic spheres, so that Mie theory is applicable. Fortunately,

fly ash particles are typically closely spherical, homogeneous, and isotropic † owing to the mechanism of their formation, as described above, at temperatures above the melting temperature of most mineral inclusions.

I.4 Scope of the Present Study

In the present study measurements of the optical constants (n and k) of coal slags, i.e. bulk ash material, are extended to higher temperatures at which the slags are molten. Measurements are reported for several slag compositions representative of fly ashes from U.S. coals, but emphasizing only constituents that effect the optical properties. Several slags with compositions similar to those of Goodwin [11] are studied so that the effect of temperature can be isolated. In addition, several slags of much lower SiO_2 content were studied to further extend the optical properties database.

Correlations are developed in Chapter IV that allow one to estimate the optical constants of molten slag as a function of composition and wavelength. The composition of most naturally occurring ash particles is within the range of application for these correlations.

The correlations developed in Chapter IV are used in Chapter V to estimate the radiative properties of ash dispersions using composition and size distribution available from Ghosal [17]. Mie theory is used to estimate the scattering properties of each particle and integration over the size and composition distributions produces the desired average radiative properties.

Finally, calculations are presented in Chapter VI to illustrate the effect of fly ash on radiation heat transfer in coal combustors using a one dimensional model. Estimates of the relative importance of fly ash, compared to CO_2 and H_2O, are computed for conditions pertinent to coal combustion environments. Variations in ash loading (dust burden) are studied for an isothermal planar layer and for a layer in radiative equilibrium. Such calculations were useful for sensitivity studies to guide the range of wavelengths and component oxides chosen for the optical constant measurements as well as guiding the ash characterization studies in closely related work [17].

---

† Some fly ash particles are hollow cenospheres or shells. Other ash particles are even nonspherical with voids or "bubbles" in them, but these particles are a minority in most ashes (i.e., ash from most coals).

Chapter II.

Theoretical and Experimental Background

This chapter presents the theoretical basis for the optical constants and experimental methods adopted in this study for determining them. The first section summarizes the definition of the optical constants and the theoretical basis for pertinent measurable quantities for weakly conducting solids (such as coal slag). The second section gives an overview of common experimental techniques for determining the optical constants of bulk materials, including the technique adopted in this study. The final section in this chapter outlines the theoretical basis for the relationship between these bulk optical properties and the scattering and absorption characteristics of particulates.

II.1 Electromagnetic Theory and the Optical Constants

II.1.1 The Maxwell Equations

The Maxwell equations † describe the behavior of electromagnetic fields in vacuum and in matter. In vector notation ($\mathbf{A} = A_x\hat{\mathbf{e}}_x + A_y\hat{\mathbf{e}}_y + A_z\hat{\mathbf{e}}_z$), the equations are written in SI units as [18-19]

$$\nabla \cdot \mathbf{D} = \rho \qquad (II.1a)$$

$$\nabla \cdot \mathbf{B} = 0 \qquad (II.1b)$$

$$\nabla \times \mathbf{E} = -\frac{\partial \mathbf{B}}{\partial t} \qquad (II.1c)$$

$$\nabla \times \mathbf{H} = \mathbf{J} + \frac{\partial \mathbf{D}}{\partial t} \qquad (II.1d)$$

where $\mathbf{E}$ is the electric field intensity, $\mathbf{B}$ is the magnetic induction, $\mathbf{D}$ is the electric displacement, $\mathbf{H}$ is the magnetic field intensity, $\mathbf{J}$ is the conduction current density, and ρ is the charge density of unbound electric charges.

---

† In 1865 James Clerk Maxwell published the theoretical foundation of modern electromagnetic theory in an essay, *"A Dynamical Theory of the Electromagnetic Field"* in volume CLV of *Philosophical Transactions of the Royal Society.*

In vacuum the two vectors $\mathbf{D}$ and $\mathbf{H}$ are simply defined by $\mathbf{D} = \varepsilon_0\mathbf{E}$ and $\mathbf{H} = \mathbf{B}/\mu_0$ where ε_0 and μ_0 are the permittivity and permeability of free space, respectively. The speed of light in vacuum, c_0, is related to the permittivity and permeability by the relation $c_0 = \sqrt{1/\varepsilon_0\mu_0}$.

In a material, the field vectors $\mathbf{E}$ and $\mathbf{H}$ are the averaged fields and in general there exist both bound and free charges. The free charge and current density are accounted for through ρ and $\mathbf{J}$, but the bound charges are capable of creating electric and magnetic moments that are allowed for by introducing *constituitive relations.* For sufficiently weak fields, the effects of bound charges in most materials are adequately described by the first order moments, the electric and magnetic dipoles; quadrupole and higher moments are negligible. For such materials we can write

$$\mathbf{D} = \varepsilon_0\mathbf{E} + \mathbf{P}, \qquad (II.2a)$$

$$\mathbf{H} = \frac{\mathbf{B}}{\mu_0} - \mathbf{M}, \qquad (II.2b)$$

where $\mathbf{P}$ is the electric polarization and $\mathbf{M}$ is the magnetization. The two vectors $\mathbf{P}$ and $\mathbf{M}$ are the average electric and magnetic dipole moments per unit volume, respectively.

In addition to the equations above, one assumes constituitive relations of the form

$$\mathbf{J} = \sigma\mathbf{E}, \qquad (II.2c)$$

$$\mathbf{B} = \mu\mathbf{H}, \qquad (II.2d)$$

$$\mathbf{P} = \varepsilon_0\chi\mathbf{E}, \qquad (II.2e)$$

where σ is the electrical conductivity, μ is the permeability, and χ is the electric susceptibility of the medium. In general, one should not regard Eqs. (II.2) as universal relations, since there are materials for which they are not valid, but as assumptions which happen to be valid for many materials including glassy slags. To further restrict the scope of this analysis, we assume relatively weak electromagnetic fields so that the materials behave *linearly* and σ, μ, and χ are independent of the fields. Finally, we limit the analysis to homogeneous, isotropic materials in which σ, μ, and χ are constant scalar quantities. These assumptions and restrictions still allow analysis of many practical situations including interaction of radiation with fly ash and slag.

II.1.2 Electromagnetic Waves in Non-Conductors

An electromagnetic wave propagating through a homogeneous, isotropic, non-conducting medium ($\rho = \mathbf{J} = 0$) is described by the vector equations

$$\nabla \cdot \mathbf{E} = 0, \tag{II.3a}$$

$$\nabla \cdot \mathbf{H} = 0, \tag{II.3b}$$

$$\nabla \times \mathbf{E} = -\mu \frac{\partial \mathbf{H}}{\partial t}, \tag{II.3c}$$

$$\nabla \times \mathbf{H} = \varepsilon \frac{\partial \mathbf{E}}{\partial t}. \tag{II.3d}$$

Assume that the permeability, μ, and permittivity, $\varepsilon \equiv \varepsilon_0(1 + \chi)$, of the medium are constants. By taking the curl ($\nabla\times()$) of Eq. (II.3c) and Eq. (II.3d) using the vector identity $\nabla \times (\nabla \times \mathbf{A}) = \nabla(\nabla \cdot \mathbf{A}) - (\nabla \cdot \nabla)\mathbf{A}$ and utilizing Eq. (II.3a) and Eq. (II.3b), the vector wave equations are obtained:

$$\mu\varepsilon \frac{\partial^2 \mathbf{E}}{\partial t^2} - (\nabla \cdot \nabla)\,\mathbf{E} = 0, \tag{II.4a}$$

$$\mu\varepsilon \frac{\partial^2 \mathbf{H}}{\partial t^2} - (\nabla \cdot \nabla)\,\mathbf{H} = 0. \tag{II.4b}$$

From these two equations one sees that any scalar component, say A_i, of either the electric field, $\mathbf{E}$, or the magnetic field, $\mathbf{H}$, satisfies the wave equation

$$\mu\varepsilon \frac{\partial^2 \mathrm{A}_i}{\partial t^2} - \nabla^2 \mathrm{A}_i = 0 \tag{II.5}$$

and the speed of propagation, c, in the medium is $c = \sqrt{1/\mu\varepsilon}$. In this case, where c is a positive real constant, the solutions are undamped waves and the medium is transparent, a result of assuming that the electrical conductivity is identically zero.

The refractive index, m, is defined as

$$m \equiv \frac{c_0}{c} = \frac{\sqrt{\mu\varepsilon}}{\sqrt{\mu_0\varepsilon_0}}. \tag{II.6}$$

Even though m is defined here in a medium with no absorption, this definition extends to absorbing media where ε is not a simple real constant, but a complex quantity.

II.1.3 Electromagnetic Waves in Real Materials

In any real material there is absorption of an electromagnetic wave as it propagates through the material. In electrical insulators, which have very few free charges and only modest ionic conduction, the absorption is generally very much less than in metals, in which there are many free electrons and the electrical conductivity is high. However, even insulators exhibit very strong absorption in certain frequency ranges.

Consider a complex time-harmonic electric field vector $\mathbf{E}_c$ of the form

$$\mathbf{E}_c(\mathbf{r},t) = \mathbf{E}_c(\mathbf{r})\exp(-i\omega t) \qquad (II.7)$$

where ω is the angular frequency and t is time. The physical electric field, $\mathbf{E}$, is just the real part of this complex electric field, that is

$$\mathbf{E} = \mathrm{Re}\{\mathbf{E}_c(\mathbf{r},t)\} = \mathrm{Re}\{\mathbf{E}_c(\mathbf{r})\}\cos(\omega t) + \mathrm{Im}\{\mathbf{E}_c(\mathbf{r})\}\sin(\omega t) \qquad (II.8)$$

where Re{} and Im{} denote the real and imaginary parts of a complex quantity, respectively. This *complex embedding* is allowed provided all the operations on $\mathbf{E}_c$ are linear operations such as addition, differentiation, or integration. Since all the operators in the Maxwell equations *are* linear, the vector quantities can all be replaced by their complex form.

The charge conservation equation,

$$\frac{\partial \rho}{\partial t} + \nabla \cdot \mathbf{J} = 0, \qquad (II.9)$$

is derived by differentiating Eq. (II.1a) with respect to time, taking the divergence of Eq. (II.1d), and combining. Then Eq. (II.1a) can be differentiated with respect to time and rewritten as

$$\nabla \cdot \left(\frac{\partial \mathbf{D}}{\partial t} + \mathbf{J} \right) = 0$$

Replacing $\mathbf{D}$, using Eq. (II.2a) and Eq. (II.2e), with $\sigma\mathbf{E}$ and introducing the complex fields we obtain

$$\nabla \cdot (\varepsilon \mathbf{E}_c) = 0 \qquad (II.10a)$$

where ε is the complex permittivity of the medium and is defined as

$$\varepsilon \equiv \varepsilon_0(1+\chi) + i\frac{\sigma}{\omega}. \qquad (II.10b)$$

The other Maxwell equations can similarly be rewritten, using the complex fields and the constituitive relations, as

$$\nabla \cdot \mathbf{H}_c = 0 \qquad (II.10c)$$

$$\nabla \times \mathbf{E}_c = i\omega\mu\mathbf{H}_c \qquad (II.10d)$$

$$\nabla \times \mathbf{H}_c = -i\omega\varepsilon\mathbf{E}_c \qquad (II.10e)$$

These equations for $\mathbf{E}_c$ and $\mathbf{H}_c$ are exactly analogous to the wave equations derived for media with no absorption, Eq. (II.3). This analogy indicates that the definition of the *complex* refractive index, m, in Eq. (II.6) is appropriate, provided that the real permittivity is replaced by the *complex* permittivity, ε, defined in Eq. (II.10b).

II.1.4 Propagation of Plane Electromagnetic Waves

In an infinite homogeneous and isotropic medium electromagnetic waves emitted from some point source propagate with spherical wave fronts, similar to ripples on a pond radiating away from a point disturbance. At distances very far from the source, the spherical wave fronts may be, and often are, approximated locally as planar. Therefore, it is instructive to look for plane wave solutions to the Maxwell equations.

A plane wave is described by the complex, time–harmonic electric and magnetic fields

$$\mathbf{E}_c = \mathbf{E}_0 \exp(i\mathbf{k}\cdot\mathbf{r} - i\omega t) \qquad (II.11a)$$

$$\mathbf{H}_c = \mathbf{H}_0 \exp(i\mathbf{k}\cdot\mathbf{r} - i\omega t) \qquad (II.11b)$$

where $\mathbf{E}_0$ and $\mathbf{H}_0$ are constant complex vectors, $\mathbf{k} = \mathbf{k}' + i\mathbf{k}''$ is the complex wave vector, and $\mathbf{r}$ is the position vector. Substituting Eq. (II.11) into the time-harmonic Maxwell equations Eq. (II.10) results in the following conditions that must be satisfied for plane wave solutions to the Maxwell equations:

$$\begin{aligned} \mathbf{k}\cdot\mathbf{E}_0 &= 0 & \mathbf{k}\times\mathbf{E}_0 &= \omega\mu\mathbf{H}_0 \\ \mathbf{k}\cdot\mathbf{H}_0 &= 0 & \mathbf{k}\times\mathbf{H}_0 &= -\omega\varepsilon\mathbf{E}_0 \end{aligned} \qquad (II.12)$$

From Eqs. (II.12) it is apparent that the Maxwell equations admit plane wave solutions when $\mathbf{E}_0$ and $\mathbf{H}_0$ are both perpendicular† to the complex wave vector, $\mathbf{k}$, and that $\mathbf{H}_0$ is perpendicular to $\mathbf{E}_0$. Also, by taking the vector product

$$\mathbf{k}\times(\mathbf{k}\times\mathbf{H}_0) = -\omega\varepsilon\mathbf{k}\times\mathbf{E}_0,$$

† The geometric property of perpendicularity for real vectors is not the necessarily the same for *complex* vectors, but for mathematical preciseness we can define two non-zero complex vectors, e.g., $\mathbf{A}$ and $\mathbf{B}$, as "perpendicular" when $\mathbf{A}\cdot\mathbf{B} = 0$.

using the identity $\mathbf{A} \times (\mathbf{B} \times \mathbf{C}) = \mathbf{B}(\mathbf{A} \cdot \mathbf{C}) - \mathbf{C}(\mathbf{A} \cdot \mathbf{B})$, and using $\mathbf{k} \times \mathbf{E}_0 = \omega\mu\mathbf{H}_0$ one obtains the magnitude of the wave vector as $\mathrm{k} = \sqrt{\mathbf{k} \cdot \mathbf{k}} = \omega\sqrt{\mu\varepsilon}$. In terms of the complex refractive index, m, k becomes

$$\mathrm{k} = \frac{\omega m}{c} = \frac{2\pi m}{\lambda_0}$$

where λ_0 is the wavelength in vacuum. If we let $m = n + ik$, where k is the absorption index (not the magnitude of the complex wave vector, k; note the difference in typeface) then a solution for plane electromagnetic waves is

$$\mathbf{A}_c = \mathbf{A}_0 \exp\left[-\frac{2\pi k r}{\lambda_0} + i\left(\frac{2\pi n r}{\lambda_0} - \omega t\right)\right] \qquad (II.13)$$

where $\mathbf{A}$ represents either $\mathbf{E}$ or $\mathbf{H}$.

II.1.5 The Poynting Vector

The power flux (or intensity) associated with an electromagnetic wave is described by the Poynting vector, $\mathbf{S} = \mathbf{E} \times \mathbf{H}$ (see Jackson [19] for a derivation) where $\mathbf{S}$ has the units of energy per unit area per unit time. The energy flow is in the direction normal to both the electric and magnetic fields and is *not* a linear function of the electromagnetic field amplitude.

For time harmonic fields, the Poynting vector can be computed from the cross product of the *physical* fields using

$$\mathbf{S} = \mathrm{Re}\{\mathbf{E}_c\} \times \mathrm{Re}\{\mathbf{H}_c\}.$$

The power flux is a rapidly varying function of time, since both $\mathbf{E}_c$ and $\mathbf{H}_c$ are varying with frequency ω. Since under most circumstances the frequency is so large that no detector can respond fast enough, it is more useful to use a time-averaged Poynting vector $\langle \mathbf{S} \rangle$ defined by

$$\langle \mathbf{S} \rangle \equiv \frac{1}{\tau} \int_t^{t+\tau} \mathbf{S}\left(t'\right) dt' \quad ; \quad (\tau\omega \gg 1) \qquad (II.14)$$

where the integration is over a time τ much longer that the period $(2\pi/\omega)$ and much smaller than the time for macroscopic change. It is usual to omit the brackets, $\langle\rangle$, and denote the time averaged Poynting vector by $\mathbf{S}$ unless otherwise stated.

For time harmonic fields, the time-average Poynting vector can be evaluated explicitly. The real parts of the time harmonic fields are

$$\mathrm{Re}\{\mathbf{E}_c(\mathbf{r})\,e^{i\omega t}\} = \tfrac{1}{2}\left[\mathbf{E}_c(\mathbf{r})\,e^{-i\omega t} + \mathbf{E}_c^*(\mathbf{r})\,e^{i\omega t}\right]$$
$$\mathrm{Re}\{\mathbf{H}_c(\mathbf{r})\,e^{i\omega t}\} = \tfrac{1}{2}\left[\mathbf{H}_c(\mathbf{r})\,e^{-i\omega t} + \mathbf{H}_c^*(\mathbf{r})\,e^{i\omega t}\right]$$

where $()^*$ denoted complex conjugate, which gives

$$\mathrm{Re}\{\mathbf{E}_c(\mathbf{r},t)\} \times \mathrm{Re}\{\mathbf{H}_c(\mathbf{r},t)\} = \frac{1}{4}\left[\mathbf{E}_c(\mathbf{r}) \times \mathbf{H}_c^*(\mathbf{r})\right] + \frac{1}{4}\left[\mathbf{E}_c^*(\mathbf{r}) \times \mathbf{H}_c(\mathbf{r})\right] + \frac{1}{4}\left[\mathbf{E}_c(\mathbf{r}) \times \mathbf{H}_c(\mathbf{r})\,e^{-2i\omega t} + \mathbf{E}_c^*(\mathbf{r}) \times \mathbf{H}_c^*(\mathbf{r})\,e^{2i\omega t}\right].$$

Using the fact that $\mathrm{Re}\{z\} = \mathrm{Re}\{z^*\}$, the time averaged Poynting vector is simply

$$\mathbf{S} = \frac{1}{2}\,\mathrm{Re}\{\mathbf{E}_c(\mathbf{r}) \times \mathbf{H}_c^*(\mathbf{r})\} \qquad (II.15)$$

since the real part of terms involving $e^{\pm i\omega t}$ vanish when integrated over times long compared to $2\pi/\omega$.

Using the plane wave solutions, Eq. (II.11), the time-averaged Poynting vector becomes

$$\begin{aligned}\mathbf{S} &= \tfrac{1}{2}\,\mathrm{Re}\{\mathbf{E}_c(\mathbf{r})\} \times \mathbf{H}_c^*(\mathbf{r})\} \\ &= \tfrac{1}{2}\,\mathrm{Re}\{\frac{\mathbf{E}_0 \times (\mathbf{k}^* \times \mathbf{E}_0^*)\exp\left(-\frac{4\pi k r}{\lambda_0}\right)}{\omega\mu}\}. \qquad (II.16)\end{aligned}$$

For media of interest here, the vectors $\mathbf{E}_0, \mathbf{H}_0, \mathbf{k}$ are perpendicular; therefore by using the vector identity

$$\mathbf{E}_0 \times (\mathbf{k}^* \times \mathbf{E}_0^*) = \mathbf{k}^*\,(\mathbf{E}_0 \cdot \mathbf{E}_0^*) - \mathbf{E}_0^*\,(\mathbf{k}^* \cdot \mathbf{E}_0)$$

and the relation for homogeneous waves $\mathbf{k}^* \cdot \mathbf{E}_0 = 0$, Eq. (II.16) can be written as

$$\mathbf{S} = \mathrm{S}_0 \exp\left(-\frac{4\pi k r}{\lambda_0}\right)\hat{\mathbf{e}} \qquad (II.17)$$

Here the direction of propagation is the direction of the real unit vector $\hat{\mathbf{e}}$ and the wave magnitude decreases with increasing distance, r, for non-zero absorption index, k. The magnitude of the power flux, S, is usually defined as the irradiance, $I = \mathrm{S}$, which is *related* to the radiance defined in radiation heat transfer. However, the precise definition of the radiance is power flux per unit solid angle, or $\partial \mathrm{S}/\partial\Omega$, where Ω is the solid angle. There is some subtle inconsistency here, since if the wave were truly a

plane wave then $\partial S/\partial\Omega \equiv 0$. The explanation is that for purposes of understanding the interaction of electromagnetic waves with matter, e.g., reflection at a boundary, it is mathematically convenient to consider the theoretical limit where the waves are planar, and ignore slight variations in the direction of wave propagation. But when one's principal interested is the power flux (power/area) for finite areas then it is important to account for the $1/r^2$ decrease with distance r from the power source. Therefore, it is more useful to distinguish between the power flux, S, for the theoretical limit of $r \to \infty$ and the radiance, I, by defining

$$I \equiv \frac{\partial S}{\partial \Omega}$$

where Ω is the solid angle about the direction of propagation, $\hat{\mathbf{e}}$. This definition admits the usual Beer's law,

$$I = I_0 \exp\left(-\frac{4\pi k r}{\lambda_0}\right) = I_0 e^{-\alpha_\lambda r} \qquad (II.18)$$

which is exactly analogous to Eq. (II.17), where the *spectral absorption coefficient*, α_λ, is defined as

$$\alpha_\lambda \equiv \frac{4\pi k}{\lambda_0}. \qquad (II.19)$$

Note that while k is dimensionless, α_λ has units of $length^{-1}$.

Another common definition of the absorption coefficient used in engineering applications is $\alpha_\lambda = \frac{\partial I}{\partial r}$, which can result in slightly more complicated interpretations of the absorption coefficient. Fortunately, for most engineering applications this definition is consistent with Eq. (II.19), so the differences will not be discussed (see Siegel and Howell [20]).

II.1.6 Normal Reflection at a Plane Boundary

Consider the reflection and transmission of radiation at normal incidence from a planar boundary between two media with complex refractive indices m_1 and m_2, respectively. A plane homogeneous wave is incident on medium 1 from medium 2 with the direction of propagation $\hat{\mathbf{e}}$ normal to the interface between medium 1 and medium 2 (see Fig. II.1). The electric fields in medium 1 and medium 2 are

$$\mathbf{E}_t \exp\left[i\omega\left(\frac{m_1 x}{c} - t\right)\right], \qquad (x > 0)$$

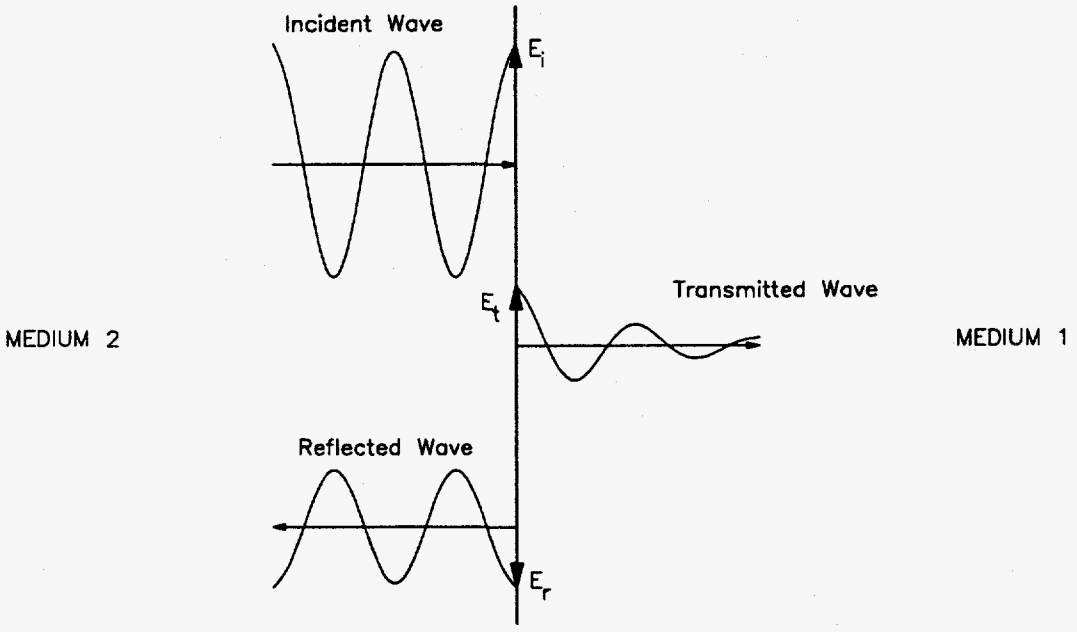

Figure II.1: Schematic of incident, reflected, and transmitted waves at the interface between to media.

and

$$\mathbf{E}_i \exp\left[i\omega\left(\frac{m_2 x}{c} - t\right)\right] + \mathbf{E}_r \exp\left[i\omega\left(\frac{m_2 x}{c} - t\right)\right] \qquad (x < 0)$$

respectively.

In the absence of surface charge or current, the electric field and magnetic field, which are both tangential to the interface at $x = 0$, are required to be continuous [19]. Thus at the interface the electric fields satisfy

$$\mathbf{E}_i + \mathbf{E}_r = \mathbf{E}_t \qquad (II.20)$$

and, using $\mathbf{H}_0 = \mathbf{k} \times \mathbf{E}_0/(\omega\mu)$, the condition for the magnetic field yields

$$\mathrm{k}_2 \frac{(\mathbf{E}_i - \mathbf{E}_r)}{\mu_2} = \mathrm{k}_1 \frac{\mathbf{E}_t}{\mu_1}. \qquad (II.21)$$

At optical frequencies and for non-magnetic media, it is usually a good assumption that $\mu_1 = \mu_2$ (for discussion, see [21]) † Since for homogeneous waves $k_1/k_2 = m_1/m_2$, Eq. (II.21) can be written as

$$\mathbf{E}_i - \mathbf{E}_r = \frac{m_1}{m_2}\mathbf{E}_t. \qquad (II.22)$$

Solving Eq. (II.20) and Eq. (II.22) for the reflection, $\tilde{r}$, and transmission, $\tilde{t}$, coefficients defined as

$$\mathbf{E}_r = \tilde{r}\mathbf{E}_i\ , \qquad \mathbf{E}_t = \tilde{t}\mathbf{E}_i,$$

we have

$$\tilde{r} = \frac{1-m}{1+m}\ , \qquad \tilde{t} = \frac{2}{1+m}; \qquad m \equiv \frac{m_1}{m_2}. \qquad (II.23)$$

Note the introduction of a relative refractive index, $m = n + ik$. From here on this quantity is just referred to as the refractive index, m, of medium 1 relative to medium 2 when medium 2 is air or vacuum.

The fraction of the incident power that is reflected is given by the reflectance R, where

$$R = |\,\tilde{r}\,|^2 = |\,\frac{1-m}{1+m}\,|^2 = \frac{(n-1)^2 + k^2}{(n+1)^2 + k^2} \qquad (II.24)$$

Eq. (II.24) is commonly referred to as the Fresnel relation for normal reflectance. If the absorption index, k, is small compared to $(n-1)$, then the reflectance is not significantly changed by small changes in k. Also, the reflectance, Eq. (II.24), is not significantly changed by re-orienting the incident beam to a *near normal* position [20].

II.2 Frequency Dependence of The Optical Constants

The optical constants of all materials vary with frequency (or free-space wavelength $\lambda_o = 2\pi c_o/\omega$). For insulating materials, if one considers a broad range of frequencies, it is found that the absorption index, k, may vary by several orders of magnitude. The real refractive index, n, varies somewhat less, but the variations in n

† To understand this point, note that the permeability is a measure of the ability of a material to set up a magnetic dipole in response to an applied magnetic field. But in **isotropic** materials, this would require "lining up" many tiny current loops in the material (e.g., bound electrons) at rates on the order of the frequency of the magnetic field. At optical frequencies or higher, the electrons would have to be reacting at relativistic velocities, and they simply cannot in most circumstances.

are largest at frequencies where k is also rapidly changing with frequency. As this behavior suggests, the absorption index, k, and refractive index, n, are not independent, but are related through the Kramers–Kronig relations [18].

This section summarizes the theoretical background for understanding the frequency dependence of the optical constants for insulating solids. First a simple oscillator model is presented to illustrate the frequency dependence of the optical constants. This model is rather specific, since it is restricted to absorption mechanisms which are reasonably modeled by damped harmonic oscillators, but it accurately predicts the behavior of the optical constants of many insulating materials at infrared frequencies. Once the specific model is discussed, the more general Kramers–Kronig relations are presented, along with a discussion of how they may be used to determine the optical constants of materials from measurements of near–normal reflectance.

II.2.1 Classical Oscillator Model for the Optical Constants

The classical harmonic oscillator model, the so–called Lorentz model, provides useful insight into the spectral dependence of the optical properties of many materials, particularly non–conductors. Although the model is rather simple, compared to more complete quantum mechanical models, it gives surprisingly good results in many cases and generally provides a good basis for understanding the frequency dependence of the optical properties.

In this classical model, the material is considered to be composed of a collection of electrically charged point masses, each bound to its equilibrium position by a linear spring (i.e., the displacement from equilibrium is proportional to the force acting on the mass). In addition to the restoring force, the model assumes a damping force which is proportional to the velocity of the mass. The governing equation is

$$m\frac{d^2\mathbf{x}}{dt^2} + b\frac{d\mathbf{x}}{dt} + K\mathbf{x} = e\mathbf{E}. \qquad (II.25)$$

Here $\mathbf{x}$ is the displacement from the equilibrium particle position, m is the mass of the particle (e.g. electron or atom), b is the damping constant, K is the spring constant, e is the particle charge driven by the local electric field $\mathbf{E}$.

If the electric field, $\mathbf{E}$, is harmonic with frequency ω, then the solution to Eq. (II.25) is

$$\mathbf{x} = \frac{(e/m)\,\mathbf{E}}{\omega_0^2 - \omega^2 - i\gamma\omega.} \qquad (II.26)$$

Here the natural frequency, ω_0, is $\sqrt{K/m}$ and $\gamma = b/m$. For a single oscillator, the polarization is $e\mathbf{x}$, and if there are N oscillators per unit volume then the polarization, $\mathbf{P}$, is simply $Ne\mathbf{x}$. Defining the *plasma frequency*, ω_p, such that $\omega_p^2 = Ne^2/m\varepsilon_0$, the polarization becomes

$$\mathbf{P} = \frac{\omega_p^2}{\omega_0^2 - \omega^2 - i\gamma\omega}\varepsilon_0\mathbf{E}. \qquad (II.27)$$

This equation describes the polarization owing to a single type of oscillator, having a single binding potential (spring constant), and a single natural frequency ω_0. If the material consists of a number of different oscillators, we can sum over all oscillators to obtain the relation

$$\mathbf{P} = \sum_j \frac{\omega_{pj}^2}{\omega_{0j}^2 - \omega^2 - i\gamma_j\omega}\varepsilon_0\mathbf{E}. \qquad (II.28)$$

Here the subscript j denotes values for one particular harmonic oscillator with plasma frequency ω_{pj}, natural frequency ω_{0j}, and damping coefficient γ_j.

From Eq. (II.28) the complex permittivity (or dielectric function) can be written as

$$\varepsilon(\omega) = \varepsilon_0\left[1 + \chi(\omega)\right] = \varepsilon_0\left[1 + \sum_j \frac{\omega_{pj}^2}{\omega_{0j}^2 - \omega^2 - i\gamma_j\omega}\right]. \qquad (II.29)$$

This expression shows that the complex dielectric function, $\epsilon = \varepsilon/\varepsilon_0$, for a collection of oscillators is a summation of the dielectric functions for each oscillator. The complex refractive index, $m = \sqrt{\epsilon}$, does not have this property.

At frequencies far from the natural frequency of a particular oscillator (j), where $\gamma_j\omega/(\omega_{0j}^2 - \omega^2) \ll 1$, that oscillator does not contribute significantly to the imaginary part of the dielectric function. If one is interested primarily in, say, infrared frequencies, then the real contribution due to higher frequency oscillators can be grouped into a single real constant, n_∞^2 so that

$$\epsilon = m^2 \simeq n_\infty^2 + \sum_j \frac{\omega_{pj}^2}{\omega_{0j}^2 - \omega^2 - i\gamma_j\omega}. \qquad (II.30)$$

Note here that n_∞^2 is necessarily larger than unity since it is the sum of unity and all the positive high frequency terms (e.g., due to oscillations of electrons about their equilibrium positions orbiting an atom).

As discussed at the beginning of this section, the classical oscillator model provides an accurate model for the optical properties of many materials (esp. non-conductors).

Before comparing its predictions with actual optical constants for real materials, consider the behavior predicted by Eq. (II.30) for a single oscillator. For illustrative purposes let $\omega_p/\omega_0 = 1.0$, $\gamma/\omega_0 = 0.1$, and $n_\infty = 1.5$. The resulting complex dielectric function, refractive index, and normal reflectivity are shown in Fig. II.2.

Several important characteristics common to many materials are illustrated in Fig. II.2. First, the imaginary part of the dielectric function ($2nk$) is *approximately* symmetrical about the natural frequency, ω_0, having a maximum near $\omega = \omega_0$. While $2nk$ is always positive, the real dielectric function, $n^2 - k^2$, is negative for a small range of frequencies higher than the natural frequency, gradually increasing to the limiting value n_∞^2 ($= 2.25$) at the high frequency limit.

The complex refractive index shown in Fig. II.2 closely follows the structure of the dielectric function, but with several interesting differences. First, the real refractive index, n, begins at the high frequency limit n_∞ and decreases gradually with decreasing frequency (increasing wavelength) until it reaches a minimum near the absorption feature at $\omega = \omega_0$, This behavior of decreasing n with decreasing frequency is called *normal dispersion*, and is exhibited by all materials over wavelength ranges where they are transparent† . A region of *anomalous dispersion*, where n decreases with increasing frequency, is seen near the region of strong absorption (large k). It is interesting to note that n is less than unity for a range of frequencies higher than ω_0; this is commonly observed near very strong absorption bands in real materials (including coal slag). The wavelength where $n = 1$ and k is still relatively small is called the *Christiansen* wavelength, and corresponds to a region where the reflectance, R, is near a minimum.

The absorption index, k, shown in Fig. II.2 is not as symmetric as the imaginary dielectric function, $2nk$, but does tend to zero on each side of the absorption peak. The peak value of k is shifted to slightly higher frequencies, compared to the peak of $2nk$. While it would be useful to have optical materials that exhibited anomalous dispersion, it is not generally possible, since k is large in those wavelength regions. To demonstrate this fact, consider that for visible light at $\lambda = 0.5\mu$m, the

† The term normal dispersion is due to a dispersion of visible light into its multitude of colors when passed through prisms and other simple transmissive optical elements. The refractive index, n, of common optical materials decreases with increasing wavelength, thus shorter wavelength light is refracted more than longer wavelength light. While this chromatic aberration is is of fundamental importance in prism spectrometers, for example, considerable effort is expended to reduce it in some other instruments. (e.g. telescopes, cameras, etc.).

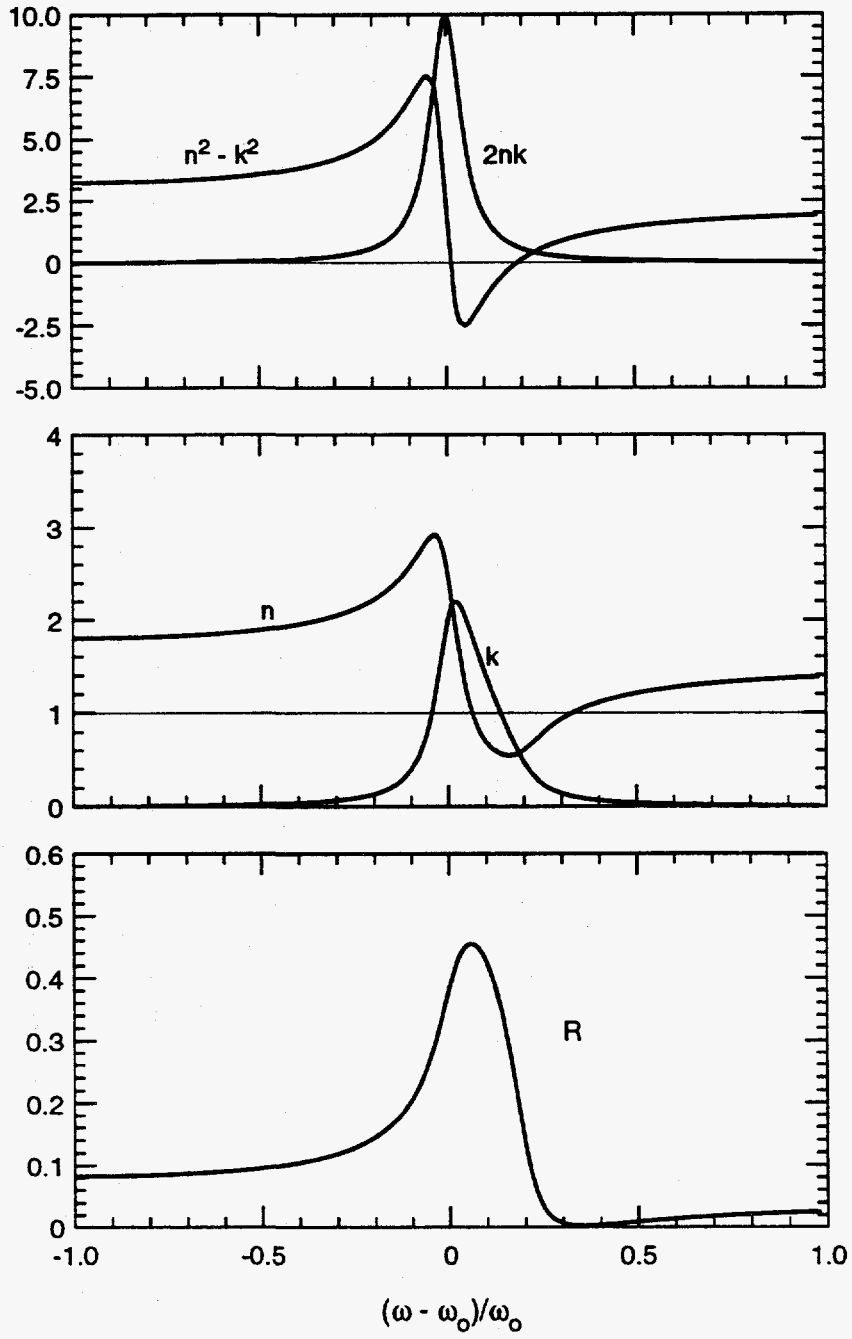

Figure II.2: The complex dielectric function, ϵ, refractive index, $m = \sqrt{\epsilon}$, and normal reflectivity from the damped harmonic oscillator model with $n_\infty = 1.5$, $\gamma/\omega_0 = 0.1$, and $\omega_p/\omega_0 = 1.0$.

transmittance of a 1 mm (1000 μm) thick layer with $k = 10^{-3}$ is only $\exp(-4\pi kL/\lambda)$ or approximately 1.2×10^{-11}.

Finally, the normal reflectance, R, resulting from the damped harmonic oscillator model is illustrated in Fig. II.2. At the two frequency limits shown, the absorption index, k, is small and the normal reflectance is approximately $(n-1)^2/(n+1)^2$. Near the absorption line, where k is large, the reflectance is increased and the contribution by k is significant. The peak in R is shifted to a slightly higher frequency than either the peak in $2nk$ or k, and drops rapidly with increasing frequency on the high frequency side of the absorption line. The minimum in R occurs near the Christiansen wavelength, where $n = 1$. Again, such behavior is commonly observed in many materials.

As an example of the optical properties of a real material consider the absorption band of liquid water near the wavelength of 3 μm illustrated in Fig. II.3. The symbols (o) show the experimental data from Hale and Querry [43] and the solid lines are for a single damped harmonic oscillator fit with $n_\infty = 1.31, \omega_o = 3355\text{cm}^{-1}, \omega_p = 915\text{cm}^{-1}$, and $\gamma = 305\text{cm}^{-1}$. The oscillator model clearly predicts the qualitative trends in the data, and is also a reasonably accurate quantitative model. The deviations of the fit from the data are due, in part, to the neglect of nearby weaker absorption bands, but it is also quite likely that the vibrational mode at 3 μm is not exactly a single damped harmonic oscillator. For example, the damping factor γ may depend on frequency.

II.2.2 Kramers-Kronig Relations

The complex refractive index, $m = n + ik$, is very frequency dependent when considered over a wide range of frequencies. By using the principle of *causality* and the *linearity* of the response of a medium to an externally applied field, along with certain physical constraints on the asymptotic behavior of the phenomenological coefficients, one can construct relationships between the real and imaginary parts of the complex refractive index (or any other similar causal analytic function). These relations are the so-called *Kramers-Kronig* relations. Since the derivation of these relations adds little physical insight, they are presented here without proof. Several standard texts outline the derivation [18,19,21], leading to the result that the frequency dependence

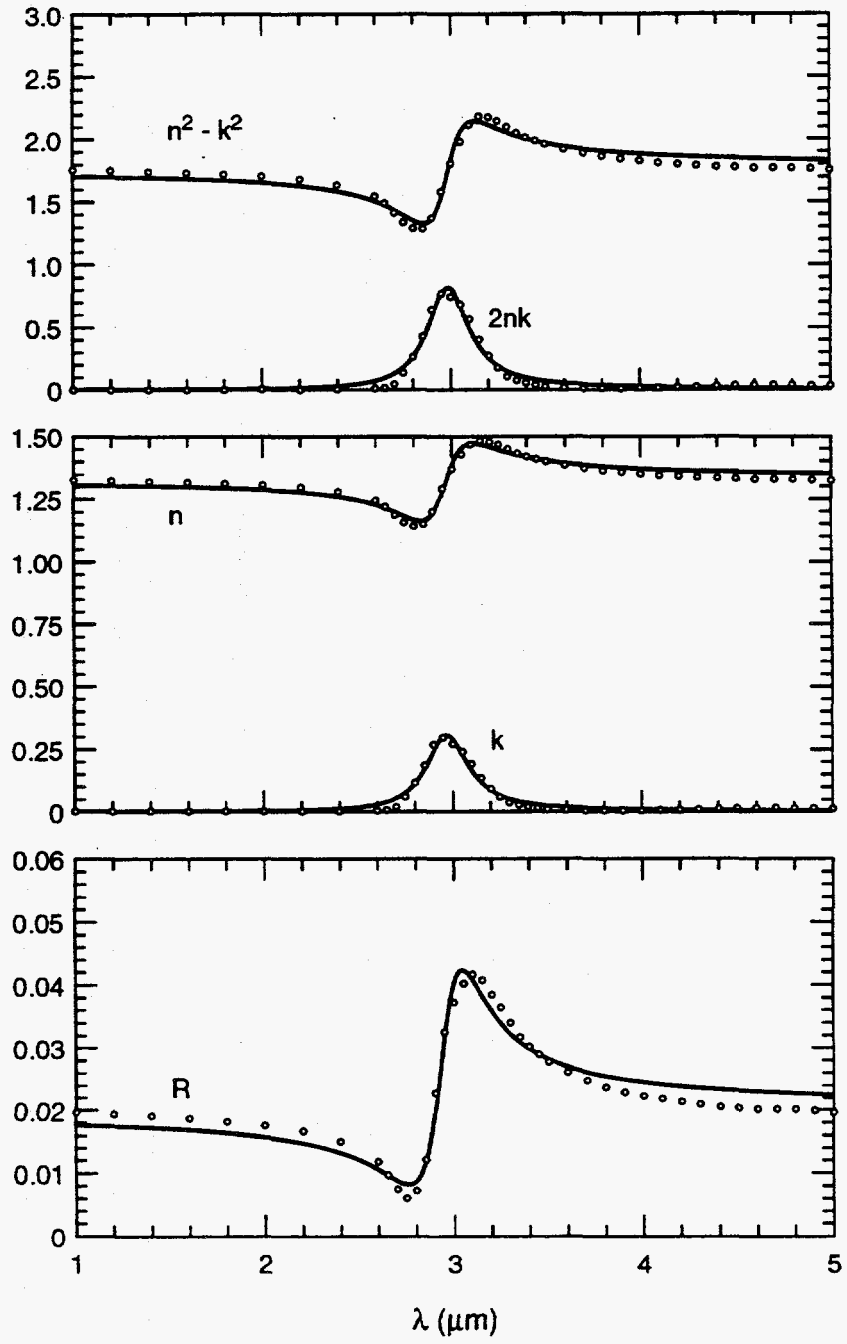

Figure II.3: The complex dielectric function, ϵ, refractive index, $m = \sqrt{\epsilon}$, and normal reflectivity of liquid water (o) in the wavelength range from 1 to 5 μm compared to a single damped oscillator model with $n_\infty = 1.31$, $\omega_0 = 3355\text{cm}^{-1}$, $\omega_p = 915\text{cm}^{-1}$, and $\gamma = 305\text{cm}^{-1}$. Data from Hale and Querry(1973), see Appendix C.

of the real and imaginary parts of the complex refractive index ($m = n + ik$) are restricted to forms which satisfy the relations

$$n(\omega) - 1 = \frac{2}{\pi} P \int_0^\infty \frac{\omega' k(\omega')}{\omega'^2 - \omega^2} d\omega' \qquad (II.31a)$$

$$k(\omega) = -\frac{2}{\pi} P \int_0^\infty \frac{n(\omega')}{\omega'^2 - \omega^2} d\omega'. \qquad (II.31b)$$

Here ω is frequency and P denotes the Cauchy principal values† of the integrals.

The Kramers–Kronig relations are quite remarkable and their physical implications were not understood prior to their derivation in the 1920's by Kramers and Kronig (independently). From Eq. (II.31) we see that if we know either n or k at all frequencies then either k or n, respectively, can be computed. However, we do not generally know n or k at *all* frequencies, therefore it is useful to formulate Kramers–Kronig relations for quantities we *can* measure directly.

Reconsider the near normal reflection of radiation from a planar interface. The complex reflectance coefficient, $\tilde{r}$, can be recast as a real reflection coefficient, r, and a phase shift upon reflection, Θ. That is, we can write

$$\tilde{r} = re^{i\Theta}$$

where the normal reflectance, R, is now just $R = \mid r \mid^2$. In this form, the Kramers-Kronig (KK) relation relating Θ and R is [18]

$$\Theta(\omega) - \pi = -\frac{\omega}{\pi} P \int_0^\infty \frac{\ln R(\omega')}{\omega'^2 - \omega^2} d\omega'. \qquad (II.32)$$

Using this relation one can measure R then compute $\Theta(\omega)$. Having Θ and R, the real and imaginary parts of the refractive index are obtained from

$$n = \frac{1 - R}{1 + R + 2\sqrt{R}\cos\Theta}, \qquad (II.33a)$$

$$k = \frac{-2\sqrt{R}\sin\Theta}{1 + R + 2\sqrt{R}\cos\Theta} \qquad (II.33b)$$

---

† The Cauchy principal value of an integral is obtained by breaking the integral into two ranges, one for each side of the singularity at $z = x$, say, and letting the limits of the integrals approach the singularity, such that

$$\mathrm{P}\int_0^\infty \frac{f(z)}{z - x} dz = \lim_{a \to 0} \int_0^{x-a} \frac{f(z)}{z - x} dz + \lim_{a \to 0} \int_{x+a}^\infty \frac{f(z)}{z - x} dz.$$

It is useful to subtract $\ln R(w)/(\omega'^2 - \omega^2)$ from the integrand in Eq. (II.32), which does not affect the integral since $\int_0^\infty 1/(\omega'^2 - \omega^2)d\omega' = 0$. The result is that the modified integrand is finite at $\omega' = \omega$, and can be more easily integrated using standard numerical schemes. The resulting formulation is

$$\Theta(\omega) - \pi = -\frac{\omega}{\pi} P \int_0^\infty \frac{\ln R(\omega') - \ln R(\omega)}{\omega'^2 - \omega^2} d\omega'. \qquad (II.34)$$

At $\omega' = \omega$ the integrand approaches the value

$$\lim_{\omega' \to \omega} \frac{\omega}{\pi} \frac{\ln R(\omega') - \ln R(\omega)}{\omega'^2 - \omega^2} = \frac{1}{2\pi R(\omega)} \frac{dR(\omega)}{d\omega} \qquad (II.35)$$

In practice the reflectance is only known over a finite spectral range, say $\omega_1 \leq \omega \leq \omega_2$. In this case the KK relation for Θ, Eq. (II.34), can be divided into an integral over three ranges, i.e.,

$$\begin{aligned} \Theta(\omega) - \pi = &- \frac{\omega}{\pi} P \int_0^{\omega_1} \frac{\ln[R(\omega')/R(\omega)]}{\omega'^2 - \omega^2} d\omega' \\ &- \frac{\omega}{\pi} P \int_{\omega_1}^{\omega_2} \frac{\ln[R(\omega')/R(\omega)]}{\omega'^2 - \omega^2} d\omega' \\ &- \frac{\omega}{\pi} P \int_{\omega_2}^{\infty} \frac{\ln[R(\omega')/R(\omega)]}{\omega'^2 - \omega^2} d\omega'. \end{aligned} \qquad (II.36)$$

If the numerator of the integrand is well behaved, i.e., finite, then the contribution to the integral at frequencies far from ω decreases as $\omega'^2 - \omega^2$ increases. Therefore, it may be possible to assume that R is constant outside the range of the measured reflectance and, as shown by Fig. II.2 or Fig. II.3, the assumption is reasonable so long as the neighboring absorption features are at frequencies far from the range of measured R. For example, assume that the reflectance outside the measured frequency interval is given by

$$R(\omega) = \begin{cases} R(\omega_1) & ; \quad \omega < \omega_1 \\ R(\omega_2) & ; \quad \omega > \omega_2 \end{cases} \qquad (II.37)$$

With this assumption Eq. (II.36) can be simplified to

$$\begin{aligned} \Theta(\omega) - \pi = &\frac{\ln[R(\omega_1)/R(\omega)]}{2\pi} \ln\left|\frac{\omega + \omega_1}{\omega - \omega 1}\right| + \frac{\ln[R(\omega_2)/R(\omega)]}{2\pi} \ln\left|\frac{\omega_2 - \omega}{\omega_2 + \omega}\right| \\ &- \frac{\omega}{\pi} \int_{\omega_1}^{\omega_2} \frac{\ln[R(\omega')/R(\omega)]}{\omega'^2 - \omega^2} d\omega'. \end{aligned} \qquad (II.38)$$

This form of the Kramers-Kronig relation, with the assumed constant values of R outside of the measured wavelength range (Eq. (II.37)), was used successfully by Goodwin [11] for determining the optical constants of room temperature coal slags.

II.2.3 Behavior of the Kramers–Kronig Relation for $k \ll n$.

From Eq. (II.24) it is apparent that if $(n-1)^2$ is much larger than k^2, then the normal reflectance is not sensitive to changes in k, and one cannot accurately find k directly from measurements of R. To see how the Kramers–Kronig relations behave in this limit reconsider the normal reflection coefficient formula, Eq. (II.23), written as

$$\tilde{r} = \frac{1-m}{1+m} = x + iy \qquad (II.39)$$

where

$$x \equiv \frac{1-n^2}{(n+1)^2+k^2}, \quad \text{and} \quad y \equiv -\frac{2k}{(n+1)^2+k^2}. \qquad (II.40)$$

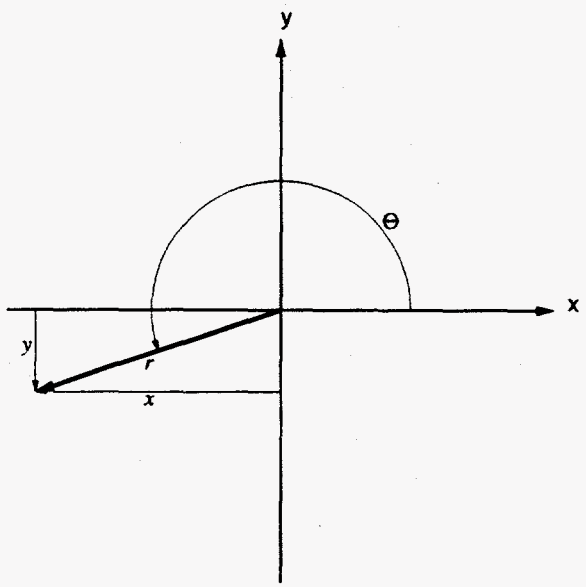

Figure II.4: Schematic showing $\tilde{r}$ in the complex plane for $n > 1$

Figure II.4 shows the representation of $\tilde{r}$ in the complex plane. If $n-1$ is positive then x is negative and since k is always positive y is always negative. If $2k$ is much smaller than $(n+1)(n-1)$ then the angle Θ is approximately π, and to first order approximation we have

$$\cos(\Theta) \simeq -1 \qquad (II.41)$$

corresponding to 180° phase change on reflection. Using this approximation in Eq. (II.33) gives

$$n \simeq \frac{1+\sqrt{R}}{1-\sqrt{R}} \qquad (II.42)$$

or

$$R \simeq \frac{(n-1)^2}{(n+1)^2}. \qquad (II.43)$$

From this analysis it is evident that if the Kramers–Kronig formulas accurately predict $\Theta \simeq \pi$ in regions of small k then they will also predict n accurately. From the discussion on damped harmonic oscillators we know that one characteristic of regions of small k is that R is approximately constant. Therefore, to the extent that R *is* a constant for frequencies where k is small, we have

$$\int_0^\infty \frac{\ln(R)\, d\omega'}{\omega'^2 - \omega^2} \simeq 0,$$

and the Kramers–Kronig relation (Eq. (II.32) or Eq. (II.38)) produces the desired result ($\Theta \simeq \pi$). At frequencies far from the region of interest R is certainly not constant, but the integrand $\ln(R)/(\omega'^2 - \omega^2)$ becomes vanishingly small and does not contribute to the integral. This feature is very important since it allows application of the Kramers–Kronig relations to data obtained over a finite frequency range.

Finally, the failure of the Kramer–Kronig to predict k accurately in regions of small k is not difficult to understand. Consider the effect of k on R by differentiating Eq. (II.24) with respect to k. The resulting equation is

$$\frac{dR}{R} = \left[\frac{2k^2}{(n-1)^2 + k^2} - \frac{2k^2}{(n+1)^2 + k^2}\right]\frac{dk}{k}. \qquad (II.44)$$

The sensitivity coefficient $(dR/R)/(dk/k)$ is shown in Fig. II.5 versus k for several values of n (n=1.1, 1.5, and 3.0). If $(dR/R)/(dk/k)$ is small then large changes in k are required to produce measurable changes in R, and conversely, small uncertainties in R correspond to large uncertainties in k. For example, if $n = 1.5$ and $k \simeq 10^{-3}$ then a one percent uncertainty in R corresponds to a 1000% uncertainty in k.

Although this sensitivity was derived using the Fresnel relations for normal reflectance, it shows a fundamental limit to all normal reflectance measurements. It is not possible to use the Kramers–Kronig analysis, or any other technique, to accurately determine k when it is small compared to $n - 1$. However, if k is larger

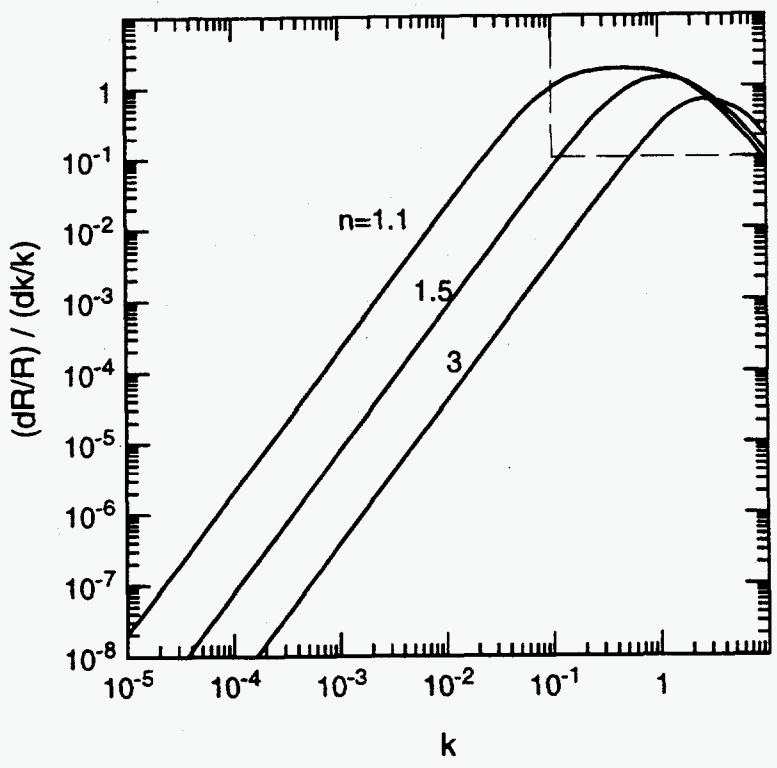

Figure II.5: The sensitivity of R to k versus k for several values of n.

than approximately 0.1, corresponding to the dashed box in Fig. II.5, then R is sensitive to k (for the values of n considered here). Also, if $n-1$ is small compared to k, say $n = 1$, then the normal reflectance is entirely due to k, and the sensitivity of R to k is two, independent of the value of k. This latter feature is of practical interest, since it allows k to be determined simply at one or two wavelengths (where $n = 1$) near a strong absorption band using only normal reflectance measurements.

Another interesting feature illustrated in Fig. II.5 is the downward turn in $(dR/R)/(dk/k)$ for large k. If k is very large compared to unity then the sensitivity of R to k is again small. This limit may be of interest for metals, where both n and k are large over a broad spectral range.

Chapter III.

Experimental Apparatus and Procedures

This chapter describes the apparatus and procedures used to measure the optical constants of molten coal slag. An electric furnace was modified to allow preparation of melts, and to facilitate near normal reflectance measurements, and transmittance measurements on molten slags. Several slags were produced to study the effect of composition on the optical constants. Synthetic slags were produced by melting mixtures of powdered oxides and "natural" slags were produced by melting fly ash.

After melts were produced, and a sufficient quantity of slag obtained, the solid slag was placed in crucibles (usually of alumina) and reheated in the electric furnace to approximately 1600°C. The near normal reflectance was measured over the wavelength range $1 \leq \lambda < 13\mu$m. The Kramers–Kronig (KK) procedure was used to compute the real refractive index, n, over the entire wavelength range for which reflectance was obtained. This KK analysis also yields the imaginary refractive index, k, but only in wavelength ranges where $k > 0.1$.

Transmittance was measured using a procedure similar to that for the reflectance measurements, except that a platinum mirror was suspended just below the surface of the molten slag. By changing the depth of this platinum mirror and making measurements at two mirror depths, the transmittance of the molten slag was measured over the wavelength range $1 \leq \lambda < 5\mu$m. The transmittance of the molten slags is too small to measure at wavelengths longer than approximately 5 μm, or for slags with more than approximately 5 wt.% Fe_2O_3.

The following sections give details of the apparatus and procedures. The first section describes the apparatus and procedures for producing synthetic and natural slags, along with a detailed description of the electric furnace used throughout the experimental work. The second section describes the optical system and the procedures used to measure the near normal reflectance of molten slags. The final section describes the apparatus and procedures used to measure the transmittance of the molten slags.

III.1 Slag Production

Slag is the bulk glassy solid (or liquid) produced by melting either powdered metal oxides (synthetic slag) or real fly ash (natural slag). There are three important aspects to slag production: 1) slag composition, 2) furnace design, and 3) melt procedures. Discussions of slag composition might ordinarily be confined within discussions of results; however, the melting characteristics of the slag depend strongly on composition and were found to have a critical influence on the experimental procedures. Therefore, the criteria used for selecting the slag composition are included here.

III.1.1 Selection of Slag Compositions

The composition of fly ash varies from particle to particle, but the refractive index is not sensitive to small variations of most minor species [11]. The primary constituents for *most* particles are SiO_2, Al_2O_3, Fe_2O_3, and CaO. Other constituents are either present in small amounts, present in large amounts in just a few particles, or do not significantly affect the optical constants in the wavelength range of interest for heat transfer analysis. Therefore, synthetic slags were produced from mixtures of these four primary constituents. An additional criterion for the choice of synthetic slag compositions was the desire to directly compare results with the lower temperature measurements of Goodwin [11]. Five slags were produced to meet this criterion.

A range of slag compositions were studied. Ideally one would like to use a full range of compositions based exclusively on composition measurements on ash particles. To some degree this was done, however there are practical constraints on the choice of composition. First, the slag must be of a composition that will melt at temperatures below 1600°C, the maximum temperature limit for the furnace. From the phase diagram for Alumino-Calcia-Silicates shown in Fig. III.1 [22], it is apparent that there are many compositions that meet this criterion and many that do not. All of the slags in this study were chosen to meet this criterion.

The next criterion is that the molten slag must be inviscid enough to allow the submerged platinum mirror to move, as was discovered after several failed attempts to measure transmittance. This requirement is only critical for transmittance measurements, and does not affect reflectance measurements. As discussed in more detail

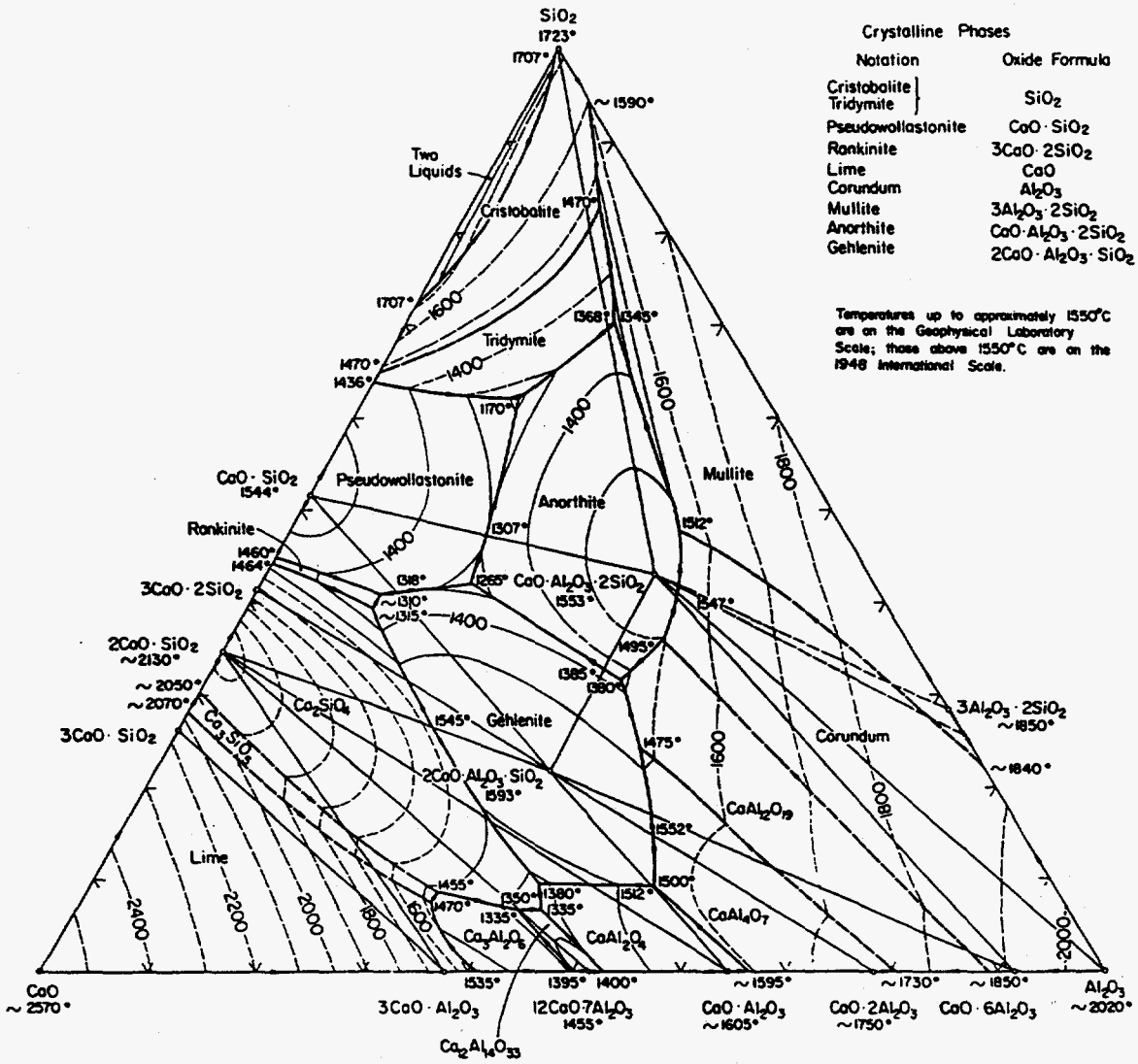

Figure III.1: Phase diagram for Al_2O_3 – CaO– SiO_2 (from Levin et al.(1964)). Compositions are in weight percent and temperatures are in centigrade(°C)

in section 3.0 of this chapter, the transmittance measurements are made by moving the crucible of liquid slag vertically relative to the submerged platinum mirror. If the slag is too viscous, then this motion causes excessive drag on the mirror, resulting in bending of the mirror support rods and/or misalignment of the mirror. Also, if the slag is too viscous then the surface deformation caused by the motion of the slag over the platinum mirror subsides too slowly. One slag (SA1S) did not meet this criterion, probably because its melting point was too near the 1600°C temperature limit.

A third criterion for slag composition is that the molten slag solution should not dissolve the alumina crucible in which it is contained. This criterion is very important, and was not met on several occasions with troublesome consequences. Most of the slags produced for this study do not strictly meet this criterion, since almost all will dissolve the alumina crucible if left at 1600°C for an extended period of time. However, most of the slags were found to meet this criterion if the duration at 1600°C was limited to approximately 12 hours.

The need for this third criterion is most easily understood by considering the effects of failing to meet it. When the crucible is dissolved the molten slag runs onto the surrounding furnace components (outer furnace tube and support tubes). Since the expansion coefficient of the alumina is larger than that of the slag, when the furnace is cooled the slag/alumina interface is stressed and, if the slag layer is strong enough, the alumina breaks (Note that the cool slag layer is in compression while the cool alumina layer is in tension; thus a thin slag layer is generally as strong as a thicker alumina layer). Loud cracking sounds occurred at temperatures below about 600°C, probably depending on the geometric configuration of the slag/alumina interface. Since replacement of the alumina components inside the furnace is both expensive and time consuming, this criterion limits the duration of a single experiment to approximately 12 hours. Slags that were found to dissolve the alumina crucible in less than 12 hours were reproduced in platinum crucibles.

III.1.2 Preparation of Powdered Oxide Mixtures

To make a synthetic slag, a mixture of high purity powdered oxides SiO_2, Al_2O_3, CaO, and Fe_2O_3 were mixed with sufficient distilled water to allow the mixture to be stirred and agitated (ultrasonically) until the slurry was visibly homogeneous. The reddish tint of the mixture, due to Fe_2O_3, became uniform when the slurry was

well–mixed. This mixture was placed on an aluminum foil platter and baked in a low temperature utility furnace at approximately 150–200°C for several hours, until the water was evaporated† . This process produced clumps of powder which were packed into a large (100 mℓ) high purity (99.8%, Coors) alumina crucible‡ . Approximately 100 g of powder was packed into a 100 mℓ crucible and placed in the high temperature furnace for melting.

Table III.1: Compositions (in wt.%) of Oxide Powder Mixtures

Slag	SiO_2	Al_2O_3	CaO	Fe_2O_3
SA00	58.00	29.00	13.00	0.00
SA01	57.42	28.71	12.87	1.00
SA05	55.10	27.55	12.35	5.00
SA10	52.20	26.10	11.70	10.0
SA20	46.40	23.30	10.40	20.0
SA4S	38.83	23.30	34.95	2.90
SA2S	18.60	43.71	30.69	7.00
SA1S	9.62	40.38	46.15	3.85

The mixture compositions for the eight synthetic slags studied here are shown in Table III.1. The naming convention of the eight slags is based in part on a scheme devised by Goodwin [11]. The first five slags, SA00, SA01, SA05, SA10, and SA20 are synthetic (S) slags produced in air (A). The last two digits give the nominal weight percent of Fe_2O_3. The base composition is SA00, and the next four SAxx slags (SA01, SA05, SA10, and SA20) are mixtures of SA00 plus xx weight percent Fe_2O_3. For example, SA05 was produced from 95 g of SA00 and 5 g of Fe_2O_3.

The next three slags (SA1S, SA2S, and SA4S) were not studied by Goodwin. Their compositions were chosen to study the effect of lower SiO_2 content. Again, these slags are synthetic (S) and produced in air (A), but the last two digits (1S, 2S, and 4S) denote the approximate molar SiO_2 content. For example, SA1S contains approximately 10 mol% SiO_2 and SA4S contained approximately 40 mol% SiO_2. The

† This drying step is very important. Failure to completely dry the powder mixture can cause an explosion when the crucible is heated in the furnace. The build-up of steam pressure in the packed crucible can eject hot powder from the top of the furnace.

‡ Since standard alumina crucibles have rather thin walls, the crucibles used for initial melt preparation were actually short (4 in) alumina tubes with one end closed and flattened. These "crucibles" had walls approximately 1/8 in thick, and were supplied by Coors.

Al_2O_3 and CaO contents of these three slags were chosen by studying Fig. III.1, and selecting compositions with sufficiently low melting points. In addition to this criterion, the criterion that the slag not dissolve the crucible was considered. To this end, compositions were chosen so that an increase in Al_2O_3 would cause the melting temperature to increase (according to Fig. III.1)† .

The iron contents of the synthetic slags SA1S, SA2S, and SA4S were not restricted by the considerations discussed above. Since the SA2S was chosen to have SiO_2 content similar to a natural slag (NAEB), it was decided to choose the Fe_2O_3 content of SA2S to be similar to that of the natural slag‡ . The Fe_2O_3 contents of slags SA4S and SA1S were chosen to be between those of SA01 and SA05, with the expectation that their transmittance could be measured and provide more information on the effect of iron content on transmittance. The transmittance of SA4S was measured, but SA1S had an excessively high melting temperature or viscosity, and its transmittance could not be measured.

III.1.3 The High Temperature Electric Furnace

The furnace used in these experiments is a Deltec DT31 heated with eight "U"-shaped Kanthal Super 33 heating elements. The heating elements hang vertically in the furnace, supported from above by external aluminum connecting posts. The heating elements are connected in two parallel circuits with four elements in series in each circuit. The maximum operating temperature of these heating elements is approximately 1700°C, when operated in an oxidizing atmosphere (air). These elements are very brittle at room temperature but become ductile at high temperature (1600°C). Thus they must be hung vertically to prevent them from bending into contact with the furnace walls and/or furnace tube.

The temperature of the furnace was controlled with a EuroTherm model 919 temperature controller equipped with a programmable control module (Love Controls, model 105). This controller used feedback from a type B shielded thermocouple

---

† This selection criterion did not prove successful in the case of SA4S, which readily melted its alumina crucible after approximately 6 hours at 1600°C, and was subsequently reproduced in a platinum crucible.

‡ The natural slag NAEB was produced from a melt of Eagle Butte fly ash, and is discussed in detail in Chapter 4

inside the furnace. A pre-cut cam on the controller was designed to produce a linear temperature increase, followed by a level temperature, and finally a linear temperature decrease. The peak temperature and cam rotation rate were adjusted to provide approximately 12°C/min linear heating rates and a maximum temperature of approximately 1550°C.

The original furnace had 2 inch diameter openings in the top and bottom for insertion of an alumina furnace tube. Preliminary experiments revealed a serious problem with this 2 inch OD furnace tube configuration. When the molten slag is contained in a small (approx. 1 inch ID) crucible the surface is concave due to surface tension combined with the small contact angle where the slag wets the alumina crucible. To minimize this problem, it was estimated that a 4 inch OD furnace tube was required so the slag could be contained in a 2.2 inch ID crucible. Based on calculations and experiments, this configuration produces a molten slag surface with a radius of curvature of several meters. No precise measurements were done to quantify this curvature, but based on measurements, including those discussed in Appendix C, the radius of curvature is large enough to prevent significant transmittance and reflectance measurement errors.

The furnace wall was constructed using SALI (Zircar) fibrous insulation board as the hot face. The 4 inch OD furnace tube was a 99.8% alumina tube (Coors) with approximately 3.5 inch ID. It is not possible to maintain a sufficiently uniform temperature inside the furnace with the large (3.5 inch) holes in the top and bottom of the furnace. Therefore, a smaller furnace tube was inserted into the top of the furnace and a fibrous ceramic (SALI) plug was fitted into the bottom opening. Figure III.2 shows a schematic of the rebuilt furnace configuration.

Based on estimates of the power loss from the furnace, the temperature uniformity inside the furnace is relatively good. Sighting through the top of the furnace (using welding glasses) shows no visible color variation, but this view is rather restricted. The major loss is by conduction through the alumina tubes and furnace insulation. With the radiation shield in place, as shown in Fig. III.2, the radiative loss through the top of the furnace is much less than these conductive losses.

Measurements of the temperature distribution along the central vertical portion of the furnace showed less than 10°C change along the central 3 in of the furnace while at a mean temperature of approximately 1520°C. This measurement was made using a type R (Pt/Pt-13%Rh) thermocouple with a bead diameter of 0.035 in and wire

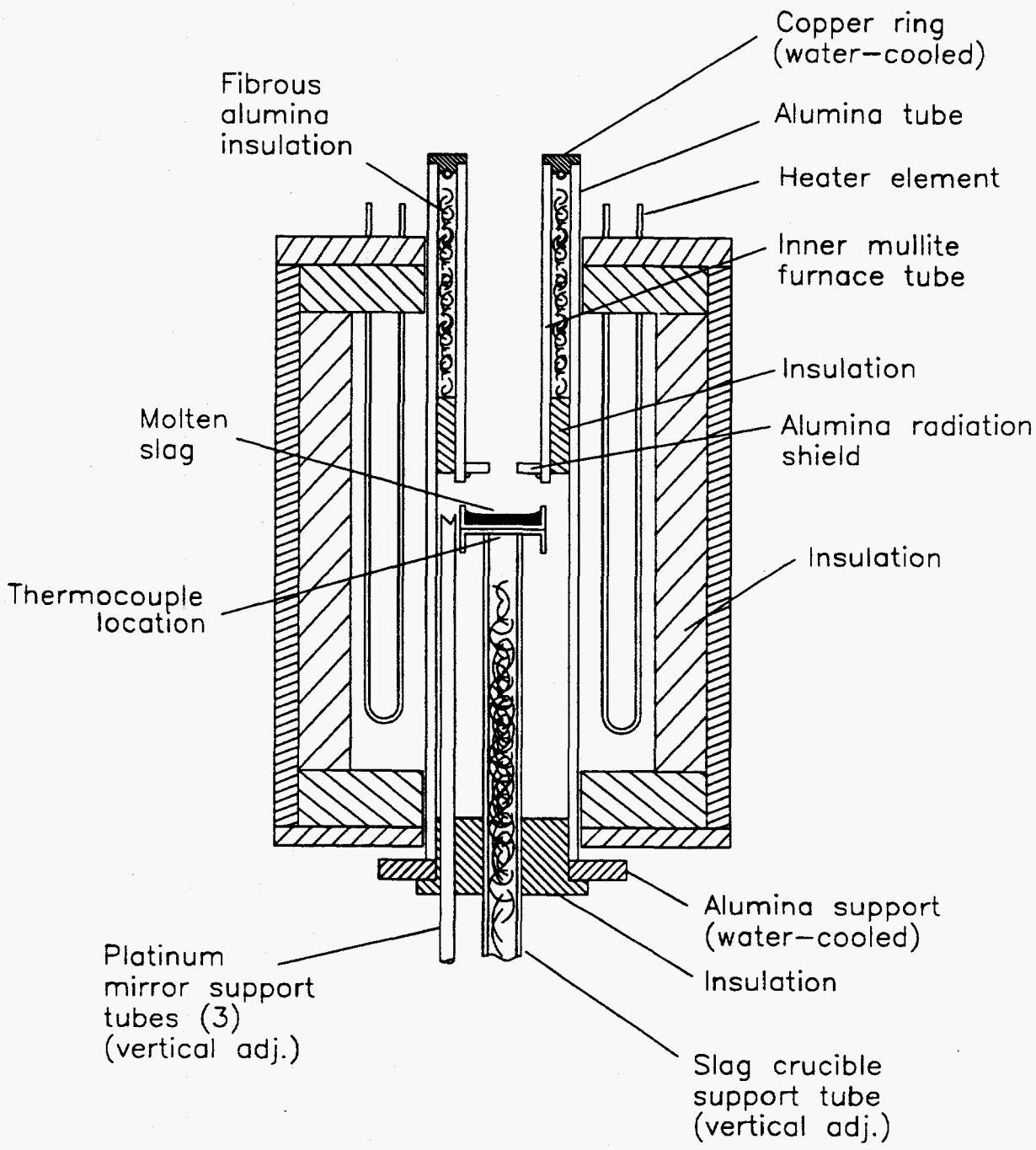

Figure III.2: Schematic of modified Deltec furnace used for melts, transmittance, and reflectance measurements.

diameters of 0.005 in. The thermocouple was positioned vertically through the top of the furnace using a long alumina thermocouple sleeve (0.125 in OD). No radiative shielding was used.

The usefulness of this furnace temperature distribution measurement is somewhat questionable, since it was made (necessarily) without the crucible of molten slag inside the furnace. The presence of the crucible and slag will affect the temperature to some extent. Specifically, the crucible, by being in direct contact with the alumina support tube and by radiating through the top of the furnace, will assume a slightly lower temperature than the walls of the furnace. During all measurements and operations, the furnace temperature was monitored at a position near the center of the furnace and directly below the crucible. Since the slag layer thickness in the crucible was approximately 1 cm during transmittance and reflectance measurements, this temperature should be quite close to the actual slag temperature.

III.1.4 Production of Slag Melts

The oxide mixtures, prepared as discussed above, were placed in the electric furnace. The temperature was increased at a linear rate of approximately 10-15°C/min until the it leveled off at approximately 1550°C. At this time the controller cam was stopped and the slag maintained a steady temperature until the cam was restarted. Figure III.3 shows the temperature history and heating rates for a typical melt cycle.

The molten slag was kept at high temperature for approximately 8 hours in a room air atmosphere. This 8 hour time limit, determined by trial and error, was found to be long enough to produce a reasonably homogeneous slag while short enough to prevent the slag from dissolving its container. These two criteria are important practical limitations which also affect the length of time available to make high temperature transmittance and reflectance measurements. Evidence that the slags were homogeneous was obtained by microprobe analysis of a cross section of the SA05 slag melt (see Appendix B). Evidence that the slags had reached a reasonable stable composition (e.g. the Fe_2O_3 valence state) was obtained during transmittance and/or reflectance measurements by comparing results at the start of the experiment with results at the end.

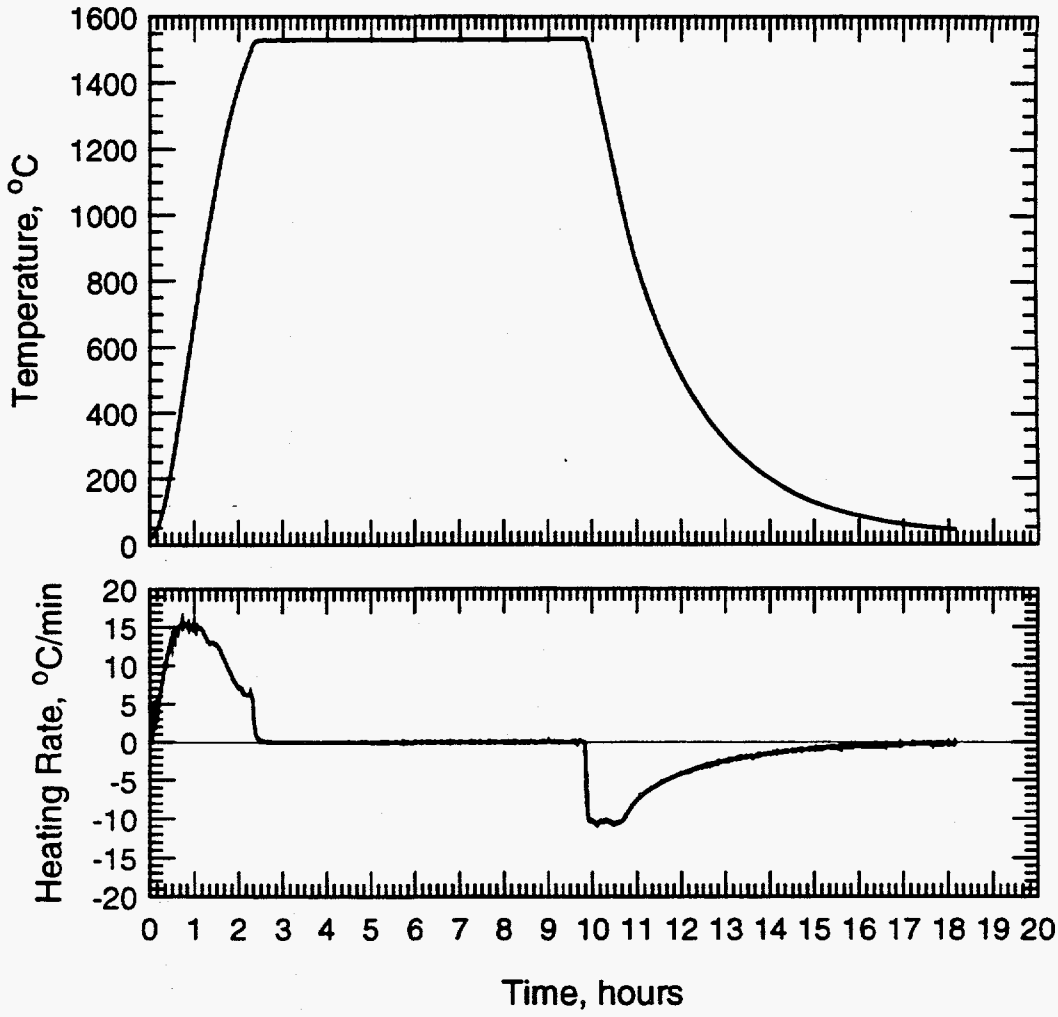

Figure III.3: Temperature and heating rate history for a typical slag melt preparation.

For most synthetic slags tested, the slag partially dissolved the alumina crucible (~2mm thick walls) and, if left at 1550–1600° C for too long, would flow out of the crucible. The precise length of time needed for this "melt–down" to occur was not determined, since it varies with slag composition, but a melt of the SA01 slag did escape from the crucible sometime between 12 hours and 24 hours. This melt–down destroyed much of the inner furnace fittings, breaking the alumina tubes during cooling, as discussed above.

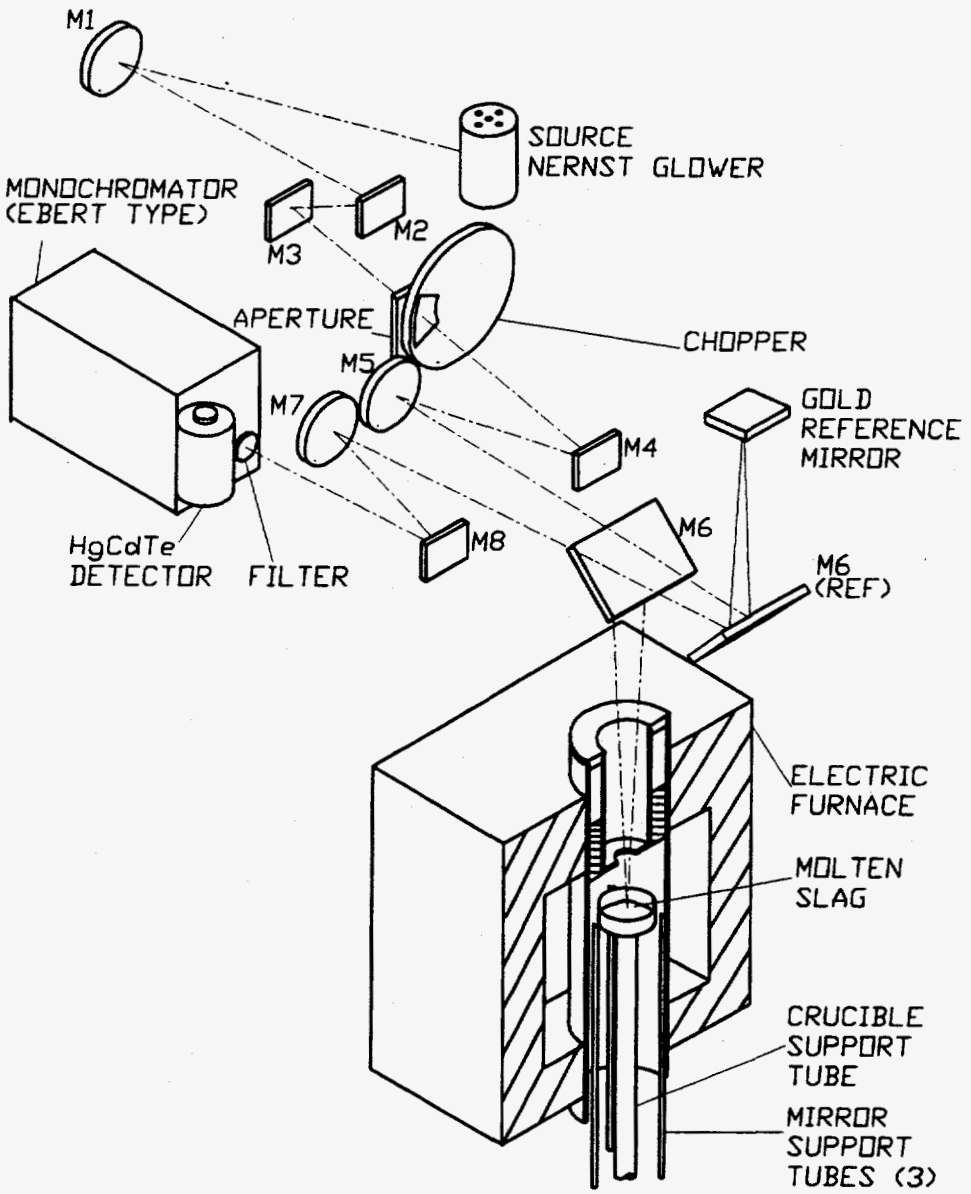

Figure III.4: Schematic of the optical system for reflectance and transmittance measurements.

III.2 Near–Normal Reflectance

The near–normal reflectance of the molten slags was measured using the apparatus illustrated in Fig. III.4. The optical system is mounted on a 4-ft by 6-ft optical table (not shown) located at one side of the electric furnace. An extension is attached to the table to allow optical components to be mounted directly above the furnace. A hood (not shown) encloses the top of the optical table and table extension to allow the entire optical system to be purged with nitrogen. A brass bellows connects the furnace tube to the table extension so that the volume inside the furnace tube (where the hot samples reside) is open to the optical system under the hood. The following section describes the apparatus in greater detail.

III.2.1 Apparatus for Reflectance Measurement

A Nernst glower (Electro–Optical Industries model 304) provides the broadband infrared source for these experiments. The glower has an electrically heated ceramic element approximately 1.5 mm diameter and 2.5 cm long. The brightness of the filament is adjustable to a maximum brightness temperature of approximately 1700°C, with radiometric feedback control to maintain a constant brightness. A metallic envelope surrounds the heated element to inhibit drafts. The ceramic element is an electrical insulator at low temperatures, and must be externally heated to higher temperatures before sufficient current flows through it to maintain it at a desired temperature. Two metallic heating elements are located near the ceramic element to provide this initial heating. The primary advantage of the Nerst glower over some other broadband infrared sources (e.g., tungsten lamps) is its ability to operate in an oxidizing atmosphere – no infrared window is required to isolate the glower from the surrounding air. Based on current experiments, the glower may also be operated in a pure nitrogen environment. It is not known if the glower would also operate in a reducing atmosphere. Finally, another possible advantage of the Nernst glower is that the emissivity of the ceramic filament is significantly larger at longer wavelengths (6-12 μm) than it is for some other broadband sources such as tungsten lamps and carbon filament lamps.

The radiation emitted from the glower is first collected by a concave gold front surface mirror (M1) with 100 mm diameter and 500 mm focal length and imaged onto

an aperture using a magnification of approximately two. Two planar front surface gold mirrors (M2 and M3) are placed between the concave mirror (M1) and the aperture to provide sufficient pathlength compactly. The image passing through the aperture has a width of approximately 3 mm and length of approximately 6 mm.

A mechanical chopper (PAR model 125A) is located immediately beyond the aperture to modulate the radiation. A chopping frequency of 670 Hz was used throughout these experiments. The chopper generates a 670 Hz electrical reference signal that is used to synchronize the lock–in amplifier with the modulated radiation.

The modulated radiation from the chopper is reflected from the planar front surface gold mirror M4 onto the concave gold front surface mirror M5. This concave mirror has a focal length (f) of 500 mm, a diameter (ϕ) of 100 mm, and is located at a pathlength of 1 m from both the aperture and the target surface (in the furnace).

A planar gold front surface mirror, M6, is located above the furnace and is mounted on a fixed axis. When M6 is in the "sample" position it reflects radiation from M5 onto the sample surface inside the furnace. When M6 is in the "reference" position the same beam from M5 is reflected onto the gold reference mirror. In either position, M6 collects the light reflected from the sample or reference surface and directs it into the front surface concave gold mirror, M7 (f=500 mm, ϕ=100 mm).

Mirror M7 images the reflected light onto the entrance slit of the monochromator *via* the planar gold front surface mirror M8. The distances from M7 to the monochromator entrance, from M7 to the sample surface, from M7 to the gold reference surface, from the sample surface to M5, and from M5 to the aperture are all 1m. Therefore, the images on the entrance slit of the monochromator and on the sample or reference surfaces all have the size and shape of the image formed by the aperture (apart from a small amount of spherical aberration and coma).

The incident radiation is spectrally resolved by the monochromator in combination with a set of longpass filters. The grating monochromator (Jarrell–Ash model 82-020) is an Ebert type monochromator with a focal length of 0.5 m, f/# of 8.6, and interchangeable gratings. The wavelength setting of the monochromator, for a given grating/filter combination, is controlled using a stepper motor which is operated using the data acquisition computer. Figure III.5 illustrates the operation of the monochromator.

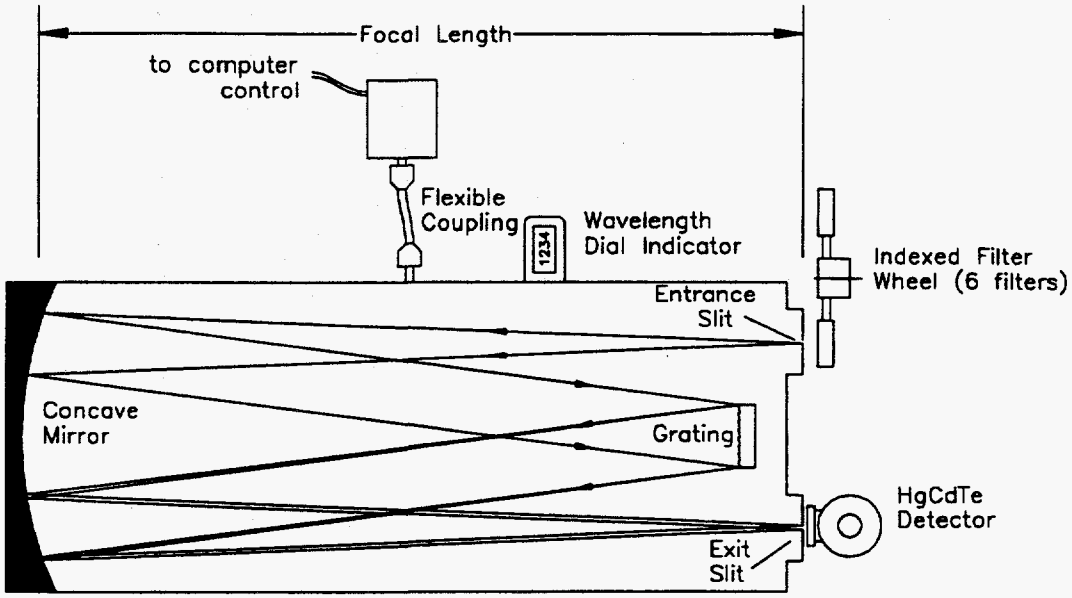

Figure III.5: Schematic of the monochromator used for reflectance and transmittance measurements.

Characteristics of the gratings used in these experiments are shown in Table III.2. The grating operates by producing an angular dispersion of incident light into a continuous range of wavelengths. When used in a monochromator, as illustrated in Fig. III.5, the result is a spectrum imaged onto the plane of the exit slit. The angular position of the grating determines which portion of the spectrum escapes the exit slit, and hence which portion of the spectrum is detected. For a finite exit slit width, Δx, a range of wavelengths, $\Delta\lambda$ escapes the monochromator. When the width of the entrance and exit slits are the same, Δx, then the slit function is an isosceles triangle with base width $\Delta\lambda = 2\alpha\Delta x$. Here α is a function of the distance from the grating to the exit slit and the groove density of the grating. For a particular monochromator configuration, the product $\alpha \times (1/d)$ is constant, where $(1/d)$ is the number of grooves per unit width on the grating (e.g., grooves/mm). As seen from Table III.2 the product $\alpha \times (1/d) \simeq 1888$ grooves nm/mm^2. The nominal spectral resolution, $\Delta\lambda$, is shown for each grating for a slit width of 1.5 mm. This slit width is narrow enough to allow adequate spectral resolution while maximizing the radiant power throughput to yield good detector signal/noise in a reasonable lock-in integration time ($\leq$ 10s).

The gratings used in this monochromator are "blazed" gratings which yields efficient reflection of first order radiation. For this grating design the blaze wavelength

Table III.2: Monochromator gratings.

ID	Blaze λ (μm)	grooves/mm	α (nm/mm)	$\Delta\lambda$ (nm) for 1.5 mm slits
1	1.2	590	3.2	9.6
2	2.6	295	6.4	19.2
3	4.0	148	12.8	38.4
4	10.0	50	37.7	113.1

is the nominal wavelength at which the grating efficiency is near maximum. The blaze wavelength is used as a guide for selecting a grating for a given wavelength range. Table III.2 shows the blaze wavelengths, along with other grating characteristics as described above.

In addition to first order diffraction, higher order diffraction is incident on the exit slit for a given grating position such that $m\lambda$ = constant. For example, if the grating is positioned to image a first order wavelength of 8 μm on the exit slit, then radiation at 4, 8/3, and 2 μm would also be imaged onto the exit slit, corresponding to second, third, and fourth order diffraction, respectively. To eliminate such shorter wavelength radiation, a longpass filter is placed before the entrance slit of the monochromator. The longpass filters are mounted on an indexed rotating wheel that allows one to move the appropriate filter in-line by rotating the filter wheel to the appropriate detent. Table III.3 shows the characteristics of the six longpass filters used in these experiments.

Table III.3: Longpass filters.

ID	Nominal Cutoff λ (μm)	0.1% Trans. λ (μm)	5% Trans. λ (μm)	λ^1_{max} (μm)	Average Trans.
1	0.84	0.785	0.810	1.57	0.90
2	1.5	1.35	1.50	2.70	0.75
3	2.0	1.80	2.00	3.60	0.80
4	3.5	3.15	3.50	6.30	0.75
5	6.125	5.80	6.06	11.60	0.80
6	7.85	7.60	7.85	15.20	0.80
1. wavelength at which second order transmittance is $\leq$0.1%					

The combination of gratings and longpass filters allows the monochromator to resolve a broad wavelength range. Table III.4 shows the grating and filter combinations for the six ranges, labeled A through F, used in these measurements. The longest wavelength range (F) has an upper limit of approximately 14 μm. This upper limit is due to the low sensitivity of the HgCdTe detector at longer wavelengths, and not due to grating or filter limitations.

Table III.4: Grating/filter combinations for monochromator ranges.

Range ID	Grating ID	Filter ID	λ_{min} (μm)	λ_{max} (μm)
A	1	1	1.0	1.5
B	2	2	1.6	2.4
C	3	3	2.4	3.8
D	3	4	3.8	6.2
E	4	5	6.4	11.8
F	4	6	11.8	14.0[1]
1. Limit set by detector sensitivity				

The detector is a Mercury–Cadmium–Telluride (HgCdTe) photoconductor (Judson model J15-D) with a liquid nitrogen (77 K) cooled dewar. The detector is mounted at the exit slit of the monochromator as shown in Fig. III.5. The detector has a peak spectral response at approximately 12 μm and a useful responsivity in the range from approximately 1 μm to 14 μm. The responsivity decreases rapidly with increasing wavelength beyond 12 μm, and the useful range may not extend beyond 13 μm or so unless the incident spectral radiation is relatively intense† . The photoconductive element has a 1 mm by 1 mm square active area mounted behind a ZnSe window. An internal cold shield limits the detection half-angle to approximately 10°.

The detector produces a resistance that is inversely proportional to the incident spectral radiant energy. A detector bias circuit and preamplifier (Judson model 000) is provided with a constant 30 mA current to convert the detector resistance to voltage. The preamplifier is capacitively coupled with a 5 Hz – 15 MHz bandwidth and provides a gain of approximately 50 db.

The signal from the preamplifier is measured using a lock-in amplifier (Stanford Research Systems model SRS–530) using the reference signal from the chopper. The

† The measured reflectance signals were not sufficiently large to extend the measurements beyond approximately 13 μm.

lock–in is a dual phase system which allows automatic correction for phase differences between the reference signal and detector signal. The measurable signals from the detector preamplifier range from approximately 20 μV to 200 mV. Time constants of 0.3 sec, 1 sec, 3 sec, and 10 sec were used for these measurements, with the larger time constants used for the smaller signals to maintain adequate signal-to-noise ratio.

A data acquisition computer system (IBM-AT compatible) was used to control the stepper motor, to read the lock–in output, to control lock–in settings, and to read the temperature of the furnace thermocouple.

The optical system, including the monochromator, Nernst glower, and chopper, is mounted on a 4-ft by 6-ft optical table with the top of the furnace located near one end of the table. A small table extension is used to mount optics hardware above the furnace (i.e., the movable mirror M6 and the gold reference mirror).

The top of the furnace tube, shown in Fig. III.2, is open to the optical system. When the furnace is hot, the length of gas above the sample is also hot. However, the corresponding length of gas above the furnace between mirror M6 and the cold reference mirror is near room temperature. Since the absorption coefficient of the water vapor and carbon dioxide in room air is sensitive to temperature, primarily through its affect on gas density, the optical pathlengths of the sample and reference paths are not identical. Of course, this is largely limited to the relatively narrow atmospheric absorption bands near 2.7 μm (CO_2), 4.3 μm (CO_2), and 6.3 μm (H_2O). In addition, the flow of gases from the furnace tube tend to contain vapors that condense on mirror M6 when in the sample position. To alleviate both of these problems an aluminum box (or "hood") was constructed to enclose the entire optical system. This hood is lowered over the optical system and sealed at the edges of the optical table. A brass bellows is attached between the top of the furnace tube and the optical table extension to form a completely sealed system. The crucible and mirror support tubes pass through holes in the insulating plug which fits into bottom of the the 4-in OD alumina furnace tube (See Fig. III.2). Small gaps exist between support tubes and an plug through which purge nitrogen can escape.

The optical system hood is purged with nitrogen at a flow rate of approximately 50 std ft^3/hr. The nitrogen is supplied by evaporating liquid nitrogen in copper tubing submerged in a heated canister of water. The detector signal near the 4.3 μm CO_2 absorption band is monitored to determine the status of the purge. A typical spectral scan is shown in Fig. III.6 repeated several times after a purge is begun,

illustrating the effect of CO_2 on the transmittance of air near 4.3 μm. By increasing the nitrogen flow rate during initial purge, the time required to effectively reduce CO_2 absorption was decreased to approximately 2-3 hours, but it was more effective (and usual practice) to maintain the purge between experiments.

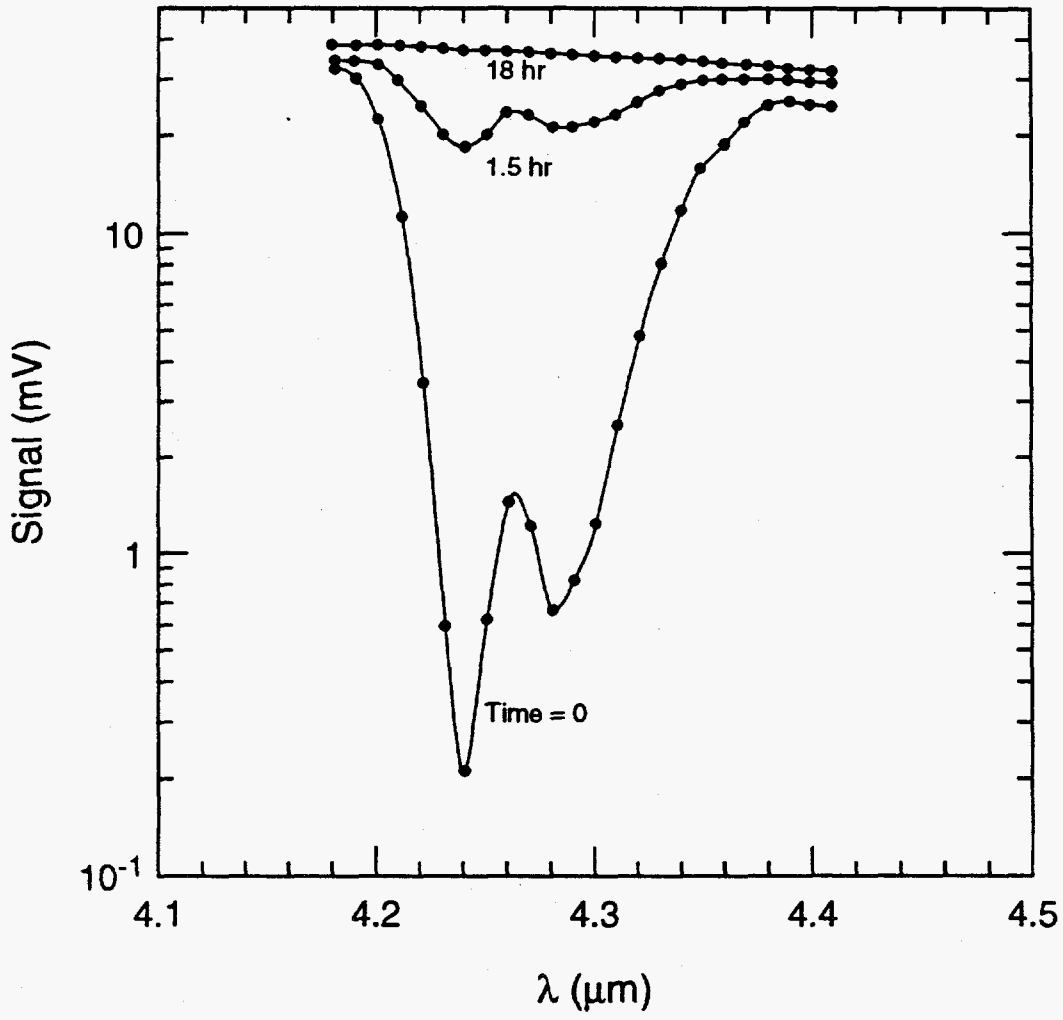

Figure III.6: Effect of nitrogen purge of optical system on detector signal in the 4.3 μm wavelength range and at various times following the start of the purge.

Another important aspect of the purge system is the ability of the nitrogen flow into the top of the furnace to decrease the rate of condensation on the mirror M6. As mentioned above, the mirror M6 is placed directly over the top furnace opening when in its sample position. Therefore, material evaporated from the slag tended to

condense on the cool mirror. With the purge flow activated, this evaporation was effectively eliminated, since a significant portion of the nitrogen flow was downward through the furnace. It was difficult to quantify the amount of flow leaving through the furnace, since the hood had many penetrations to accommodate adjustment wires and rods. By monitoring the reference signal over a long period of time it was determined that the small amount of persistent condensation did not significantly affect the reflectance measurements.

In early experiments it was noticed that small amounts of dust under the hood would be swept into the furnace by the purge flow. This problem was effectively eliminated by placing a small forced–air filter (Norelco) under the purge hood. Leaving the hood closed with the filter and purge running continuously removed most of the airborne dust under the hood.

Access to the optical system was rather restricted once the purge hood was in place. All major adjustments to the optical system were made prior to lowering the hood over the system. Many of the minor adjustments required during the experiments, including positioning of the movable mirror M6, were made with small wires and rods extending through the hood. A rubber glove with an extendable sleeve was mounted near the monochromator to allow the gratings and filters to be changed without letting room air into the optical system. A small hole in the top of the purge hood allowed transfer of liquid nitrogen from an external dewar to a dewar under the hood, which in turn was used to regularly (approx. 2 hr intervals) refill the detector dewar.

III.2.2 Reflectance Measurement Procedure

The following procedure was used to measure the near–normal reflectance of the slags:

1. The nitrogen purge is started to reduce the CO_2 and H_2O concentrations under the purge hood. The detector signal at 4.24 μm is monitored to determine the status of the purge.

2. An alumina (or platinum) crucible is filled with chips of solid slag produced by the melt procedure. The crucible is placed on the support tube in the furnace

and the temperature is increased at a rate of approximately 10-15°C/min until the furnace temperature is approximately 1600°C.

3. The slag is left at 1600°C for approximately 2 hours to become homogeneous and for the system temperature to stabilize. A thermometer under the purge hood (away from the furnace) indicates a steady temperature in the range from 34°C to 40°C.

4. The vertical position of the slag surface is checked for alignment and adjusted as necessary (usually not necessary). The detector signal is maximum when the slag surface is properly positioned.

5. The monochromator wavelength dial indicator is checked for conformity with the computer acquisition system. Several trial reflectance measurements are made at several wavelengths to establish steady performance.

6. The near-normal reflectance is measured by first measuring the sample signal at several wavelength settings with the mirror M6 in the forward (sample) position. Next mirror M6 is moved to the reference position and the signal reflected from the gold reference mirror is measured. The reflectance, R, is the ratio of the sample signal, I_s, to the reference signal, I_r, corrected by the reflectance of gold, $R_g \simeq 0.992$, such that

$$R = R_g \frac{I_s}{I_r}. \qquad (III.1)$$

7. The reflectance is measured sequentially over the entire wavelength range from 1-13 μm using appropriate grating and filter combinations as shown in Table III.4. Measurements are repeated at several wavelengths during the procedure to ensure that they are repeatable. This procedure typically required approximately four hours, with the entire reflectance procedure including furnace heating and stabilization requiring approximately six to eight hours.

Once the reflectance data are obtained, the Kramers-Kronig relations are applied to determine n over the entire wavelength range and k at wavelengths where $k > 0.1$, as discussed in Chapter II.

III.3 Transmittance Measurements

The transmittance apparatus is identical to that used for near–normal reflectance measurements except that the mirror M6 is fixed in the forward sample position, and a platinum mirror is suspended below the molten slag surface. The arrangement inside the furnace and the associated optical path is illustrated in Fig. III.7.

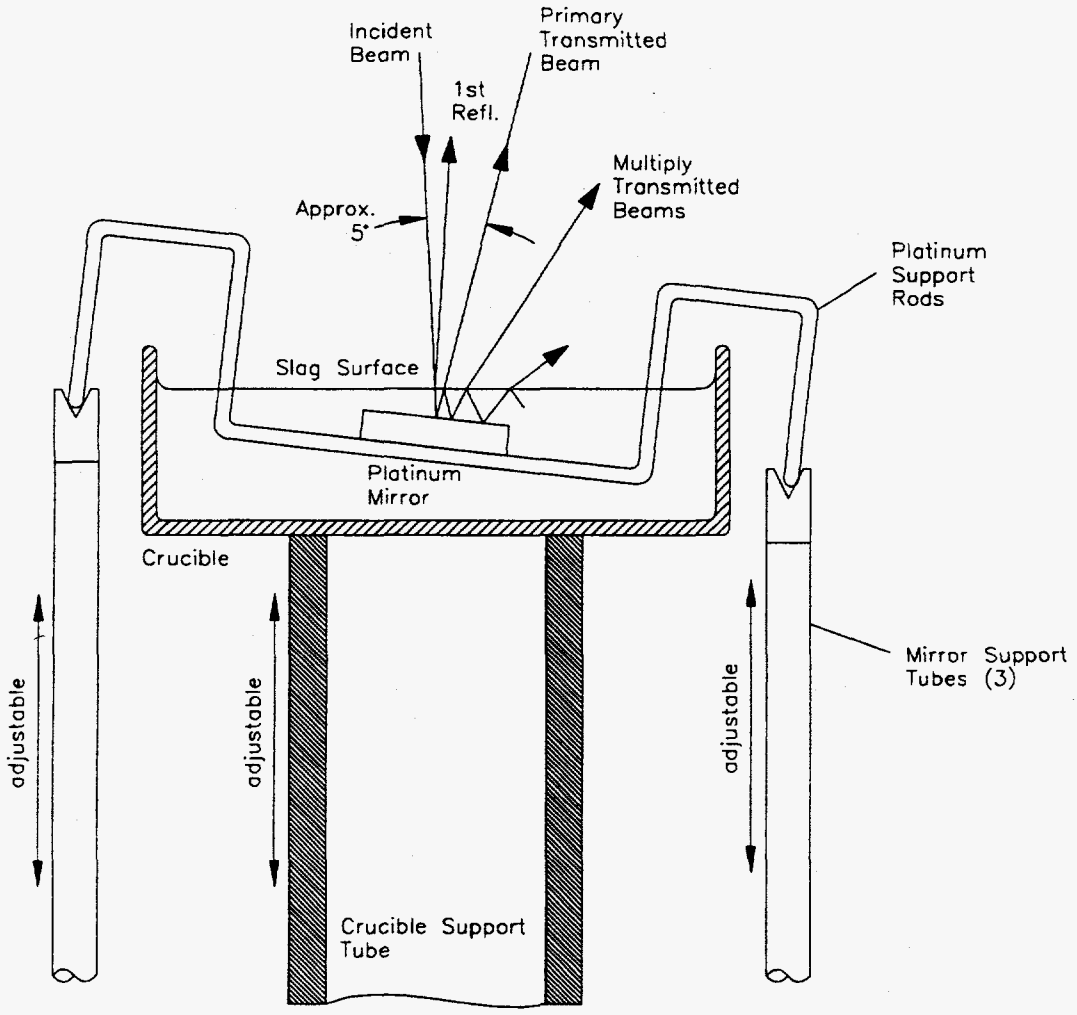

Figure III.7: Schematic of the submerged platinum mirror configuration for transmittance measurements. The angle of the mirror surface to the horizontal is exaggerated for illustrative purposes.

The platinum mirror of diameter $\sim$ 1/2-in is supported at a depth from 200 to 1500 μm below the surface. This depth is adjusted by keeping its position fixed with

respect to the three mirror support tubes while adjusting the vertical position of the crucible.

The platinum mirror is supported by three platinum rods (2 mm dia) which rest on mirror support tubes. The platinum rods are welded at the center to form an integral support structure. Small diameter (e.g., 30 Ga) platinum wires placed between the mirror and each rod allow the mirror to be electrically spot welded to the rod structure.

One of the mirror support tubes of alumina has a fixed position, but the other two can be moved vertically on micrometer translation stages to adjust the orientation of the platinum mirror. These adjustments are made before transmittance measurements begin, and are periodically checked to ensure proper alignment. It was found that the platinum rods would slowly creep, causing misalignment, so that periodic adjustment of the support tubes was necessary.

The platinum mirror is oriented to make an angle of approximately 2.5° with the free surface of the molten slag. With this orientation it is possible to collect only the beam that is reflected *once* from the submerged platinum mirror, and to reject the beam that is reflected from the slag surface and the beams multiply reflected from the mirror. Thus, the collected beam intensity is proportional to $I_o(1 - R)^2 R_{\mathrm{Pt}} \exp(-4\pi k 2h/\lambda)$, where I_o is the incident beam intensity, R is the reflectance of the slag surface, R_{Pt} is the reflectance of the platinum mirror, and h is the depth of the submerged platinum mirror. By measuring the signal at two mirror depths, h and $h + \delta$, and taking the ratio, the reflectance factors cancel and we have

$$\exp\left(-\frac{4\pi k 2\delta}{\lambda}\right) = \frac{I(h+\delta)}{I(h)}, \qquad (III.2)$$

or

$$k = -\frac{\lambda}{8\pi\delta} \ln\left(\frac{I(h+\delta)}{I(h)}\right). \qquad (III.3)$$

Two tests were made to ensure that only the once-reflected beam is collected. First, when the mirror is submerged to its maximum depth and the wavelength is set where k is large (≥ 0.01), the collected signal vanishes when no reflection from the slag surface is being collected. A second test was made was to ensure that k is independent of h. Measuring k for several different starting depths, h, and changes in depth, δ, assured that multiply reflected beams were rejected.

The experimental procedure for measuring the transmittance is similar to that for reflectance measurements. The primary difference in the two procedures is that the mirror $M6$ is left in the forward "sample" position during the entire scan. As described above, the "sample" and "reference" paths for transmittance measurements refer to paths of different depths, $h + \delta$ and h. For transmittance measurements the monochromator is fixed at a single wavelength and the vertical position of the crucible is adjusted about a fixed submerged mirror. Once the transmittance at that wavelength is determined, the monochromator is adjusted to the next measurement wavelength.

The difference in depth, δ, is measured from the movement of the micrometer translation stage to which the crucible support tube is attached. A dial micrometer attached to the crucible support tube provided a second measure of the change δ. A large graduated knob was mounted on the original (smaller) micrometer knob to increase the readability and precision while maintaining a minimum graduation of 10 μm. The translation stage was found to produce accurate and repeatable positioning to within approximately 2 μm. Since the positions were always chosen to fall on an integral multiple of 10 μm, the effective readability was less than 2 μm. Referring to Eq. (III.3), this uncertainty in δ corresponds to approximately 1% uncertainty in k for $\delta \simeq 200$ μm. This level of precision was only achievable if a very light touch was applied when adjusting the mirror depth, and if the adjustment was done slowly to allow the slag to flow smoothly over the mirror surface.

Chapter IV.

Experimental Results

This chapter describes the results of the slag melt preparation and subsequent reflectance and transmittance measurements. Section IV.1 gives the composition of the slag melts, along with their densities measured at room temperature. The results of high temperature reflectance and transmittance measurements are presented in sections IV.2, IV.3, and IV.4. The remainder of the chapter develops correlations for the optical constants and attempts to explain the observed effects.

IV.1 Slag Compositions and Densities

As discussed in the previous chapter, nine synthetic slags were produced from powdered oxides. Once the slags were produced, and cooled to room temperature, a small sample of slag was extracted from the melt. Electron microprobe measurements were made for slags SA00, SA01, SA05, SA10, SA20, and NAEB. The results of the microprobe measurements for the SAxx slags are presented in Table IV.1 along with initial compositions for the three slags SA1S, SA2S, and SA4S. Table IV.2 shows the results from Table IV.1 recomputed on a mole percent basis. Table IV.3 shows the microprobe results for the *natural* slag NAEB.

The microprobe results show good agreement with the original oxide mixture compositions presented in Table III.1; with the largest difference being in the Fe_2O_3 content. The microprobe results consistently indicate that the Fe_2O_3 content of the final slag is somewhat less than expected. The cause of this decrease in Fe_2O_3 may be due to composition inhomogeneity – with iron content increasing with depth in the slag. A careful microprobe analysis of this composition distribution is presented in Appendix B which supports this explanation for the Fe_2O_3 deficiency near the free surface of the slags, but do not fully explain why the small composition gradient occurs. The effect may be density stratification, with the heavier iron settling toward the bottom of the crucible.

Table IV.1: Composition of synthetic slags.

	Oxide Weight Percent			
Slag	SiO_2	Al_2O_3	CaO	Fe_2O_3
SA00	60.31	28.57	11.04	0.08
SA01	59.40	28.49	11.28	0.82
SA05	55.10	27.60	12.40	4.90
SA10	53.10	27.46	9.94	9.50
SA20	46.36	25.97	8.94	18.73
SA4S*	38.83	23.30	34.95	2.90
SA2S*	18.60	43.71	30.69	7.00
SA1S*	9.62	40.38	46.15	3.85
* Estimate based on initial oxide mixture.				

Table IV.2: Slag compositions in mole fractions.

	Oxide Mole Percent			
Slag	SiO_2	Al_2O_3	CaO	Fe_2O_3
SA00	67.76	18.92	13.29	0.03
SA01	67.05	18.95	13.64	0.35
SA05	63.70	18.81	15.36	2.13
SA10	63.59	19.38	12.75	4.28
SA20	59.21	19.55	12.24	9.00
SA4S	42.62	15.07	41.11	1.20
SA2S	23.29	32.25	41.17	3.30
SA1S	11.41	28.22	58.65	1.72

The densities of the nine slags were measured using a specific gravity bottle. By measuring the mass of several small chips of slag, m_1, the mass of the specific gravity bottle carefully filled with water m_2, and the mass of the bottle filled with water with the pieces of slag inside, m_3, the specific gravity of the slag can be found from the relation

$$\frac{\rho}{\rho_{\text{water}}} = \frac{m_2}{m_1 + m_2 - m_3}. \qquad (IV.1)$$

For these measurements approximately 1-2g of slag was used. The specific gravity bottle filled with water had a mass $m_2 \simeq 71.5$g. A Mettler balance was used to accurately determine the mass to the nearest 0.001g (approx.). The density of each

Table IV.3: Composition of Eagle Butte slag (NAEB)

Oxide	Wt.%	Mol%
SiO_2	28.75	31.32
Al_2O_3	17.57	11.28
Fe_2O_3	6.93	2.84
CaO	33.25	38.82
Na_2O	1.75	1.85
K_2O	0.00	0.00
BaO	2.52	1.08
TiO_2	1.12	0.31
MgO	7.53	12.22
P_2O_5	0.57	0.26
SO_3	0.01	0.01

slag was measured several times and the uncertainty was typically found to be less than or approximately equal to 1%. Most of the errors could be traced to improperly filling the bottle, or allowing air bubbles to be trapped in the bottle. After gaining experience it was relatively easy to obtain repeatable results to within 1%. The resulting densities are shown in Table IV.4.

Table IV.4: Measured densities of the slags.

Slag	Density (g/cc)
SA00	2.54
SA01	2.56
SA05	2.61
SA10	2.68
SA20	2.89
SA4S	2.79
SA2S	3.07
SA1S	2.98
NAEB	3.03

In a later section, the density of the slag will be shown to be an important parameter for modeling the optical constants. An approximate formula is presented that allows one to estimate the density based on composition.

IV.2 Reflectance Measurements

The near-normal reflectances of the nine molten slags were measured using the procedure described in Chapter III. The reflectances of SA00, SA05, SA10, and SA20 are shown in Fig.IV.1. As shown, the reflectance, R, is approximately 5% at a wavelength of 1 μm, decreases to a minimum of less than 1% near 8 μm, increases to a maximum of 11-14% near 10 μm, then decreases at longer wavelengths. As discussed in Chapter II, this behavior indicates that the molten slags have relatively weak absorption in the short wavelength region, where R is gradually decreasing with increasing wavelength (normal dispersion). Where the reflectance reaches a local minimum the absorption is increasing, while the subsequent steep rise in R indicates a strong absorption in that wavelength range.

The effect of composition on the reflectance is illustrated in Fig. IV.1 and Fig. IV.2. In Fig. IV.1 the Fe_2O_3 concentration is increasing from approximately 0 wt.% for SA00 to approximately 19 wt.% for SA20. There is a corresponding decrease in SiO_2 content for the four slags. As shown, the reflectance near 1 μm increases with Fe_2O_3 content. Another significant feature is the shift in the wavelength of minimum reflectance, with the minimum shifting to longer wavelengths with increasing Fe_2O_3 (and decreasing SiO_2). Finally, the maximum reflectance decreases with increasing Fe_2O_3 content. Since the sharp rise in reflectance near 8-10 μm is due to a silica absorption band near 10 μm, one can deduce that as the SiO_2 content is decreased the absorption band shifts to slightly longer wavelengths and the peak absorption decreases. This result will be confirmed by the analysis of the reflectance data in following sections.

The reflectance of the slags SA4S, SA2S, and SA1S, shown in Fig. IV.2, further demonstrates the effects of composition on reflectance. For these slags the SiO_2 content is decreased substantially, with SA1S having approximately 10 wt.% SiO_2. The trends illustrated in Fig. IV.1 are reasonably consistent with those illustrated in Fig. IV.2. That is, the absorption band responsible for the sharp rise in reflectance shifts to longer wavelengths as the SiO_2 content is decreased. However, the peak reflectance for SA2S and SA1S occurs at longer wavelengths than could be measured.

The slag SA01 is identical to slag SA00 except that slag SA01 has approximately 0.82 wt.% Fe_2O_3 and slag SA00 has almost no Fe_2O_3. The microprobe measurements showed that SA01 had approximately 1 wt% more SiO_2 than slag SA00. The effect

of these small differences on the reflectance is slight, as illustrated in Fig. IV.3. The maximum difference occurs at longer wavelengths where $R_{SA01} - R_{SA00}$ is approximately 0.5%. In the short wavelength range ($\lambda < 8$ μm), the difference is less than approximately 0.2%.

Finally, the low silica, high calcia (and high density) slag NAEB was the only "natural" slag studied. It contains significant quantities of MgO, BaO, and minor amounts of several other oxides (see Table IV.3). Based on the SiO_2 composition (28 wt.%) the reflectance near the SiO_2 absorption band is expected to lie somewhere between that of SA4S (42 wt.% SiO_2) and SA2S (23 wt.% SiO_2). Figure IV.4 confirms this expectation. In the shorter wavelength region ($\lambda < 8$ μm) the reflectance of NAEB is higher that that of SA4S or SA2S. From this result one can conclude that the reflectance in the 1-8 μm region is dependent on factors other than just SiO_2 content. This result is expected, and is analysed in detail in the following sections.

IV.3 Kramers–Kronig Analysis of the Reflectance

The Kramers–Kronig (KK) analysis described in Section II.2.2 was used to compute the complex refractive index from the reflectance measurements for the nine slags. A computer program was written to perform the integration in Eq.(II.38) using the trapezoid rule† . As discussed in section II.2.3, the refractive index n was determined for all wavelengths but the absorption index k was determined only at wavelengths where k is larger than approximately 0.1, that is, only where the reflectance depends significantly on k.

The results of the KK calculations for slags SA00, SA05, SA10, and SA20 are shown in Fig. IV.5. We see the expected trends in n and k versus wavelength. The real refractive index, n, has normal dispersion at wavelengths below approximately 8 μm, corresponding to the wavelength range where k is relatively small (compared to $n-1$). At wavelengths longer than 8 μm the strong absorption feature corresponds to the region of anomalous dispersion in n.

The effect of Fe_2O_3 content on n and k is evident in Fig. IV.5. In the short wavelength range ($\lambda < 8\mu$m) increasing the iron content increases n, and in the long

† Higher order integration schemes (e.g., Romberg integration) were also studied but produced the same results.

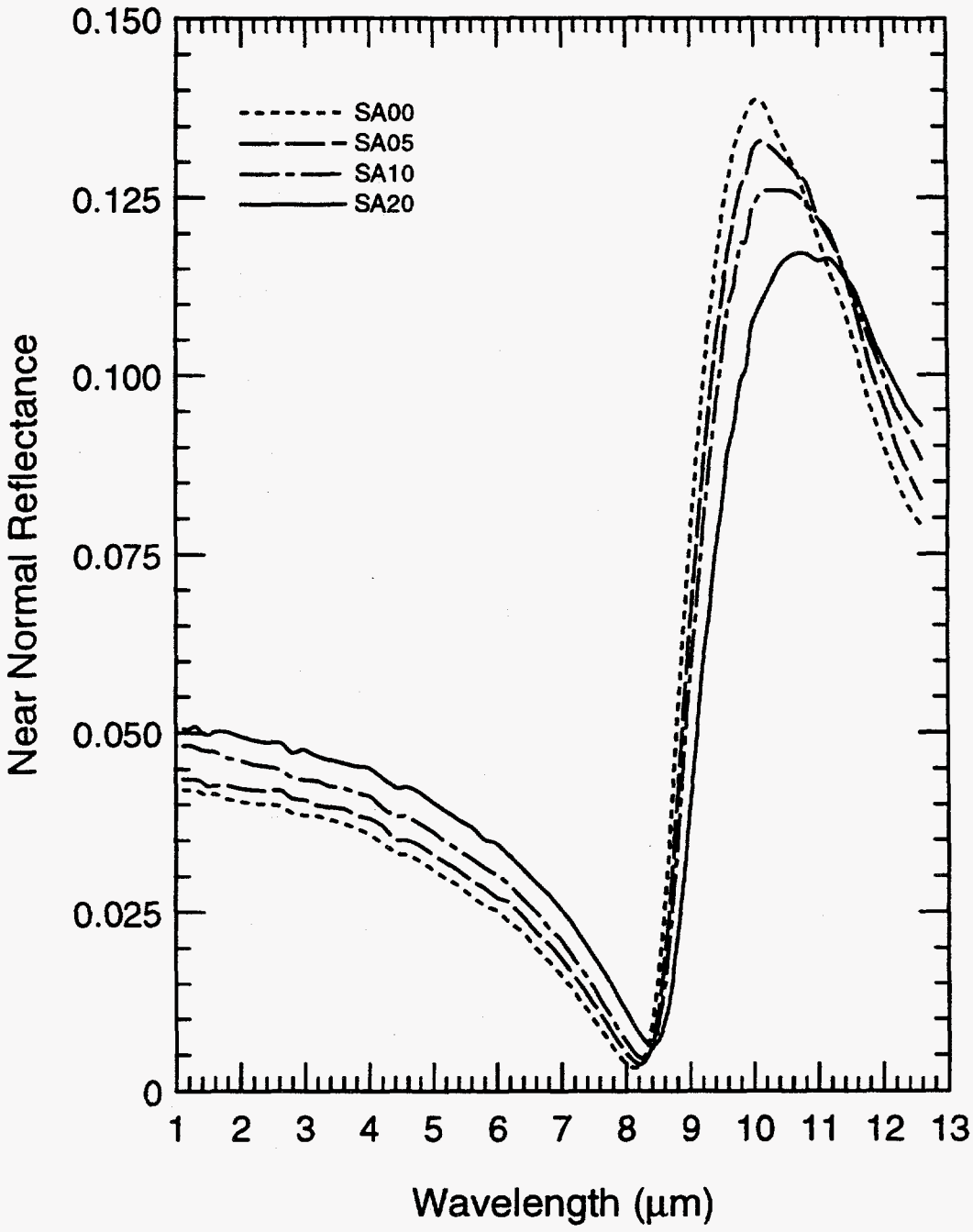

Figure IV.1: Near normal reflectance of molten slags SA00, SA05, SA10, and SA20 versus wavelength.

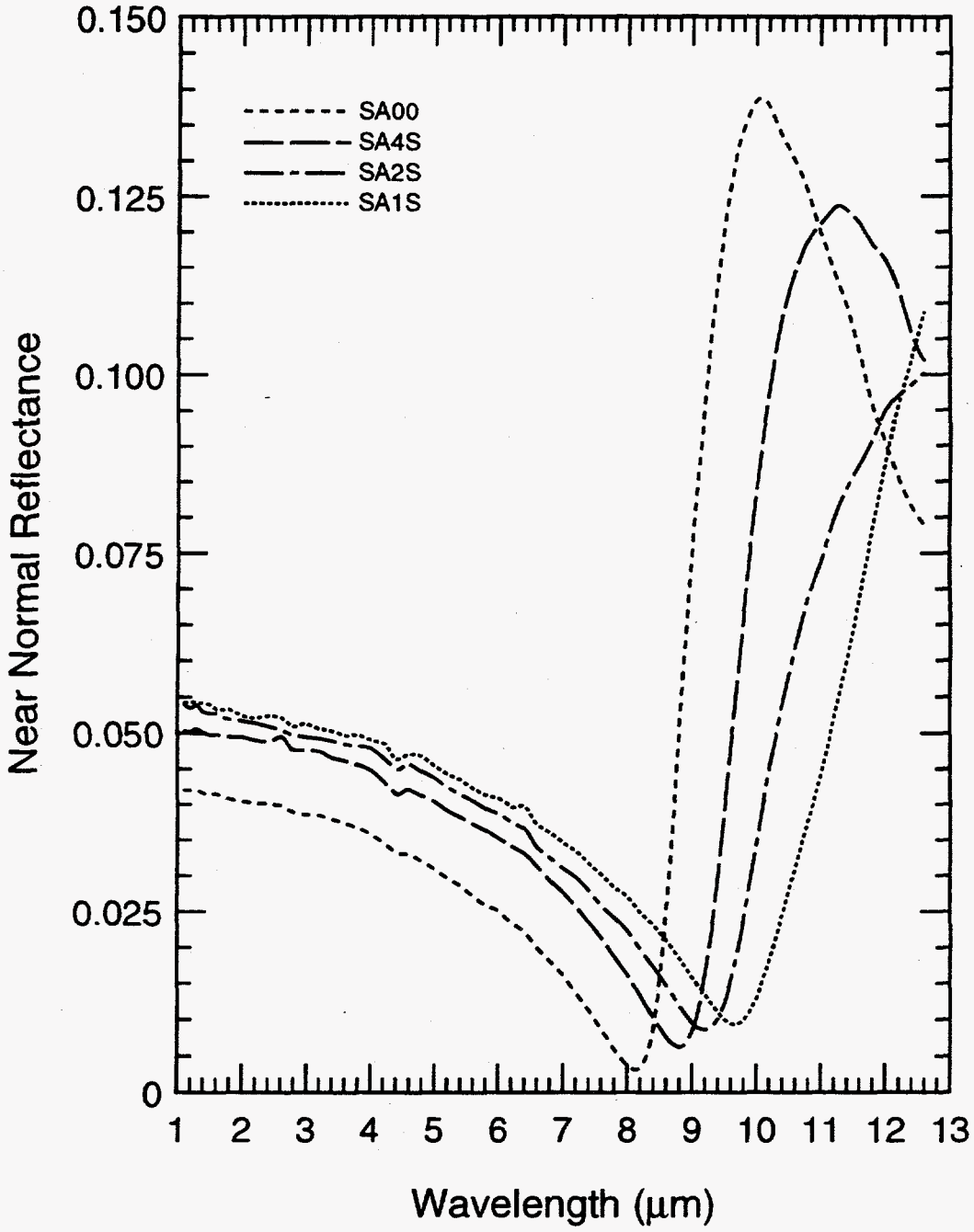

Figure IV.2: Near normal reflectance of molten slags SA00, SA4S, SA2S, and SA1S versus wavelength.

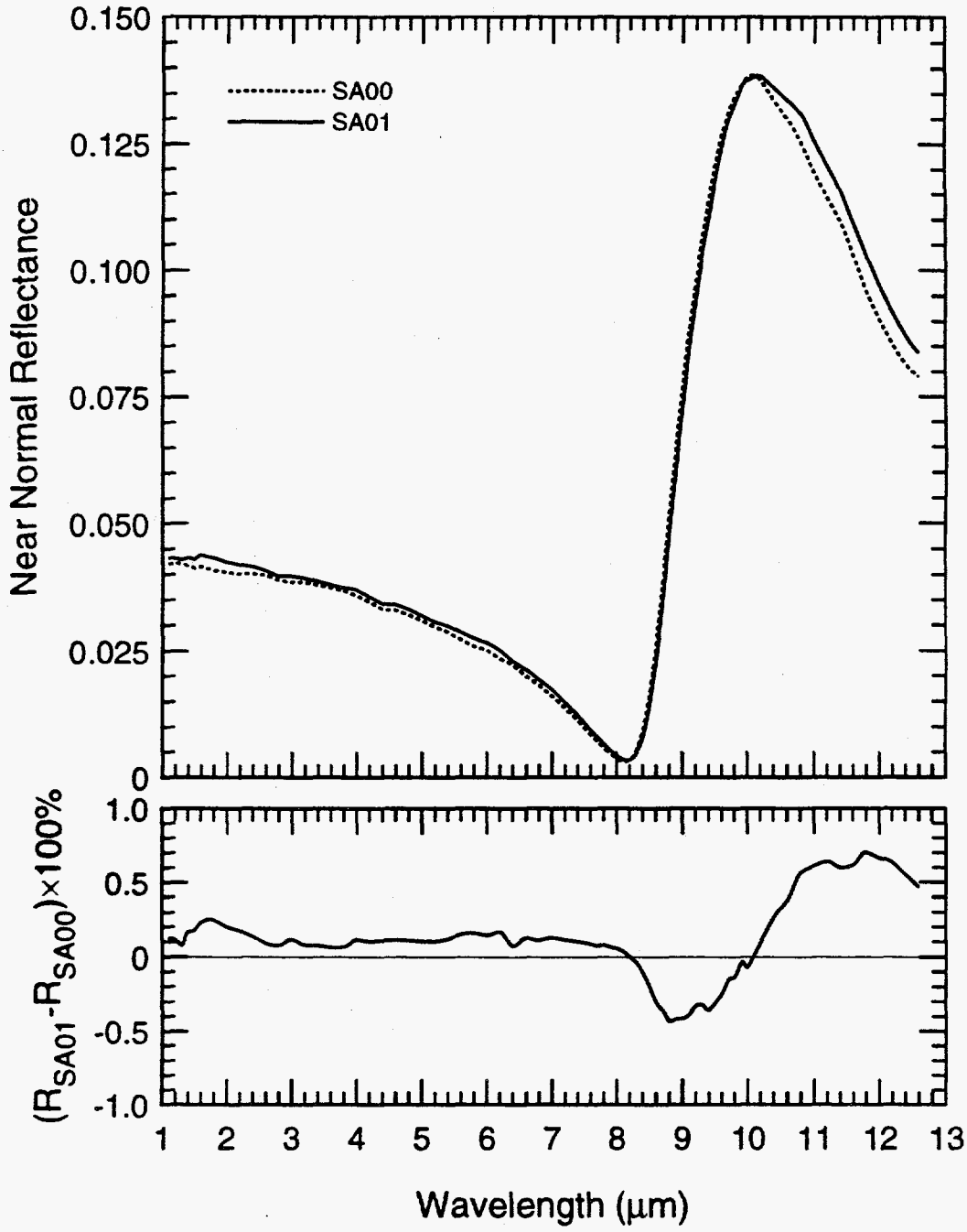

Figure IV.3: Near normal reflectance of molten slags SA00 and SA01 versus wavelength (top), and the difference between the reflectance of the two slags.

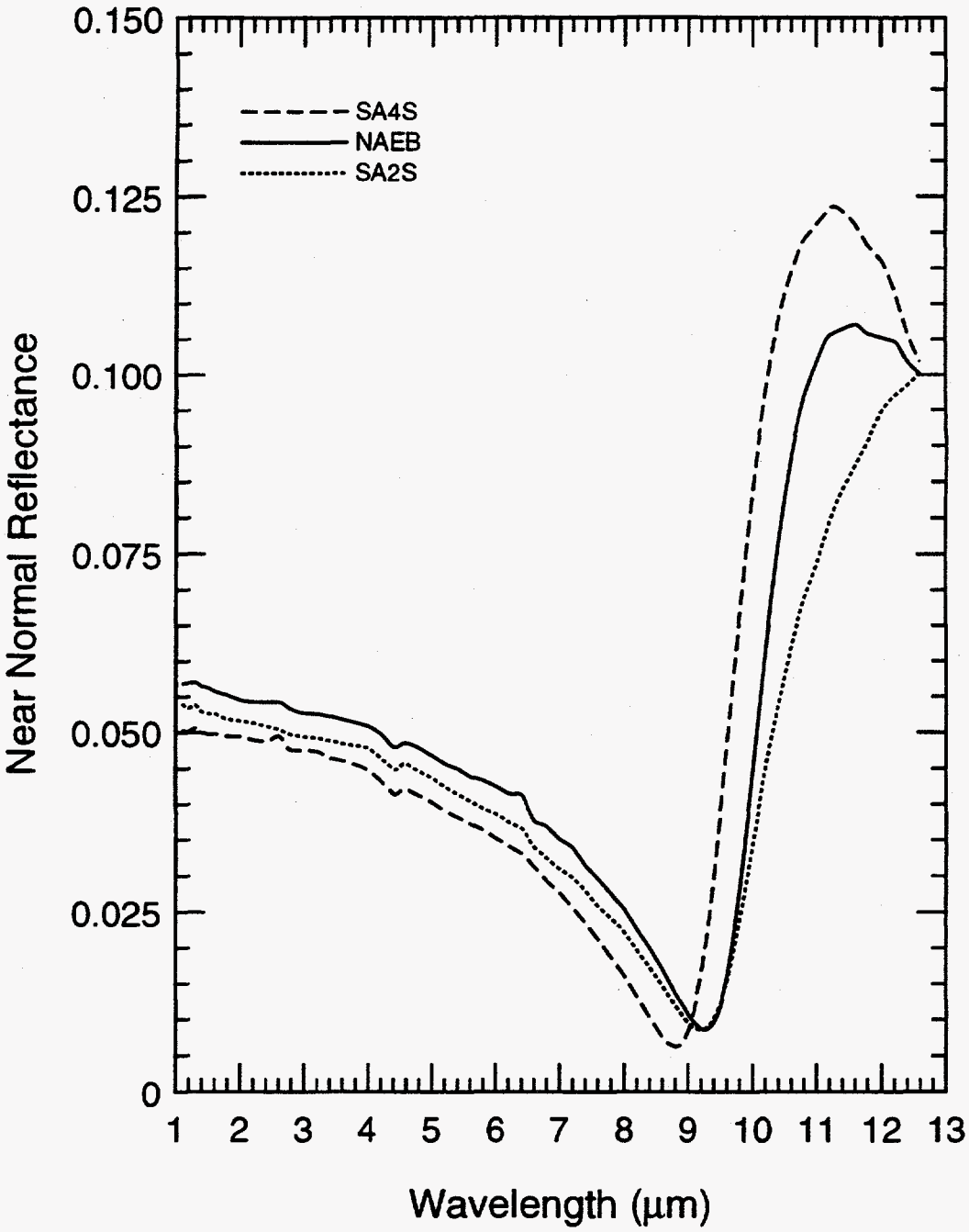

Figure IV.4: Near normal reflectance of molten slags SA2S, SA4S, and NAEB versus wavelength.

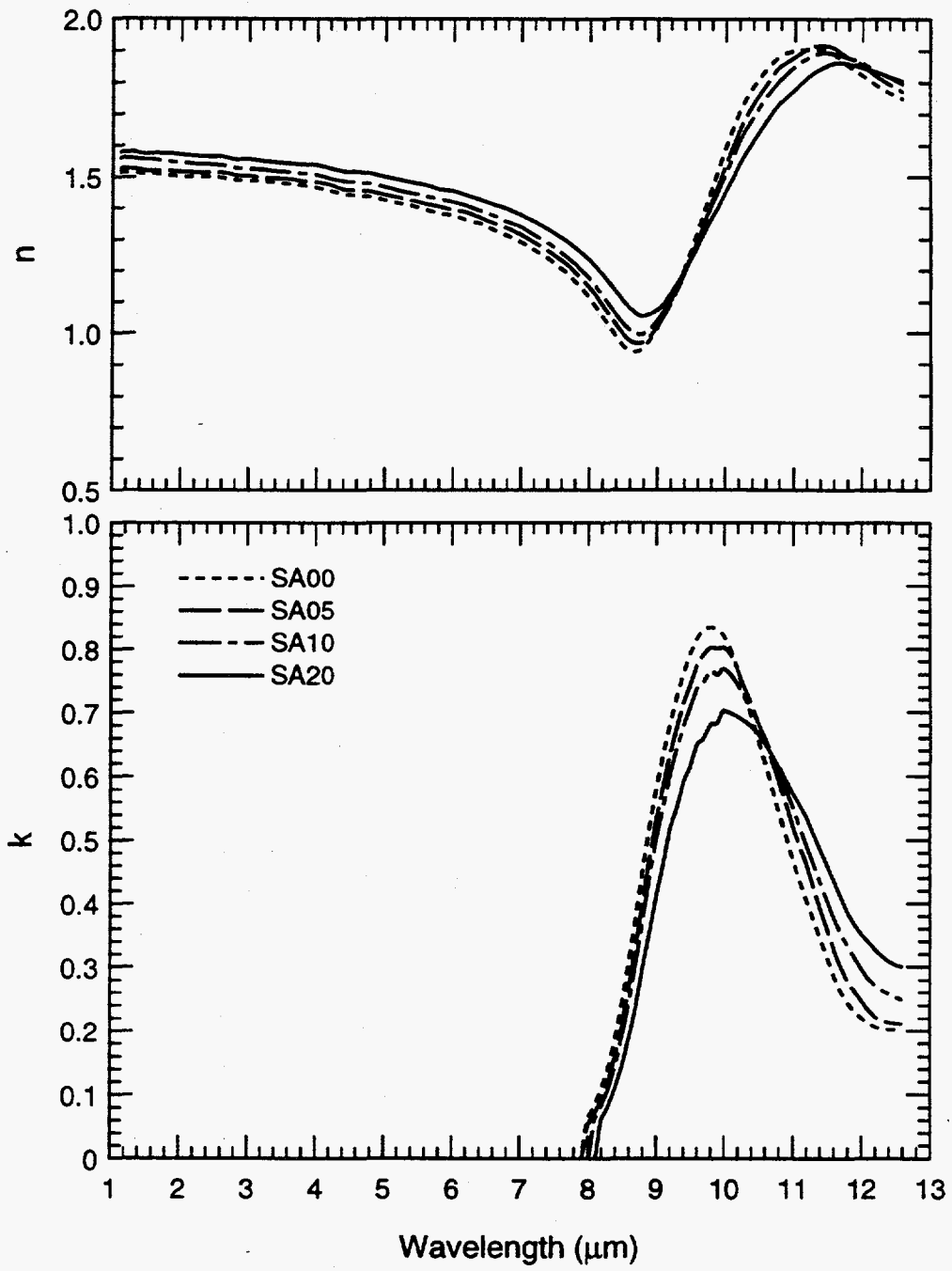

Figure IV.5: Refractive index (n and k) of molten slags SA00, SA05, SA10, and SA20 determined by Kramers–Kronig analysis of near normal reflectance.

wavelength range ($\lambda > 8\mu$m) the increase in Fe_2O_3 produces a weaker and somewhat broader absorption band. These effects are quantified, and correlated with the slag composition in later sections.

The effect of composition is further illustrated in Fig. IV.6 where n and k for SA00, SA20, SA4S, and SA2S are presented. The most significant feature illustrated here is the effect of lower SiO_2 content on the absorption band near 10 μm. It is evident that the absorption band generally becomes weaker and broader with decreasing SiO_2, but it is also evident that the band shifts to longer wavelengths as SiO_2 content decreases.

IV.4 Transmittance of Molten Slags

The transmittances of three molten slags, SA01, SA4S, and SA05, were measured. Several attempts to measure the transmittance of slags with higher Fe_2O_3 content (e.g., SA10) failed due to insufficient signal with which to align the submerged mirror after initially submerging it. This critical first step in the process proved to be very difficult in all cases – several attempts to measure the transmittance of the three slags above failed before finally achieving proper alignment.

Once the submerged mirror was aligned the transmittance was measured at several wavelengths. The submerged mirror would typically drift out of alignment after several wavelength measurements, and was periodically checked and corrected during the wavelength scan. This need for regular realignment slowed the measurement process, with a typical scan taking several hours (4-8). Transmittance measurements were repeated several times at several wavelengths during the course of the experiment to determine if the properties of the slag were changing. No significant changes were observed.

The alignment drift was not identical for the three slags. The problem was worse for the SA01 and SA05 slags. The SA4S slag was probably less viscous than the SA01 and SA05 slags, thus offering less resistance to the motion of slag around and over the surfaces of the submerged mirror. The alignment of the mirror for the SA4S slag was reasonably steady throughout the measurement.

In addition to the initial alignment difficulties and drift discussed above, there were other difficulties that made the transmittance measurements very tedious. The

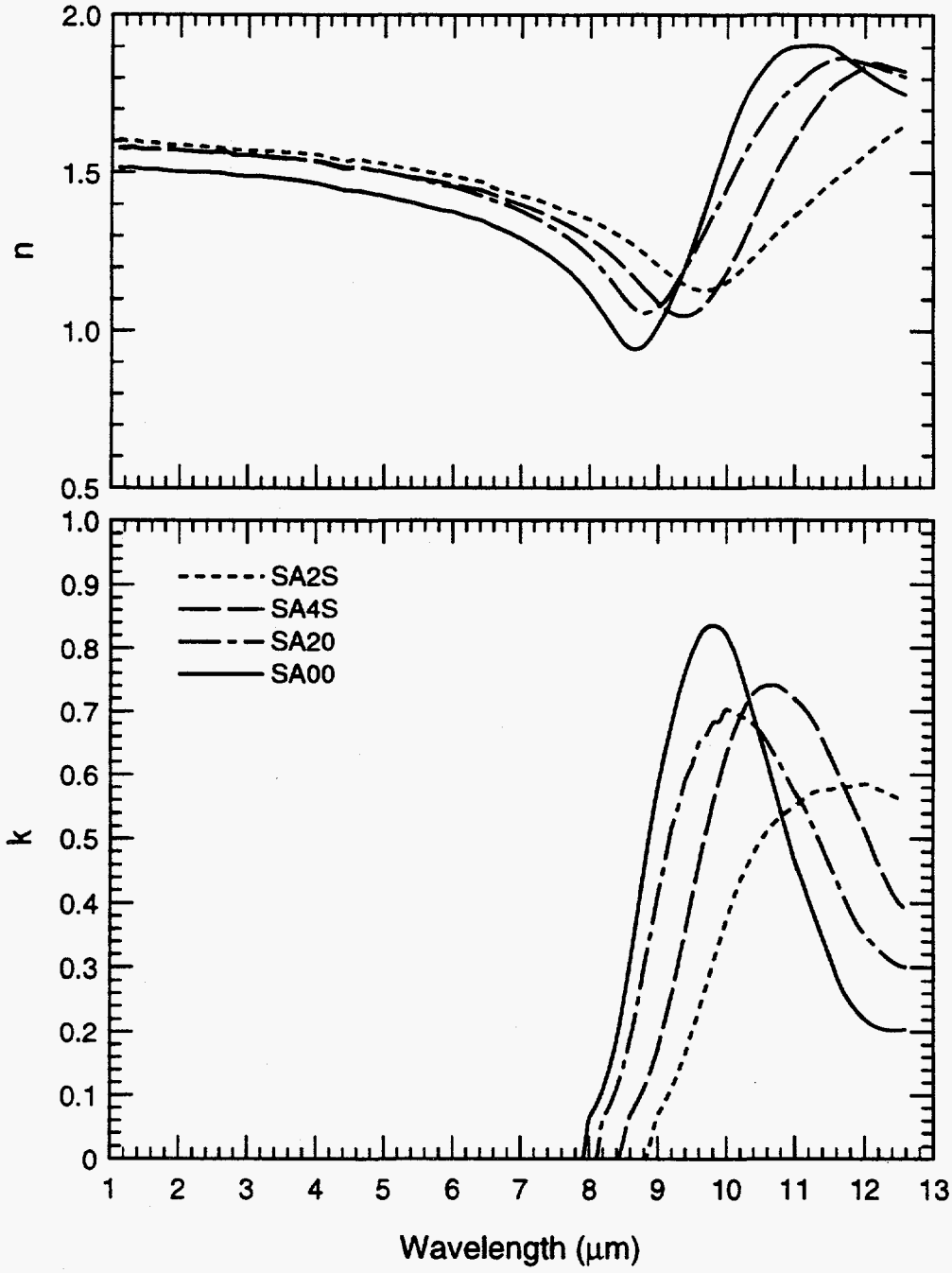

Figure IV.6: Refractive index (n and k) of molten slags SA00, SA20, SA4S, and SA2S determined by Kramers-Kronig analysis of near normal reflectance.

most significant problem was the presence of bubbles in the molten slag. This was particularly troublesome with slag SA01, as discussed below.

During the transmittance experiments the reflection from the pool of slag was visible in the longpass filter in front of the monochromator. When the platinum mirror was aligned it could be seen as a dark region in the pool, with a bright spot where the image of the Nernst glower fell. If the mirror was too deep, or the emission from the slag too large, the mirror could not be seen. For example, the mirror was not visible when submerged in slag SA05, but was visible in slag SA01, and visible in slag SA4S only when the mirror was very shallow.

Small bubbles could be seen in the slag, appearing as faint dark spots. The bubbles could be seen to move as the crucible was raised and lowered, flowing away from the center of the mirror when the slag layer above the mirror was thinning. The detector signal would drop when a bubble passed through the image of the Nernst glower. With some effort and sufficient time, one could rid the detection volume of detectable bubbles by varying the molten slag layer thickness, hence stirring the slag. The bubbles were generally sparse and non-uniformly distributed. Of course, since the transmittance measurement continually stirred the slag, it was necessary to continually check for bubbles.

The transmittance measurements yield a direct measure of k, as discussed in Chapter III. Figure IV.7 shows the results for slags SA01, SA4S, and SA05. As expected, k increases with increasing iron content, and increases with wavelength for wavelengths longer than approximately 4 μm. At the long wavelength limit of the transmittance spectra, near 5 μm, it is apparent that k for SA05 and SA01 are converging to similar values, while k for SA4S is lower. This trend is expected since the absorption in the 4-5 μm range is due primarily to multiphonon absorption by SiO_2, and not by Fe_2O_3. SA4S has significantly less SiO_2 than either SA01 or SA05.

The effect of temperature on k in the 1-5 μm range is illustrated in Fig. IV.8. For the entire wavelength range the absorption index increases with increasing temperature. Both the room temperature slags and the molten slags approach a value independent of Fe_2O_3 content near 5 μm, but the room temperature slags approach a lower value.

The effect of temperature on k was investigated by Goodwin [11] for temperatures below approximately 1200 K. Thin wafers of slag SA05 were placed in a furnace

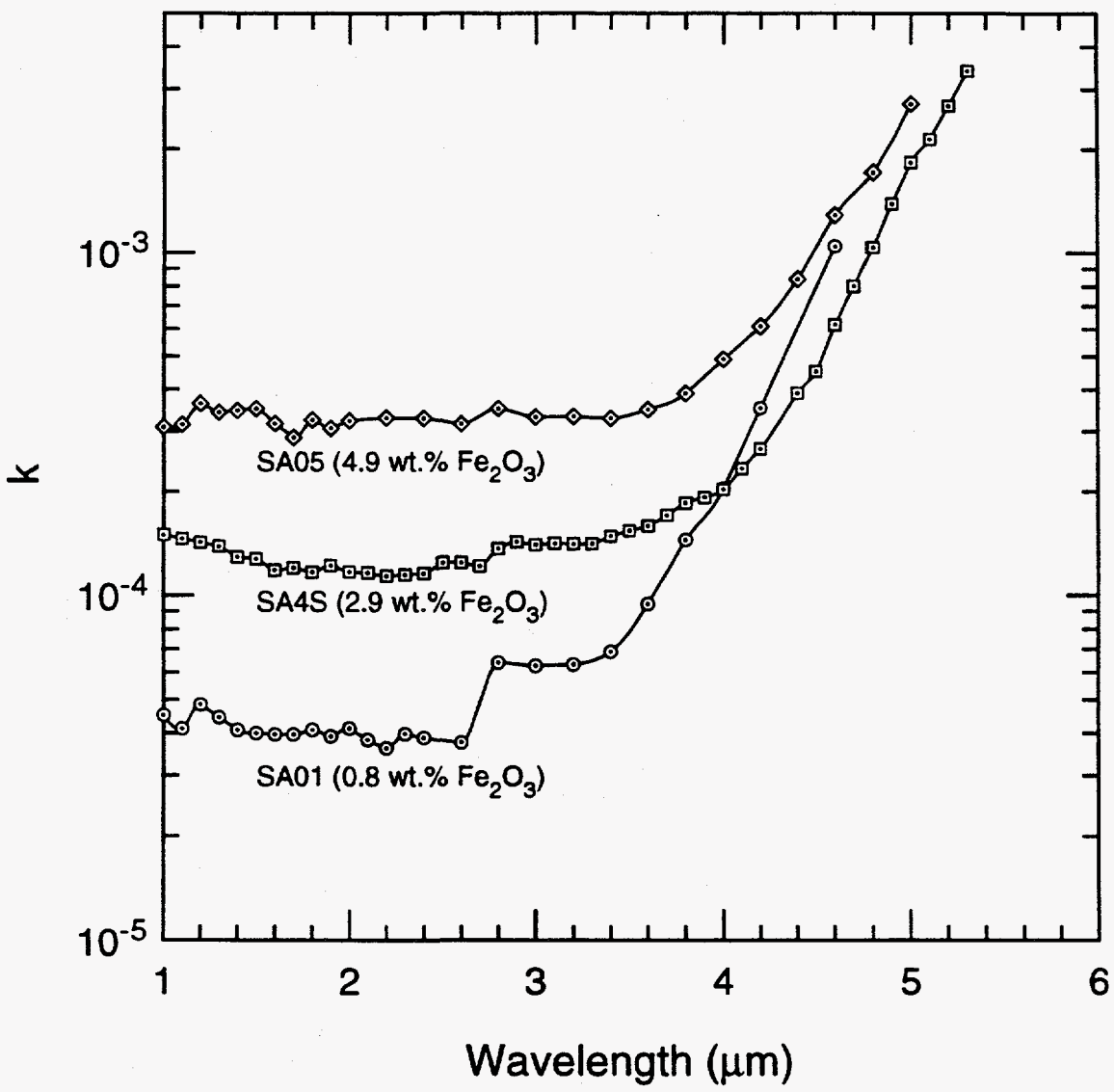

Figure IV.7: The absorption index of molten slags SA01, SA4S, and SA05 as determined from transmittance measurements.

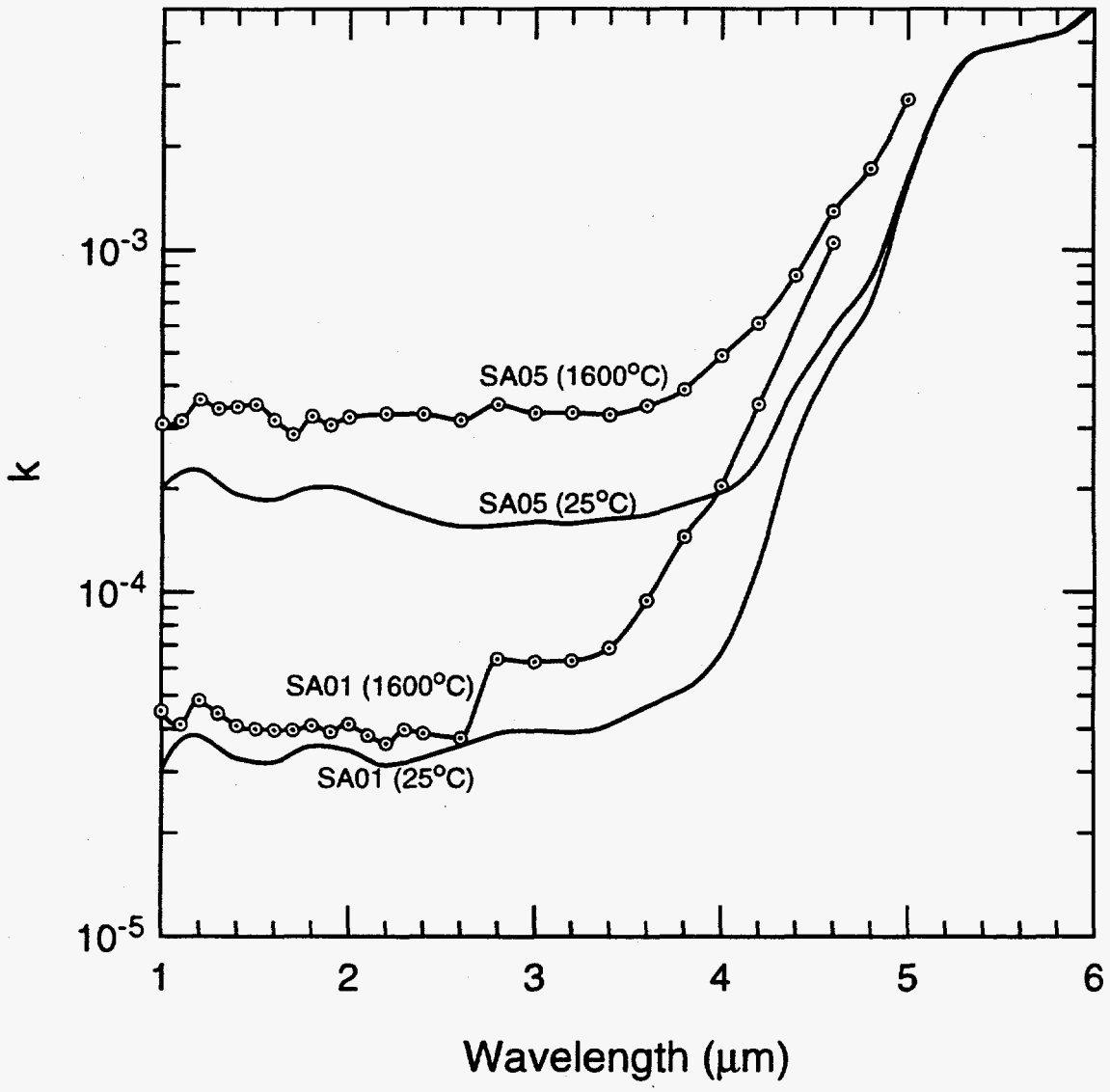

Figure IV.8: The effect of temperature on the absorption index of SA01 and SA05 in the 1-5μm range.

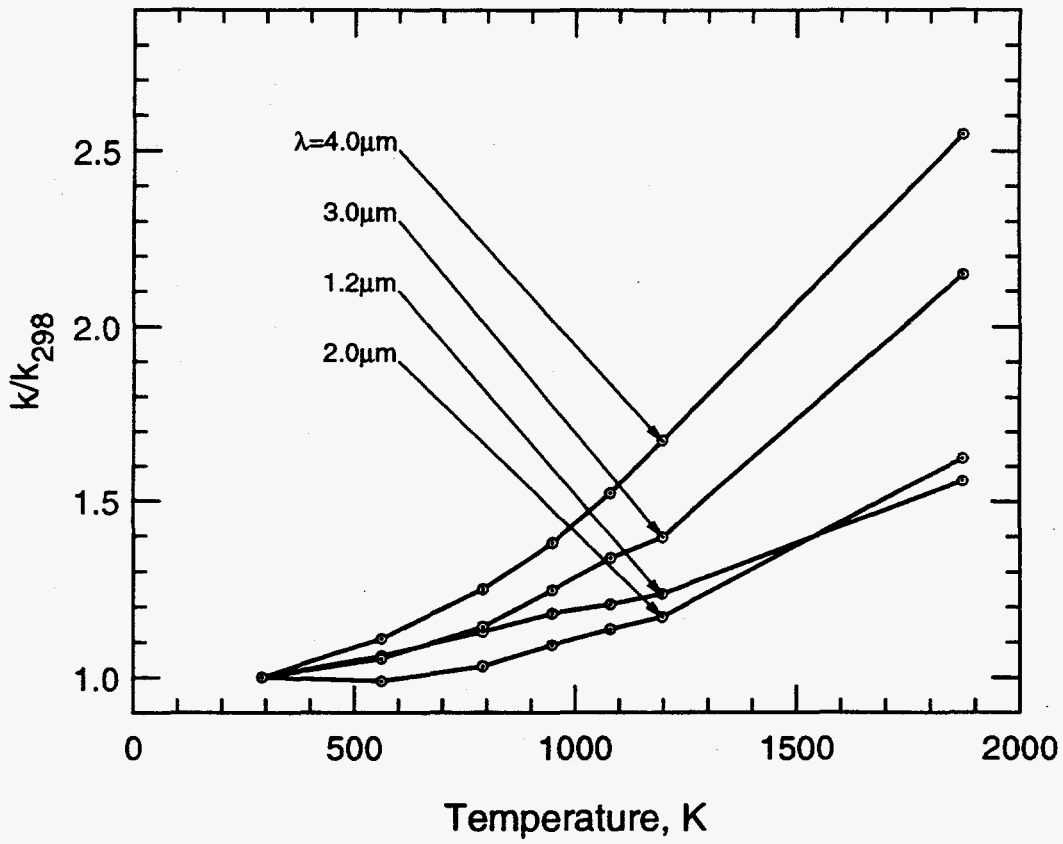

Figure IV.9: The effect of temperature on the absorption index of SA05 at several wavelengths.

and transmittance measurements were made. The resulting data are illustrated in Fig. IV.9, along with the new values at 1873 K. The curves for $k(T)$ demonstrate that the results for the molten slag are in agreement with the trends predicted by the lower temperature measurements.

It is significant that there are no discontinuities in the optical properties through the transition from lower temperatures where the slags are solid (but glassy) to higher temperatures where the slags are liquid. Unlike crystalline solids which undergo a discontinuous structural change, or phase change, the properties of glassy solids change more gradually and continuously with temperature from the solid to liquid states.

Referring to Fig. IV.8, it is evident that the high temperature slags have an absorption feature near 2.8 μm that is absent in the low temperature data. This

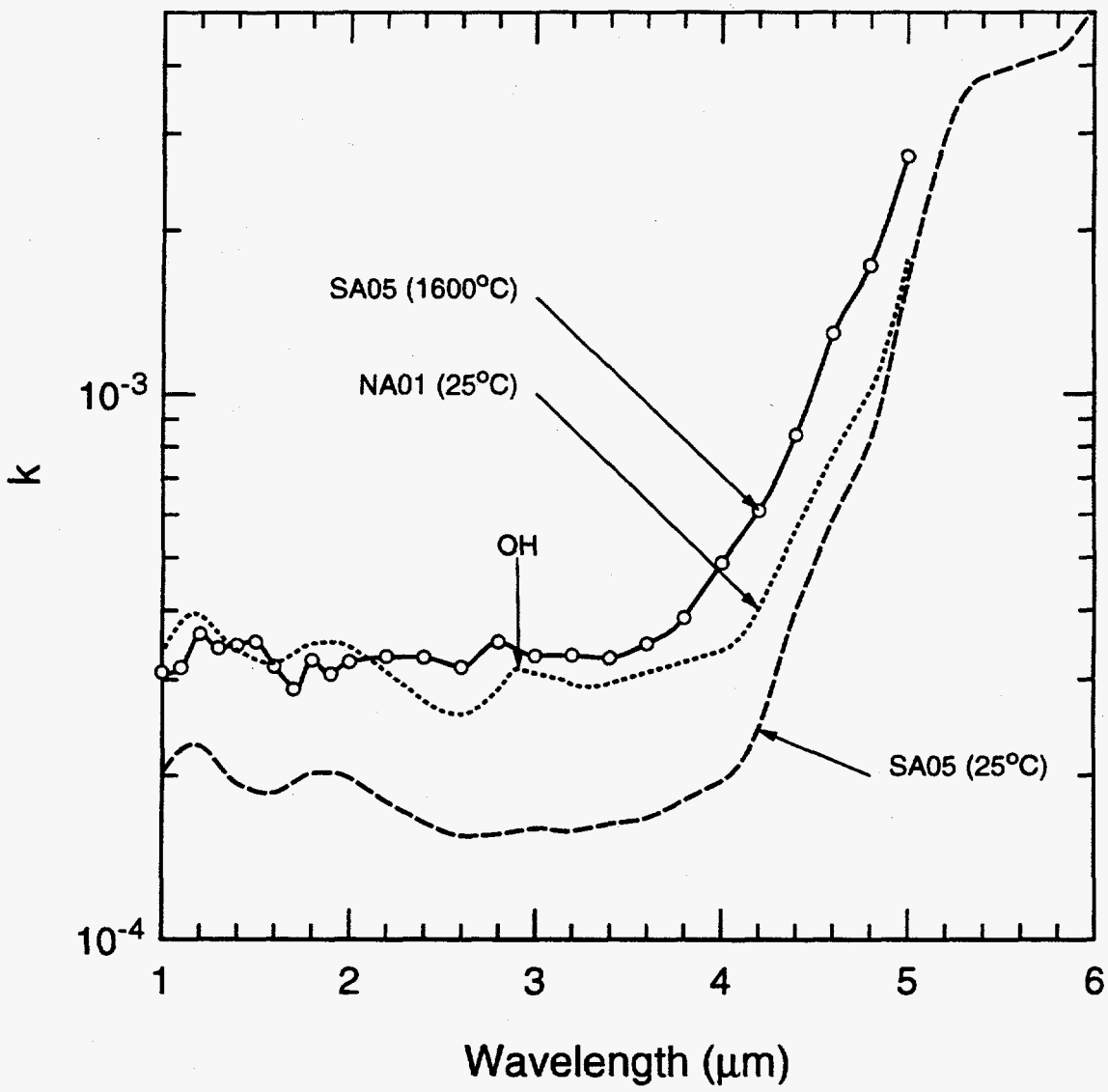

Figure IV.10: Comparison of k for SA05 with slag produced from natural slag NA01 (5.68 wt.% Fe_2O_3).

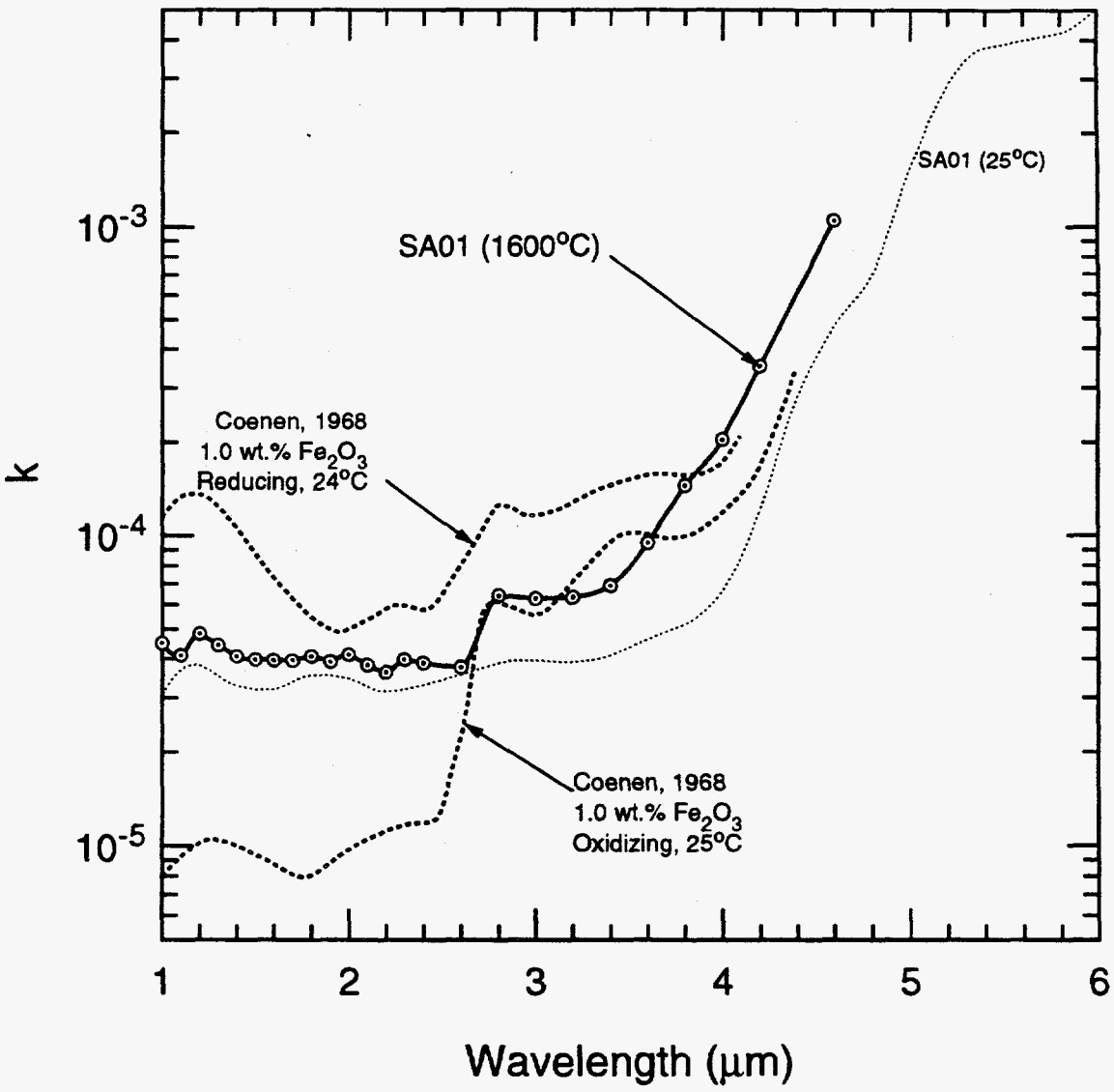

Figure IV.11: Comparison of k for SA01 with sodium-silica slags produced in air and reducing environments.

feature is probably due to OH absorption in the slag. The slag samples prepared here were mixed with water to facilitate good mixing, while Goodwin mixed the powered oxides dry and held the melts longer at high temperature to ensure good mixing. In a coal furnace there is ample water (combustion product); thus the slags mixed in water are probably more typical of real fly ash. Also, the clays (and perhaps other minerals) in the coal that form the ash also contain OH. Goodwin made transmittance measurements of slag produced from real ash, NA01, with composition similar to that of SA05. It showed a slight increase in absorption near 2.8 μm, as illustrated in Fig. IV.10. Note that the slag NA01 had approximately 5.68 wt.% Fe_2O_3 thus higher absorption than room temperature SA05.

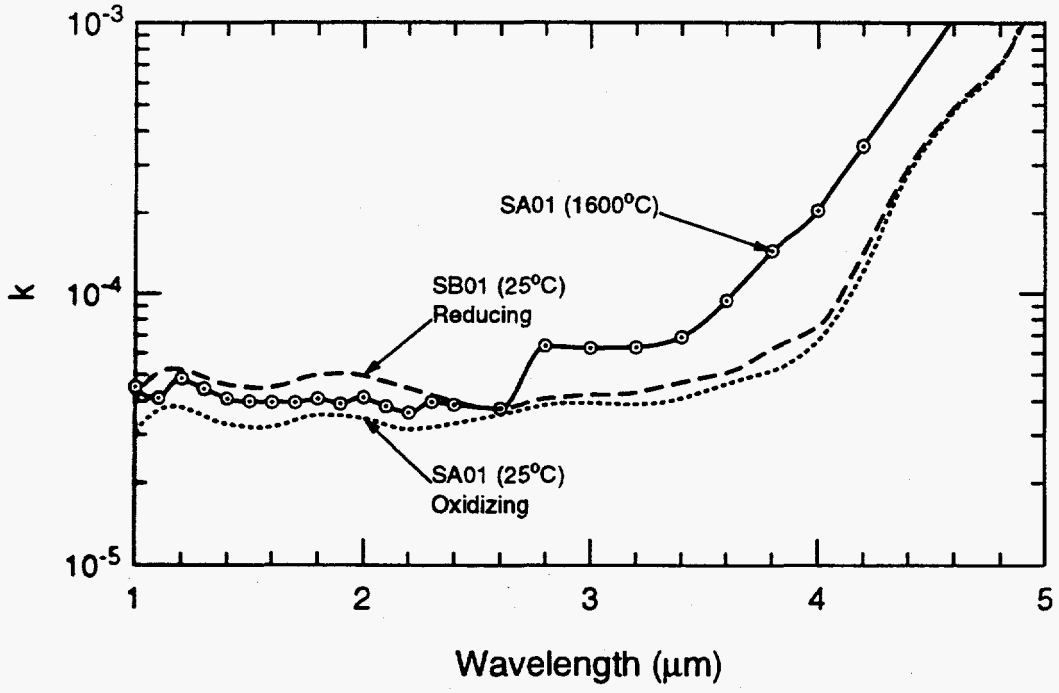

Figure IV.12: Comparison of k for SA01 with room temperature slags SA01 and SB01 (Goodwin, 1986), produced in oxidizing and reducing atmospheres, respectively.

The 2.8 μm absorption feature, presumably attributable to OH absorption, is also evident in the transmittance of some sodium–silica glasses investigated by Coenen [23], as illustrated in Fig. IV.11. Coenen also investigated the effect of producing the iron bearing glass in oxidizing and reducing environments and the

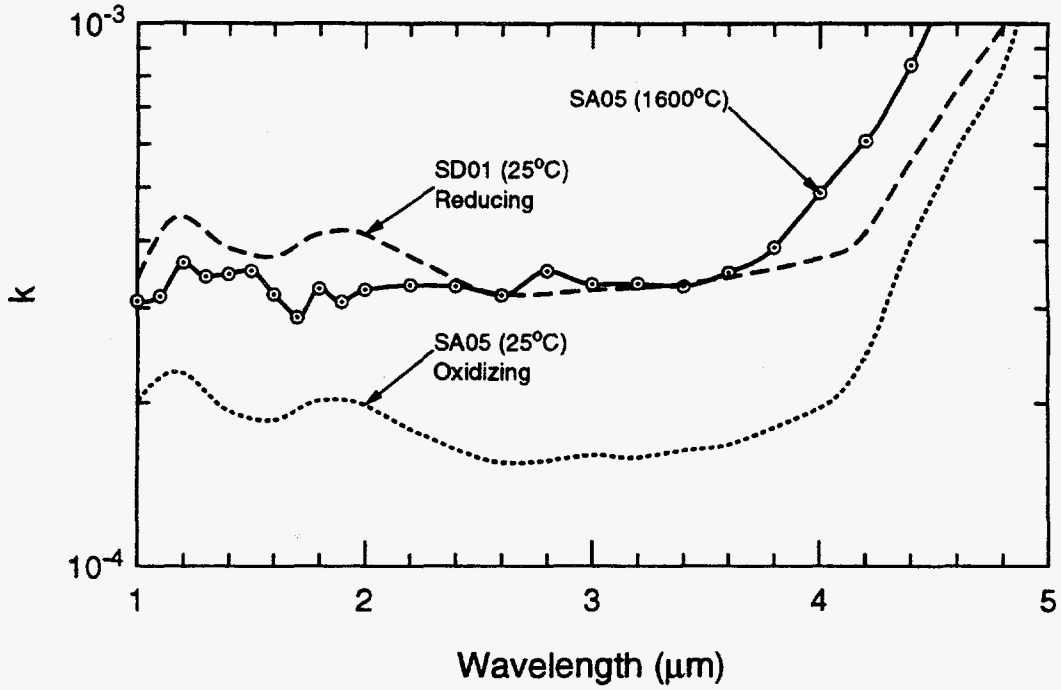

Figure IV.13: Comparison of k for SA05 with room temperature slags SA05 and SD05 (Goodwin, 1986), produced in oxidizing and reducing atmospheres, respectively.

effect of temperature in the range from 25°C to 1400°C. The glass produced in an oxidizing environment has weaker absorption in the 1-4 μm range. Nevertheless, at wavelengths below approximately 2.6 μm, k for the molten slag SA01 is much closer to the values measured by Goodwin for room temperature slags.

Figures IV.12 and IV.13 show the effect of oxidation state on k. The high temperature absorption index lies above that of room temperature slag produced in an oxidizing environment, and generally somewhat below that of room temperature slag produced in an reducing environment. However, near the 2.8 μm OH absorption band and at longer wavelengths the high temperature slag has somewhat higher absorption than either slag at room temperature.

The major conclusion to be drawn here is that increasing the Fe_2O_3 content of the slag increases k in the wavelength range from 1-4 μm. In addition, for slags produced in an oxidizing environment (air) the absorption index increases with increasing temperature. However, the temperature effect may be much less significant than the effect of the oxidation state of the Fe_2O_3 – slags produced in a reducing environment

show significantly higher absorption index in the 1-4 μm range than those of similar composition produced in an oxidizing atmosphere. Finally, OH in the slag produces a sudden absorption increase for increasing λ near 2.8 μm. This effect is significant for slags with low iron (Fe_2O_3< 1wt.%), but is of decreasing importance for slags with higher iron content. Both slags produced from real ash and those produced here by wet mixing of pure oxides show this OH absorption feature. Slags produced by dry mixing of pure oxides did not show significant OH absorption.

IV.5 Correlations for the Optical Constants of High Temperature Slag

IV.5.1 The Density of Glass.

The density of glasses, of which coal slags are a subset, vary considerably with composition. In silica glass most of the volume of the glass is attributable to oxygen. For example, in a silica glass where oxygen contributes only 53% of the mole fraction it may contribute up to 98.7% of the total glass volume [24]. Therefore, to a considerable degree the density of glass is a measure of its oxygen content, with denser glasses typically containing less oxygen. Of course, predicting the exact density of glass is complicated by the fact that the mean volume occupied by the oxygen ions (O^{--}) varies with glass composition, and from site to site. Glass does not have long range order of the type seen in crystals, but is a polymer of oxides interwoven by bonds with slightly varying bond angles and lengths. Free spaces in the glass have sizes that vary throughout a given glass, and with glass composition. Many texts exist on the structure of glasses and the resulting properties, but are largely beyond the scope of this work. See, for example, Volf [24] and Holloway [25] for further discussion of glass and its properties. A brief discussion of the structure of glass is presented in Appendix F.

The density of glass cannot generally be computed from the weighted average of the densities of the free oxides since, for example, the structure of tetrahedral SiO_4 in glass is slightly different than the tetrahedral structure in crystalline quartz. In the glass, the "tetrahedral" structure is not precisely tetrahedral, since that would imply long range order not found in glass. Instead, the bond angles and distances about a given Si atom are perturbed from the ideal tetrahedral arrangement found in perfect

Table IV.5: Density of free oxides and oxides in glass at room temperature

Oxide	Density of Free Oxide (g/cm^3)	Density of Oxide in Glass (g/cm^3)
SiO_2	2.20	2.28
Al_2O_3	3.97	2.50
CaO	3.31	3.90
Fe_2O_3	5.24	5.24*
Na_2O	2.27	3.10
BaO	5.72	7.00
TiO_2	4.86	3.80
MgO	3.58	3.30
* Density of free oxide.		

crystals. For example, consider the calculation of the density as the mass weighted sum of specific volumes for free oxides given in Table IV.5. For oxide density ρ_i, the mean density of the mixture is given approximately by

$$\frac{1}{\rho} \simeq \sum_i \frac{x_i}{\rho_i} \qquad (IV.2)$$

where x_i is the weight fraction of oxide i. The results are summarized in Table IV.6.

Using Eq. (IV.2) to estimate the slag density consistently overpredicts the density, as expected. The error is typically on the order of 10%, which is somewhat less than the density variation with composition. For example, the density of SA00 is approximately 16% lower than that of NAEB or SA2S. For some applications it may be more important to know how the density varies with addition of some oxide than to predict the exact value. For such applications use of Eq. (IV.2) is probably sufficient.

An improved estimate is obtained by recognizing that the contributing density of an oxide in glass is not the same as its free density [24]. Therefore, Volf suggested that the densities of oxides in glass shown in Table IV.5 be used. Using these *effective* oxide densities in place of the oxide densities in Eq. (IV.2) produces better agreement with the experimental results, with average errors of approximately 3%, as shown in Table IV.6.

Finally, the densities of the slags decrease with increasing temperature owing to thermal expansion. Typically silicate glasses have relatively small coefficients of

Table IV.6: Estimate of density based on oxide composition.

		using free oxide density		using oxide in glass density	
Slag	Measured	Est.	% Error	Est.	% Error
SA00	2.54	2.73	-7.67	2.46	3.33
SA01	2.56	2.75	-7.41	2.47	3.55
SA05	2.61	2.83	-8.24	2.54	2.56
SA10	2.68	2.89	-7.76	2.59	3.42
SA20	2.89	3.05	-5.53	2.73	5.43
SA4S	2.79	2.97	-6.27	2.79	0.09
SA2S	3.07	3.40	-10.82	2.87	6.53
SA1S	2.98	3.48	-16.70	3.04	-1.88
NAEB	3.03	3.16	-4.38	3.01	0.53
Slag from previous study (Goodwin, 1986)					
SA00	2.54	2.77	-9.11	2.51	1.14
SA05	2.60	2.83	-8.98	2.57	1.04
SA10	2.64	2.90	-9.98	2.64	-0.11
SB20	2.72	3.03	-11.29	2.77	-1.87

thermal expansion on the order of a few parts per million per degree centigrade change in temperature at room temperature. Holloway [25] gives the *linear* thermal expansion coefficient for Aluminosilicate glass at room temperature as $3.3 \times 10^{-6}/°C$. If this expansion coefficient is used to compute the change in density, then from 25 to 1600°C the density would only decrease by 1.6%. Since the expansion coefficient increases somewhat with increasing temperature, the true density decrease may be somewhat larger.

IV.5.2 The Normal Dispersion Region.

In the wavelength range from 1 μm to approximately 8 μm the real refractive indices of the slags decrease with increasing wavelength† . In this wavelength range the absorption index, k, is very small compared to the real refractive index. However,

† This is called normal dispersion, since prisms with negative $dn/d\lambda$ are most common, and disperse light "normally".

as will be shown here, the normal dispersion of n *does* depend on the position of the SiO_2 vibrational absorption band, even though it lies at much longer wavelengths.

In Chapter II the oscillator model for the complex dielectric function was presented (Eq.(II.30)). In this model the complex dielectric function is given by

$$\epsilon = (n + ik)^2 = n_\infty^2 + \sum_j \frac{\omega_{p,j}^2}{\omega_{o,j}^2 - \omega^2 - i\gamma_j\omega}$$

where n_∞ is the sum of contributions by high frequency absorption bands. If we ignore the imaginary terms and retain only the terms which contribute to n, we can write

$$n^2 - k^2 = n_\infty^2 + \sum_j \frac{\omega_{p,j}^2 \left(\omega_{o,j}^2 - \omega^2\right)}{\left(\omega_{o,j}^2 - \omega^2\right)^2 + (\gamma_j\omega)^2} \qquad (IV.3)$$

If $\omega^2 >> \omega_o^2$ we can approximate Eq. (IV.3) by the expression

$$n^2 - k^2 \simeq n_\infty^2 + \sum_j \frac{\omega_{p,j}^2}{\omega_{o,j}^2 - \gamma_j^2 - \omega^2} \qquad (IV.4)$$

This model can be expressed in terms of wavelength, $\lambda = 1/\omega$ (†), as

$$n^2 - k^2 \simeq n_\infty^2 + \sum_j \frac{\left(\omega_{p,j}^2 \lambda_{o,j}^2\right) \lambda^2}{\lambda^2 - \lambda_{o,j}^2} \qquad (IV.5)$$

Here γ_j has been included in the constant term $\lambda_{o,j}$ through the formula

$$\lambda_{o,j}^2 \equiv \frac{1}{\omega_{o,j}^2 - \gamma_j^2}.$$

This general form for the normal dispersion fits most dielectric materials ($k << n$), and if we are interested only in the near infrared spectrum it can be approximated as [26]

$$n^2 - 1 = C - \frac{B\lambda^2}{\lambda_o^2 - \lambda^2} \qquad (IV.6)$$

Equation IV.6 was fitted to the measured n of the nine slags studied here. A least squares procedure was used to determine C, B, and λ_o using n only at wavelengths

---

† Here ω indicates wavenumber, which is proportional to frequency but has units of $length^{-1}$. Note that to convert from wavenumbers to frequency multiply by $2\pi c_o$, where c_o is the vacuum speed of light.

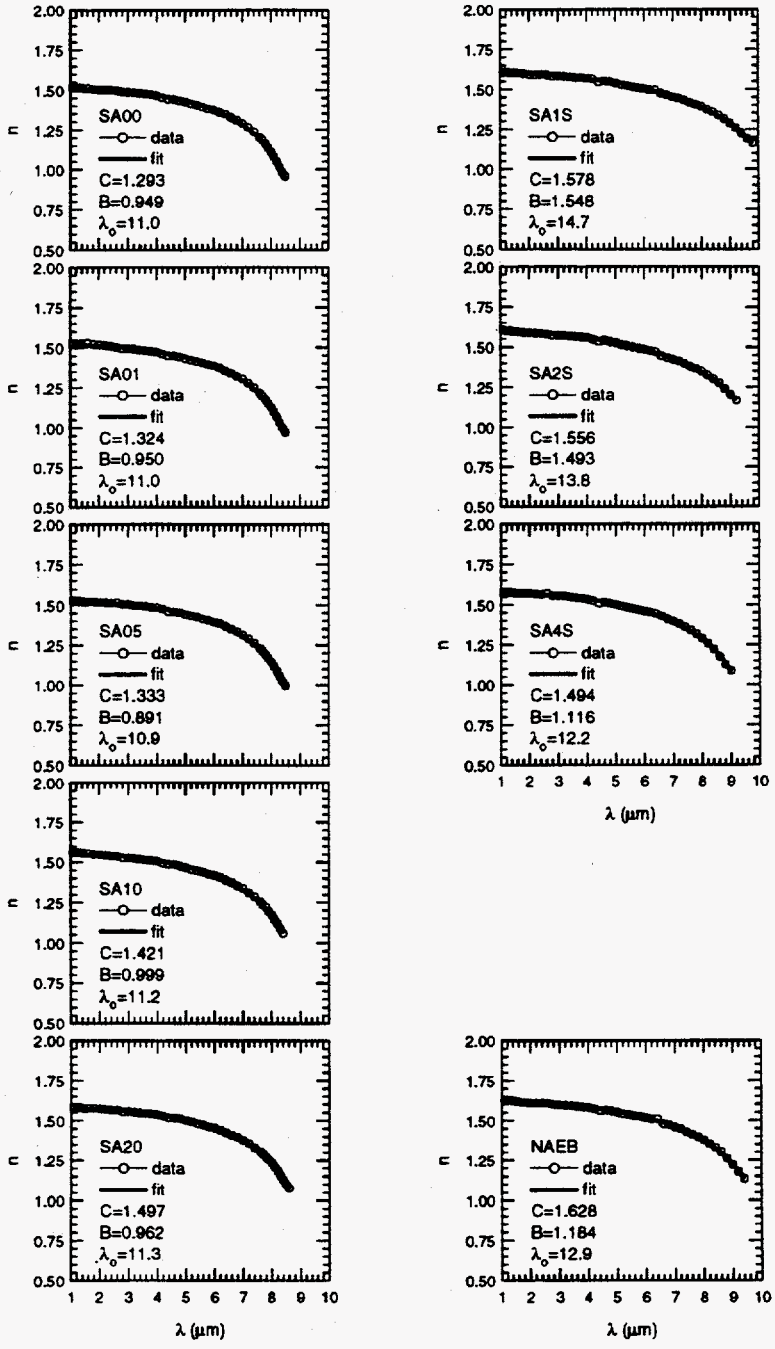

Figure IV.14: Best fit of the equation $n^2 - 1 = C - B\lambda^2/(\lambda_o^2 - \lambda^2)$ to the measured refractive index, n, for the nine slags.

Table IV.7: Values of constants for best fit of normal dispersion model to measured refractive indices.

Slag	C	B	λ_o (μm)	Range (μm)	rms diff.	Max diff. (at λ, μm)
SA00	1.293	0.949	11.03	1–8.5	0.0045	-0.0094 (4.4)
SA01	1.324	0.950	11.02	1–8.5	0.0052	0.0118 (1.6)
SA05	1.333	0.891	10.95	1–8.5	0.0040	-0.0104 (4.4)
SA10	1.421	0.999	11.18	1–8.4	0.0051	0.0108 (1.2)
SA20	1.497	0.962	11.26	1–8.6	0.0033	0.0069 (1.3)
SA4S	1.494	1.116	12.22	1–9.0	0.0044	-0.0151 (4.4)
SA2S	1.556	1.493	13.84	1–9.2	0.0039	0.0097 (1.1)
SA1S	1.578	1.548	14.72	1–9.8	0.0037	-0.0104 (4.4)
NAEB	1.628	1.184	12.90	1–9.4	0.0048	-0.0127 (4.4)

where $dn/d\lambda < 0$. The fits are illustrated in Fig. IV.14. Table IV.7 summarizes the best fit parameter values for each slag along with the errors of the fit. In all cases the maximum error did not exceed approximately 0.015, and the RMS error was typically less than 0.005.

To make use of the normal dispersion fit the variations of C, B and λ_o with slag composition and density were investigated. As expected, λ_o increased with decreasing Si content. A correlation for λ_o versus the mole fraction of SiO_2 was found and is illustrated in Fig. IV.15. The correlation is

$$\lambda_o \simeq 15.2 - 6.53\hat{x}_{SiO_2}. \qquad (IV.7a)$$

Here λ is in μm and $\hat{x}_{SiO_2}$ is the mole fraction of SiO_2 in the slag ($0 < \hat{x}_{SiO_2} < 1$).

A similar correlation was found for B, which also correlated well with the mole fraction of SiO_2. The constant B is seen to decrease with increasing SiO_2 content, with an approximate relationship

$$B \simeq 1.65 - 1.10\hat{x}_{SiO_2}. \qquad (IV.7b)$$

The parameter B is dimensionless. This correlation is illustrated in Fig. IV.16

Finally, the parameter C was found to correlate best with the density of the slag; it did not correlate well with SiO_2 content. The correlation

$$C \simeq -0.124 + 0.556\rho, \qquad (\rho \text{ in g/cm}^3) \qquad (IV.7c)$$

is shown in Fig. IV.17.

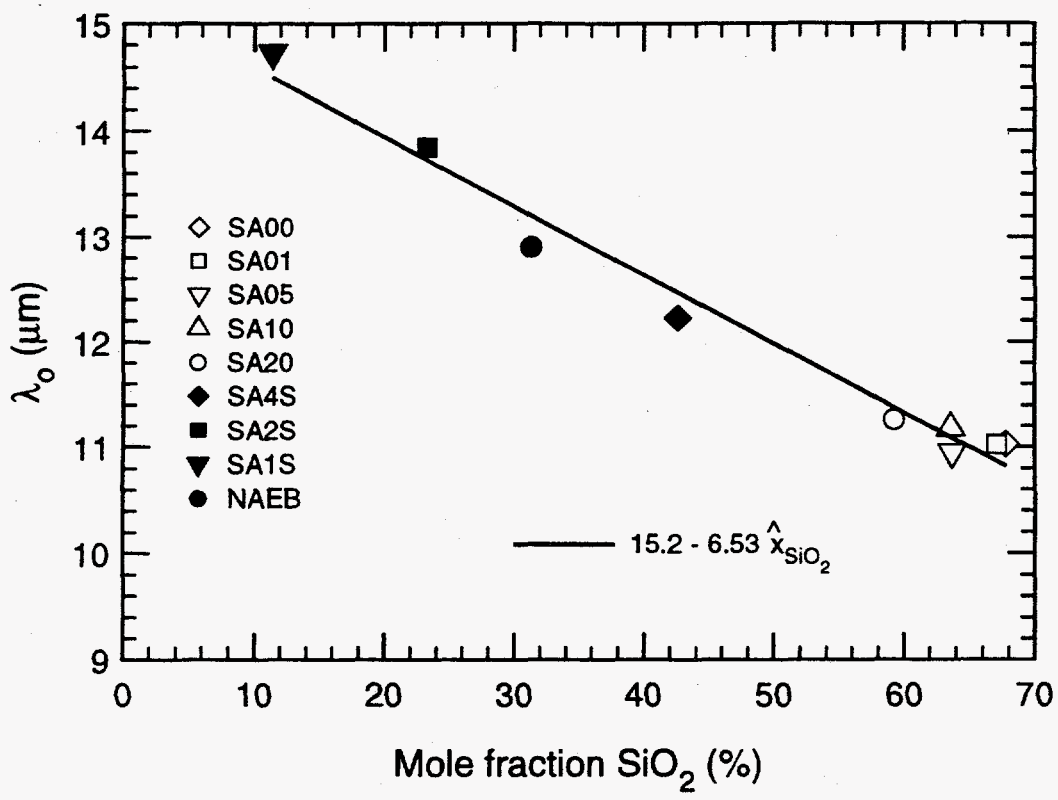

Figure IV.15: Variation of the parameter λ_o with mole percentage of SiO_2.

An interpretation of these results is that the parameters λ_o and B are related to the absorption properties at longer wavelengths, namely the SiO_2 absorption band. When the long wavelength absorption band is strong, B is large and n decreases faster with increasing wavelength. The more Si-O-Si bonds present, the stronger is the band and the more rapidly n changes at shorter wavelengths. The parameter λ_o is related to the center frequency of the long wavelength absorption band. In contrast, C is related to the strength of the ultraviolet and higher frequency absorption bands. These bands are dependent, for the most part, on transitions in the electronic shells of the atoms. Therefore, the strength of the high frequency absorption bands is strongly dependent on the number of atoms per unit volume, or density. The density of a material depends on atomic weight (number or protons and neutrons in the nucleus) divided by the effective volume occupied by the atom ($\propto$(outer shell radius)^3). This ratio generally increases with the atomic number and atomic weight; for example, lead, barium, tungsten, and uranium metals, oxides and glasses are all very dense and have

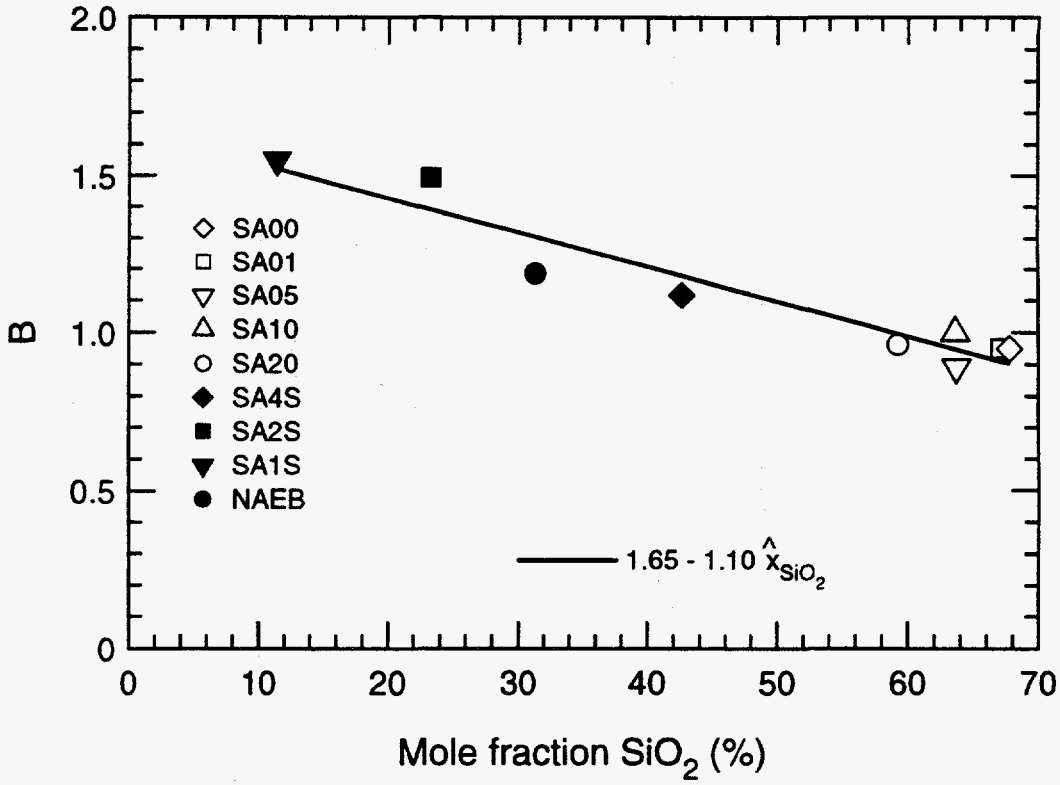

Figure IV.16: Variation of the parameter B with mole percentage of SiO_2.

high refractive indices. Of course, the value of C also depends on the wavelength and strength of the electronic absorption bands.

The correlations in Eq. (IV.7) were used to generate values for λ_o, B, and C using the measured values for $\hat{x}_{SiO_2}$ and ρ for each slag. A comparison of the resulting values of $n(\lambda)$ determined from Eq. (IV.6) are presented for slags SA00 and NAEB in Fig. IV.18. We see that the fit is reasonably good, with typical differences of less than ± 0.05. Evidently, the correlation for C underpredicts the value of C required to give the best fit to the NAEB data by approximately 0.037 (2.3%). Table IV.8 summarizes the use of the correlations in Eq. (IV.7) to predict the measured values of n for all nine slags studied.

Finally, it is often more difficult to know the density of ash than it is to know the composition. For example, computer controlled scanning electron microscopes can measure the compositions of individual fly ash particles, but their densities are

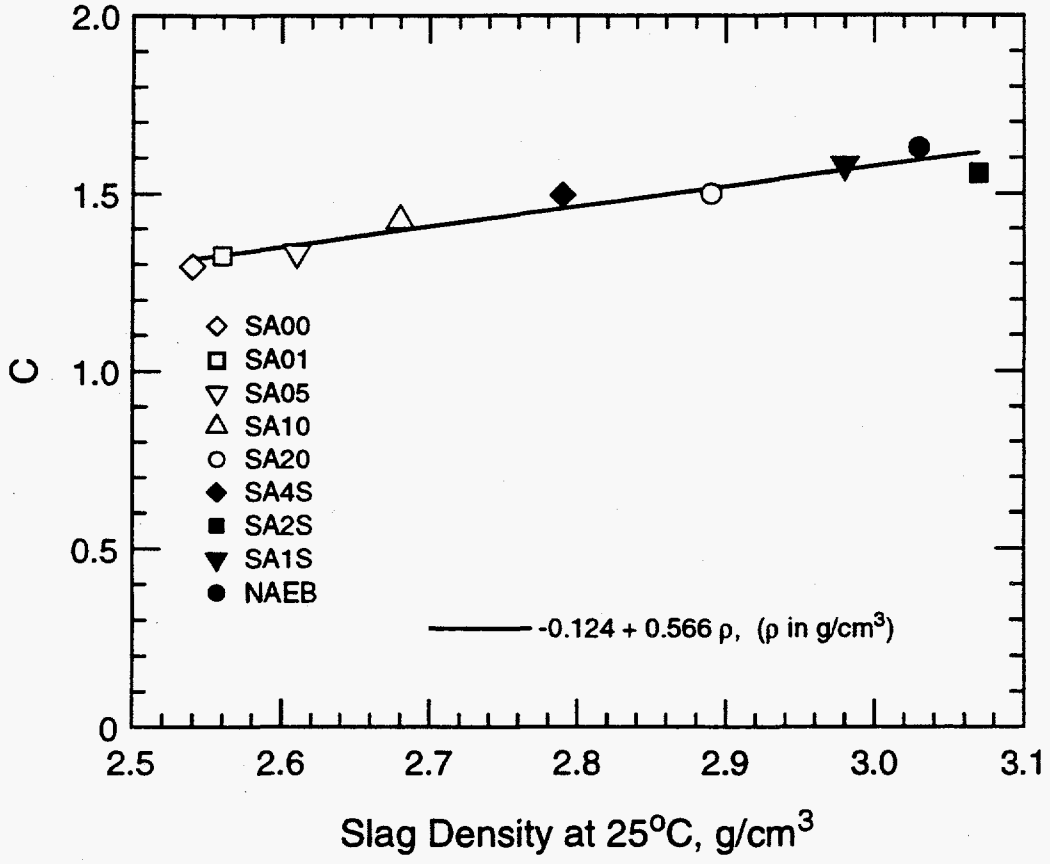

Figure IV.17: Variation of the parameter C with slag density, ρ.

more difficult to measure [17]. Therefore, it is useful to use Eq. (IV.2) to estimate the density based on the composition. Using the densities of oxides in glass presented in Table IV.5, one can estimate ρ for a glass with a specified composition and then use Eq. (IV.7) to obtain n only from a knowledge of the composition of the ash or slag. Table IV.9 summarizes the errors introduced by using this estimate of density. We see that the RMS errors are typically less than 0.03; NAEB is exceptional with an RMS error of 0.069.

IV.5.3 A Mixture Rule for n.

The foregoing correlation for the refractive index, n, uses only the density and mole fraction of SiO_2, and ignores other differences in composition. It is assumed

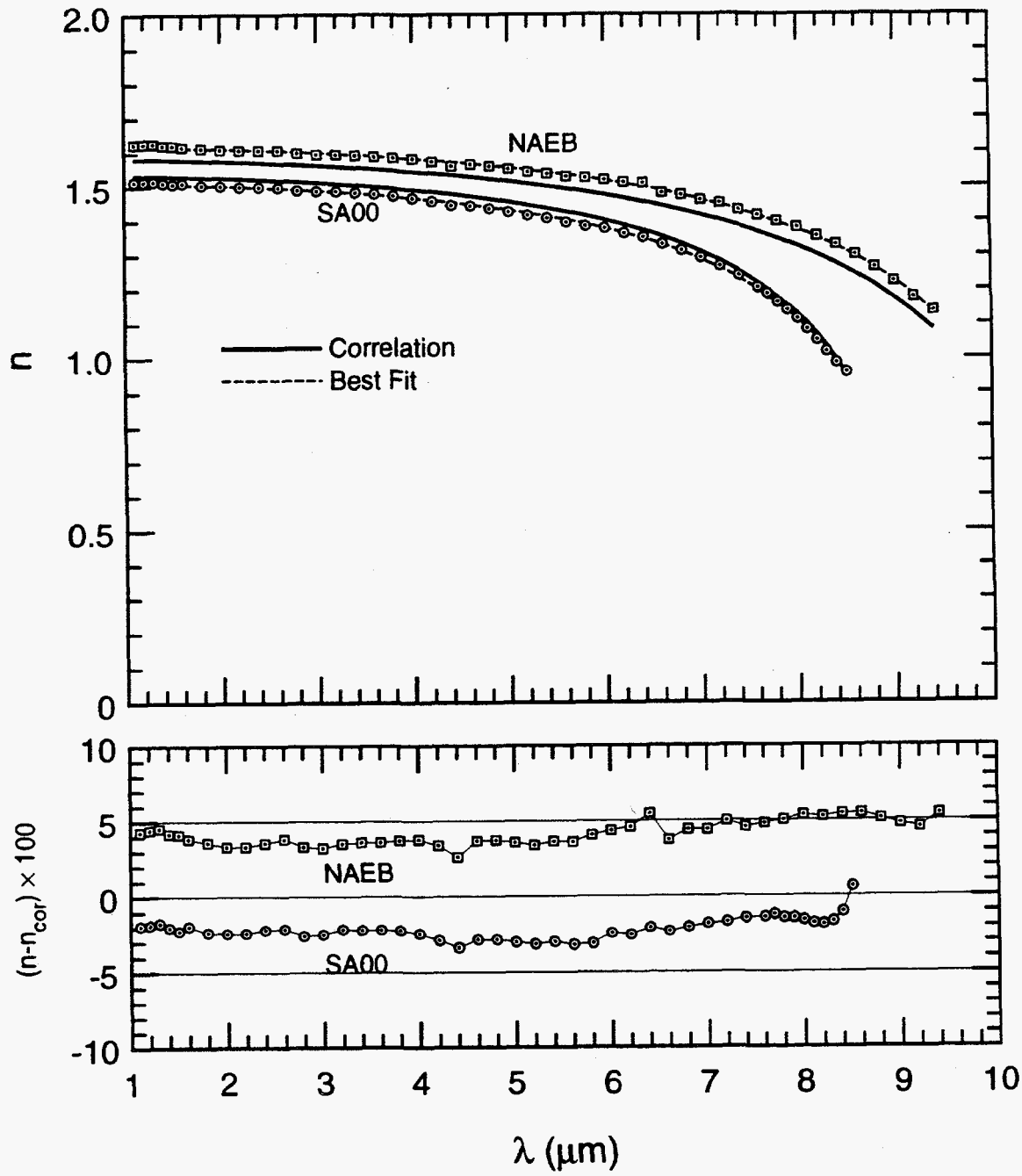

Figure IV.18: Comparison of the normal dispersion correlation with measured values of refractive index.

Table IV.8: Evaluation of correlation for normal dispersion model with measured refractive index, n. Values of constants based on measured compositions and densities.

Slag	C	B	λ_o (μm)	Range (μm)	rms diff.	Max diff. (at λ, μm)
SA00	1.314	0.905	10.78	1–8.5	0.0097	0.0212 (8.3)
SA01	1.325	0.912	10.82	1–8.5	0.0105	0.0292 (8.4)
SA05	1.353	0.949	11.04	1–8.5	0.0060	-0.0146 (4.4)
SA10	1.393	0.951	11.05	1–8.4	0.0107	0.0198 (1.2)
SA20	1.512	0.999	11.33	1–8.6	0.0046	-0.0102 (4.4)
SA4S	1.455	1.181	12.42	1–9.0	0.0146	0.0227 (2.6)
SA2S	1.614	1.394	13.68	1–9.2	0.0243	-0.0408 (9.0)
SA1S	1.563	1.524	14.45	1–9.8	0.0133	0.0395 (9.8)
NAEB	1.591	1.305	13.15	1–9.4	0.0183	0.0300 (6.4)

Table IV.9: Evaluation of correlation for normal dispersion model of n using estimate of ρ based on weighted sum of oxide densities in glass.

Slag	C	B	λ_o (μm)	Range (μm)	rms diff.	Max diff. (at λ, μm)
SA00	1.268	0.905	10.78	1–8.5	0.0189	0.0442 (8.3)
SA01	1.274	0.912	10.82	1–8.5	0.0247	0.0468 (8.3)
SA05	1.314	0.949	11.04	1–8.5	0.0140	0.0297 (8.5)
SA10	1.342	0.951	11.05	1–8.4	0.0284	0.0375 (7.8)
SA20	1.421	0.999	11.33	1–8.6	0.0298	0.0460 (8.6)
SA4S	1.455	1.181	12.42	1–9.0	0.0146	0.0227 (2.6)
SA2S	1.500	1.394	13.68	1–9.2	0.0156	0.0270 (1.1)
SA1S	1.597	1.524	14.45	1–9.8	0.0075	0.0245 (9.8)
NAEB	1.444	1.305	13.15	1–9.4	0.0687	0.0968 (9.4)

that the other constituents affect n only through their influence on density. Based on the accuracy of the foregoing correlations, this assumption may be quite reasonable, at least for the narrow range of compositions studied here. However, in this section an alternative correlation is presented that uses more compositional information to estimate the refractive index in the region of normal dispersion – a mixture rule. This approach has a much greater likelihood of predicting n for compositions differing significantly from those studied here. The following development follows closely that of Born and Wolf [26] and Goodwin [11].

To deduce the refractive index of a mixture of oxides from the refractive indices of pure oxides, or other mixtures, it is necessary to relate the refractive index to a physical quantity that is additive. One such quantity is the polarizability [11], since it relates the interaction of an applied electric field to local perturbations of the electric field in the vicinity of a single atom or molecule. However, to facilitate the summing over many species it is necessary to introduce the mean molar refractivity.

The mean molar refractivity of a material, A, is defined as

$$A = \frac{1}{3} N_m \alpha \qquad (IV.8)$$

where N_m is Avogadro's number (6.02×10^{23} atoms/mole) and α is the mean polarizability of the atom or molecule. The polarizability is a measure of the polarization of a given molecule induced by its interaction with an electric field, and the mean polarizability is an average over all orientations for that interaction.

To relate n to the mean polarizability of a molecule, consider the interaction of an electric field E with a molecule having polarizability α. The dipole moment of the molecule is the product of the polarizability and the local electric field, E_{loc}, at the molecule. Note that the molecule changes an applied electric field locally by interaction with its own electric field. For a collection of molecules the polarization, P, is the dipole moment per unit volume, or

$$P = \varepsilon_0 N \alpha E_{loc} \qquad (IV.9)$$

Here N is the number density of molecules and ε_0 is the permittivity of free space. The dielectric constant, ϵ, of an isotropic medium is defined as the ratio of the displacement to the electric field, or

$$\epsilon = D/E = \frac{(\varepsilon_0 E + P)}{E} \qquad (IV.10)$$

Substituting Eq. (IV.9) into Eq. (IV.10) gives

$$\frac{\epsilon}{\varepsilon_0} - 1 = N\alpha \frac{E_{loc}}{E}$$

For a real dielectric constant, $\epsilon/\varepsilon_0 = n^2$, as discussed in Chapter II. The relationship between the local field, E_{loc}, and the space averaged field, E, is a superposition of the external electric field and the local electric field, which is proportional to the polarization, that is,

$$E_{loc} = E + cP/\varepsilon_0 \qquad (IV.11)$$

Table IV.10: Dispersion equation parameters for pure oxides.

Oxide	form	density (g/cm^3)	C	B	λ_o, μm	Ref.*
SiO_2	fused silica	2.20	1.104	0.8975	9.896	[27]
Al_2O_3	sapphire	3.97	2.082	5.281	17.93	[28]
CaO		3.31	2.31	11.32	33.90	[29]
Fe_2O_3	hematite	5.24	8.3636	0.0	0.0	[30]
TiO_2	rutile	4.86	5.031	7.764	15.60	[31]
MgO		3.58	1.9625	2.470	15.56	[32]
* References and tabulated values from Goodwin [11].						

The constant c is the Lorentz local field factor, and is 1/3 for isotropic (or cubic) sites. If we assume $c = 1/3$ then the polarizability becomes

$$\alpha = \frac{3}{N}\frac{(n^2-1)}{(n^2+2)}. \qquad (IV.12)$$

This is called the Clausius–Mossotti relation, and is valid for a wide range of dielectric media. The critical assumptions are Eq. (IV.11) and the local field factor of 1/3.

Substituting Eq. (IV.12) in Eq. (IV.8), we can write the molar refractivity of a material as

$$A = \frac{\hat{M}}{\rho}\frac{(n^2-1)}{(n^2+2)} \qquad (IV.13)$$

Here $\hat{M}$ is the molecular weight of the material. If there are several components in the material (e.g., components with different polarizabilities) then we can write

$$A = \sum_i \hat{x}_i A_i \qquad (IV.14)$$

where $\hat{x}_i$ is the mole fraction of material i having molar refractivity A_i. This summation assumes that the refractivity of a given material is not altered by the presence of the other materials. Essentially this requires that the chemical bonds constituting the separate materials are not significantly altered when incorporated in the composite material. This is not always exactly true, but it is probably reasonably accurate for coal slag as evidenced by the accuracy of the predictions given below.

Substituting Eq. (IV.14) into Eq. (IV.13) we obtain

$$\frac{n^2-1}{n^2+2} = \rho \sum_i \left(\frac{x_{m,i}}{\rho_i}\right)\frac{(n_i^2-1)}{(n_i^2+2)} \qquad (IV.15)$$

where $x_{m,i}$ is the mass fraction of species i, ρ_i is its density, and n_i is its refractive index.

The mixture rule, Eq. (IV.15) is relatively simple to use once the refractive indices of the constituents of a slag, n_i, are known. Goodwin [11] suggests using the values shown in Table IV.10 (see [27-33]) to compute n_i using the normal dispersion formula

$$n_i - 1 \simeq C_i - \frac{B_i \lambda^2}{\lambda_{o,i}^2 - \lambda^2}. \qquad (IV.16)$$

It is significant that the values of C_i, B_i, and $\lambda_{o,i}$ tabulated in Table IV.10 are for oxides in a chemical form where the bonds are expected to be similar to the bonds of the same metal cations in the slag. For example, fused silica has a tetrahedral structure of Si singly bound to four neighboring oxygens, and is expected to have a similar structure in slag.

As demonstrated in the previous section, the infrared absorption wavelength, λ_o, shifts to significantly larger values when the silica content is decreased. To account for this shift in the infrared absorption band it is necessary to modify the dispersion relation for SiO_2 to the form

$$n_{SiO_2} = C_{SiO_2} - \frac{B_{SiO_2} \lambda^2}{\left(\lambda_{o,SiO_2} + \delta\lambda_o\right)^2 - \lambda^2} \qquad (IV.17)$$

In addition to this λ_o correction for SiO_2, a small correction term was added to the mixture density, ρ, in Eq. (IV.15) to improve the fit. The final mixture rule is thus

$$\frac{n^2 - 1}{n^2 + 2} = (\rho + \delta\rho) \sum_i \left(\frac{x_{m,i}}{\rho_i}\right) \frac{n_i^2 - 1}{n_i^2 + 2}. \qquad (IV.18)$$

Equation IV.18 was fitted to the refractive index data for all nine slags to find the best values for the free parameters $\delta\lambda_o$ and $\delta\rho$. The results of the fit to n for the nine slags are illustrated in Figs. IV.19 and IV.20. An approximate correlation for $\delta\lambda_o$ is

$$\delta\lambda_o \simeq 2.82 - 2.90\hat{x}_{SiO_2}. \qquad (IV.19)$$

As expected, the resonance wavelength λ_o shifts to longer wavelengths as the silica content is decreased.

The correction $\delta\rho$ was typically very small for all the slags studied here. Furthermore, the $\delta\rho$ correction was not particularly well correlated with the measured slag

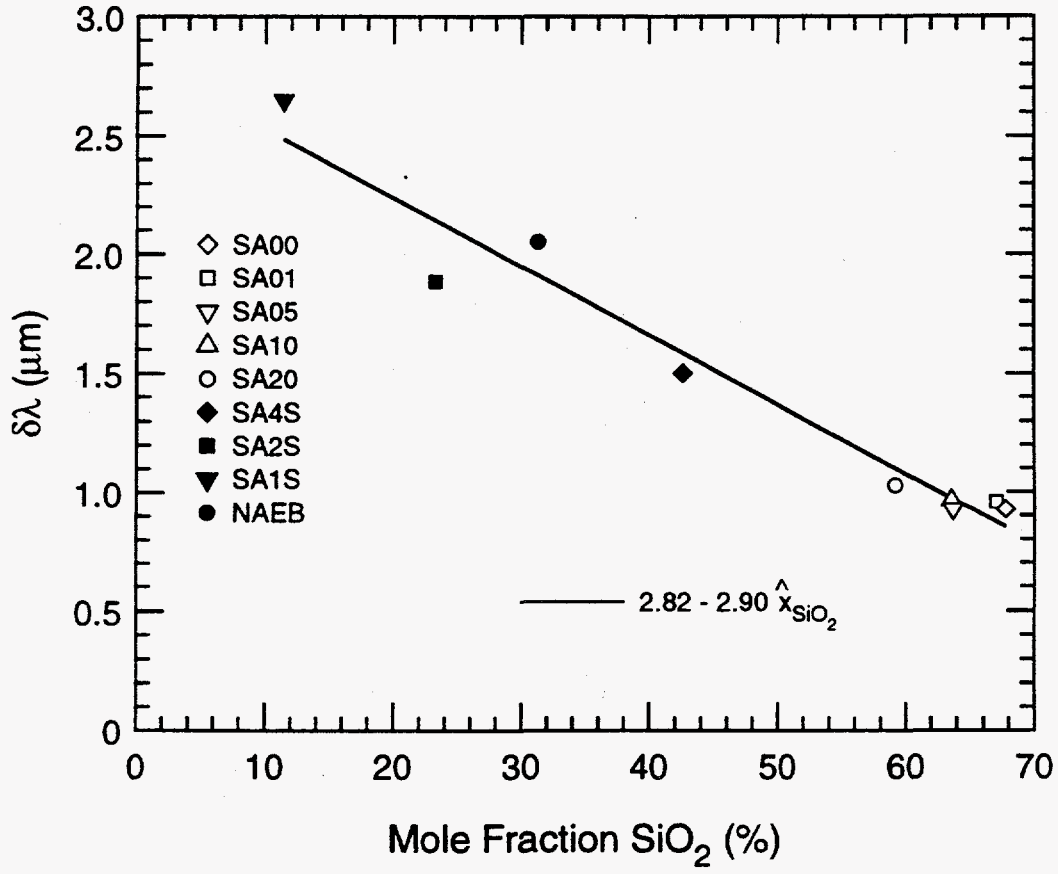

Figure IV.19: Correlation for $\delta\lambda_o$ in the mixture rule for the normal dispersion fit to the measured refractive index, n.

composition or density. (R=-0.73)† This result suggests that the mixture rule, along with the correction for λ_o shift, is fairly robust, and that the $\delta\rho$ correction may not be warranted.

---

† The linear correlation coefficient, R, for a set of data (x_i, y_i) is defined as [50]

$$\mathrm{R} = \frac{\sum_i (x_i - \overline{x})(y_i - \overline{y})}{\sqrt{\sum_i (x_i - \overline{x})^2}\sqrt{\sum_i (y_i - \overline{y})^2}}.$$

When data points fall exactly on a line with positive slope, R = 1 and we say x and y have completely positive correlation. When data points fall exactly on a line with negative slope, R = −1 and we say x and y have completely negative correlation. When R = 0 we say x and y are uncorrelated.

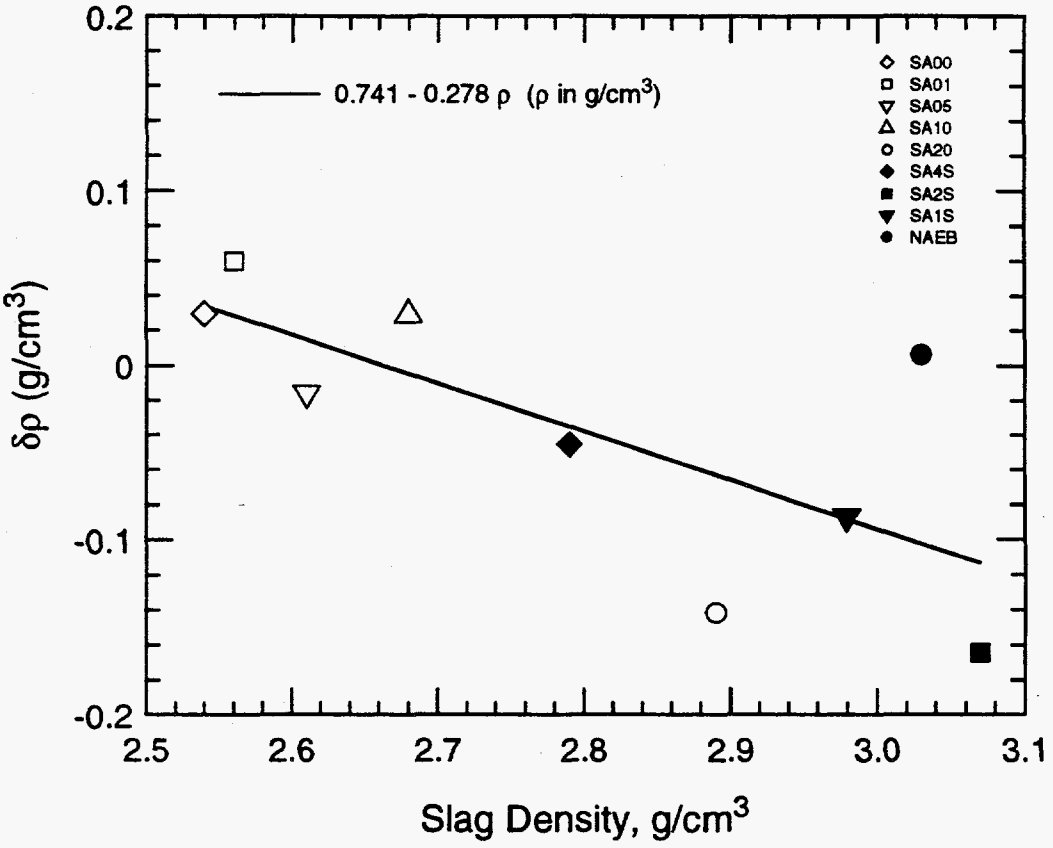

Figure IV.20: Correlation for $\delta\rho$ in the mixture rule for the normal dispersion fit to the measured refractive index, n.

A summary of the errors of the correlation, the best fit parameters, and the effects of using the correlations for $\delta\lambda_o$ and $\delta\rho$ is presented in Table IV.11. The results show excellent agreement between the correlation and the measured data. A comparison of the measured and calculated n for two typical slags, SA00 and SA4S, is presented in Fig. IV.21. The rms differences reported in Table IV.11 between the best two parameter fit using the mixture rule model and the experimental data are typically 0.003-0.005. This is quite good agreement, considering only $\delta\lambda_o$ and $\delta\rho$ are adjusted to produce the fit. In the second set of results, labeled "One parameter correlation", $\delta\lambda_o$ is computed using the correlation (Eq. (IV.19)) and $\delta\rho$ is held at zero. The differences again are quite small, although somewhat larger than if we use the correlation $\delta\rho = 0.741 - 0.278\rho$ as shown under the "Two parameter correlation" heading.

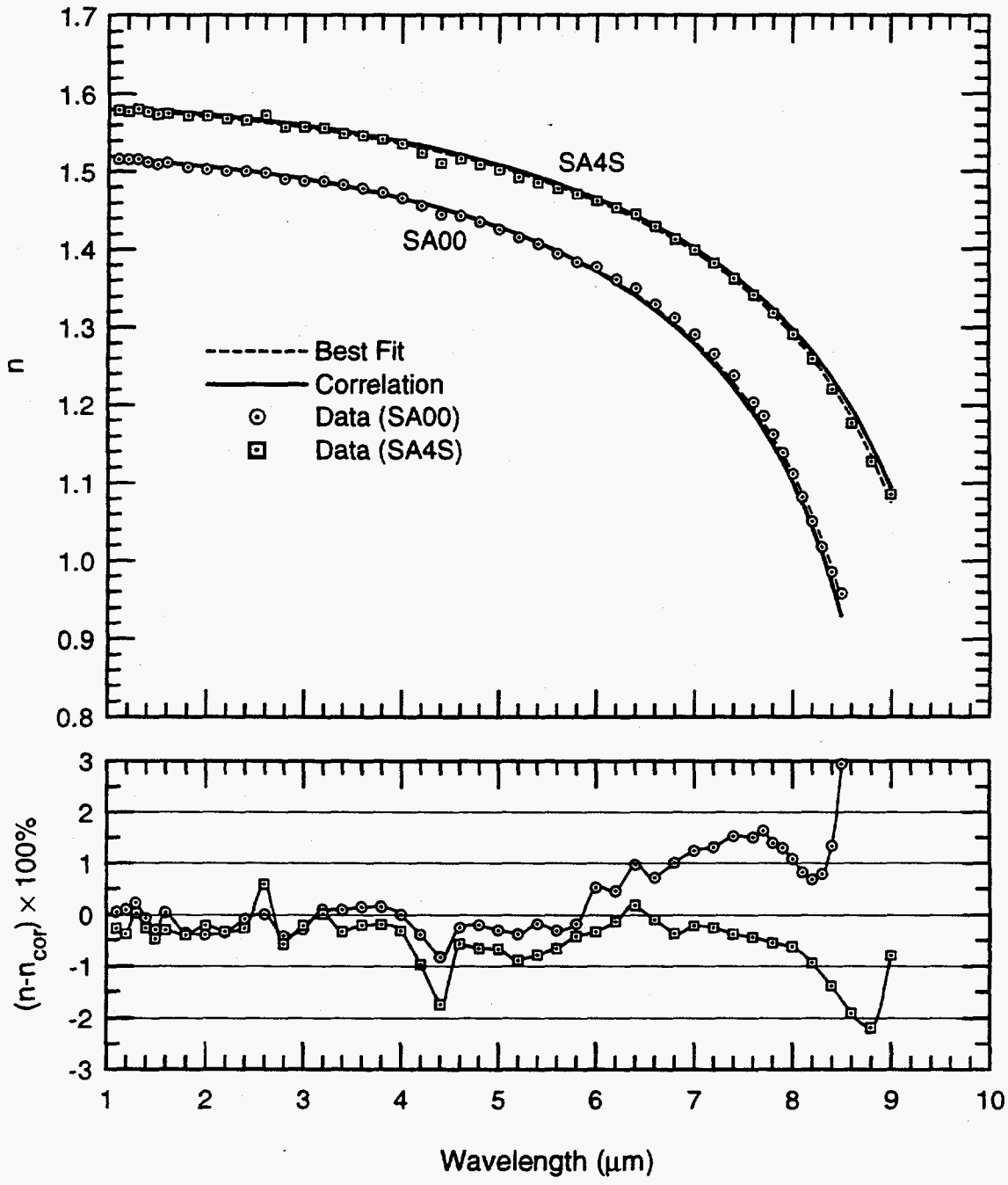

Figure IV.21: Comparison of measured n with calculation using the mixture rule in the region of normal dispersion.

Table IV.11: Evaluation of the mixture rule correlation for n.

Slag	$\delta\rho$ (g/cm^3)	$\delta\lambda_o$ (μm)	Range (μm)	RMS diff.	Max. diff. (at λ)
Best two parameter fit					
SA00	0.030	0.926	1–8.5	0.0047	0.0094 (7.4)
SA01	0.060	0.957	1–8.5	0.0057	0.0107 (7.0)
SA05	-0.016	0.926	1–8.5	0.0047	0.0094 (7.0)
SA10	0.029	0.963	1–8.4	0.0052	-0.0113 (4.4)
SA20	-0.142	1.028	1–8.6	0.0032	0.0107 (8.6)
SA4S	-0.046	1.498	1–9.0	0.0042	-0.0143 (4.4)
SA2S	-0.164	1.884	1–9.2	0.0041	-0.0101 (4.4)
SA1S	-0.087	2.650	1–9.8	0.0038	0.0103 (6.4)
NAEB	0.006	2.050	1–9.4	0.0047	0.0133 (6.4)
One parameter correlation: $\delta\lambda_o = 2.82 - 2.90\hat{x}_{SiO_2}$, $\delta\rho = 0$					
SA00	0.0	0.855	1–8.5	0.0109	0.0285 (8.5)
SA01	0.0	0.876	1–8.5	0.0147	0.0281 (8.5)
SA05	0.0	0.973	1–8.5	0.0066	-0.0192 (8.3)
SA10	0.0	0.976	1–8.4	0.0053	0.0125 (1.2)
SA20	0.0	1.103	1–8.6	0.0317	-0.0425 (2.8)
SA4S	0.0	1.584	1–9.0	0.0128	-0.0254 (4.4)
SA2S	0.0	2.145	1–9.2	0.0390	-0.0490 (2.8)
SA1S	0.0	2.489	1–9.8	0.0180	-0.0296 (4.4)
NAEB	0.0	1.912	1–9.4	0.0079	0.0305 (9.4)
Two parameter correlation: $\delta\lambda_o = 2.82 - 2.90\hat{x}_{SiO_2}$, $\delta\rho = 0.741 - 0.278\rho$					
SA00	0.035	0.855	1–8.5	0.0086	0.0295 (8.5)
SA01	0.029	0.876	1–8.5	0.0114	0.0288 (8.5)
SA05	0.015	0.973	1–8.5	0.0081	-0.0196 (8.3)
SA10	-0.004	0.976	1–8.4	0.0057	0.0135 (1.2)
SA20	-0.062	1.103	1–8.6	0.0194	-0.0267 (2.8)
SA4S	-0.035	1.584	1–9.0	0.0072	-0.0219 (8.8)
SA2S	-0.112	2.145	1–9.2	0.0159	-0.0253 (9.0)
SA1S	-0.087	2.489	1–9.8	0.0041	0.0110 (9.8)
NAEB	-0.101	1.912	1–9.4	0.0241	0.0358 (6.4)

IV.5.4 The SiO_2 Absorption Region (8-13μm).

The absorption band in the wavelength range $8 < \lambda < 13$ μm is predominantly due to vibrational absorption by Si–O–Si and Si-O^- molecular structures in the glassy slag (a description of the structure of silica glass is presented in Appendix F). In this wavelength range ($8 < \lambda < 13$ μm) the optical constants can be reasonably modeled as a Lorentz harmonic oscillator (or multiple oscillators). The resulting oscillator fit parameters are functions of slag composition.

A computer code was written to calculate the best fit parameters, ω_o, γ, n_∞^2, and ω_p in the single oscillator form of Eq.(II.30),

$$\epsilon = (n + ik)^2 = n_\infty^2 + \frac{\omega_p^2}{\omega_o^2 - \omega^2 - i\gamma\omega}. \qquad (IV.20)$$

The parameters were computed to produce the least square error between the measured reflectance and the reflectance calculated using n and k from Eq. (IV.20). Calculations were performed for all nine slags and the resulting best fit parameters are shown in Fig. IV.22, along with correlations for these parameters.

As mentioned above, the absorption in this region is predominantly due vibrational absorption by Si–O–Si and Si-O^- bonds. In general there is a distribution of bond strengths and bond angles that results in a rather broad range of absorption frequencies. The breadth of this absorption frequency distribution depends on temperature and SiO_2 content. Low temperature, high SiO_2 glasses and slags have multiple narrow ranges of absorption frequencies with the most predominant range being centered about the Si–O–Si bond frequency and a somewhat weaker range centered about the lower frequency of the Si–O^- bond. In contrast, the molten slags and slags with a large content of network-breaking oxides (e.g., CaO, Na_2O, Fe_2O_3) have a higher proportion of the lower frequency Si–O^- bonds but, overall, exhibit a broader distribution of absorption frequencies. Therefore the population of the higher frequency Si–O–Si bonds should be a function of the number of Si atoms relative to other non-network forming atoms. We do not have enough data to correlate the distribution of absorption frequencies to each network breaking oxide; so, instead, we correlate ω_o to the mole fraction of SiO_2, which is a measure of the *relative* number of Si atoms. By contrast, the strength of the absorption in the slag (ω_p/ω_o) is a function of the concentration or density of absorbing bonds, and not just the relative population of one type of bond to another. Therefore, it is reasonable to use the

molar concentration, [Si], to account for increases in absorption that may be due to changes in bond concentration.

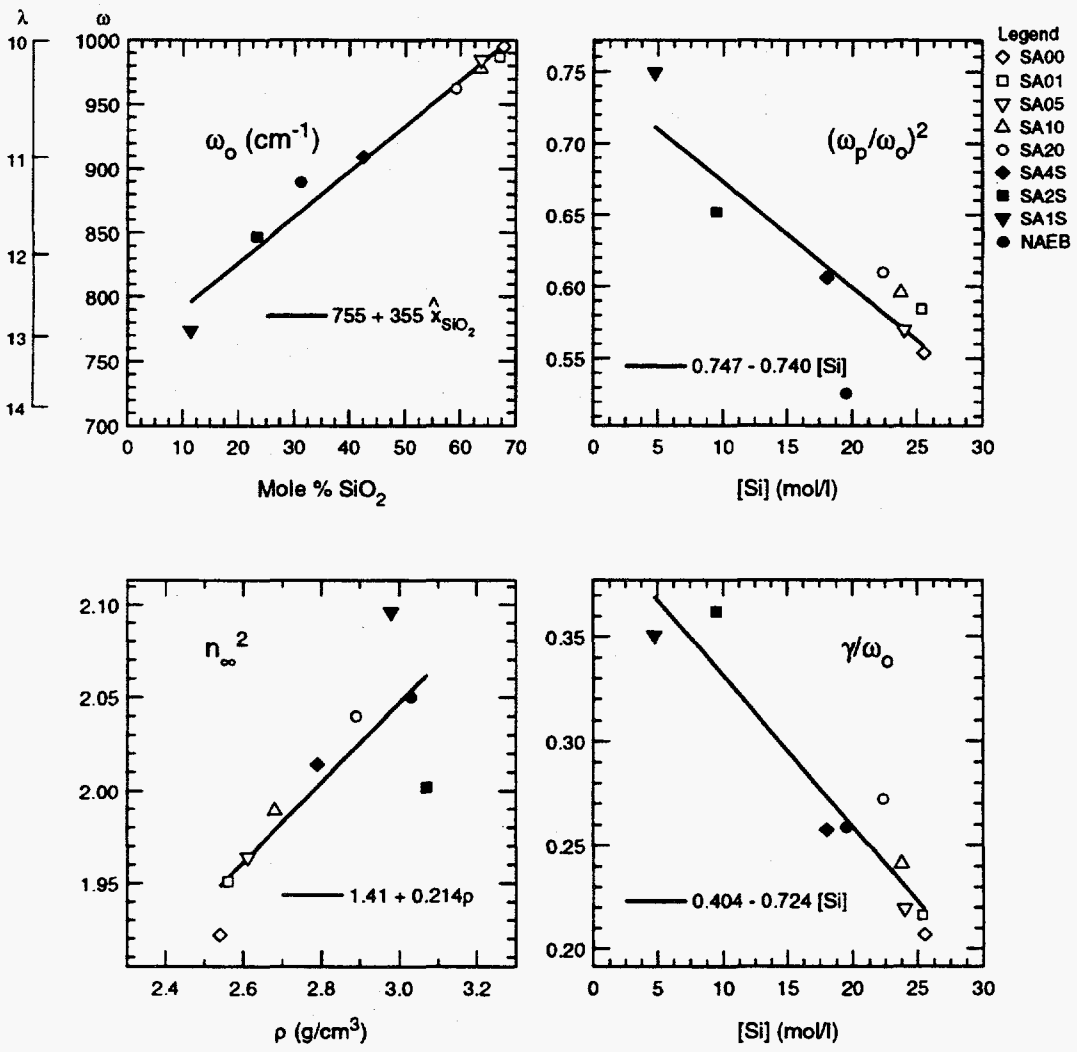

Figure IV.22: Single Lorentz oscillator fit parameters for the nine molten slags.

As expected, the oscillator frequency, ω_o is a strong function of the mole fraction, $0 < \hat{x}_{SiO_2} < 1$, of silica. The frequency shifts from approximately 850 cm^{-1} (11.7 μm) for 20 mol.% SiO_2 to approximately 1000 cm^{-1} (10 μm) for 70 mol.% SiO_2. From fits for the nine slags the expression

$$\omega_o \simeq 755 + 355\hat{x}_{SiO_2} \qquad (IV.21)$$

is found to predict the oscillator frequency quite accurately. Note that extrapolating this expression to $\hat{x}_{SiO_2} = 1$ gives $\omega_{o,SiO_2} \simeq 1110$ cm^{-1}, which is approximately the same as the highest vibrational frequency (1100 cm^{-1}) of pure fused silica at room temperature [34]. The linear correlation coefficient for Eq. (IV.21) is approximately $R \simeq 0.99$.

In addition to shifting to longer wavelengths, the SiO_2 absorption band becomes broader and weaker as SiO_2 is replaced by other constituents (all of which have no fundamental absorption band in the wavelength range of interest). These effects are quantified by the correlations

$$\frac{\gamma}{\omega_o} \simeq 0.404 - 0.724\,[\mathrm{Si}] \qquad (IV.22)$$

and

$$\left(\frac{\omega_p}{\omega_o}\right)^2 \simeq 0.747 - 0.740\,[\mathrm{Si}] \qquad (IV.23)$$

Here [Si] is the molar concentration of Si atoms in the slag in units of mol/l and may be computed using

$$[\mathrm{Si}] = \frac{\rho x_{SiO_2}}{\hat{M}_{SiO_2}} \qquad (IV.24)$$

where ρ is the slag density, x_{SiO_2} is the mass fraction of SiO_2, and $\hat{M}_{SiO_2}$ is the molecular weight of SiO_2 (60 g/mol). For example, if the weight percent of SiO_2 is 63% and the density is 2.6g/cm^3, then the molar concentration [Si] is $(2.6)(1000)(63/100)/60 \simeq 27.3$ mol/l.

The correlations Eq. (IV.22) and Eq. (IV.23) have linear correlation coefficients of -0.95 and -0.85, respectively. These correlations are not as good as that of Eq. (IV.21), but nevertheless predict the proper trend quite well.

Finally, the high frequency contribution to the oscillator fit, n_∞^2, is reasonably fitted by the correlation

$$n_\infty^2 \simeq 1.41 + 0.21\rho \qquad (IV.25)$$

where ρ is the slag density in g/cm^3. The linear correlation coefficient for Eq. (IV.25) is only 0.82, but the variation of n_∞^2 with composition is not particularly large.

Correlations for each parameter ω_o, ω_p/ω_o, γ/ω_o, and n_∞^2, in the oscillator fit were computed using mole fraction of SiO_2, weight fraction of SiO_2, molar concentration [Si], and density as independent variables. Of the these four possible correlations for each parameter, the correlations above were the best (largest R^2), although the

differences between correlations with mole fraction SiO_2 and [Si] were very small, as expected.

Comparisons of the n and k values predicted by these correlations with the measured values for the SA00 and SA4S molten slags are shown in Fig. IV.23 and Fig. IV.24, respectively. This degree of agreement is typical, with the difference between the calculated and measured n and k being within 0.05 except near the short wavelength limit.

In addition to this single oscillator correlation, two, three, and four oscillator fits were also computed. The resulting differences between the correlated and measured optical constants were reduced somewhat, but the large number of fitting parameters seems unreasonable since there are only nine data sets (for the nine slags). Also, the single oscillator fits produce acceptable accuracy compared to the likely errors involved in estimating the composition and density distributions of real fly ashes.

IV.5.5 The Absorption Index in the 4-8μm Region.

In the wavelength range $4 < \lambda < 8$ μm the absorption index, k, of the molten slags could not be directly measured using the thin film transmittance technique described in Chapter III. However, Goodwin [11] measured k for low iron slags (e.g., SA00) in this wavelength range at several temperatures up to a maximum of approximately 1200 K and found that a two–phonon model reasonably predicted the temperature dependence of k. Using Goodwin's data a model is developed that allows one to estimate the absorption index in the 4-8 μm range for the molten slags studied here.

As mentioned, a two–phonon model was shown to reasonably fit the absorption index, k, in the wavelength range from 4-8 μm, where the fit is of the form

$$k = k_o + k_b \left[1 + \frac{2}{\exp\left(\frac{C_2}{2\lambda T}\right) - 1} \right] . \qquad (IV.26)$$

Here k_o is the contribution to the absorption that is not due to the two–phonon process and k_b is the contribution attributable to two–phonon absorption. The constant $C_2 \simeq 14388 \mu$mK is the second radiation constant. As illustrated in Fig. IV.25, the absorption index increases with both increasing wavelength and temperature in

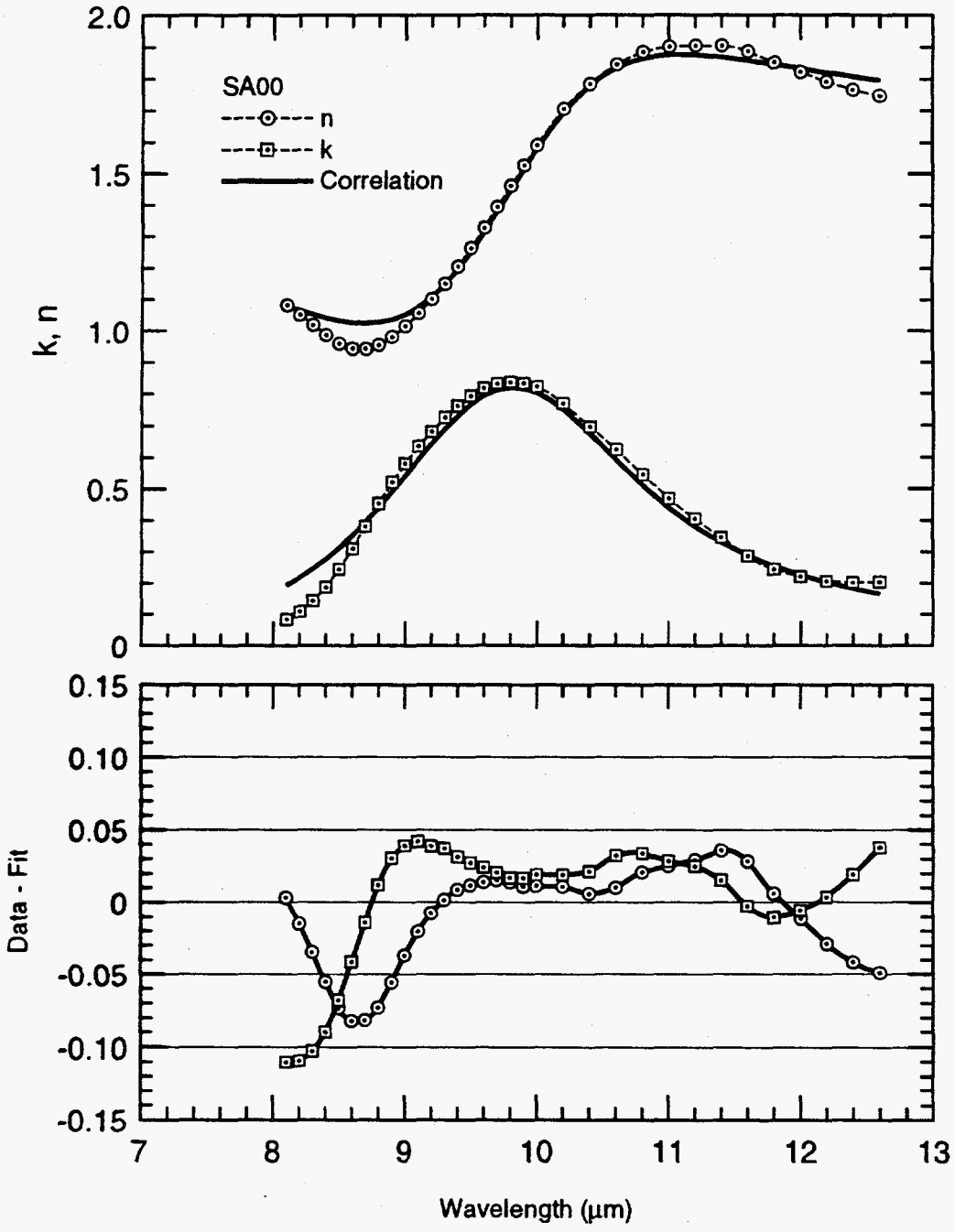

Figure IV.23: Comparison of correlation with measured n and k for molten slag SA00.

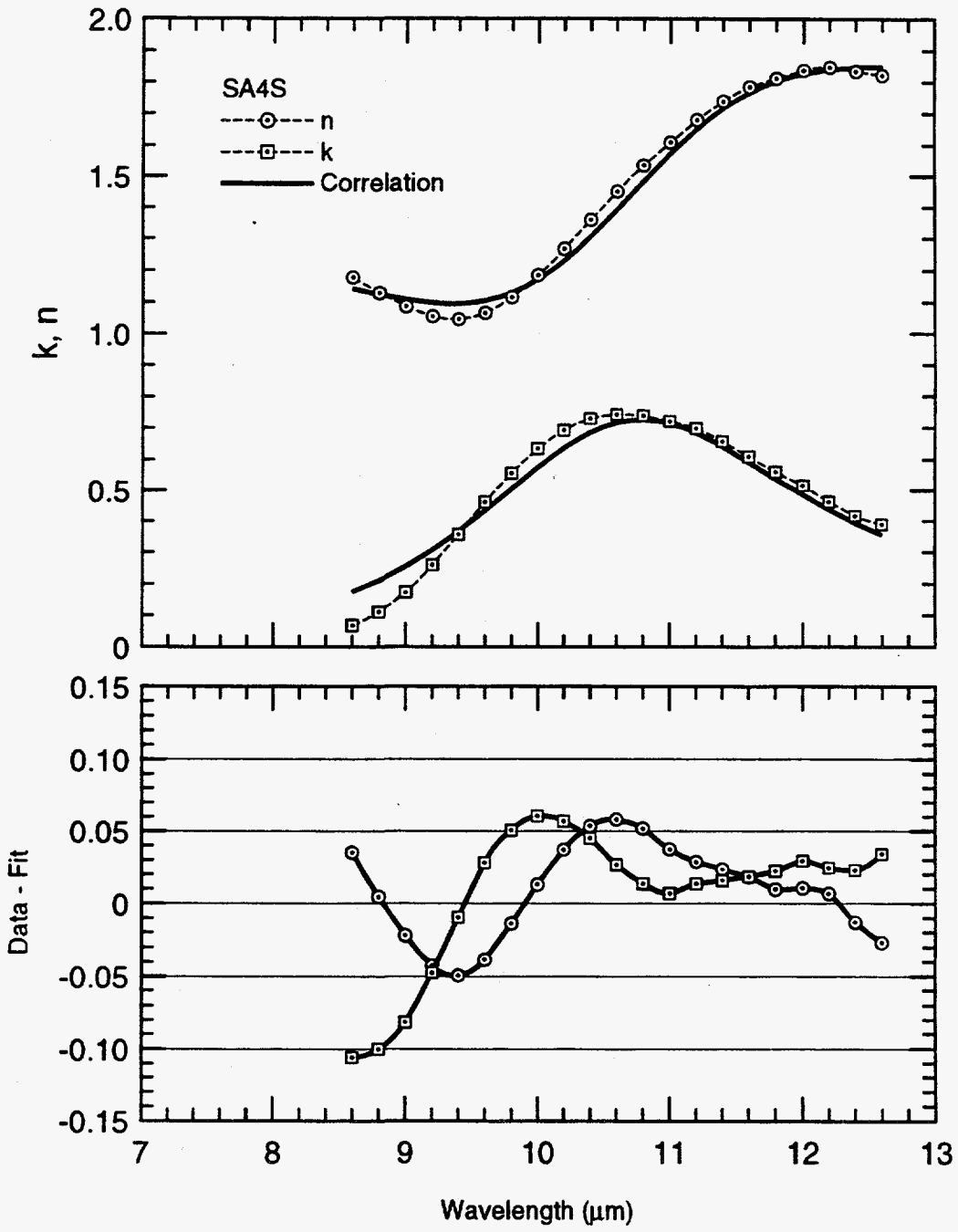

Figure IV.24: Comparison of correlation with measured n and k for molten slag SA4S.

this wavelength range, just as the two–phonon expression predicts. Goodwin used measurements of k at various temperatures to deduce k_o and k_b at each wavelength.

Instead of computing k_o and k_b directly from the measured k at two temperatures, it is useful to note that in this region k varies from transparent ($k < 10^{-4}$) to highly absorbing ($k > 10^{-1}$). Also, in this region between the fundamental vibrational frequency (here ~ 1100 cm^{-1}) and the transparent frequencies (here ~ 2500 cm^{-1}) the absorption coefficients ($\alpha = 4\pi k\omega$) of many insulating solids have been found to vary exponentially with frequency. That is, the absorption index, k, is of the form [33]

$$k \sim \frac{A}{\omega} e^{-\gamma\omega} \qquad (IV.27)$$

This form is almost universally observed in most non-metallic solids, including oxides, alkali halides, alkaline earth fluorides, and semiconductors. For a discussion of the basis for this relation, see Mitra [33].

The absorption index in Fig. IV.25 has the form of Eq. (IV.27) at the short wavelengths, but to model the knee near 5.5 μm a second exponential region is suggested. Specifically, we assume

$$k_b = \begin{cases} \frac{A_o}{\omega} e^{-w/B_0} & , \quad \omega < \omega^* \\ \frac{A_1}{\omega} e^{-w/B_1} & , \quad \omega > \omega^* \end{cases} \qquad (IV.28)$$

where ω^* is the frequency at which the two exponentials cross,

$$\omega^* = \frac{\ln(A_1/A_0)}{\left(\frac{1}{B_1} - \frac{1}{B_0}\right)}. \qquad (IV.29)$$

The values of k_o and k_b were determined by using Eq. (IV.26) and Goodwin's measured values of k at 295 K and 1200 K (Fig. IV.25) for slag SA00. Next the two-exponential model (Eq. (IV.28)) was fitted to k_b. The resulting fit is illustrated in Fig. IV.26 along with the remaining contribution k_o not attributable to two–phonon absorption. The constants in Eq. (IV.28) are summarized in Table IV.12. Finally, the expression

$$k_o \simeq A_{k_o} \exp\left[-\left(\frac{\omega - B_{k_o}}{C_{k_o}}\right)^2\right] \qquad (IV.30)$$

can be used to estimate the contribution k_o, where the constants are given in Table IV.12. This form was chosen arbitrarily but since the contribution by k_o is not large the resulting error in k is not important.

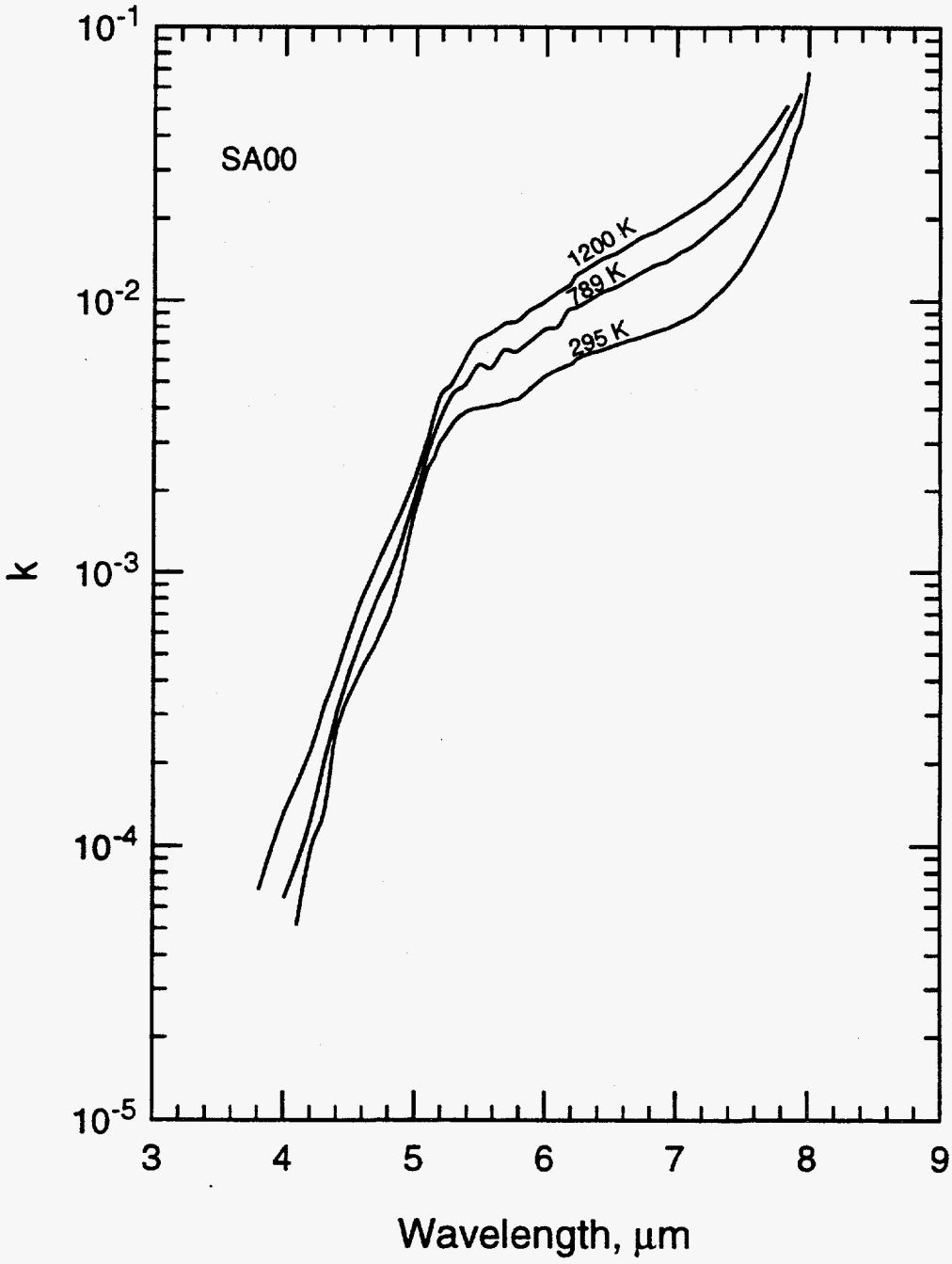

Figure IV.25: Effect of temperature on the absorption index in the 4-8 μm range for synthetic slag SA00. Data from Goodwin, 1986.

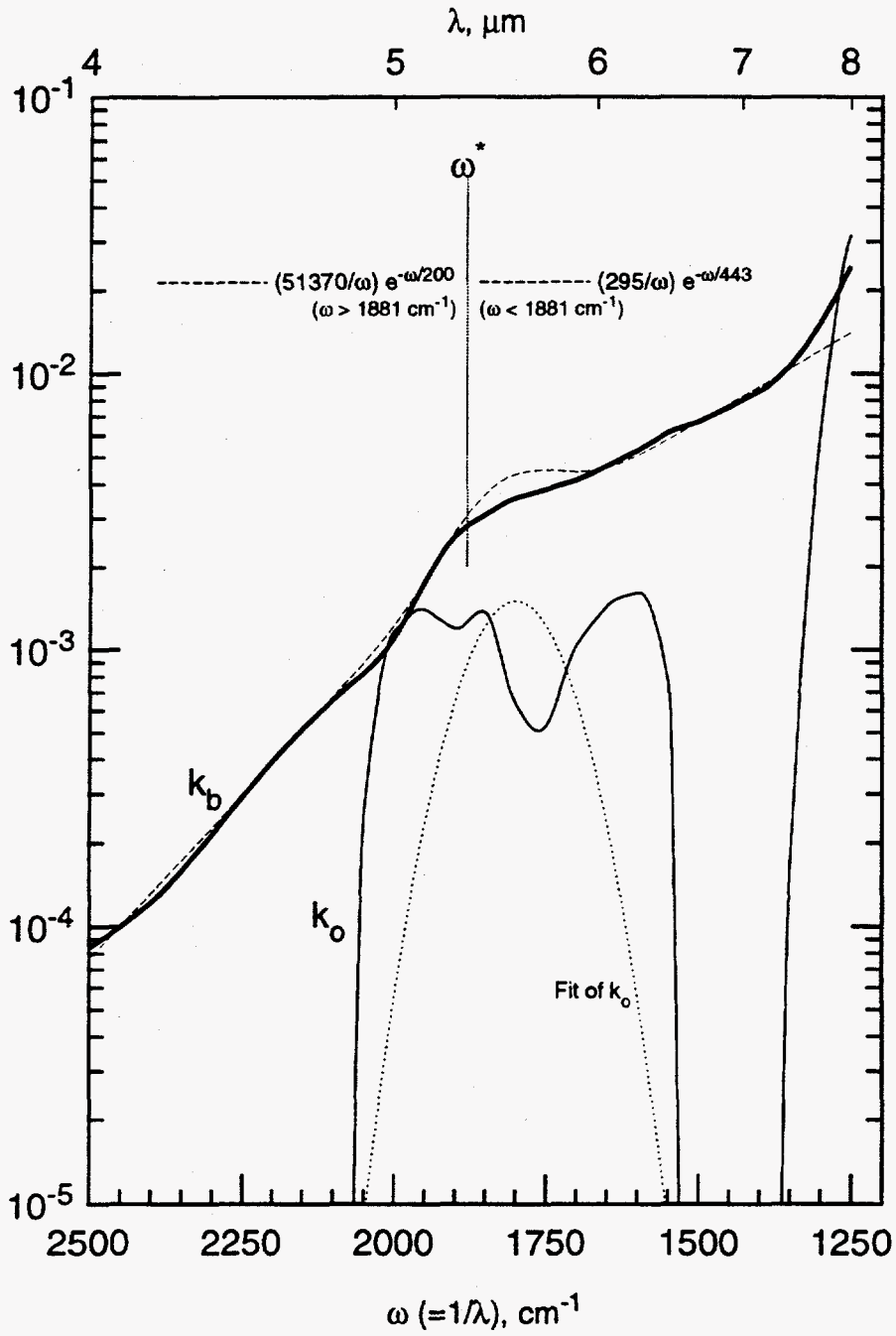

Figure IV.26: Fit of the two-exponential model (dashed line) to the function k_b (thick line) determined from measurements of k for slag SA00 at 295 K and 1200 K (Goodwin, 1986). Also shown is the function k_o (thin line) determined from the same data and its model (dots).

Table IV.12: Fit parameters for k in the 4-8 μm range for slag SA00.

Parameter	Value	Parameter	Value
A_0	295 cm^{-1}	A_{k_o}	0.0015
B_0	443 cm^{-1}	B_{k_o}	1800 cm^{-1}
A_1	51370 cm^{-1}	C_{k_o}	110 cm^{-1}
B_1	200 cm^{-1}		

An approximate expression for k is obtained by combining Eq. (IV.26) with Eq. (IV.28) and Eq. (IV.30). The resulting approximation is illustrated in Fig. IV.27 for temperatures up to 1873 K, along with the measured k from Fig. IV.25. As expected, the agreement is reasonably good, with the largest error occurring at the long end of the 4-8 μm range – near the short wavelength edge of the fundamental absorption band. In this region the absorption is becoming dominated by single phonon processes and is not expected to match the correlation.

The two–phonon absorption model used here assumes that the contribution at frequency ω is due to a combination of two single absorption events at half the frequency $\omega/2$ (or twice the wavelength). The above expressions were derived assuming that the spectral distribution of fundamental absorption frequencies is that of SA00. If the distribution of fundamental absorption frequencies is shifted to lower frequencies (i.e., longer wavelengths) because the composition contains less SiO_2 than the SA00 slag, then one should expect a corresponding shift in the frequency distribution of the two–phonon processes. To account for this shift, recall that the oscillator model predicted that the fundamental frequency, ω_o, depends on the mole fraction of SiO_2, $\hat{x}_{SiO_2}$ *via* Eq. (IV.21), i.e.,

$$\omega_o \simeq 755 + 355\hat{x}_{SiO_2}.$$

To account for this frequency shift the frequency, ω, in all of the above expressions should be shifted to account for compositional effects. That is, one replaces ω in the above expressions by $\omega' = \omega + \delta\omega$ where

$$\delta\omega \simeq 355\,(0.678 - \hat{x}_{SiO_2})\,. \qquad (IV.31)$$

Here 0.678 is approximately the mole fraction of SiO_2 in SA00. Figure IV.30 in the following section illustrates the effect of this shift. As shown, the agreement in the 4-5 μm range with measured k for SA00, SA05, and SA4S is quite good.

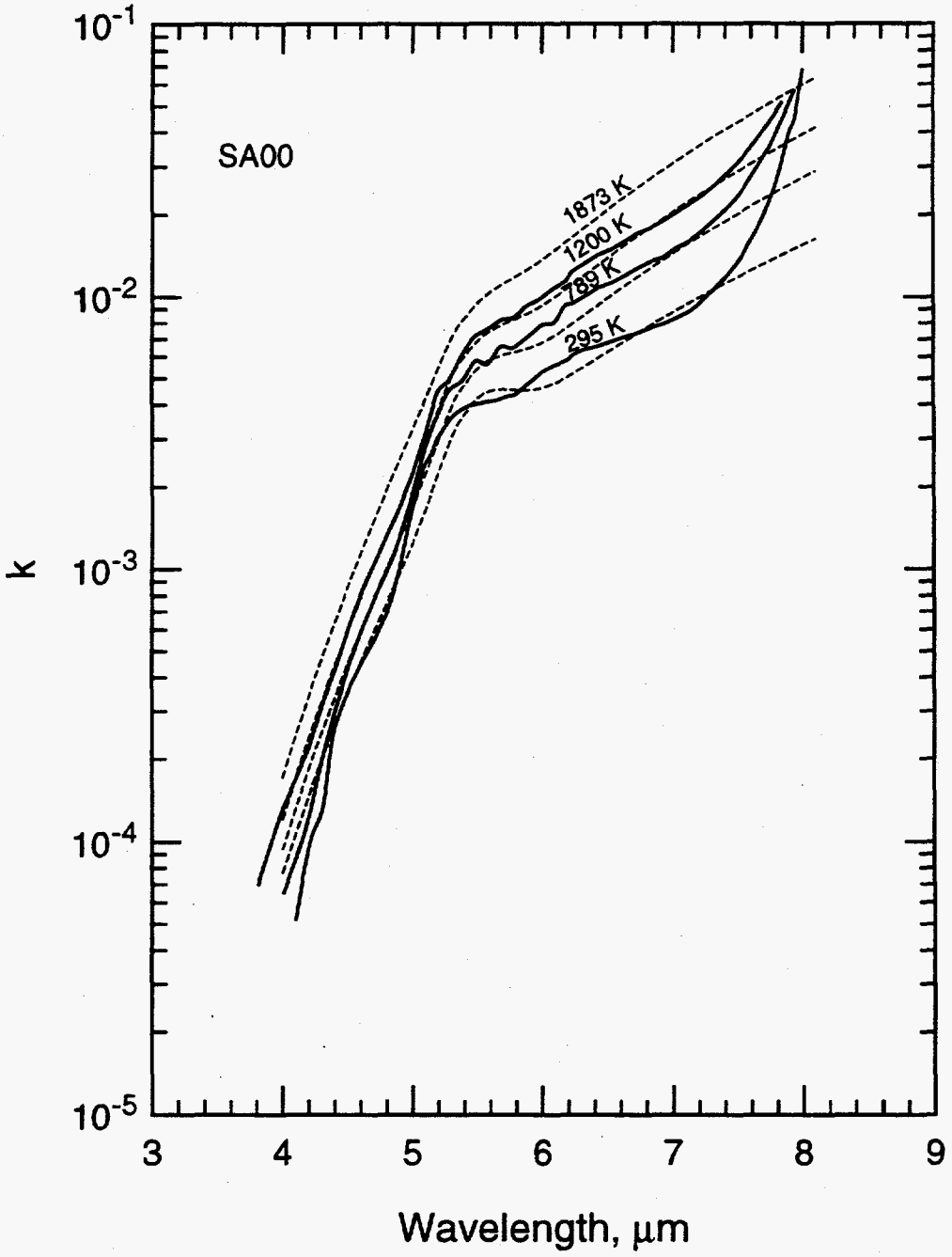

Figure IV.27: Fit (dashed) of correlation for k to measured absorption index (solid) in the 4-8 μm range for Goodwin's (1986) slag SA00.

IV.5.6 The Absorption Index in the 1-4μm Region.

In the short wavelength limit of the measurements, between 1 and 4 μm, absorption in the slags is due primarily to the presence of Fe_2O_3. The level of absorption depends on the total iron concentration as well as the valence state of the iron. For example, slags produced in a reducing atmosphere have an abundance of ferrous iron cations, Fe^{2+}, while those produced in an oxidizing atmosphere (as were the slags in this study) have a lower ferrous iron content. Fully reduced samples show increased absorption bands near 1.1 and 1.9 μm owing to transitions involving the split d energy levels of the Fe^{2+} cation. In samples with significant levels of ferric iron, Fe^{3+}, absorption throughout the visible spectrum is attributable to transitions involving charge transfer between the Fe^{2+} and Fe^{3+} cations, i.e., intervalence charge transfer. This is what makes iron-bearing glasses and the naturally occuring mineral obsidian black. Goodwin [11] studied the effect of the valence state of iron in coal slags in some detail and developed correlations that allow one to estimate the absorption index from the valence state and iron content. However, because of the lack of valence state information for the slags studied here it is difficult to improve on Goodwin's correlations. Instead, a simpler correlation is presented that is expected to predict the general trends associated with iron content, that is, higher iron slags have higher absorption indices in the visible and near infrared (1-4 μm).

If one assumes k is constant over the wavelength range from 1-4 μm and that the constant value is the average of the measured k over this range, then a plot of $\bar{k}$ versus mass fraction of Fe_2O_3 shows that the average k increases with Fe_2O_3 mass fraction. The results for several slags is presented in Fig. IV.28, where all data points except those labeled 1600°C are from Goodwin's work. A simple quadratic fit through these points (intersecting 0,0) shows that to reasonable accuracy

$$\bar{k} \simeq (4.02x + 16.9x^2) \times 10^{-3}. \qquad (IV.32)$$

As expected, this correlation underpredicts $\bar{k}$ for slags that are fully reduced ($Fe^{2+}/Fe = 1$) and tends to overpredict $\bar{k}$ for slags produced in an oxidizing atmosphere. However, given the likely uncertainty in knowing the valence state and Fe_2O_3 composition distributions for real fly ashes, the error (rms $\simeq 0.06 \times 10^{-3}$, max $\simeq 0.16 \times 10^{-3}$ for SE10) is probably acceptable.

As discussed above, if more detailed knowledge of the valence state and Fe concentration is known for a dispersion of fly ash, then the more accurate correlations developed by Goodwin [11] may be used.

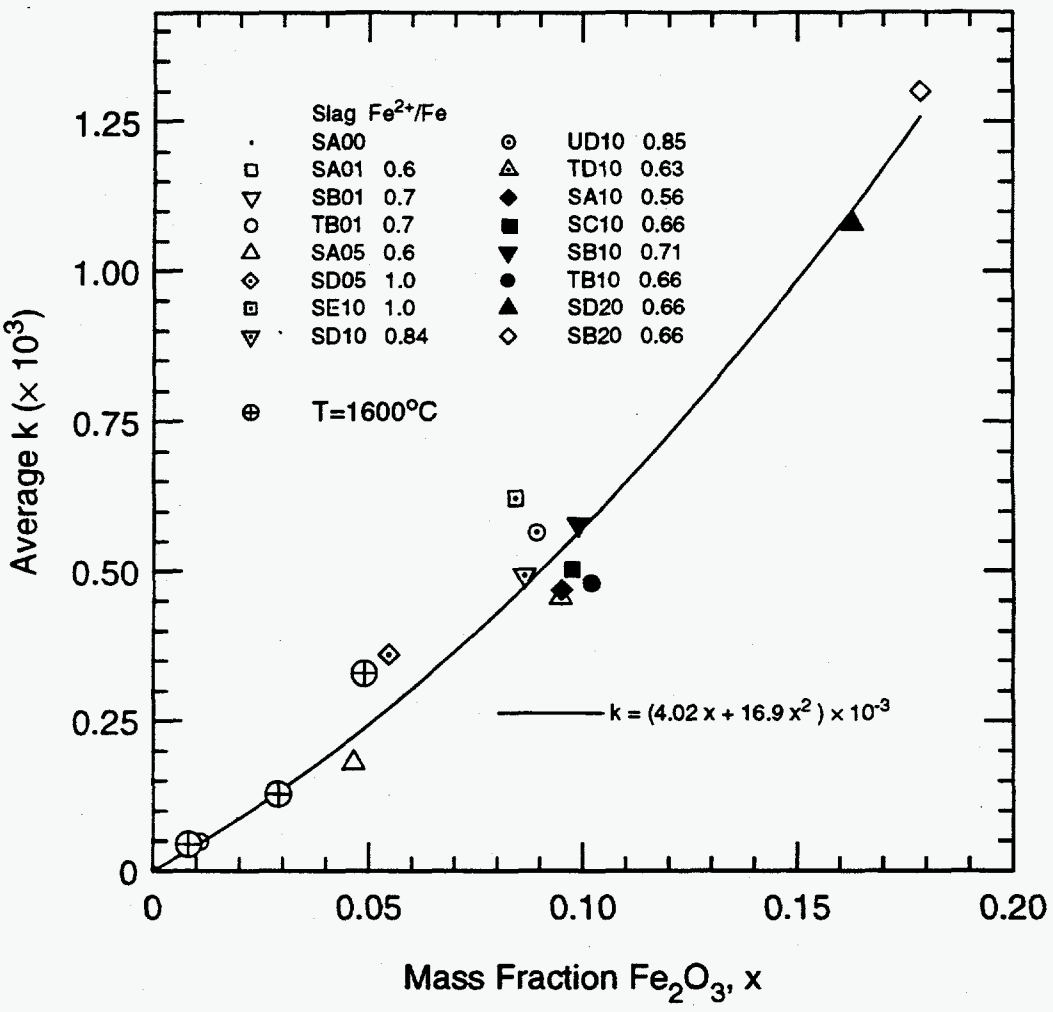

Figure IV.28: Correlation for the average absorption index in the 1-4 μm region owing to Fe_2O_3 content.

IV.5.7 A Combined Model for the Complex Refractive Index

In this section the separate correlations for n and k are combined to produce an algorithm that can be applied to a broad range of ash particle compositions. The resulting model provides an estimate of n and k over the entire wavelength range from 1 μm to 13 μm. A summary of the entire algorithm is presented below along with some estimate of the bounds on the slag compositions that are expected to produce acceptable results.

Density Calculation

Throughout these calculations the density of the slag comprising individual particles is required. However, since this may not be available, the procedures described in section IV.5.1 may be used to estimate ρ from the composition of the particles, which is more readily measured. Equation IV.2 with the oxide densities in Table IV.5 may be used. The effective density for oxides in glass give somewhat better results than those of the free oxides.

Real Refractive Index, n

The combined model for the calculation of n requires only two correlations. At the shorter wavelengths (the region of normal dispersion) the mixture rule developed in section IV.5.3 is used. For this calculation the inputs to the correlation are the weight fractions of the oxides SiO_2, Al_2O_3, CaO, Fe_2O_3, TiO_2, and MgO; the mole fraction of SiO_2, and the density of the slag. The contribution of each oxide in Eq. (IV.15) is computed using ρ_i from Table IV.10, the weight fraction of the oxide, $X_{m,i}$, and the factor $(n_i^2-1)/(n_i^2+2)$ where n_i is computed using Eq. (IV.16) and the constants λ_o, C, and B from Table IV.10. Only the weight fractions of the six oxides in Table IV.10 are included. The sum of these weight fractions in Eq. (IV.15) are not normalized to unity, but for most slags probably account for a large fraction of the total weight. If there are significant contributions by other constituents, then their constants λ_o, C, and B should be used (where possible). Fortunately most coal ash particles are primarily composed of the six oxides listed above.

At long wavelengths the single oscillator model for n, Eq. (IV.20), is used to compute n, i.e., the real part of $\sqrt{\epsilon}$. The inputs are the mole fraction of SiO_2, the molar concentration of Si, and the density of the slag. The oscillator parameters are computed using Eq. (IV.21), Eq. (IV.22), Eq. (IV.23), and Eq. (IV.25).

At some wavelength longer than approximately 7 μm the mixture rule yields a value of n that is smaller than that found from the oscillator fit. If the wavelength at which $n_{\text{mix}} = n_{\text{osc}}$ is denoted by λ_n, then for $\lambda < \lambda_n$ the mixture rule should be used while for $\lambda > \lambda_n$ the oscillator fit should be used. The resulting curve is reasonably smooth but there is a discontinuity of slope at $\lambda = \lambda_n$.

Absorption Index , k

The correlation for k is somewhat complicated by the fact that three distinct phenomena are responsible for the absorption. At short wavelengths the absorption is due to Fe_2O_3 content, at long wavelengths it is due to vibrational absorption by SiO_2,

while at intermediate wavelengths it is due to combination and overtone mechanisms, i.e., multiphonon processes.

At short wavelengths (1-4 μm) k is modeled as a constant given by Eq. (IV.32). To accommodate the transition to the two–phonon mechanism near 4 μm the absorption coefficient is modeled as

$$k = k_1 + k_2. \qquad (IV.33)$$

Here k_1 is given by

$$k_1 = \begin{cases} \bar{k}\,(x_{Fe_2O_3}) & ; \quad \lambda < 4.5\mu\text{m} \\ \bar{k}\,(x_{Fe_2O_3})\exp(4.5-\lambda) & ; \quad 4.5 \le \lambda < 8.5\mu\text{m} \\ 0 & ; \quad \lambda > 8.5\mu\text{m} \end{cases} \qquad (IV.34)$$

where $\bar{k}(x_{Fe_2O_3})$ is given by Eq. (IV.32). The short wavelength value is exponentially decreased for $\lambda > 4.5\mu$m until it becomes negligible at 8.5 μm compared to k_2.

The second term, k_2, in Eq. (IV.33) is the contribution by either the oscillator model correlation (long wavelengths) or the two–phonon model correlation (intermediate wavelengths). The transition from the two–phonon model to the oscillator model requires some modification of the oscillator model solution for k.

From Fig. IV.23 and Fig. IV.24, one notices that the oscillator model overpredicts k at the short wavelength edge of the absorption band. Unfortunately this error prevents the intersection of the extrapolated curve for k_{osc} at shorter wavelengths with k from the two–phonon model. To remedy this problem an alternative formulation for k is now introduced that applies to the short wavelength side of the absorption band.

Consider the oscillator model for $\epsilon = \epsilon' + i\epsilon''$ given by Eq. (IV.20). Here $\epsilon' = n^2 - k^2$ and $\epsilon'' = 2nk$ are the real and imaginary parts of ϵ, respectively. The peak value in the imaginary part of ϵ is ϵ''_{max} and occurs at a frequency ω_{max}. This peak and the associated frequency can be found by iteration. At frequencies less than ω_{max} the ordinary oscillator model is used to compute $k = \epsilon''/2n$. At higher frequencies the absorption index is computed using

$$k = \frac{\epsilon''_{max}}{2n}\frac{\omega_o}{\omega}\exp\left[-2\left(\frac{\omega_o-\omega}{\gamma}\right)^2\right], \quad \omega > \omega_{max}. \qquad (IV.35)$$

Here ω_o and γ have their usual meanings and are given by the oscillator correlations presented in section IV.5.4. The resulting absorption index calculated from

Eq. (IV.35) matches the measured k very well, and also is guaranteed to intersect the two-phonon model. Therefore, the transition from the two-phonon model described in section IV.5.5 to the oscillator model is found by finding the intersection between $k(\lambda)$ given by the two models. At wavelengths shorter than this intersection the two-phonon model is used for k_2, while at longer wavelengths the modified oscillator model is used. The transition from one model to the other has a discontinuous slope but otherwise seems reasonable given the sparseness of measurements of k in the 4-8 μm range.

Putting all of these elements together in a single computer subroutine allows quick calculation of the optical constants of a slag from its composition. Such a calculation is shown in Fig. IV.29 where the computed optical constants are compared to measured results for molten slag SA05. The computed absorption index, k, in the region between 5 and 8 μm provides a credible transition from the short wavelength data to the long wavelength data, although the calculated k may be slightly too high. Given the lack of measured data it is probably unwarranted to attempt further corrections.

In the wavelength range from 4 to 5 μm the model accurately predicts the slope and magnitude of the increase in k. Also, as Fig. IV.30 illustrates, the frequency shift of the SA4S absorption data relative to SA01 or SA05 is predicted by the model. The convergence of the SA01 and SA05 absorption indices near 5 μm is also predicted by the model, since both slags have approximately the same SiO_2 content. In all cases it seems that the correlation slightly overpredicts k in this region. The small discrepancies in the model for k at wavelengths shorter than 4 μm is entirely expected, as discussed in section IV.5.6, since the model for k in this region does not account for the ferrous/ferric ratio.

The comparisons between the overall correlations and the experimental data in Fig. IV.31 and Fig. IV.32 provide further evidence that the correlation is reasonably robust. The model not only predicts the shift of the fundamental SiO_2 absorption band associated with SiO_2 content, as discussed in section IV.5.4, but also provides the expected form of k in the intermediate wavelength range (4-8 μm).

Model Limitations

As expected, there are bounds on the applicability of the correlations for the optical constants given here. Obviously if the composition of interest lies outside the range of compositions used to develop the correlations, it is difficult to gauge the accuracy

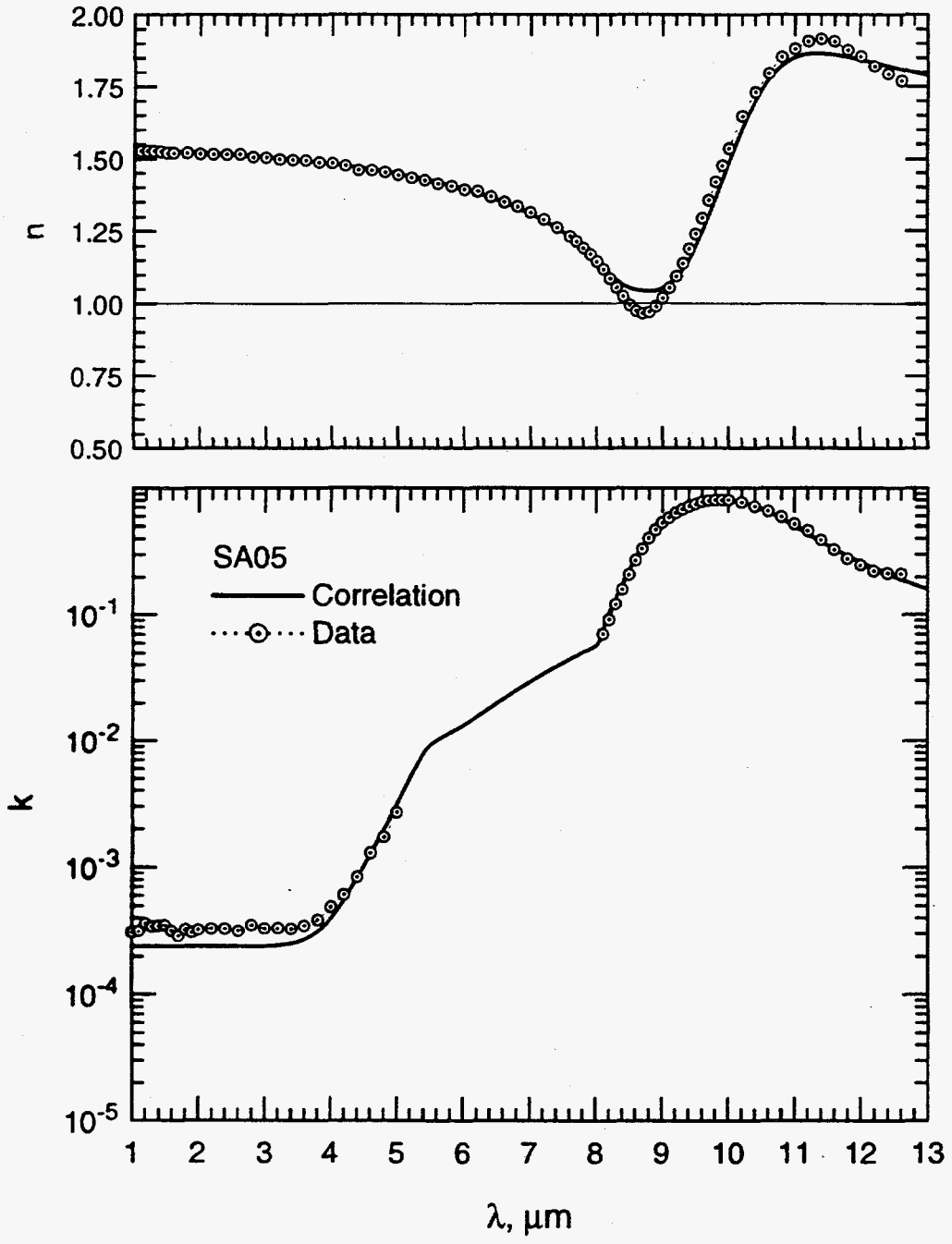

Figure IV.29: Comparison of the overall correlation formulae for the optical constants with measured data for slag SA05 at 1600°C.

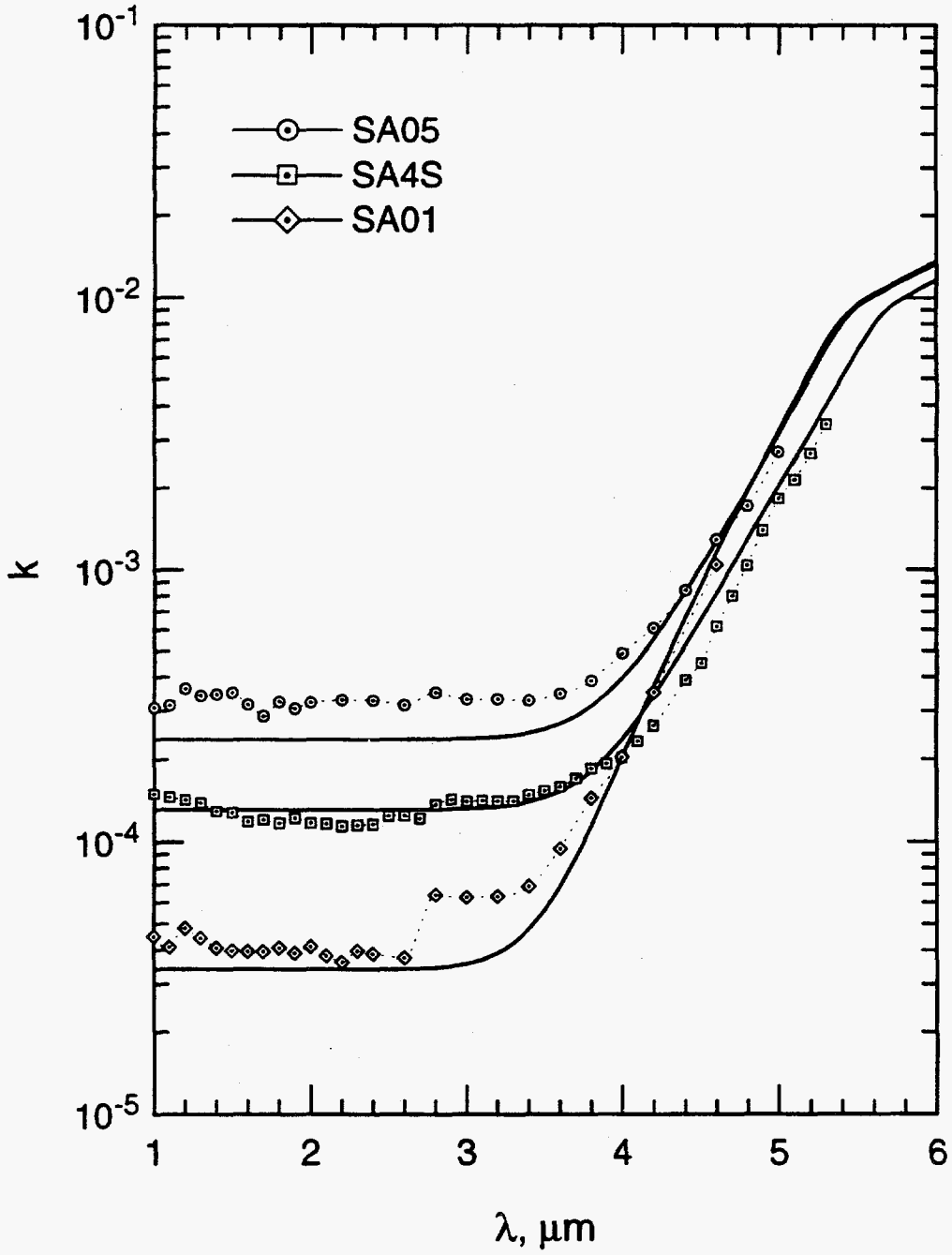

Figure IV.30: Comparison of the absorption indices of molten slags SA01, SA4S, and SA05 with correlations in the 1-5 μm wavelength range.

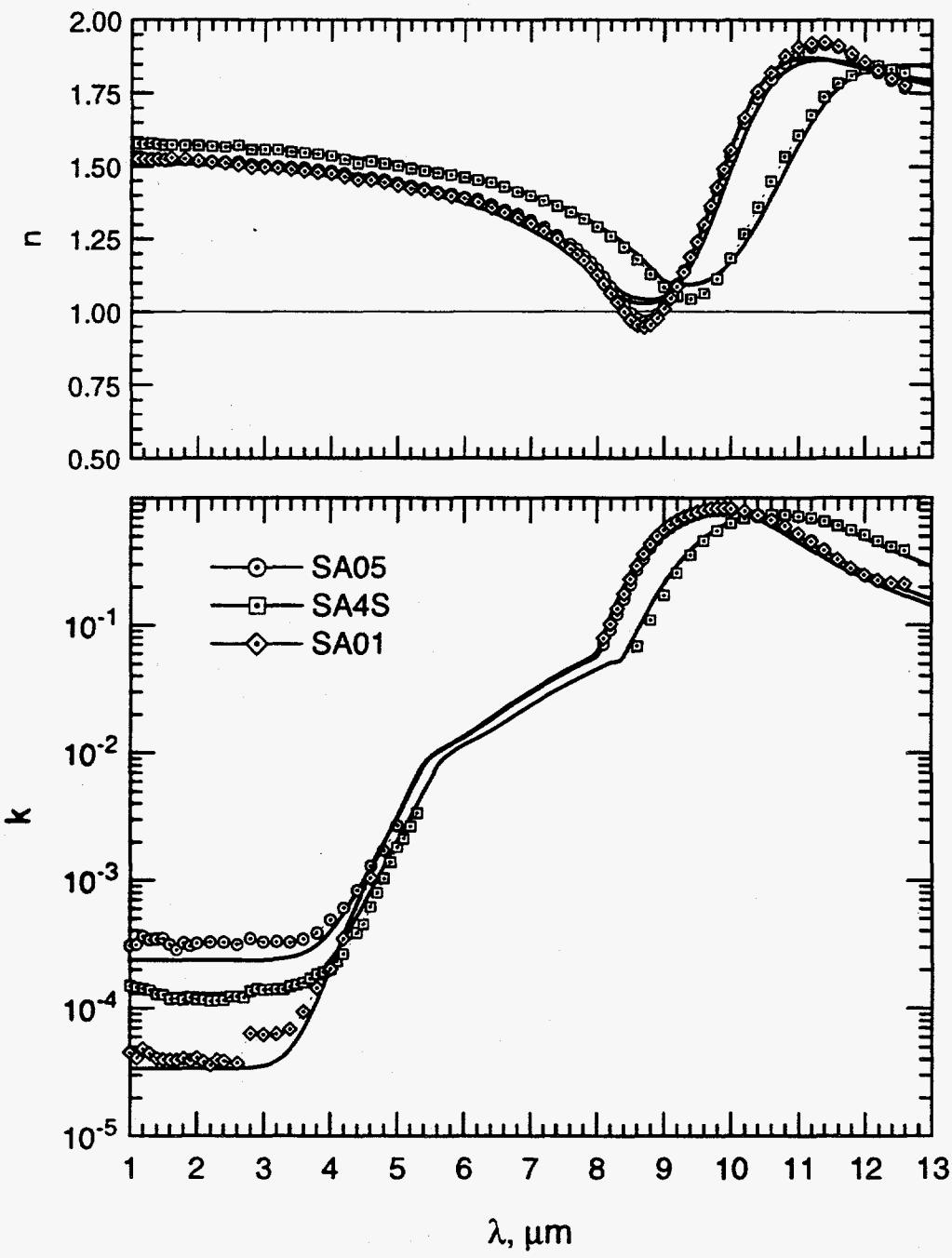

Figure IV.31: Comparison of the optical constants correlation with data for molten slags SA01, SA4S, and SA05 at 1600°C.

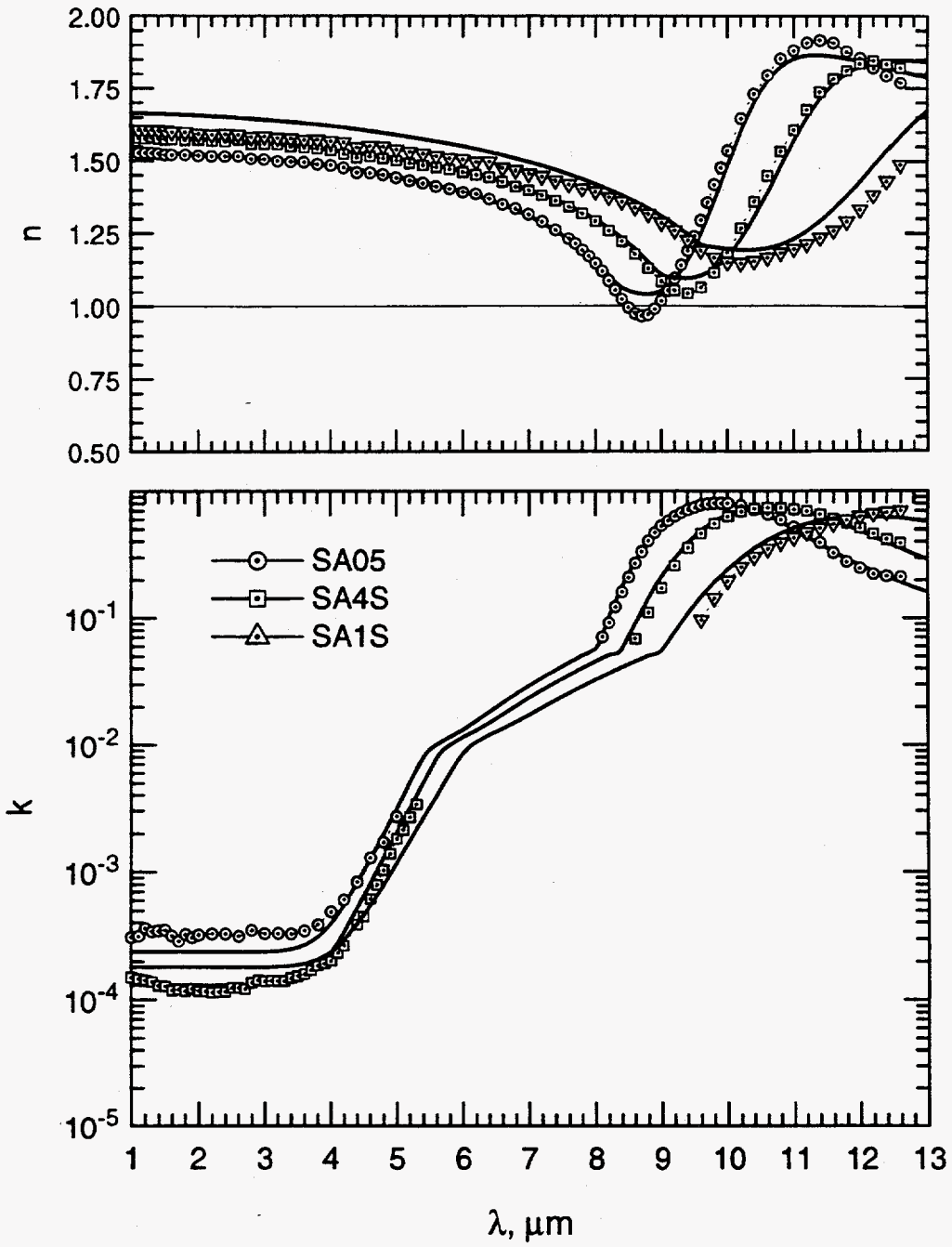

Figure IV.32: Comparison of the optical constants correlation with data for molten slags SA05, SA4S, and SA1S at 1600°C.

of the results. In the following chapter the correlation is used to calculate the optical constants of thousands of fly ash particles whose compositions were measured using computer controlled scanning electron microscopy. Some particle compositions do not resemble alumino-silicates, but, for instance, are very high in other elements, e.g., TiO_2 (rutile) and sulfur (iron pyrite). The model cannot be expected to correctly estimate the optical constants of such particles, which, however, occur infrequently in the ashes studied here.

Without further experience and experimental data it is not possible to establish a strict range of applicability. However, an estimate of the properties of acceptable compositions is useful. Therefore, for subsequent calculations using the correlations in this chapter it is suggested that the following *minimal* conditions should be met for the composition to be acceptable:

1. SiO_2 weight percentage, $0 < x_{SiO_2} < 95\%$. Pure quartz particles are not included.

2. The sum of the weight percentages of SiO_2, Al_2O_3, CaO, Fe_2O_3, MgO, and TiO_2 must be 80% or higher.

3. The weight percentage of Fe_2O_3 must be less than 30%.

It should be borne in mind that these are minimal criterion – it is not well established how accurate the results will be when the composition is far from those studied here. Nevertheless, it is fortunate that for most ashes studied by Ghosal [17] the bulk of the particles meet these criteria, and a significant fraction have compositions somewhere between those of SA00 and SA4S. This issue is discussed further in Chapter V.

Chapter V.

Radiative Properties of Fly Ash

In this chapter the correlations developed in Chapter IV for the optical constants of hot slags are used to estimate the radiative properties of dispersions of fly ash. In the first section the radiative properties of ash dispersions are defined. In the second section the characteristics of some fly ashes from representative U.S. coals are presented. In the third section the composition distributions for several of these ashes are used to compute their optical constants using the correlations developed in Chapter IV. In the fourth section the results of Mie scattering calculations are presented, based on the measured size and computed refractive index distributions. Radiative properties of dispersions of several ashes are documented. These results are used in Chapter VI to evaluate the effects of ash on radiative heat transfer through a planar layer of combustion products gases.

V.1 Radiative Properties of Dispersions

The radiative transfer of energy in an absorbing, emitting, and scattering medium is described by the radiative transport equation [35]

$$\nabla \cdot [\hat{\Omega} I_\lambda(\mathbf{r}, \hat{\Omega})] + \beta_\lambda I_\lambda(\mathbf{r}, \hat{\Omega}) = \alpha_\lambda I_{b\lambda}(T) + \frac{\sigma_\lambda}{4\pi} \int_{4\pi} \Phi_\lambda(\hat{\Omega} \cdot \hat{\Omega}') I_\lambda(\mathbf{r}, \hat{\Omega}') d\Omega' \quad (V.1)$$

Here $I_\lambda(\mathbf{r}, \hat{\Omega})$ is the spectral radiance at position $\mathbf{r}$ in direction $\hat{\Omega}$ at wavelength λ and $I_{\lambda b}(T)$ is the Planck blackbody function. The spectral absorption coefficient, α_λ, spectral scattering coefficient, σ_λ, and scattering phase function, $\Phi_\lambda(\hat{\Omega}, \hat{\Omega}')$ are generally functions of position, $\mathbf{r}$, and wavelength, λ. The extinction coefficient, β_λ, is the sum of the scattering and absorption coefficients. The spectral radiative heat flux vector is defined in terms of the spectral radiance by

$$\mathbf{q}_\lambda(\mathbf{r}) = \int_{4\pi} \hat{\Omega} I_\lambda(\mathbf{r}, \hat{\Omega}) d\Omega. \quad (V.2)$$

The total heat flux vector is the integral of the spectral heat flux vector over all wavelengths, that is

$$\mathbf{q}(\mathbf{r}) = \int_0^\infty \mathbf{q}_\lambda(\mathbf{r}) d\lambda = \int_0^\infty \int_{4\pi} \hat{\Omega} I_\lambda(\mathbf{r}, \hat{\Omega}) d\Omega d\lambda. \quad (V.3)$$

The radiative transport described by Eq. (V.1) depends on three radiative properties of the medium: 1) the spectral absorption coefficient, α_λ, 2) the spectral scattering coefficient, σ_λ, and 3) the spectral scattering phase function, $\Phi_\lambda(\hat{\Omega} \cdot \hat{\Omega}')$. For coal combustion systems, the first includes contributions from gases as well as particles, while the second and third relate only to macroscopic particles.

Suppose the medium is a dispersion comprising many scattering and absorbing particles with a broad distribution of sizes. For each differential class of particles with diameter D within dD, we can write Eq. (V.1) to describe the contribution of that particle class to the radiative transport. If the fraction (by number) of particles within the size class D is $\phi(D)dD$ then the radiative transport equation for a medium composed of only that class of particles is

$$\nabla \cdot [\hat{\Omega} I_\lambda] + \phi(D)\beta_\lambda(D)dD\, I_\lambda = \phi(D)\alpha_\lambda(D)dD\, I_{b\lambda}(T) + \phi(D)\frac{\sigma_\lambda(D)dD}{4\pi}\int_{4\pi} \Phi_\lambda(\hat{\Omega} \cdot \hat{\Omega}', D) I_\lambda(\hat{\Omega}')d\Omega'. \quad (V.4)$$

Here $\alpha_\lambda(D)$, $\sigma_\lambda(D)$, $\beta_\lambda(D)$, and $\Phi_\lambda(\hat{\Omega} \cdot \hat{\Omega}', D)$ are the radiative properties for the class of particles with diameter D. Integrating Eq. (V.4) over all diameter classes one finds that the average radiative properties are

$$\alpha_\lambda = \int_0^\infty \phi(D)\alpha_\lambda(D)dD \quad (V.5)$$

$$\sigma_\lambda = \int_0^\infty \phi(D)\sigma_\lambda(D)dD \quad (V.6)$$

and

$$\Phi_\lambda(\mu) = \frac{\int_0^\infty \phi(D)\sigma_\lambda(D)\Phi_\lambda(\mu, D)dD}{\int_0^\infty \phi(D)\sigma_\lambda(D)dD} \quad (V.7)$$

Here $\mu = \hat{\Omega} \cdot \hat{\Omega}'$ is the cosine of the angle between the two directions $\hat{\Omega}$ and $\hat{\Omega}'$.

Suppose that in addition to a distribution of particle sizes there is also a distribution of particle compositions. One approach for including this added complexity is to write the particle distribution function as, $\phi = \phi(D, C)$, where C represents the composition of the particles. For this approach one could divide the ash particles into classes of like compositions and use a correlation similar to that developed in Chapter IV to estimate the optical properties for a composition class. With this approach the choice of composition classes is not obvious. An alternative approach is to write the distribution function as $\phi = \phi(D, n, k)$, and divide the ash into *classes* of like optical constants. This approach allows for composition variations within a class provided

these variations do not significantly affect the optical constants. While both of these approaches should produce the same results, this latter approach is adopted here and is probably more reasonable for purposes of computing the radiative properties of fly ash since it allows one to ignore composition variations that do not affect the optical constants.

Let the fraction of particles with diameters D and optical constants n and k be $\phi(D,n,k)\,dD\,dn\,dk$, then the average spectral radiative properties are

$$\alpha_\lambda = \int_0^\infty \int_0^\infty \int_0^\infty \phi(D,n,k)\alpha_\lambda(D,n,k)\,dD\,dn\,dk, \qquad (V.8)$$

$$\sigma_\lambda = \int_0^\infty \int_0^\infty \int_0^\infty \phi(D,n,k)\sigma_\lambda(D,n,k)\,dD\,dn\,dk, \qquad (V.9)$$

and

$$\Phi_\lambda(\mu) = \frac{\int_0^\infty \int_0^\infty \int_0^\infty \phi(D,n,k)\sigma_\lambda(D,n,k)\Phi_\lambda(\mu,D,n,k)\,dD\,dn\,dk}{\sigma_\lambda}. \qquad (V.10)$$

In practice it is useful to replace the integrals over n and k with summations over a finite number of compositional classes, each class having approximately constant n and k. For example, suppose that $\phi_i(D)dD$ is the fraction of particles with size D within dD with optical constants n_i and k_i. Then the integrals over n and k can be replaced with the summations

$$\alpha_\lambda = \sum_i \int_0^\infty \phi_i(D)\alpha_{\lambda,i}(D)dD, \qquad (V.11)$$

$$\sigma_\lambda = \sum_i \int_0^\infty \phi_i(D)\sigma_{\lambda,i}(D)dD, \qquad (V.12)$$

and

$$\Phi_\lambda(\mu) = \frac{\sum_i \int_0^\infty \phi_i(D)\sigma_{\lambda,i}(D)\Phi_{\lambda,i}(\mu,D)dD}{\sum_i \int_0^\infty \phi_i(D)\sigma_{\lambda,i}(D)dD}. \qquad (V.13)$$

Here the subscript i denotes values for the class of particles with $n = n_i$ and $k = k_i$.

The scattering and absorption efficiencies for a particle illuminated by a plane monochromatic wave are defined as

$$Q_s = \frac{\text{Scattered Power}}{\text{Power incident on the cross sectional area}} \qquad (V.14)$$

$$Q_a = \frac{\text{Absorbed Power}}{\text{Power incident on the cross sectional area}} \qquad (V.15)$$

These efficiencies are not limited to unity. In fact, for very large particles (compared to λ) $Q_s + Q_a \to 2$. If the particle is non-absorbing then $Q_s \to 2$. An interpretation of this result is that for a large non-absorbing particle some fraction of the incident light is reflected or refracted by the particle, up to a total fraction of unity, while the remainder of the scattering is attributable to diffraction whereby the particle affects the incident wavefront beyond its physical radius. Very small particles ($\pi D/\lambda \ll 1$) have Q_a and Q_s values much less than unity. Particles with dimensions comparable to λ can have Q_s and Q_a values several times unity.

Assuming that one can calculate (or otherwise estimate) the scattering and absorption efficiencies, $Q_{s,i}$ and $Q_{a,i}$, and the scattering phase function, $\Phi_{\lambda,i}(\mu)$ for a spherical particle with diameter D, and prescribed optical constants, n_i and k_i, for incident radiation at wavelength, λ, the scattering and absorption cross sections are, by definition,

$$C_{s,i}(D,\lambda) = Q_{s,i}(D,\lambda)\frac{\pi D^2}{4} \tag{V.16}$$

$$C_{a,i}(D,\lambda) = Q_{a,i}(D,\lambda)\frac{\pi D^2}{4} \tag{V.17}$$

If the number density of particles is N_i (total number of particles of class i per unit volume of medium) and the number fraction of these particles with diameter D is $\phi_i(D)dD$, then their contribution to the scattering coefficient for particles with optical constants n_i and k_i is

$$\sigma_{\lambda,i}(D)\ dD = N_i Q_{s,i}(D,\lambda)\frac{\pi D^2}{4}\phi_i(D)dD \tag{V.18}$$

The volume fraction of particles in class (n_i, k_i) is

$$C_{v,i} = N_i \int_0^\infty \frac{\pi D^3}{6}\phi_i(D)dD \tag{V.19}$$

In terms of the volume fraction of particles, C_v, Eq. (V.18) can be written as

$$\sigma_{\lambda,i}(D)\ dD = \frac{3}{2}\frac{C_{v,i}}{D_{32,i}}\frac{Q_{s,i}(D,\lambda)D^2\phi_i(D)dD}{\int_0^\infty D^2\phi_i(D)dD} \tag{V.20}$$

Here $D_{32,i}$ is the Sauter mean diameter,

$$D_{32,i} = \frac{\int_0^\infty D^3\phi_i(D)dD}{\int_0^\infty D^2\phi_i(D)dD} \tag{V.21}$$

If we define the size-averaged scattering efficiency as

$$Q_{s,i}(\lambda) = \frac{\int_0^\infty Q_{s,i}(D,\lambda)D^2\phi_i(D)dD}{\int_0^\infty D^2\phi_i(D)dD}, \tag{V.22}$$

and integrate over particle diameter, the resulting expression for the scattering coefficient for particles of class (n_i, k_i) is

$$\sigma_{\lambda,i} = \frac{3}{2}\frac{C_{v,i}}{D_{32,i}} Q_{s,i}(\lambda) \tag{V.23}$$

Similarly, the absorption coefficient is

$$\alpha_{\lambda,i} = \frac{3}{2}\frac{C_{v,i}}{D_{32,i}} Q_{a,i}(\lambda) \tag{V.24}$$

where $Q_{a,i}(\lambda)$ is the size-averaged absorption efficiency. A similar analysis gives the size-averaged scattering phase function for class (n_i, k_i) as

$$\Phi_{\lambda,i}(\mu) = \frac{\int_0^\infty Q_{s,i}(D,\lambda)\Phi_{\lambda,i}(\mu, D)D^2\phi_i(D)dD}{Q_{s,i}(\lambda)\int_0^\infty D^2\phi_i(D)dD} \tag{V.25}$$

Finally, the overall radiative properties for the medium are the sums of those for each composition class, i.e.,

$$\sigma_\lambda = \sum_i \sigma_{\lambda,i}, \tag{V.26}$$

$$\alpha_\lambda = \sum_i \alpha_{\lambda,i}, \tag{V.27}$$

and the scattering phase function is

$$\Phi_\lambda(\mu) = \frac{\sum_i \sigma_{\lambda,i}\Phi_{\lambda,i}(\mu)}{\sum_i \sigma_{\lambda_i}} \tag{V.28}$$

Note that the $\Phi_{\lambda,i}(\mu)$ are weighted by the scattering coefficient for each class.

It should be noted that in the above formulation D was described as the diameter of a spherical particle. In fact, this formulation is somewhat more general than that. One could regard D as an "effective" diameter for irregularly shaped, randomly orientated particles. The restriction that D be the diameter of a spherical particle is only important when one introduces Mie theory to compute the scattering and absorption efficiencies; in such a case the particles are strictly assumed to be spherical.

Several results can be anticipated on the basis of the formulation above. First, for very small particles ($x = \pi D/\lambda \ll 1$) in the Rayleigh limit of Mie theory, the scattering efficiency is proportional to x^4. Since D_{32} is proportional to the diameter of the particles, the scattering coefficient for the medium is proportional to $C_v D^3$. If the density of the particles are all approximately ρ then C_v is proportional to the

mass loading of particles (ρC_v). Thus the scattering coefficient is proportional to the product of the mass loading of particles and the average volume of a single particle. If a given mass dispersion of particles were divided into finer particles the scattering would decrease proportionately to D^3. Conversely, if a very fine dispersion of particles formed larger agglomerates the scattering would increase as D^3 for the new particles. In contrast, the absorption efficiency for very small particles is proportional to x, or the diameter of the particles. Thus the absorption coefficient for a dispersion of very fine particles is essentially constant for a constant mass loading. For this reason if a dispersion of soot, for instance, is composed of very fine particles then one should not expect the absorption coefficient to have significant dependence on the size distribution of the soot particles. The scattering albedo, $\omega = \sigma/(\sigma + \alpha)$ will decrease with particle volume but be independent of mass loading.

Another limiting case that can be easily understood is the large particle limit, where Q_a and Q_s are approximately constant with $Q_a + Q_s \rightarrow 2$. In this limit the scattering and absorption coefficients for a fixed mass loading decreases as $1/D$. Decreasing the particle size increases both the scattering and absorption coefficients in the same proportion. The scattering albedo, ω, will be independent of particle size and mass loading. It is also interesting to note that for very large particles Q_a will not exceed the hemispherical emittance of the constituent material (i.e. $Q_a \leq 1$), thus $0.5 \leq \omega \leq 1$.

V.2 Characteristics of Fly Ash Dispersions

In a recent study [17] a considerable amount of detailed information on the size and composition distributions of fly ash were presented for six representative U.S. coals. This section essentially summarizes the portions of that study that are required to compute the radiative properties of fly ash. For additional detail see Ghosal [17] and Ghosal, et. al. [36].

V.2.1 Fly Ash Size Distribution

Fly ash particles are typically closely spherical with sizes ranging from very small, submicron particles to very large particles of adventitious rock (>100 μm). However, to a reasonable approximation it has been found that the size distribution for fly ash particles is generally well-modeled by a lognormal distribution function.

The particle size distribution function, $\phi(D)$, is defined so that $\phi(D)dD$ is the fraction of particles with diameter D within dD. For a lognormal distribution †

$$\phi(D) = \frac{1}{D\sqrt{2\pi}\sigma_u} \exp(-\frac{(\ln D - \ln D_n)^2}{2\sigma_u^2}), \qquad (V.29)$$

where $\sigma_u = \ln \sigma_g$. Here the number median diameter is D_n (half the particles are smaller than D_n) and σ_g is the geometric standard deviation. It is more convenient to recast Eq. (V.29) in terms of $u = \ln D$ and write it as a differential function

$$\phi dD = \frac{1}{\sqrt{2\pi}\sigma_u} \exp(-\frac{(u - \overline{u})^2}{2\sigma_u^2})du = f(u)du \qquad (V.30)$$

where $du = d(lnD) = dD/D$, $\overline{u} = \log D_n$ and $f(\exp(u))$ is the log-normal distribution function used by Ghosal. In this form we can easily interpret the distribution as a normal distribution centered about $\overline{u}$ with approximately 68.3% of the particles within $\pm\sigma_u$ of $\overline{u}$ and approximately 95.4% of the particles within $\pm 2\sigma_u$ of $\overline{u}$.

The i^{th} moment of ϕ is obtained by multiplying Eq. (V.30) by D^i and normalizing so that the integral over all diameters is unity. If we adopt the notation where ϕ_i is the i^{th} moment, then

$$\phi_i(D)dD = \frac{1}{\sqrt{2\pi}\sigma_u} \exp(-\frac{[u - (\overline{u} + i\sigma_u^2)]^2}{2\sigma_u^2})du. \qquad (V.31)$$

For $i = 0$ we have $\phi_0 = \phi$, which is just the differential *number* distribution function described above. If $i = 3$, then ϕ_3 is the differential *volume* distribution function where $\phi_3 dD$ is the fraction of the total particle *volume* due to particles with diameter D within the range from D to $D + dD$. The function ϕ_3 is the volume distribution

---

† The notation here is slightly different than that used by Ghosal [17]. Here $\phi(D)dD$ is the fraction of particles with diameter D within dD. Ghosal defines $f(D) = \phi/D$ so that $f(D)d(\ln D)$ is the fraction of particles at D within $d \ln D$.

function. Similarly, ϕ_2 is the differential *area* distribution function and ϕ_1 is the differential *diameter* distribution function.

Written in the form of Eq. (V.31) it is apparent that $\exp(\overline{u} + i\sigma_u^2)$ is the median diameter of the i^{th} moment, but all moments of the distribution function have the same standard deviation, $\sigma_u = \log(\sigma_g)$. For example, for $i = 3$ the *volume median diameter* is

$$D_v = \overline{D_3} = \exp(\overline{u} + 3\sigma_u^2). \qquad (V.32)$$

One half of the total particle volume is due to particles with diameter smaller than $\overline{D_3}$. Similarly, the *area median diameter*, $\overline{D_2}$, is given by

$$D_a = \overline{D_2} = \exp(\overline{u} + 2\sigma_u^2). \qquad (V.33)$$

The notation D_v for volume median diameter and D_a for area median diameter is consistent with Ghosal [17], but the more general notation $\overline{D_i} = \exp(\overline{u} + i\sigma_u^2)$ is used here instead.

As was seen in the previous section the Sauter median diameter, defined in Eq. (V.21), can be written as

$$D_{32} = \frac{\int_0^\infty D^3\phi(D)dD}{\int_0^\infty D^2\phi(D)dD} = \exp(\overline{u} + \frac{5}{2}\sigma_u^2) \qquad (V.34)$$

Note that D_{32} is larger for distributions with a broader distribution of particle diameters (i.e.,larger σ_u) and has a minimum of $D_n = D_0$ when all particles are of a single diameter (i.e., $\sigma_u = 0$).

Based on the ash samples studied by Ghosal [17], most fly ashes have a volume median diameter in the range 10-15 μm and a geometric standard deviation ranging from 2 to 3. Figure V.1 shows a plot of σ_g versus $\overline{D_3}$ for several ash samples. The San Miguel ash has a much larger $\overline{D_3}$ than the other ashes. Ghosal has shown by density classification of the ash samples that this abnormality is due to a larger fraction of non-solid particles, or cenospheres in this ash. The Eagle Butte ash has the broadest distribution, with $\sigma_g \simeq 3.5$. Some of the ash samples were collected in a baghouse downstream of a cyclone separator, as noted on Fig. V.1. The ashes sampled from a cyclone tend to have smaller σ_g, although even the baghouse sample of Kentucky #9 ash has $\sigma_g \simeq 2.3$.

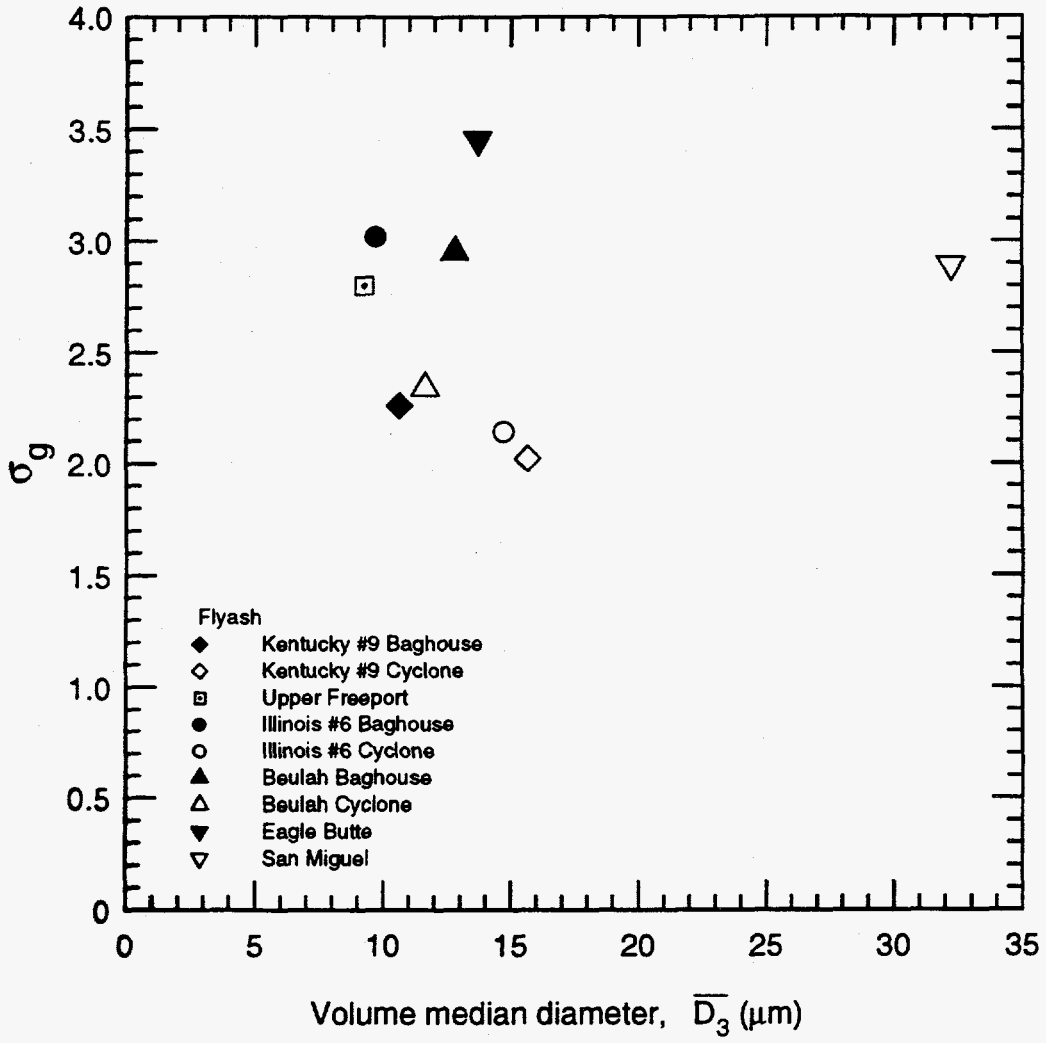

Figure V.1: Geometric standard deviation versus volume median diameter for several fly ash samples (from Ghosal,1993).

V.2.2 Composition Distribution

In addition to size distribution, Ghosal also presents composition distributions which were measured using a computer controlled scanning electron microscope. In this technique the elemental compositions of approximately 1000 particles or more were measured and tabulated for several fly ash samples. The resulting oxide weight fractions were then computed assuming each element was oxidized.

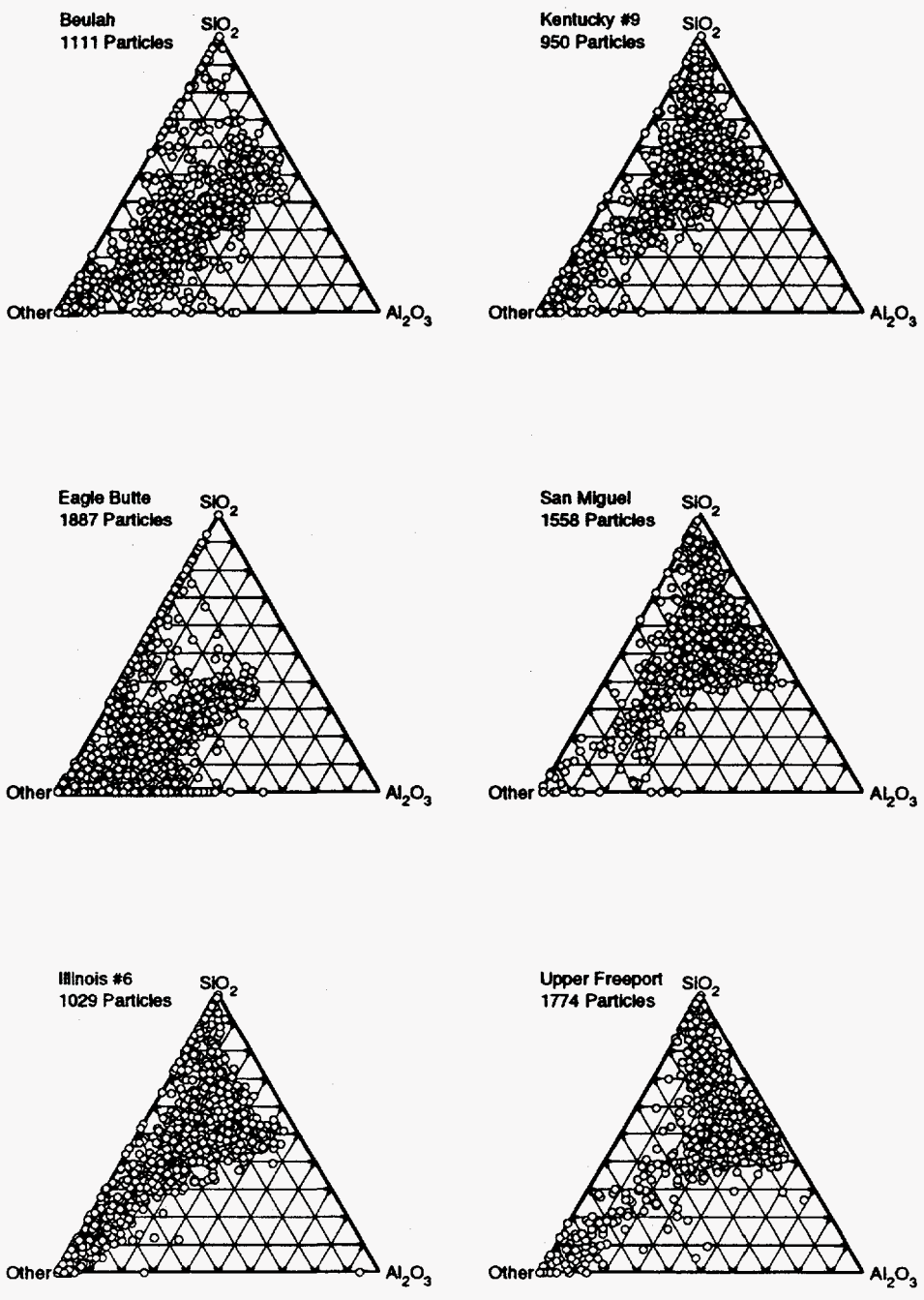

Figure V.2: Ternary plots showing the SiO_2, Al_2O_3, and other weight fractions for six different fly ash samples.

Ternary plots of the compositions for six fly ash samples are presented in Fig. V.2. These ternary plots have vertices labeled SiO_2, Al_2O_3, and "Other", where "Other" is the sum of all oxide weight fractions except SiO_2 and Al_2O_3. For example, particles with 50 wt.% SiO_2 and 50 wt.% Al_2O_3 fall at the midpoint between the vertices labeled SiO_2 and Al_2O_3, while particles with no SiO_2 or Al_2O_3 will fall at the vertex labeled "Other". As we see, the Kentucky #9, San Miguel, Upper Freeport, and Illinois #6 ashes all appear similar. Each has a rather dense population of alumino-silicate particles throughout the central portion of the ternary diagram. In contrast, the Beulah and Eagle Butte ashes have many more particles which have lower levels of SiO_2 and Al_2O_3. It is difficult to obtain quantitative information from such ternary plots, since one can display only three constituents.

More quantitative composition distribution information is obtained by plotting the volume fraction of ash with oxide composition x versus x. Here x is one of twelve measured oxide composition fractions ($0 \leq x \leq 1$). Such plots are shown for the five ashes Beulah, Eagle Butte, Illinois #6, Kentucky #9, and Upper Freeport in Figs V.3–V.7. Consider the composition distributions shown in Fig. V.3. The top left plot shows the volume fraction of SiO_2 versus the weight fraction $x = x_{SiO_2}$. As illustrated, most of the particles in this ash have less than 40% SiO_2, with significant volume fraction (3.5%) having less than 1% SiO_2 content. The distribution function for Fe_2O_3 in the Beulah ash shows that most ash particles (by volume) have less than 5% Fe_2O_3. Table V.1 summarizes the results in Figs V.3–V.7.

Note that for these and all subsequent volumetric quantities it is necessary to restrict the data to the smallest 90% of the particles because of the limited number of particles found in the larger sizes. For example, it was found that one 30 μm particle could significantly change the entire composition distribution, although we have no way of knowing if that one particle was representative or an exception. This issue will become more apparent in subsequent plots.

In addition to knowing the distribution of ash particle compositions, it is also interesting to plot the average composition versus particle diameter, as illustrated in Figs V.8–V.12. Here the average composition is computed for all particles with diameter D within dD, and the weight percentage of each oxide is plotted versus diameter. A thick line indicates diameters which constitute the smallest 90% of particles.

A number of observations can be made based on the results shown in Figs V.8–V.12. First, most ashes show an increase in average SiO_2 content with increasing

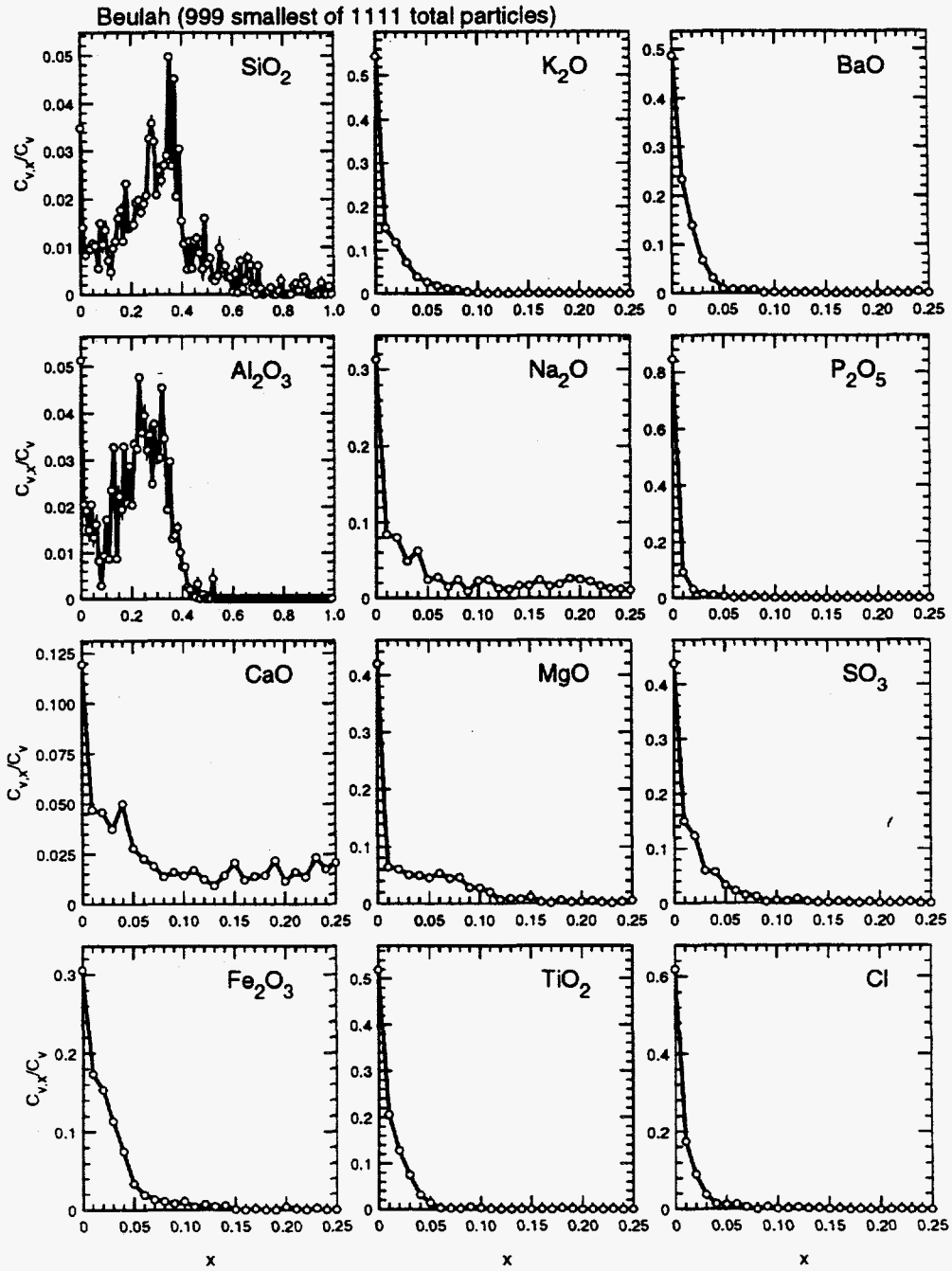

Figure V.3: Composition distributions for Beulah lignite ash.

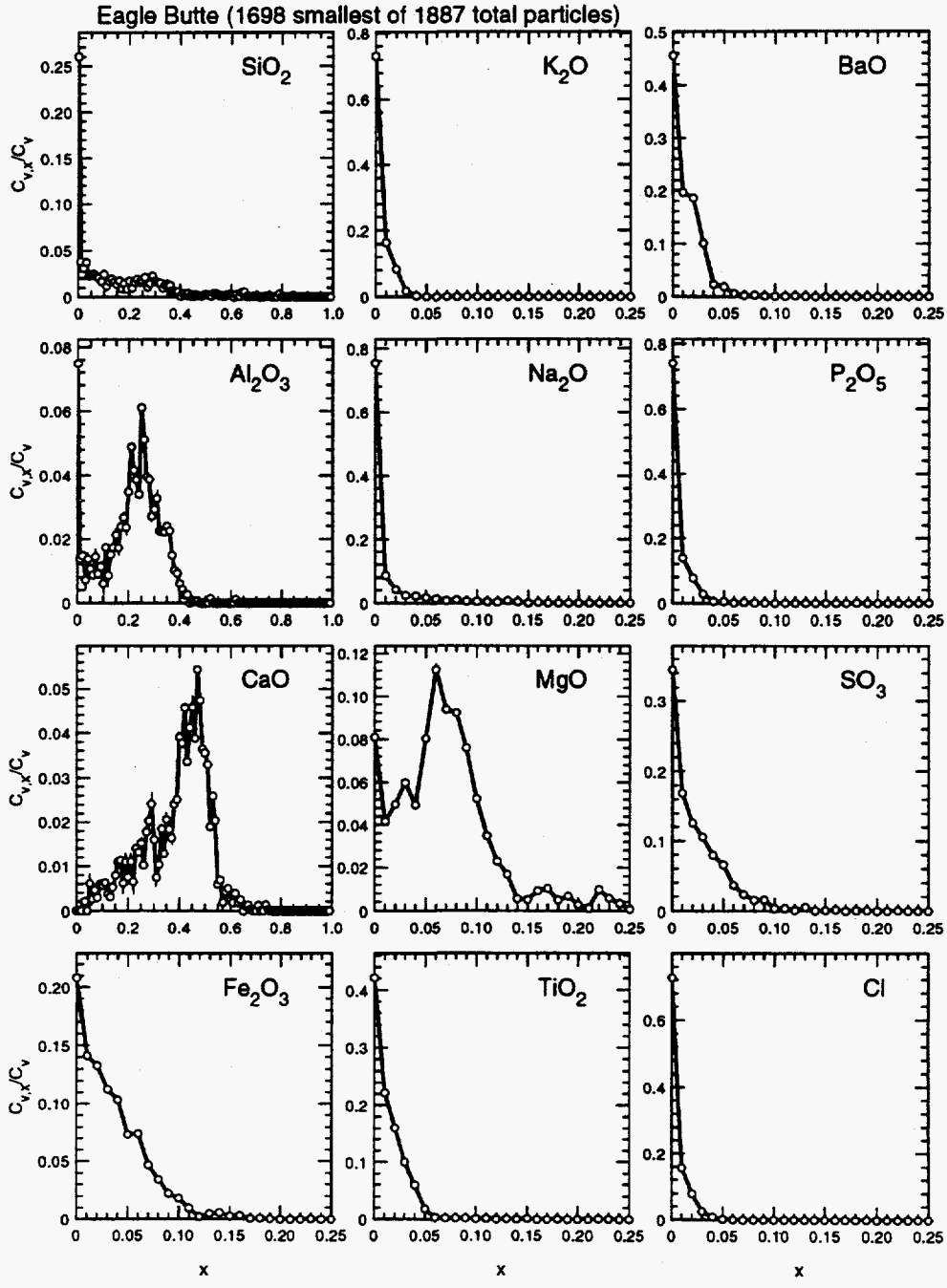

Figure V.4: Composition distributions for Eagle Butte sub–bituminous ash.

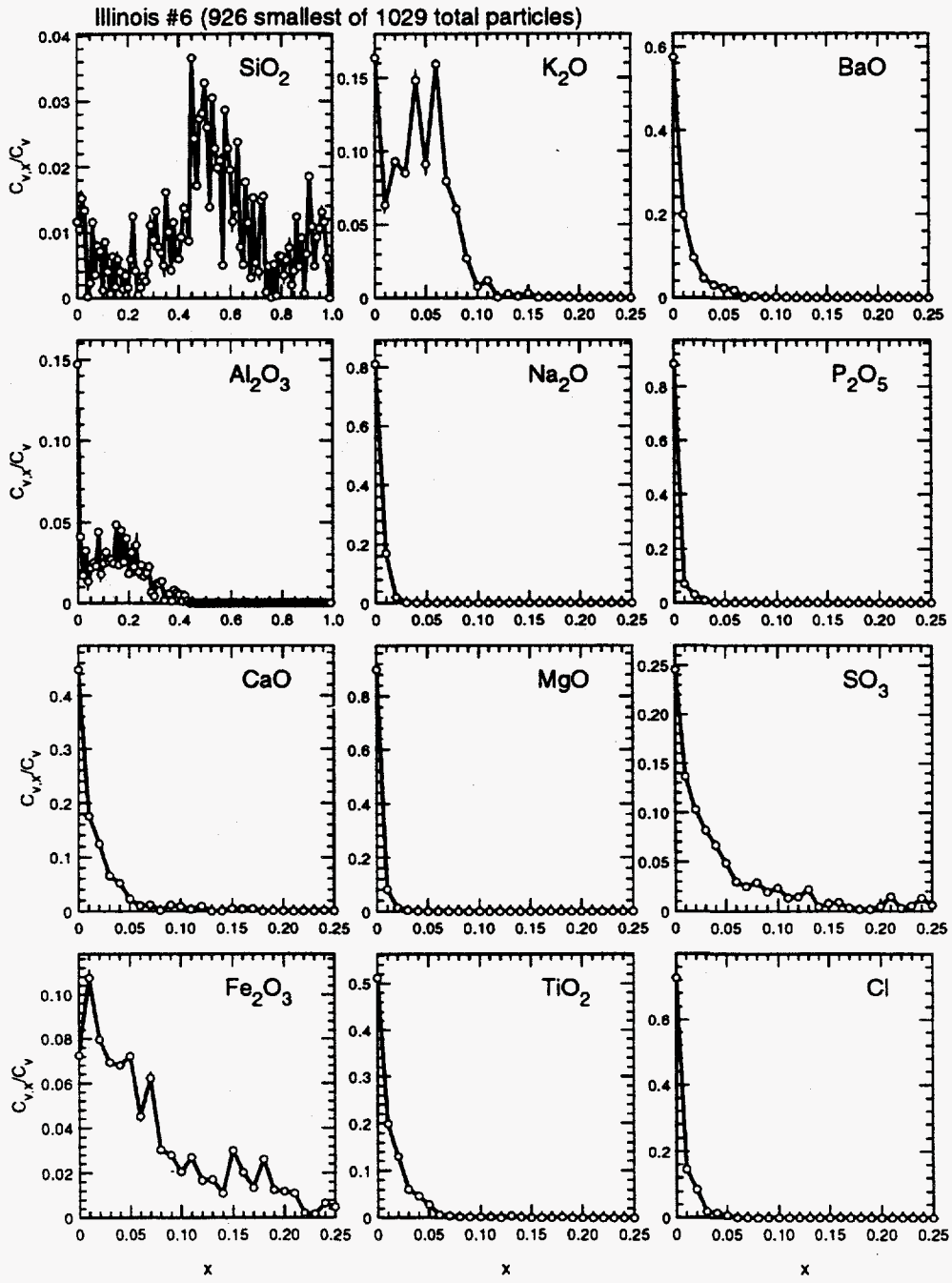

Figure V.5: Composition distributions for Illinois #6 bituminous ash.

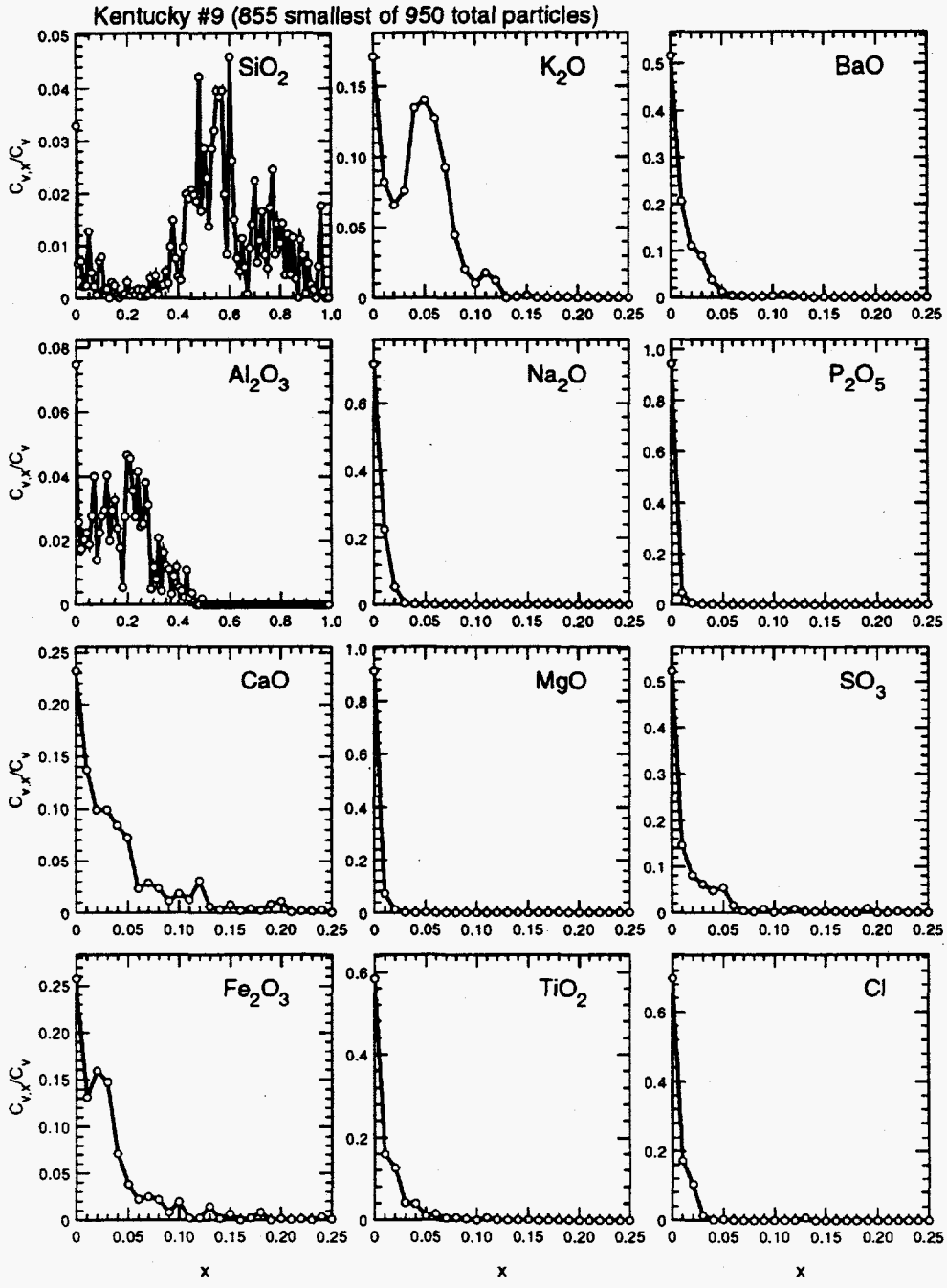

Figure V.6: Composition distributions for Kentucky #9 bituminous ash.

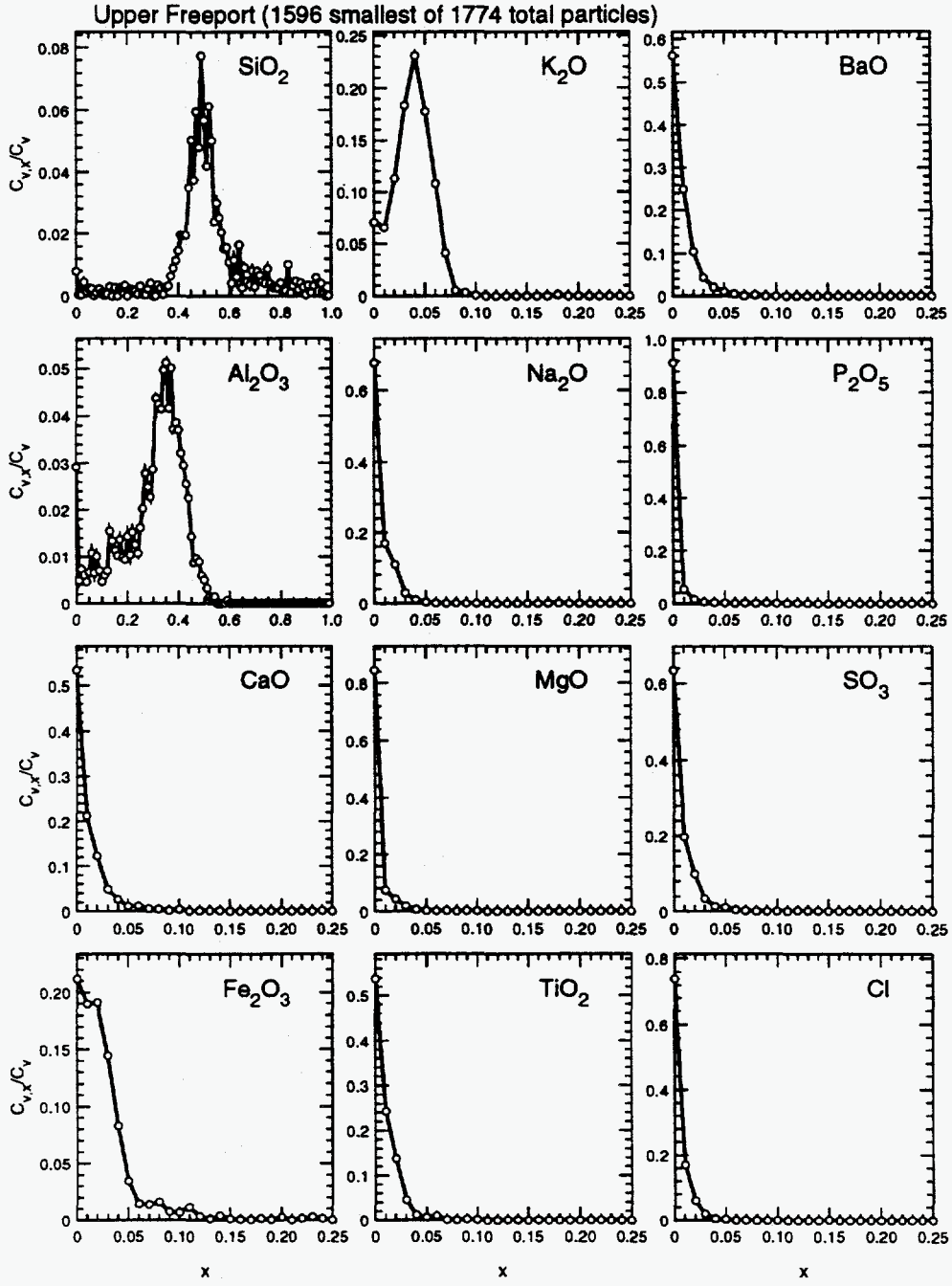

Figure V.7: Composition distributions for Upper Freeport bituminous ash.

Table V.1: Summary of observations based on composition distributions.

Beulah Lignite Figure V.3	Typically less than 40 wt.% SiO_2. High Al_2O_3/SiO_2 ratio. Low Fe_2O_3. Moderately high CaO(broad range of wt.%). Low but significant levels of Na_2O
Eagle Butte Sub–Bituminous Figure V.4	Very low SiO_2. Much with no SiO_2. Very high CaO. Moderately high Fe_2O_3 (5-10wt%). Significant quantities of MgO.
Illinois #6 Bituminous Figure V.5	Average (40-60 wt.%) levels of SiO_2. Broad range of SiO_2 content. High Fe_2O_3 (10-20 wt.%). Moderately High K_2O (0-10 wt.%).
Kentucky #9 Bituminous Figure V.6	Average (40-70 wt.%) SiO_2 levels. Broad range of SiO_2 levels Low to moderate Fe_2O_3 (0-5 wt.%). Moderately high K_2O levels (0-8 wt.%)
Upper Freeport Bituminous Figure V.7	Average (40-60 wt.%) SiO_2 levels. Relatively narrow range of SiO_2 and Al_2O_3 levels Low to moderate Fe_2O_3 (0-5 wt.%). Moderately high K_2O levels (0-7 wt.%)

diameter, most notably the bituminous ashes Illinois #6 and Kentucky #9. The high iron ash, Illinois #6, shows decreasing Fe_2O_3 and SO_3 contents with increasing diameter, suggesting the presence of smaller pyrite-like particles. The sub–bituminous Eagle Butte ash and the bituminous Upper Freeport ash show no significant average composition variations with diameter. The Beulah ash (lignite) shows weak composition variation with diameter, although SiO_2 does increase with diameter as CaO decreases.

The extrapolation of these trends in average composition versus diameter to all particle diameters is probably not warranted as indicated by the spikiness of the curves for the 10% of largest particles. The number of composition measurements for larger diameter particles is so small that the statistical confidence in computing a

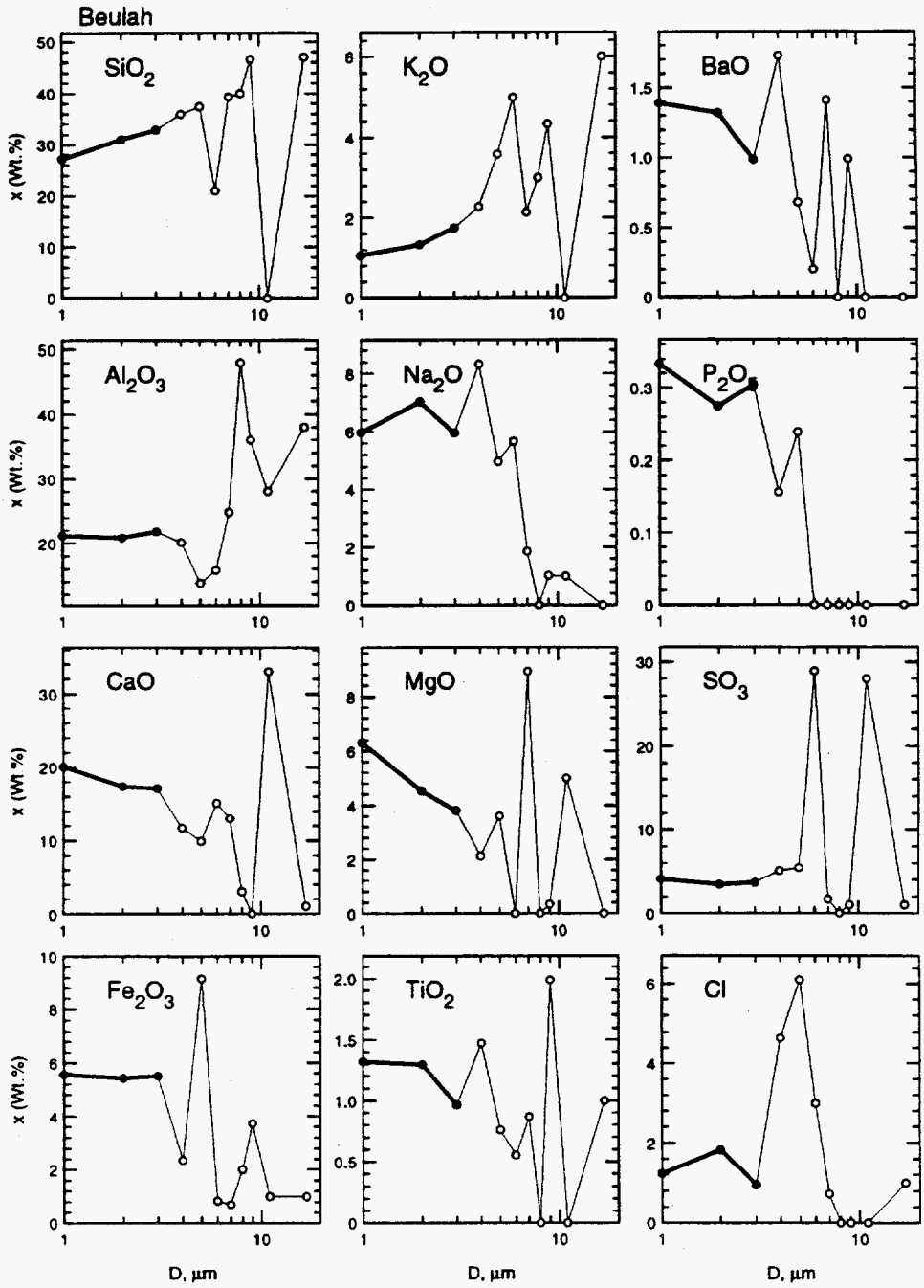

Figure V.8: Average composition versus diameter for Beulah lignite ash.

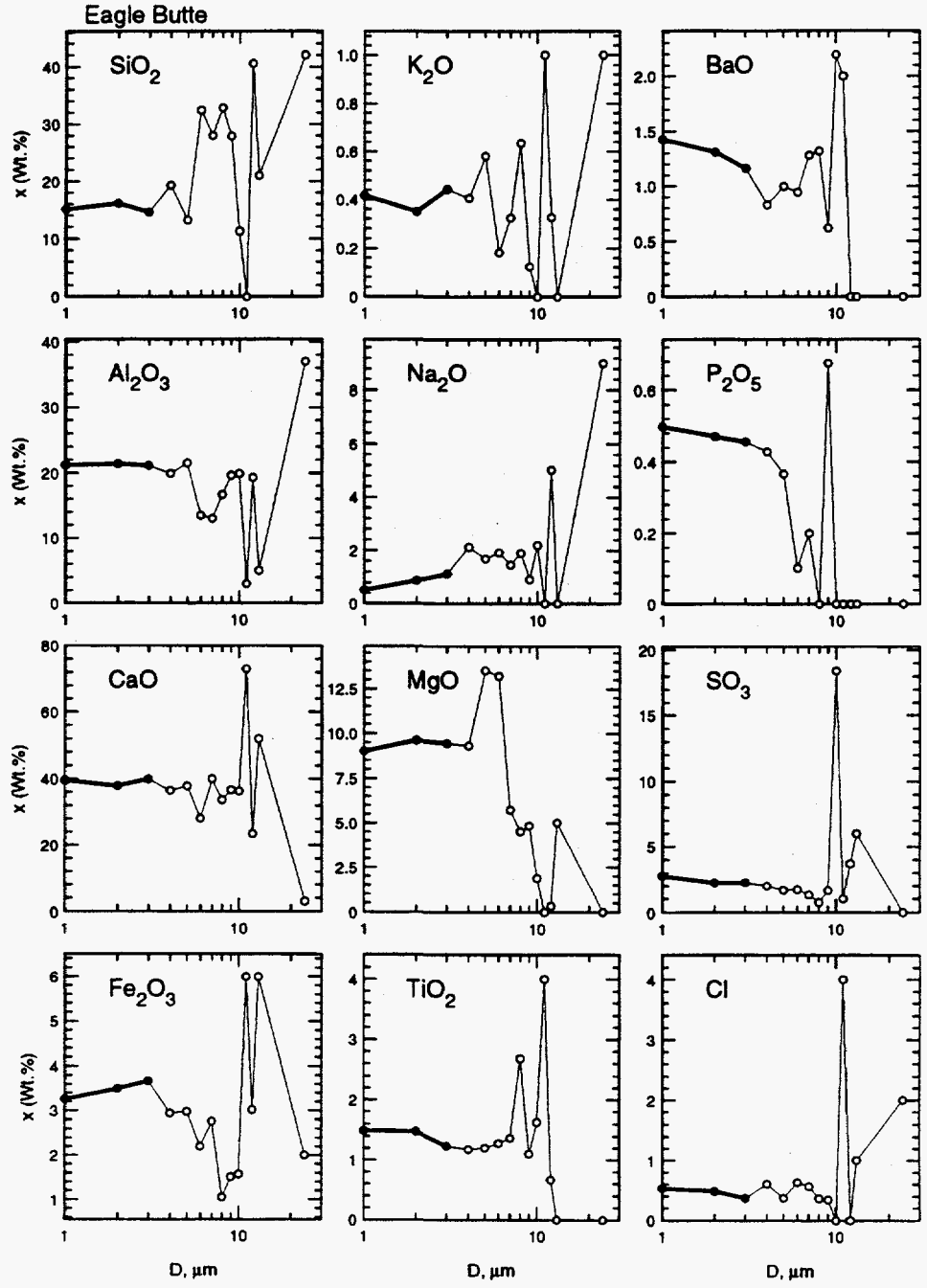

Figure V.9: Average composition versus diameter for Eagle Butte sub–bituminous ash.

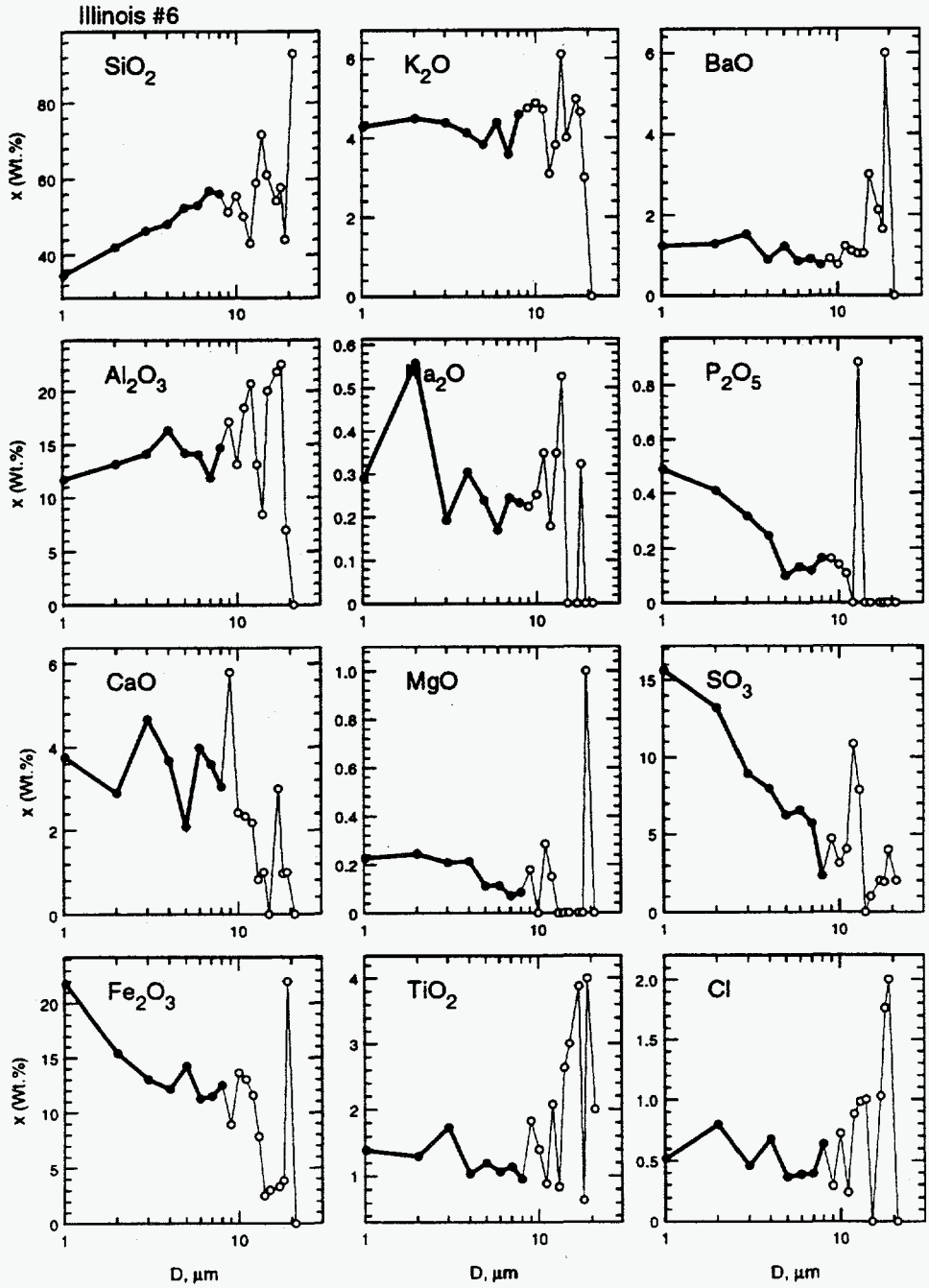

Figure V.10: Average composition versus diameter for Illinois #6 bituminous ash.

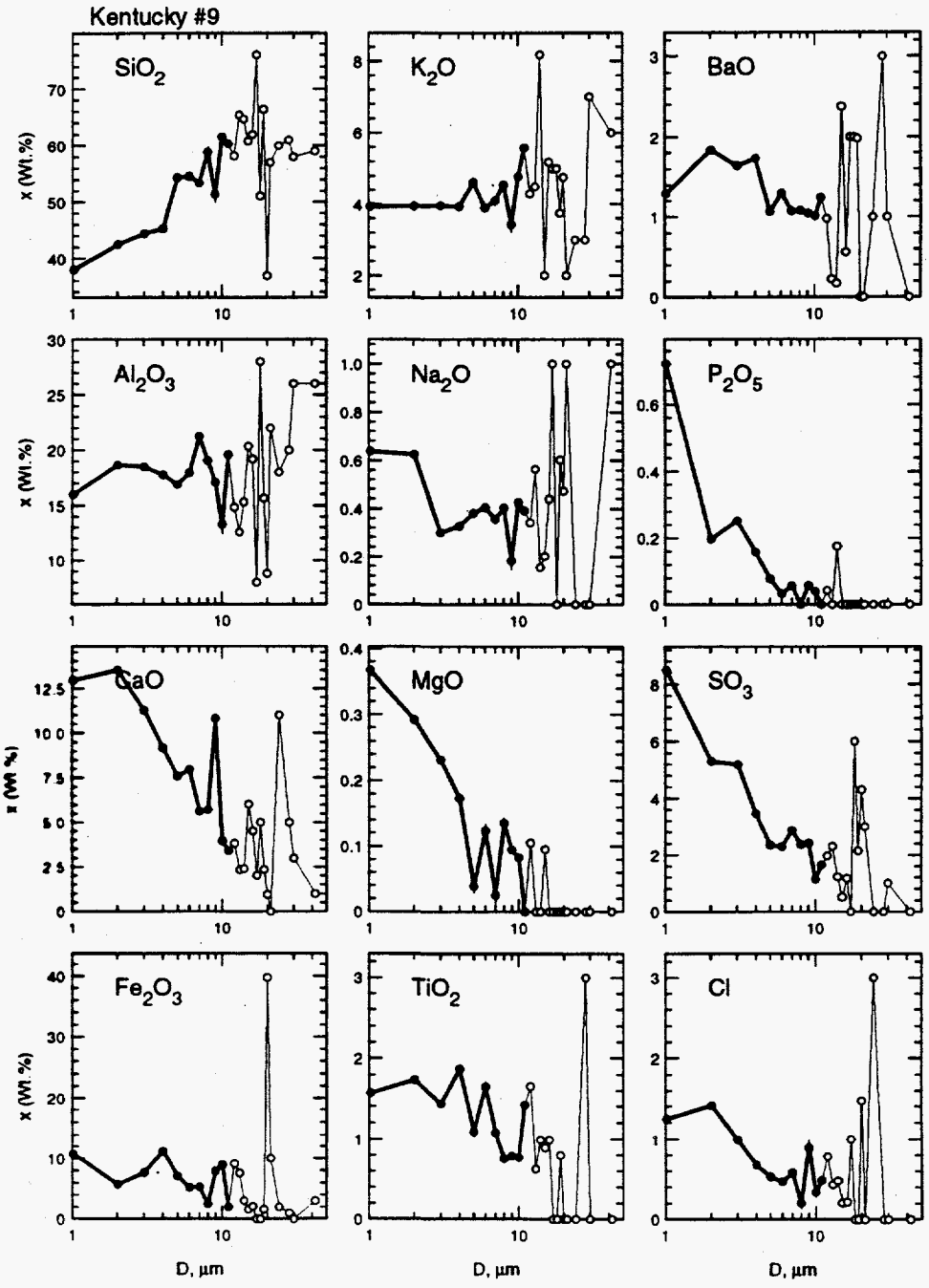

Figure V.11: Average composition versus diameter for Kentucky #9 bituminous ash.

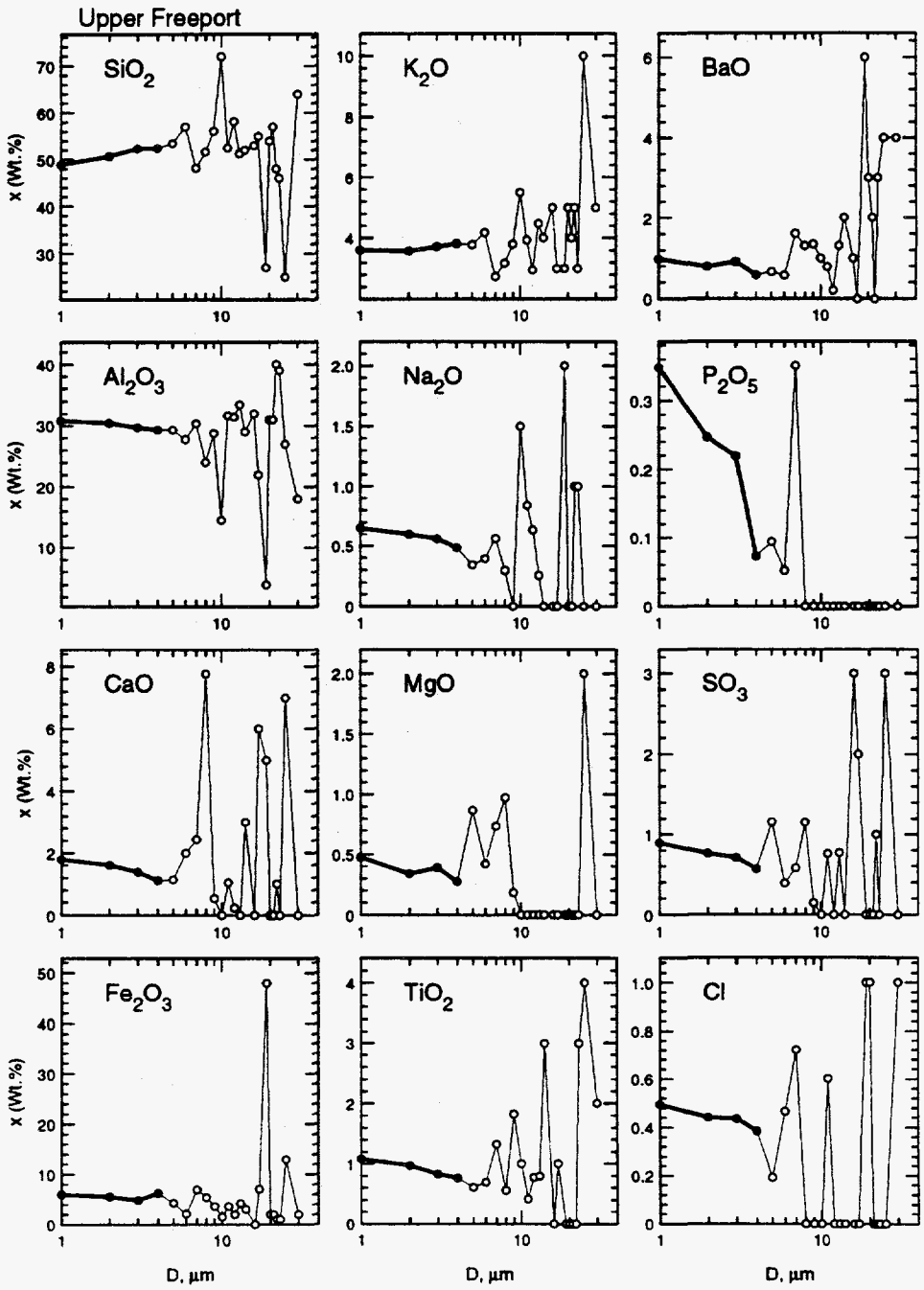

Figure V.12: Average composition versus diameter for Upper Freeport bituminous ash.

meaningful average composition is low. This is not unexpected since the log–normal size distribution predicts so few large particles.

V.2.3 Summary of Fly Ash Characteristics.

In this section the size and composition distributions for several fly ashes have been reviewed, based on work of Ghosal [17]. Generally it is found that there is significant particle-to-particle composition variation, as suggested by the ternary plots in Fig. V.2. These results were further quantified by calculations of composition distribution functions as presented in Figs V.3–V.7. It has also been observed that there may be significant average composition variations with particle size, as illustrated in Figs V.8–V.12. Specifically, an increase in SiO_2 with increasing diameter is observed. However, the limited sample size used for these analyses makes it difficult to extrapolate these trends to include the increasingly rare large particles in the distribution.

V.3 The Optical Constants of Fly Ash

In this section the optical constant distributions of the fly ashes are computed using the composition distribution data presented in the previous section and the correlations for computing optical constants from composition developed in Chapter IV. The result is an estimate of the optical constants for many hundreds of individual ash particles.

As discussed in Chapter IV, it is necessary to restrict the optical constants calculations to compositions that can be reasonably approximated by the range of data used to develop the correlations. However, some extrapolation beyond this narrow data set is allowed here. Generally the correlation should be expected to be valid for alumino-silicate particles with moderate CaO contents and reasonably low levels of Fe_2O_3. Three tests were established to decide the applicability of the correlations. The correlations are used if an ash particle meets these three criteria:

1. Less than 95 wt.% SiO_2. Pure quartz particles are not modeled.

2. The sum of SiO_2, Al_2O_3, CaO, Fe_2O_3, MgO, and TiO_2 should constitute 80 wt.% or more of the composition. These are the principal oxides used to estimate the refractive index.

3. The iron content as Fe_2O_3 should be less than 30 wt.%. This eliminates essentially pure pyrite (FeS_2), hematite (Fe_2O_3), and magnetite (Fe_3O_4) particles that are not modeled by the correlation.

The application of these acceptance tests allows calculations of the optical constants for the preponderance of particles in the five ashes studied here. Table V.2 shows that for two ashes, Eagle Butte and Upper Freeport, more than 93 vol.% of the ash particles passed all three tests. More than 85 vol.% of the Kentucky #9 ash particles passed the tests, but less than 70 vol.% of particles in the Eagle Butte and Illinois #6 ashes passed. Of the ash particles that failed, most failed to meet criterion 2, although Illinois #6 had many particles that had more than 30 % Fe_2O_3.

Once the ashes were subjected to the three composition criteria, the portion that passed was used to compute an average composition. This average is presented in Table V.2. In subsequent sections calculations based on average composition refer to this composition, based only on accepted particles.

The optical constants of all accepted particles were computed using the correlations developed in Chapter IV. The results for ashes having the narrowest composition distribution, Upper Freeport, and the broadest composition distribution, Eagle Butte, are presented in Fig. V.13 and Fig. V.14, respectively.

It is difficult to learn much from the data presented in Fig. V.13 or Fig. V.14, although it is evident that the Upper Freeport ash has a narrower distribution of optical constants than does the Eagle Butte ash. This is consistent with the corresponding breadths of the composition distributions.

A better way to illustrate these optical constants distributions is to plot them in the (n, k) plane for all particles at fixed wavelengths. The resulting (n, k) distribution plots for the Upper Freeport and Eagle Butte ashes are shown in Fig. V.15 and Fig. V.16.

The optical constants distributions of Fig. V.15 and Fig. V.16 show much more clearly the particle-to-particle variation of n and k. At short wavelengths ($\lambda < 4$ μm) the absorption index, k, varies by almost 4 orders of magnitude, from low iron particles

Table V.2: Properties of fly ash distributions for calculation of optical constants and radiative properties.

Ash	Upper Freeport	Beulah	Eagle Butte	Illinois #6	Kentucky #9
Average Composition (wt.%)					
SiO_2	54.83	41.39	25.36	60.92	61.67
Al_2O_3	29.52	28.00	21.73	17.97	19.93
CaO	1.04	12.05	31.31	1.84	3.72
Fe_2O_3	2.64	2.26	2.83	5.06	2.43
MgO	0.17	3.82	6.58	0.07	0.04
Na_2O	0.41	1.37	2.90	0.23	0.45
BaO	1.55	0.78	0.83	1.16	0.97
TiO_2	1.01	0.98	1.05	1.56	0.83
Single Particle Data					
Sample Size	1597	1000	1699	927	855
Accepted	1496	641	1646	478	628
Accepted Vol%	93.3	63.1	97.6	69.2	85.2
Vol% Failed 1	0.5	0.2	0.0	3.0	1.9
Vol% Failed 2	1.4	33.0	2.1	20.9	7.9
Vol% Failed 3	5.1	4.8	0.2	10.6	5.1
Particle Acceptance Tests: 1. $0 \leq x_{SiO_2} \leq 95$ wt.% 2. $x_{SiO_2} + x_{Al_2O_3} + x_{CaO} + + x_{Fe_2O_3} + x_{MgO} + x_{TiO_2} \geq 80$ wt.% 3. $x_{Fe_2O_3} < 30$ wt.%					
Measured Size Distribution					
$\bar{D}_3$	9.34	12.69	14.28	10.10	10.36
σ	2.76	2.98	2.80	2.85	2.33

where $k \leq 10^{-6}$ to higher iron particles with $k \sim 10^{-3}$ or larger. The variation in n is relatively narrow for the Upper Freeport ash, while n varies from 1.3 to 1.7 for the Eagle Butte ash.

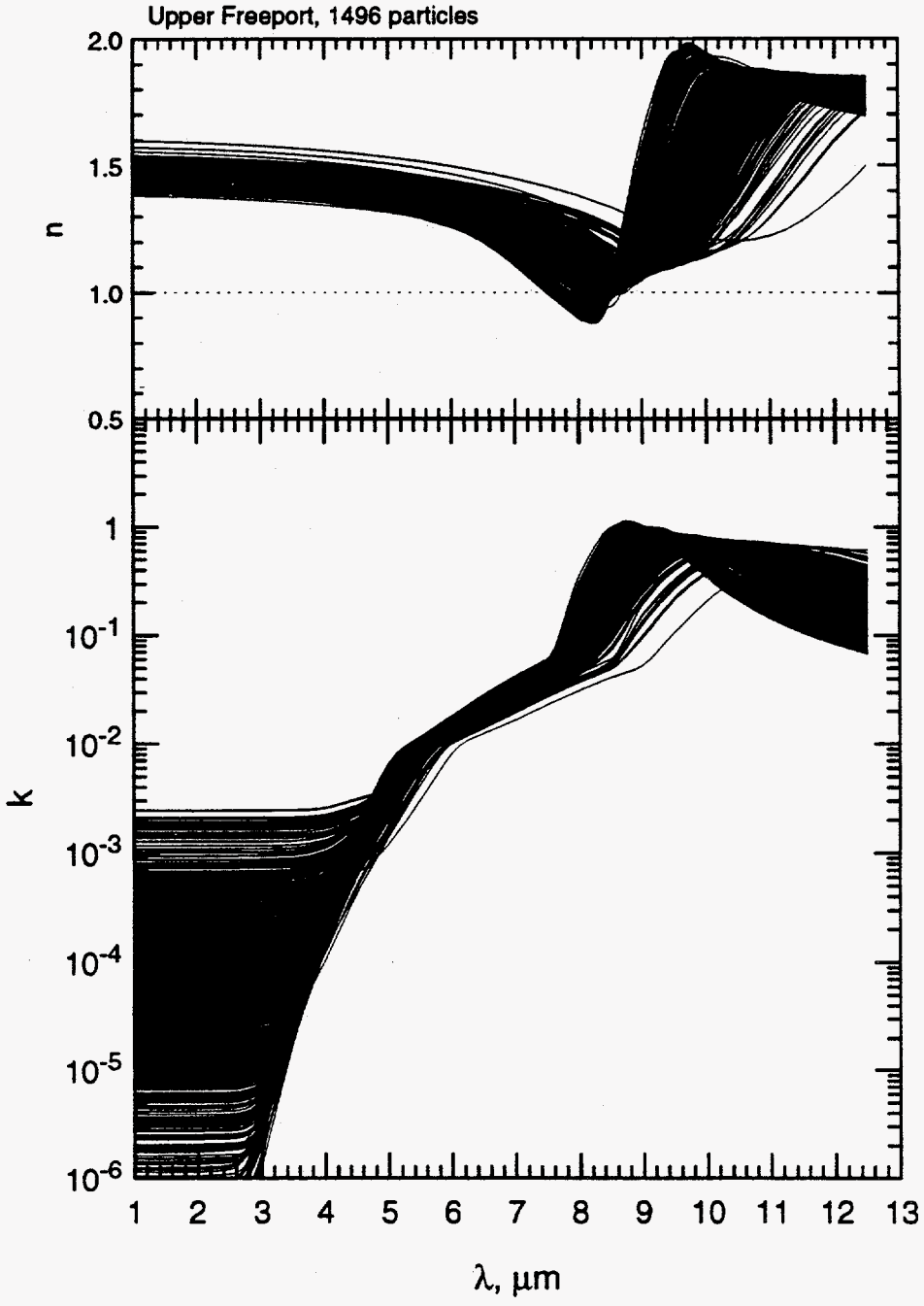

Figure V.13: Optical constants for 1496 individual particles of the Upper Freeport fly ash.

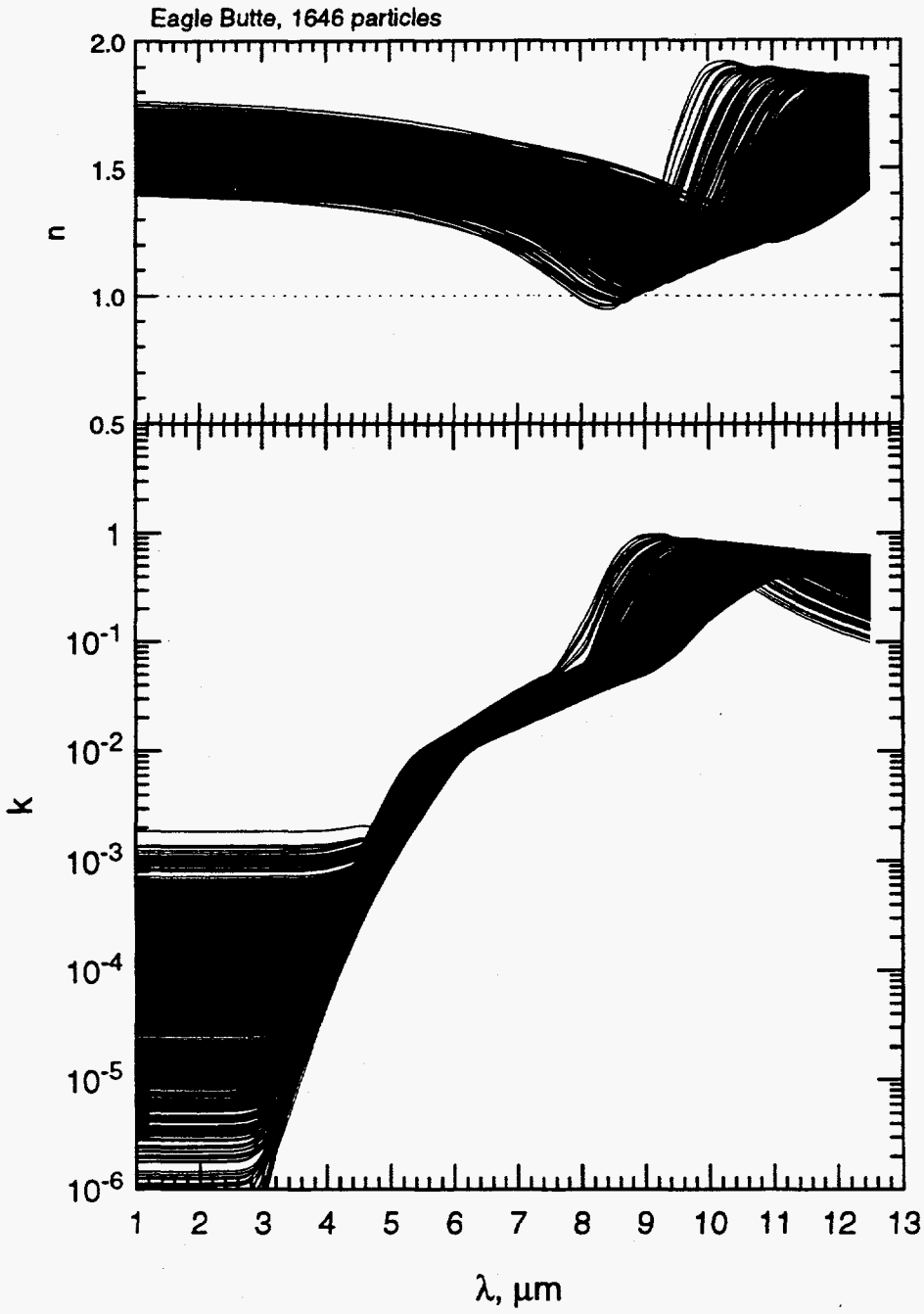

Figure V.14: Optical constants for 1646 individual particles of the Eagle Butte fly ash.

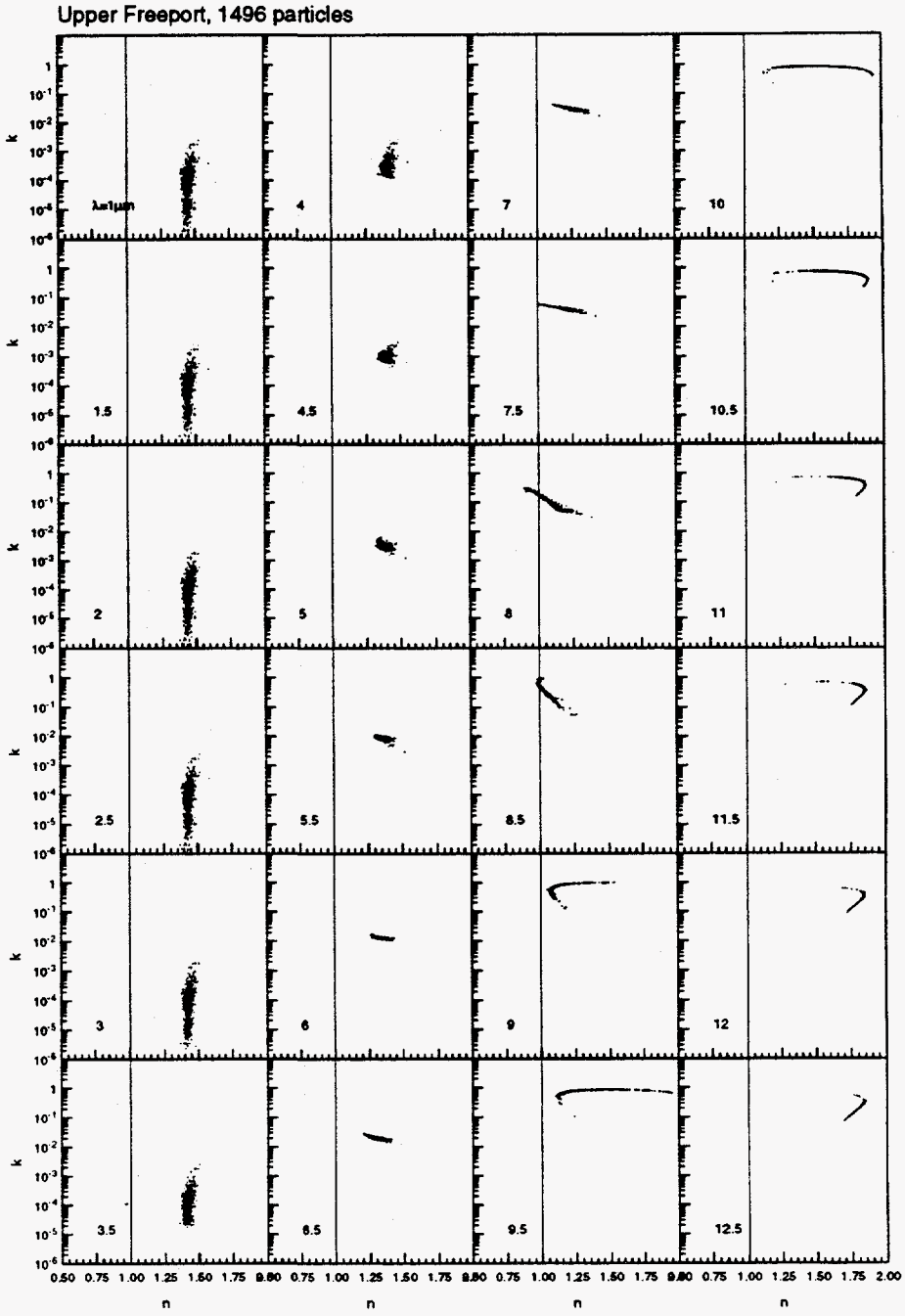

Figure V.15: Optical constants for 1496 individual particles of the Upper Freeport fly ash at 24 discrete wavelengths.

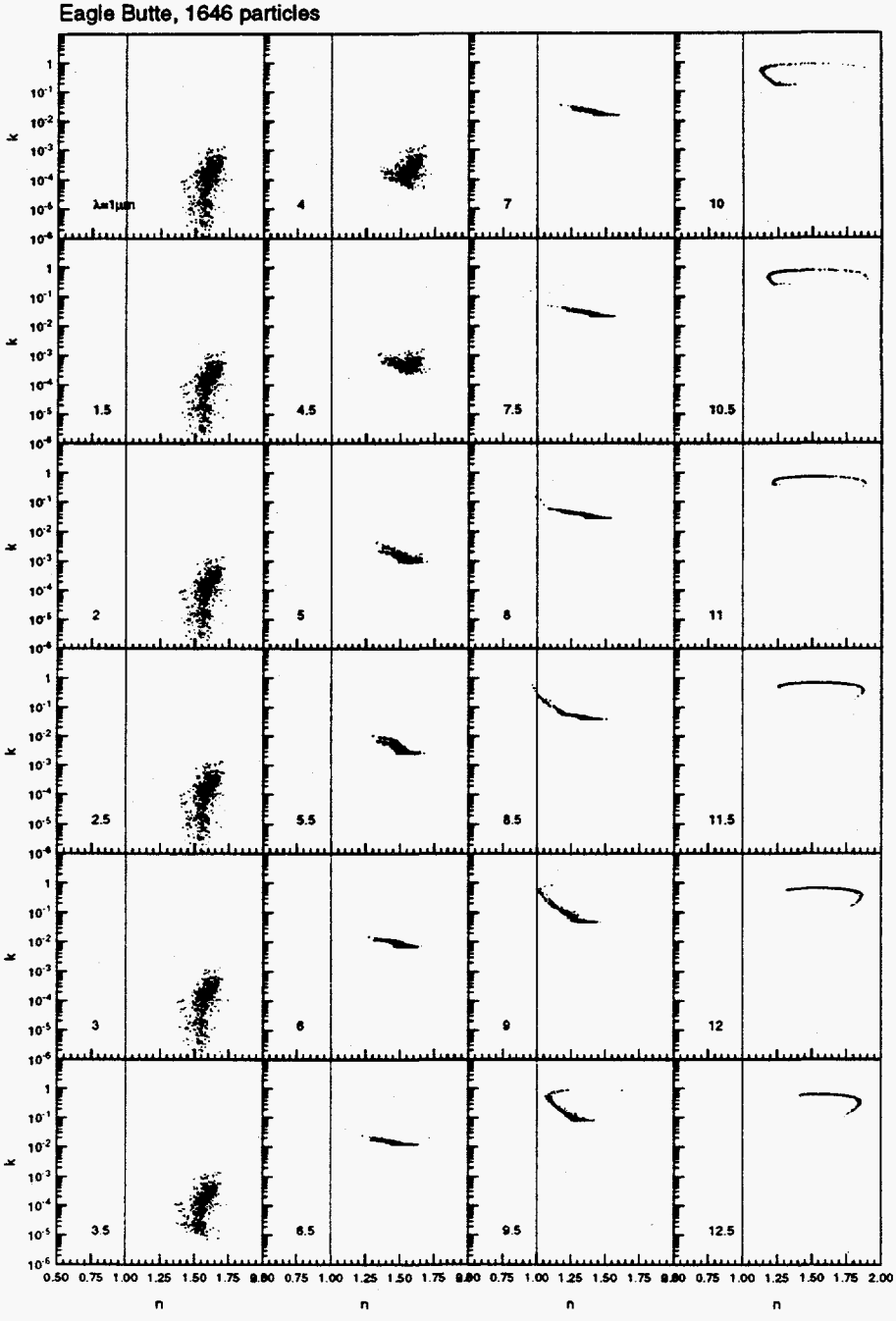

Figure V.16: Optical constants for 1646 individual particles of the Eagle Butte fly ash at 24 discrete wavelengths.

In the intermediate wavelength range, from $4 \leq \lambda \leq 6.5$ μm, k does not vary much, although the Eagle Butte ash does show significantly more particle-to-particle variation than does the Upper Freeport ash.

At longer wavelengths ($\lambda > 7$ μm) the absorption is due to SiO_2 vibrational absorption, as discussed in Chapter 4. In this region a single oscillator model for the optical constants is used in which the oscillator parameters depend on composition. The distributions of n and k in this wavelength region follow a distinctive contour through the (n, k) plane, rather than being scattered about a mean value as seen at shorter wavelengths. This contour is predominantly due to variations in the oscillator frequency, ω_o, with particle-to-particle SiO_2 variations. To illustrate this effect, consider the curves shown in Fig. V.17. Here the single oscillator model (Eq.(II.30)) was used to generate n and k for $n_\infty^2 = 2.0$, $(\omega_p/\omega_o)^2 = 0.65$, and $\gamma/\omega_o = 0.3$. The oscillator frequency was varied from $800 \leq \omega_o \leq 1000\text{cm}^{-1}$. The resulting contours are quite similar to those in Fig. V.15 and Fig. V.16. The contours essentially follow a single contour that is traced out by varying $\omega^2 - \omega_o^2$. A plot of actual n and k for a real ash is not likely to have such a sharply defined contour, but n and k must be strongly correlated in this wavelength range, so a similar structure probably exists for all coal ashes, insofar as they contain significant fractions of silica.

As a final step in specifying the optical constants for a fly ash of a given composition distribution, it is useful to reduce the amount of data prior to performing Mie scattering calculations. Accordingly the (n, k) distribution is divided into a finite number of discrete classes, with the (n, k) space divided into a grid of cells. The volume fraction of ash within each (n_i, k_i) class is computed and sorted in order of decreasing volume fraction. The list of cells is truncated after 95% of the total ash volume is accounted for. Plots of the truncated list of cells are illustrated in Fig. V.18 and Fig. V.19 for the Upper Freeport and Eagle Butte ashes. Each class (or cell) in Fig. V.18 or Fig. V.19 has an associated volume fraction. Similar classifications were made for the Kentucky #9, Illinois #6, and Beulah ashes.

V.4 The Absorption and Scattering Properties of Fly Ash Dispersions

In this section the radiative properties of dispersions of ash are computed by assuming that the ash particles are spherical, homogeneous, and isotropic with the size and optical constant distributions described in the previous sections. This is

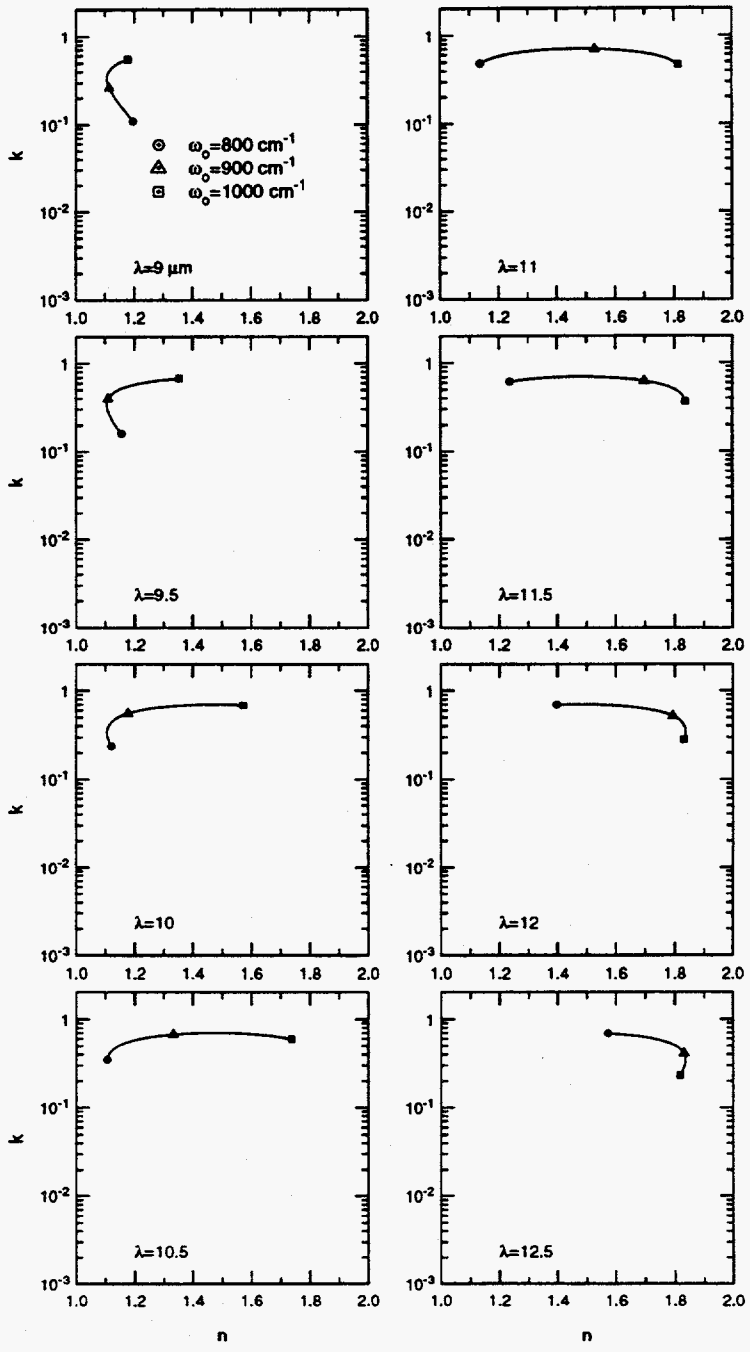

Figure V.17: Effect of ω_o variations on the optical constants correlation in the wavelength range from 9 to 12.5 μm for constants $n_\infty^2 = 2$, $(\omega_p/\omega_o)^2 = 0.65$, and $\gamma/\omega_o = 0.3$.

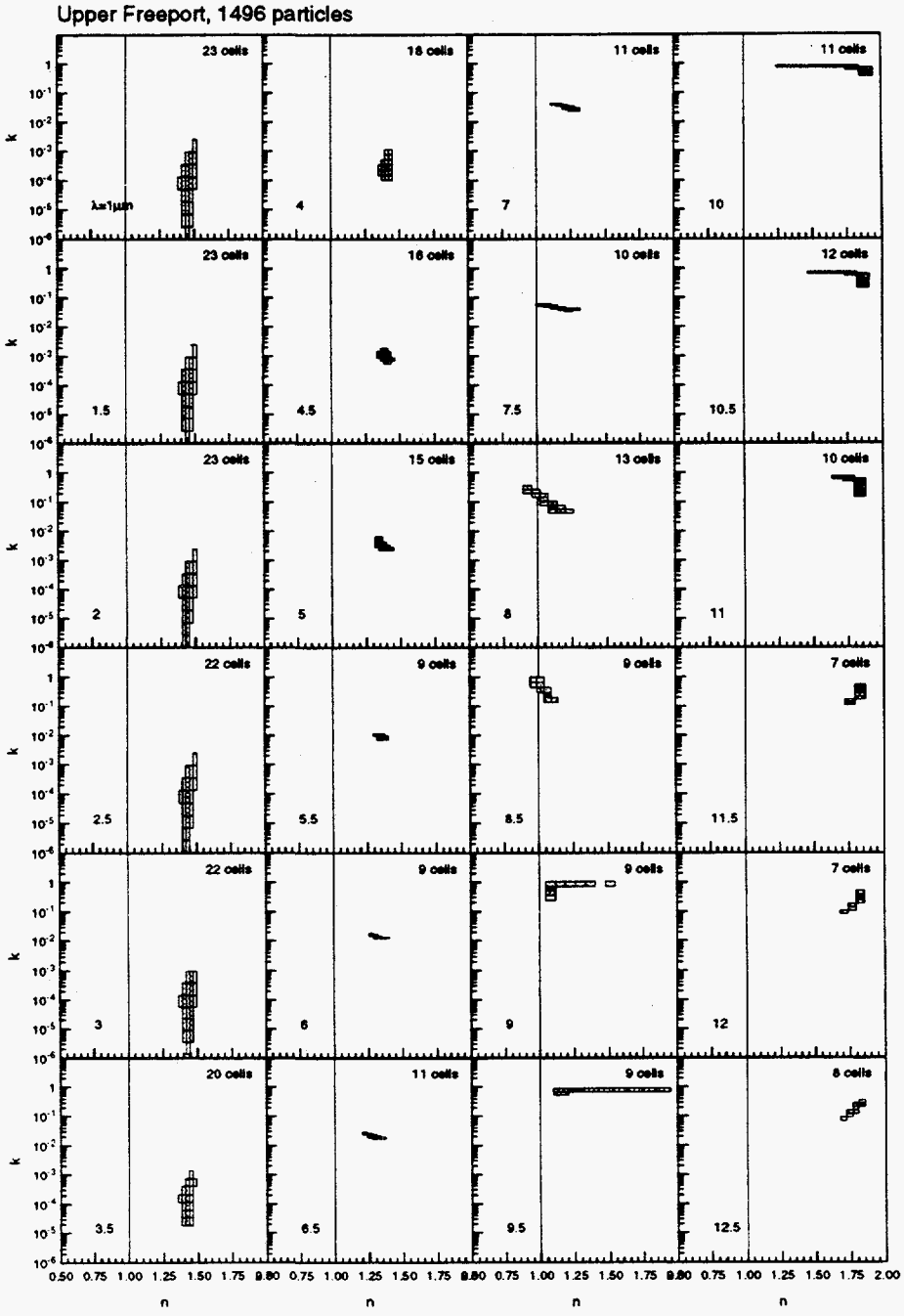

Figure V.18: Discretized classes of optical constants for the Upper Freeport fly ash at 24 discrete wavelengths.

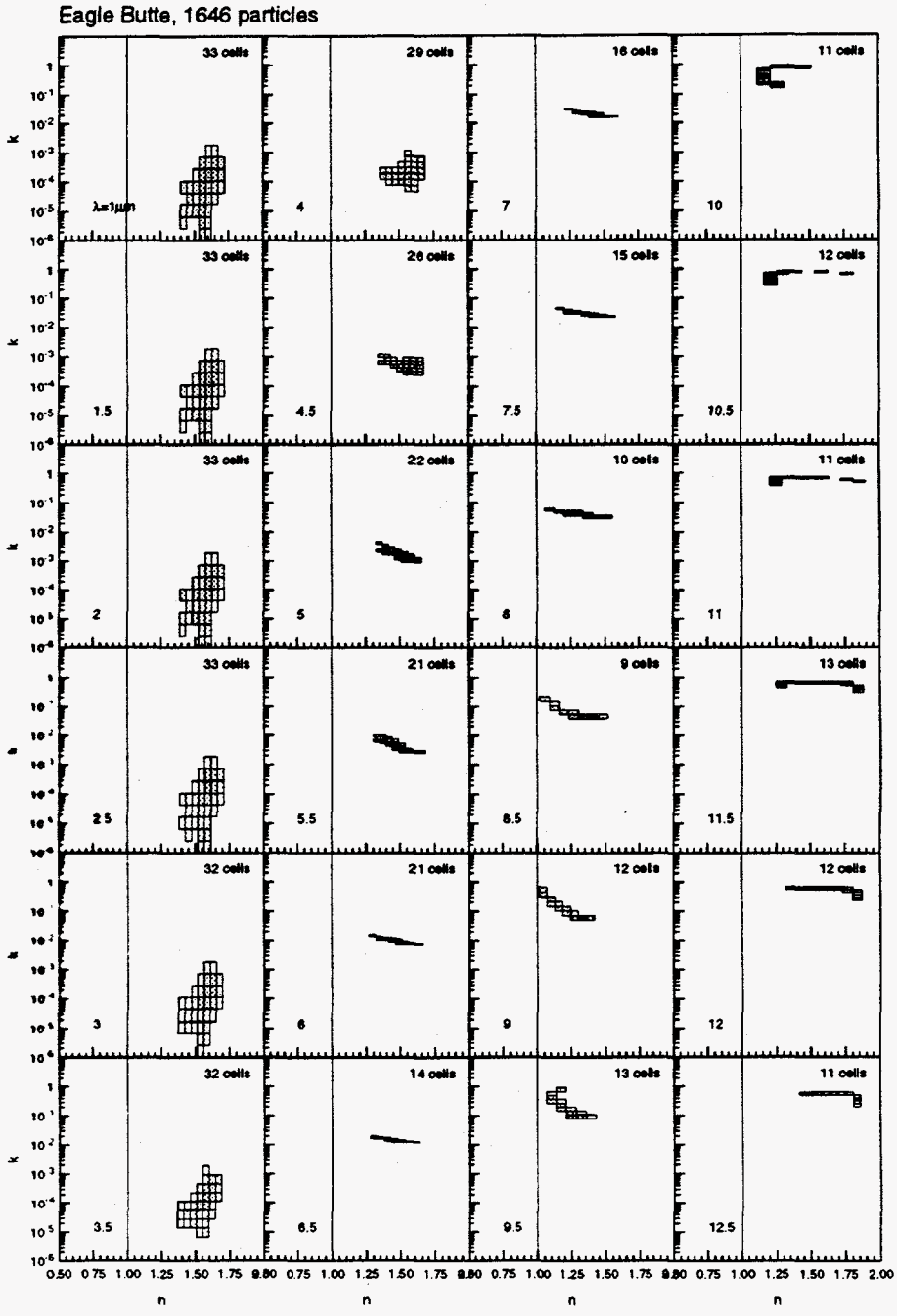

Figure V.19: Discretized classes of optical constants for the Eagle Butte fly ash at 24 discrete wavelengths.

a good model for the vast majority of ash particles because they are formed by rapid quenching of molten droplets. These assumptions allow one to use standard Mie scattering theory to compute the absorption and scattering characteristics of a single particle. Specifically, the absorption and scattering efficiencies, Q_a and Q_s, are computed along with the asymmetry parameter, g, which is the first moment of the scattering phase function.

V.4.1 The Size and Composition Averaged Properties

The procedure for computing the average scattering properties follows the analysis described in the previous sections. For a given ash the scattering properties are computed using Mie scattering codes (see Appendix D). The size distribution averaged quantities Q_a, Q_s, and g are computed at a single wavelength for a single optical constant class (n_i, k_i). Each class is assumed to have the same size distribution since, as shown by Ghosal [17], the changes in composition with particle size are generally small for the range of sizes and ash samples studied (approximately 1-10μm). Finally the composition averaged scattering properties are computed using the volume fraction of ash in each class ($C_{v,i}/C_v$) and the relations

$$Q_s(\lambda) = \sum_i \frac{C_{v,i}}{C_v} Q_{s,i}(\lambda), \qquad Q_a(\lambda) = \sum_i \frac{C_{v,i}}{C_v} Q_{a,i}(\lambda), \tag{V.35}$$

and

$$g(\lambda) = \sum_i \frac{C_{v,i}}{C_v} \frac{Q_{s,i}(\lambda)}{Q_s(\lambda)} g_i(\lambda) \tag{V.36}$$

Note that the asymmetry parameter, $g_i(\lambda)$ is defined as

$$g_i(\lambda) = \frac{1}{2} \int_{-1}^{1} \Phi_{\lambda,i}(\mu) d\mu \tag{V.37}$$

thus its average is computed by weighting with the scattering efficiency, as is done for $\Phi_\lambda(\mu)$.

The scattering properties were calculated using the best fit size distributions shown in Table V.3 for five ashes studied by Ghosal [17]. Note that the radiative properties of the sixth ash, San Miguel, were not computed here since it has a large fraction of non-solid particles or cenospheres [17]. While the composition distribution (and optical constants distribution) for the San Miguel ash is typical of most fly

Table V.3: Parameters of best fit log-normal distributions to data for five ashes studied by Ghosal, 1993

Fly Ash	$\overline{D_0}$, μm	$\overline{D_3}$, μm	D_{32}, μm	σ_g
Beulah	0.355	12.69	6.991	2.98
Eagle Butte	0.594	14.28	8.405	2.80
Illinois #6	0.376	10.10	5.836	2.85
Kentucky #9	1.21	10.36	7.244	2.33
Upper Freeport	0.424	9.34	5.579	2.76

ashes, the size distribution is exceptionally large (e.g., $\overline{D_3} \simeq 32\mu$m) because of these non-solid particles.

The results of the size and composition-averaged Mie scattering calculations for each of the actual size distributions are shown in Fig. V.20. Starting at the bottom, the absorption efficiency for all five ashes is less than approximately 0.03 at $\lambda = 1\mu$m, and decreases with increasing wavelength until it begins to rapidly increase near 4 μm as k increases. In this wavelength range, $1 \leq \lambda \leq 4$ μm, the absorption efficiency depends primarily on the Fe_2O_3 content of the ash, with the higher iron Illinois #6 and Eagle Butte ashes having higher absorption. The decrease in Q_a with increasing wavelength is primarily attributable to the decrease in the particle size parameter, $x = \pi D/\lambda$, with increasing wavelength. As was discussed previously, when x is very small Q_a is proportional to x. If the incident flux (power per unit area) is q, then the power absorbed by the particle is $qQ_a\pi D^2$. When Q_a is proportional to x the absorbed power is proportional to the volume of the particle. This limit is extended to somewhat larger particles provided xk is very small so that the particle remains weakly absorbing, but eventually the absorption efficiency will approach a constant and the power absorbed by the particle will become proportional to the surface area. In this limit the incident radiation is significantly attenuated near the surface and does not penetrate the entire volume of the particle† .

At wavelengths longer than 4 μm the absorption efficiencies of the three bituminous ashes (Upper Freeport, Kentucky #9, and Illinois #6) are very similar. The lower SiO_2 ashes, Eagle Butte and Beulah, show the expected shift in the maximum

† It should also be pointed out that Q_a for a particle is a generally monotonic function of x [18]. There are surface modes and resonances that cause "spikes" in Q_a over narrow ranges of x, but the overall trends are as described here. Many of these variations in Q_a are reduced or eliminated when one averages over a distribution of particle sizes.

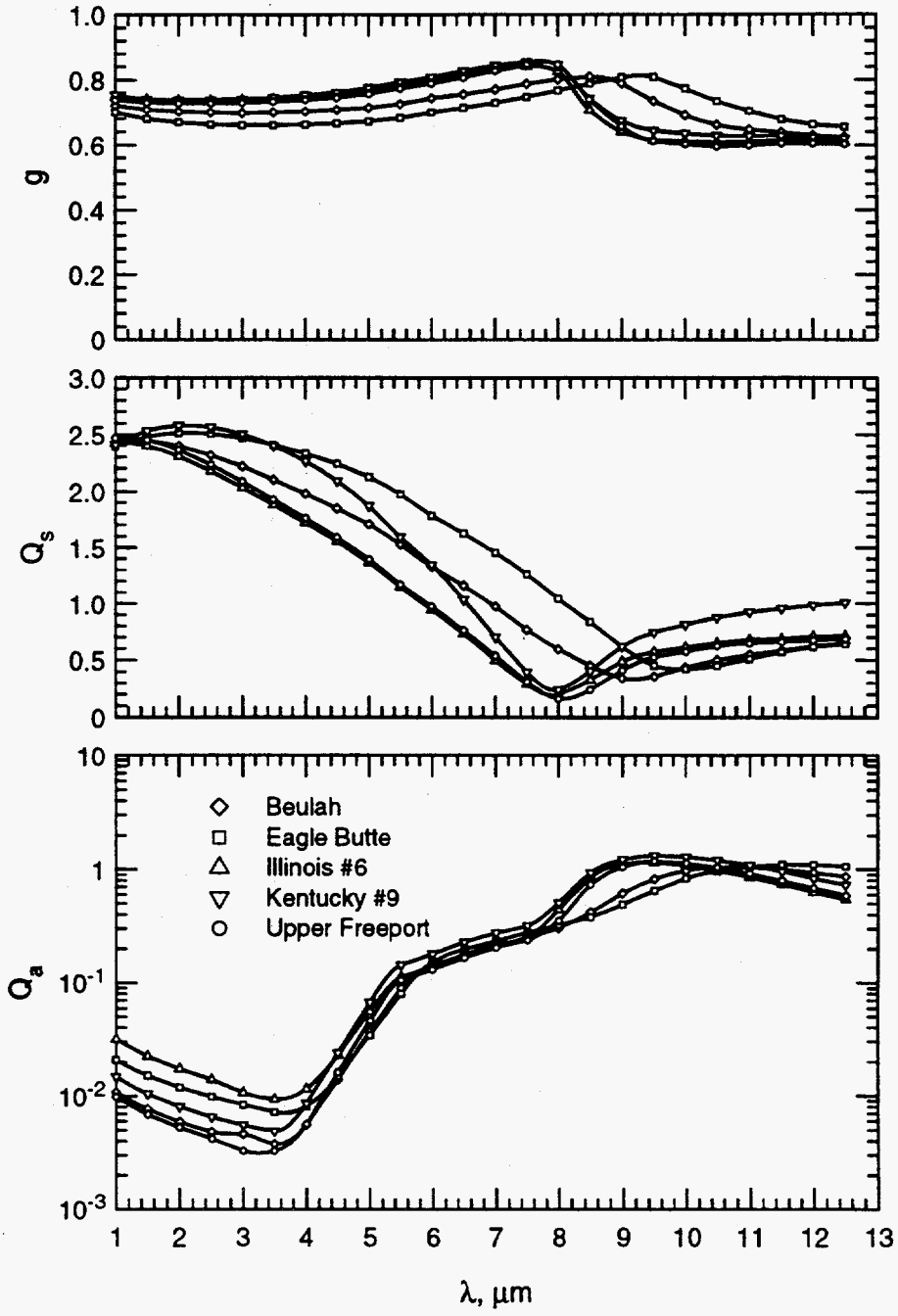

Figure V.20: Size and composition averaged scattering properties for five fly ashes.

of Q_a to longer wavelengths. In all cases the maximum Q_a is near unity, indicating that the ash particles absorb essentially all incident radiation.

The scattering efficiencies for the five ashes are also shown in Fig. V.20. The scattering efficiencies of all ashes is approximately 2.5 at $\lambda = 1$ μm (for which $x \gg 1$) and have minima near 8-10 μm – the exact wavelength of the minimum Q_s increases for the low SiO_2 ashes due to the shift of minimum n to longer wavelengths. The scattering efficiency of the Upper Freeport ash is almost identical to that of the Illinois #6 ash. Compared to these two bituminous ashes, the lower SiO_2 ashes, Eagle Butte and Beulah, have a higher Q_s at wavelengths below their minimum Q_s, and a somewhat lower Q_s at longer wavelengths. The Kentucky #9 ash has a higher Q_s than the Upper Freeport ash at all wavelengths shown here, despite their similar compositions and optical constants. This difference is attributable to differences in their size distributions. While both ashes have comparable volume median diameters ($\overline{D_3} \simeq 9.34$ for Upper Freeport and $\overline{D_3} \simeq 10.36$ for Kentucky #9), the Upper Freeport ash has a significantly broader distribution of particle sizes ($\sigma_g \simeq 2.76$, compared to 2.33 for Kentucky #9). As a result many more of the particles in the Upper Freeport ash are very small, and as a result, scatter less. Note also that these efficiencies (Q_a and Q_s) contain no dependence on loading. When we say here that the Kentucky #9 ash scatters more than the Upper Freeport ash, we are comparing scattered power per unit of particle surface area. Since the surface area for a dispersion of ash depends on the loading and size distribution, the scattering per unit mass may be significantly different. These effects will be described further below.

The top plot in Fig. V.20 shows the asymmetry parameter for the five ashes. For all ashes g lies approximately in the range $0.6 \leq g \leq 0.8$, but there are ash-to-ash variations. Note that $g = 1$ corresponds to pure forward scattering, while $g = 0$ corresponds to isotropic scattering. Here $g \simeq 0.7$ indicates that significantly more of the scattered power is in the forward direction than is in the backward direction. Although not explicitly illustrated here, a significant fraction of the scattering is in a relatively narrow forward lobe (due to diffraction), with the remainder being somewhat more isotropically distributed.

Table V.4: Log-Normal size distribution parameters.

Size	$\overline{D_0}$, μm	$\overline{D_3}$, μm	D_{32}, μm	σ_g
A	0.30	10.79	5.945	2.98
B	1.00	11.37	7.582	2.46
C	4.00	15.91	12.64	1.97

V.4.2 The Effects of Size Distribution on Average Properties

The effects of the size distribution parameters for constant composition distribution were studied using the three log-normal size distributions given in Table V.4. The size distributions (designated A, B, and C) were chosen to span the ranges of $\overline{D_0}$, $\overline{D_3}$, and D_{32}, measured by Ghosal [17]. The effects of the size distribution on the scattering properties are shown in Fig. V.21, Fig. V.22, and Fig. V.23 for the composition distributions of the Upper Freeport, Kentucky #9, and Eagle Butte ashes, respectively. Note that g, Q_s, and Q_a are dependent only on the optical constants and size distribution. The effect of ash loading becomes important when one computes the radiative properties for a dispersion of ash in a medium (e.g., see Eq. (V.23) and Eq. (V.24)), and is discussed in Chapter VI. In addition to size distributions A, B, and C, each figure also contains a distribution D, which is the actual size distribution for each particular ash composition distribution. For example, in Fig. V.21 size distribution D is that of actual Upper Freeport ash, as determined by Ghosal [17].

For all three ash composition distributions (Fig. V.21-V.23) the increase in D_{32} from distribution A to distribution C causes an increase in the absorption efficiency, although a less pronounced increase occurs near the peak of the SiO_2 absorption band. This result can be explained, qualitatively, as a pathlength effect, as was described above to explain the decrease in Q_a with wavelength in the $1 < \lambda < 4\mu$m range. If a particle is weakly absorbing ($kx = k\pi D/\lambda \ll 1$) the absorbed power is proportional to the volume of the particle. On the other hand, if the particle is strongly absorbing then absorption takes place near the surface of the particle and is proportional to the area of the particle. Thus the absorption efficiency (absorbed power/power incident on particle area) should be proportional to the diameter for weakly absorbing particles and independent of diameter for strongly absorbing particles. Realistic ash distributions contain weakly absorbing particles, strongly absorbing particles,

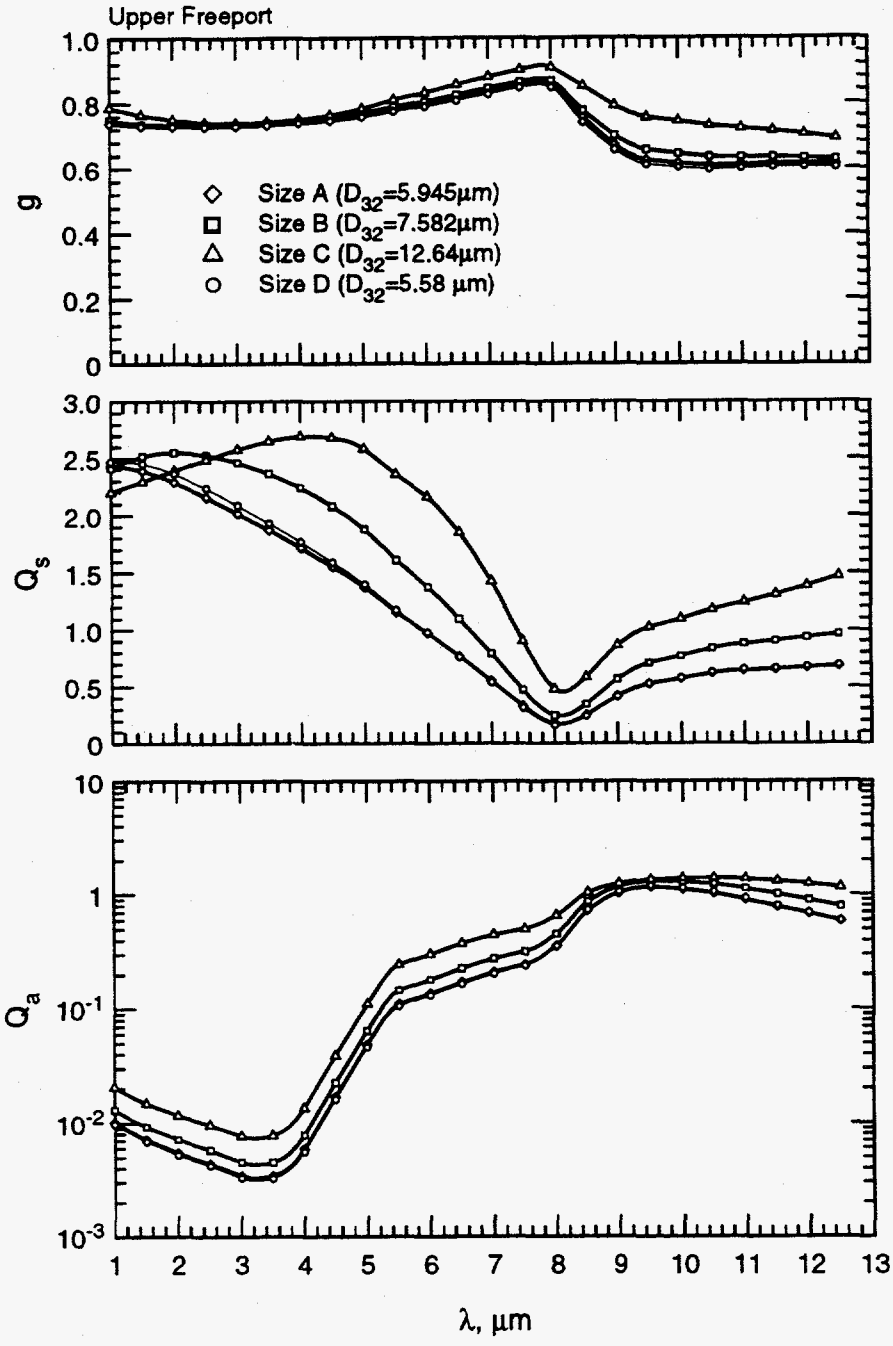

Figure V.21: The effect of size distribution on the scattering properties of the Upper Freeport fly ash.

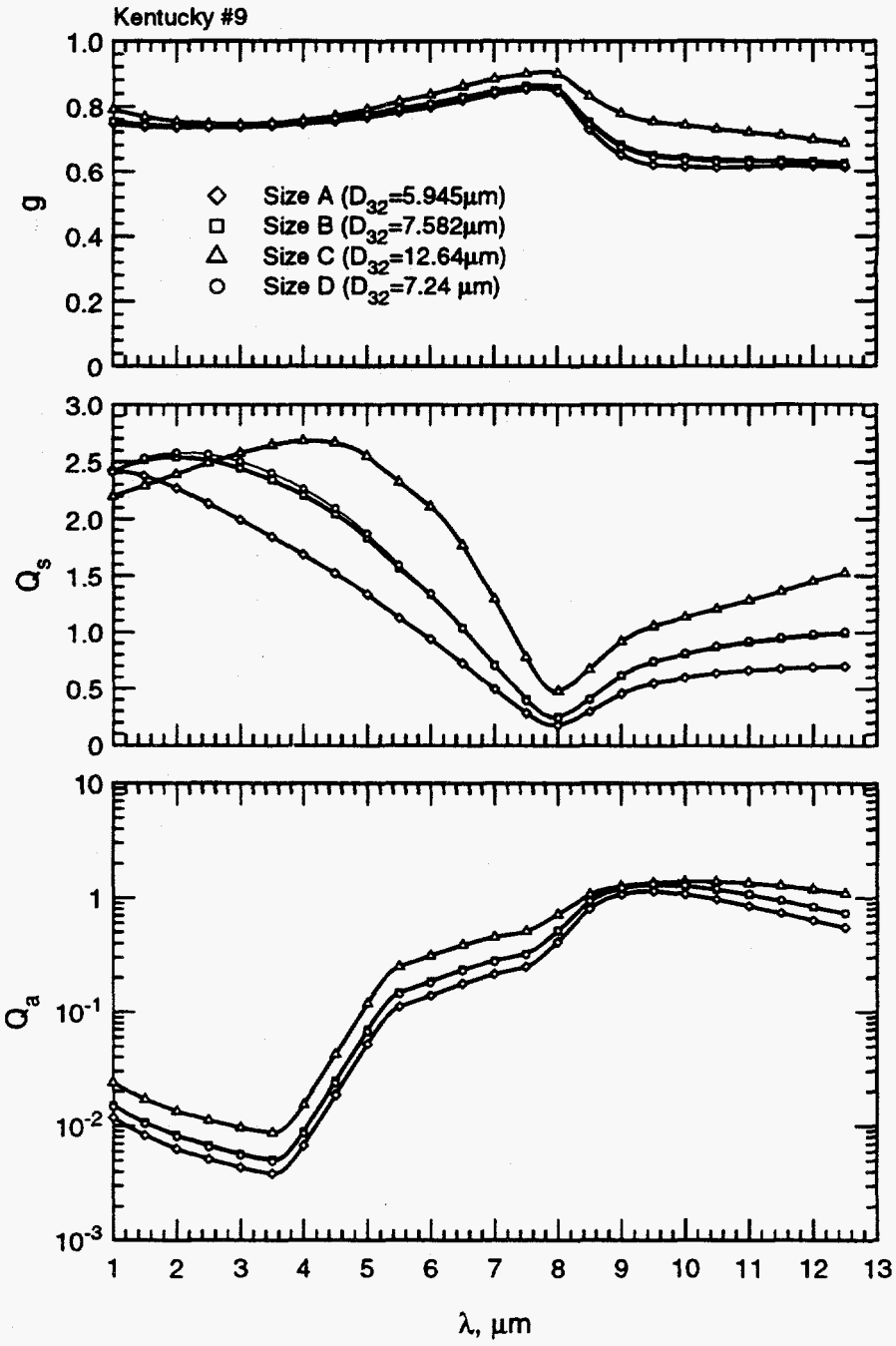

Figure V.22: The effect of size distribution on the scattering properties of the Kentucky #9 fly ash.

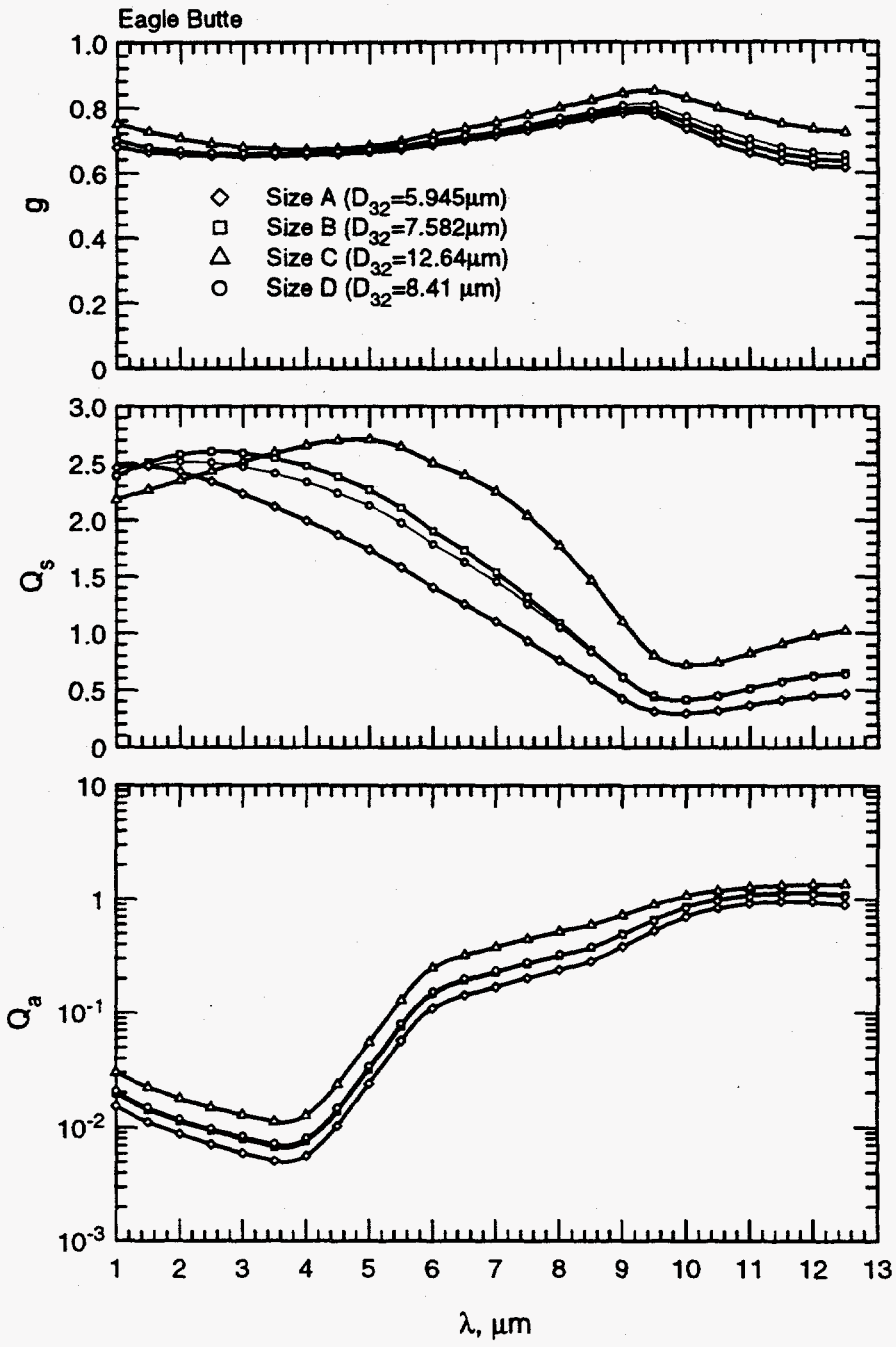

Figure V.23: The effect of size distribution on the scattering properties of the Eagle Butte fly ash.

and many between these limits, nevertheless, the majority are weakly absorbing for $\lambda < 8$ μm and strongly absorbing at longer wavelengths. Based on this discussion, one should be able to discriminate between volumetric absorption and surface absorption by normalizing Q_a with a measure of the particle size, for example D_{32}.

Figure V.24 shows a plot of Q_a/D_{32} for the Upper Freeport ash. Similar results are obtained for other ashes. The ratio Q_s/D_{32} is independent of the size distribution except at long wavelengths where absorption is strong, which is consistent with the pathlength effect described above. It is important to note that the absorption *coefficient* for a dispersion of ash is proportional to $\alpha_\lambda \propto C_v Q_a/D_{32}$. The volume fraction C_v is approximately constant for a given mass loading of ash; thus, the absorption coefficient for fly ash is insensitive to size distribution at wavelengths shorter than approximately 8 μm, and decreases with increasing particle size at longer wavelengths.

In the wavelength range from 1-8 μm, or in the case of Eagle Butte, 1-10 μm, increasing D_{32} from distribution A to distribution C causes an increase in the scattering efficiency over most of that wavelength range (e.g., see Fig. V.21-V.23). However, the scattering *coefficient*, which is proportional to Q_s/D_{32}, does not generally increase with increasing D_{32}. For example,Fig. V.25 shows the quantity Q_s/D_{32} for the Upper Freeport ash. The scattering coefficient ($\sigma_\lambda \propto Q_s/D_{32}$) decreases with increasing D_{32} at shorter wavelengths because Q_s is approximately constant. By contrast, Q_s/D_{32} is approximately independent of the ash size distribution in the wavelength range from $6 < \lambda < 12$ μm. It is significant to note that at shorter wavelengths the particle size parameter $x = \pi D/\lambda$ for most particles is relatively large. In this limit the scattering efficiency approaches a constant ($Q_s \rightarrow 2$). This is consistent with the results near $\lambda = 1\mu$m where most ashes show $Q_s \simeq 2.5$ independent of the size of the distribution. At longer wavelengths these results tend to suggest that the scattered power is proportional to the volume of the particle, although this is rather approximate.

V.4.3 The Effects of Composition on Average Properties

The effect of composition on the size and composition distribution averaged absorption and scattering properties is studied by comparing results for fixed size distributions (A, B, and C) but varying composition distributions. Figures V.26–V.28 show the effects of changing only the composition. In Fig. V.26 five curves are

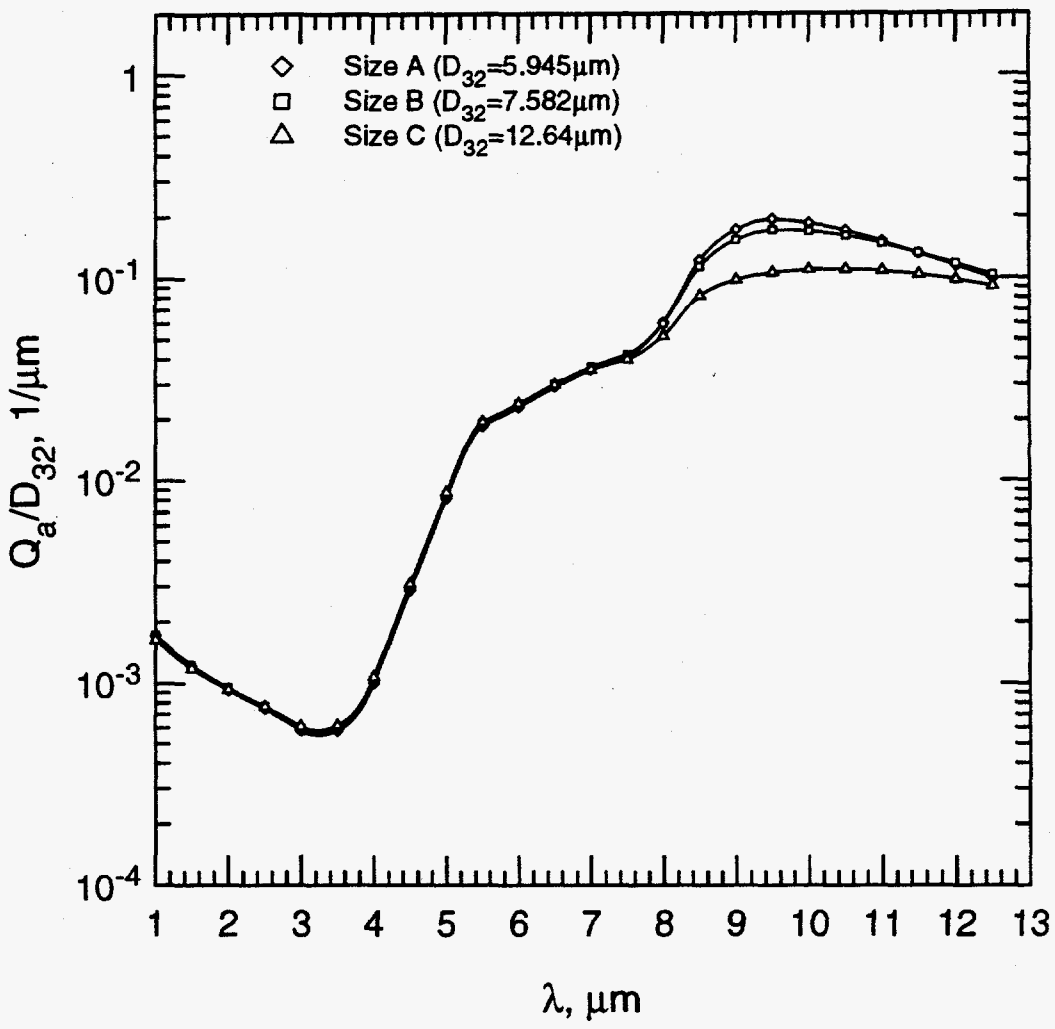

Figure V.24: Absorption efficiency of Upper Freeport ash normalized by D_{32}.

shown where the composition distributions appropriate to the five ashes are used but each with size distribution A. Figures V.27 and V.28 show similar results for size distributions B and C, respectively.

These results confirm that the differences between the scattering efficiencies of Upper Freeport, Illinois #6, and Kentucky #9 ash are primarily due to differences in their size distribution. Apart from the difference in absorption in the 1–4 μm range attributable to differences in Fe_2O_3 content, these three ashes from bituminous coals have very similar radiative properties when their size distributions are the same. The

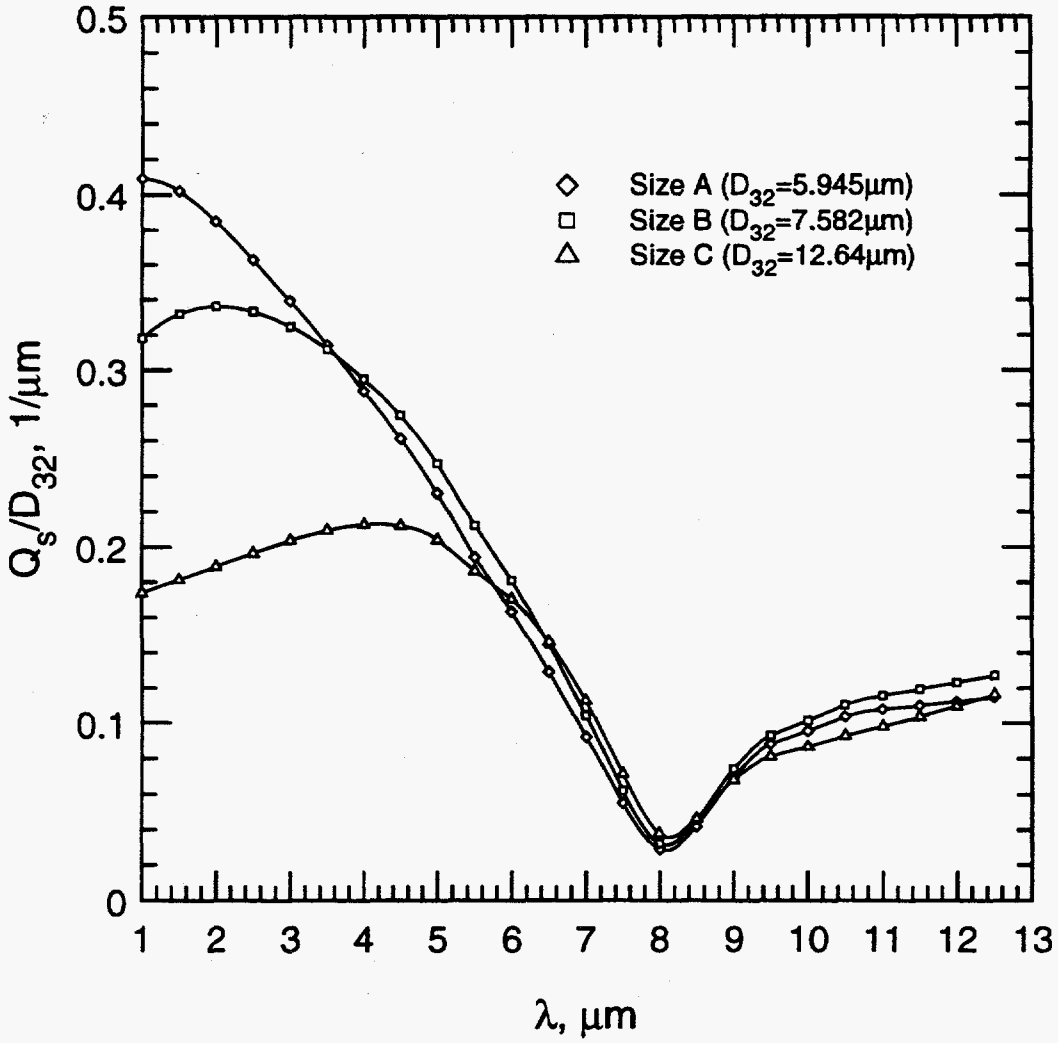

Figure V.25: Scattering efficiency of Upper Freeport ash normalized by D_{32}.

radiative properties of the Eagle Butte and Beulah ashes differ from these three ashes primarily due to their low SiO_2 content.

V.4.4 The Effects of Particle-to-Particle Composition Variations

In all the previous calculations the full composition distribution functions were used, thus accounting for particle-to-particle composition variations. Size integrated Mie scattering calculations were made for many different optical constants classes

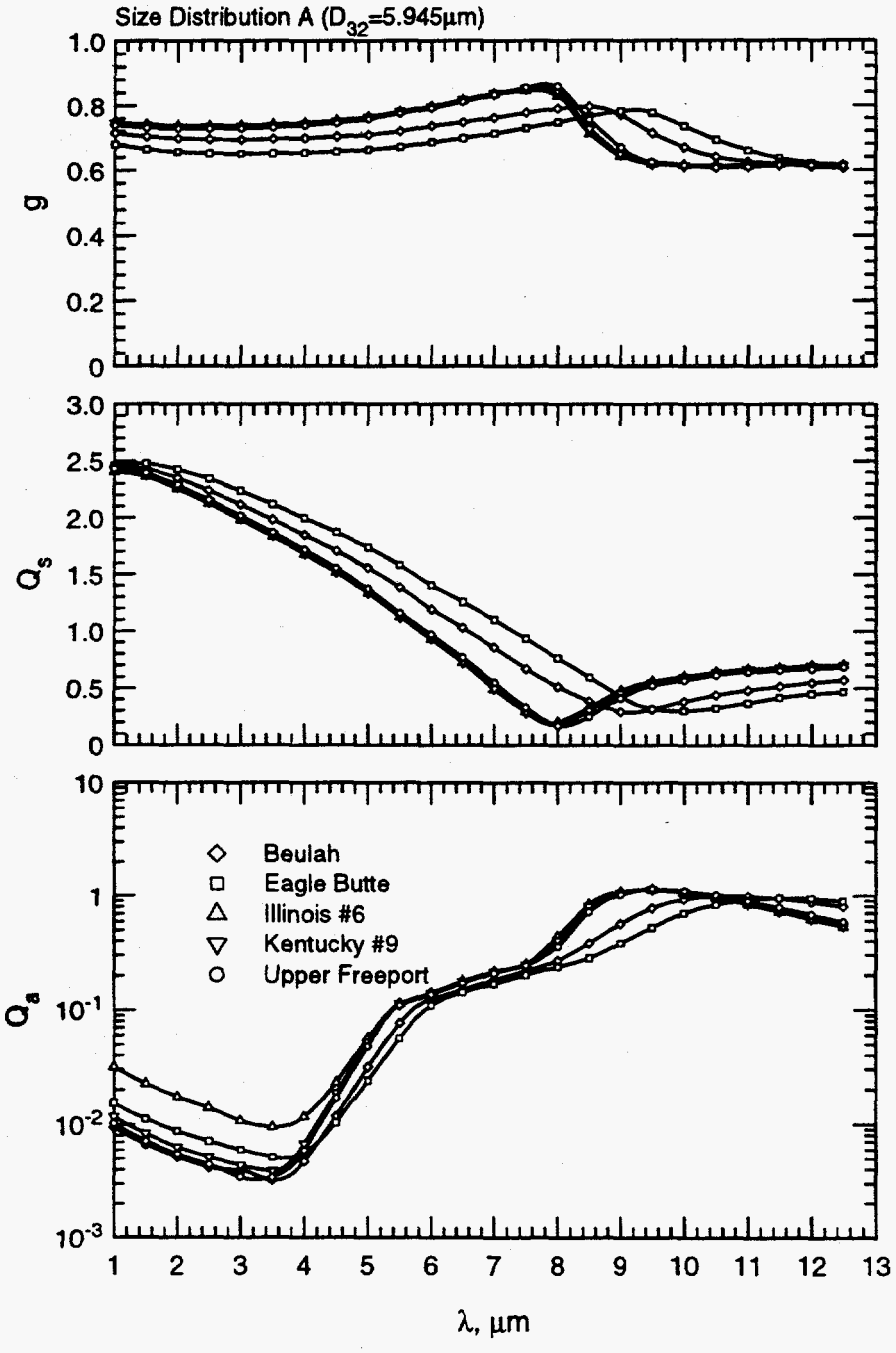

Figure V.26: The scattering properties of dispersions of different ash compositions, but all having size distribution A.

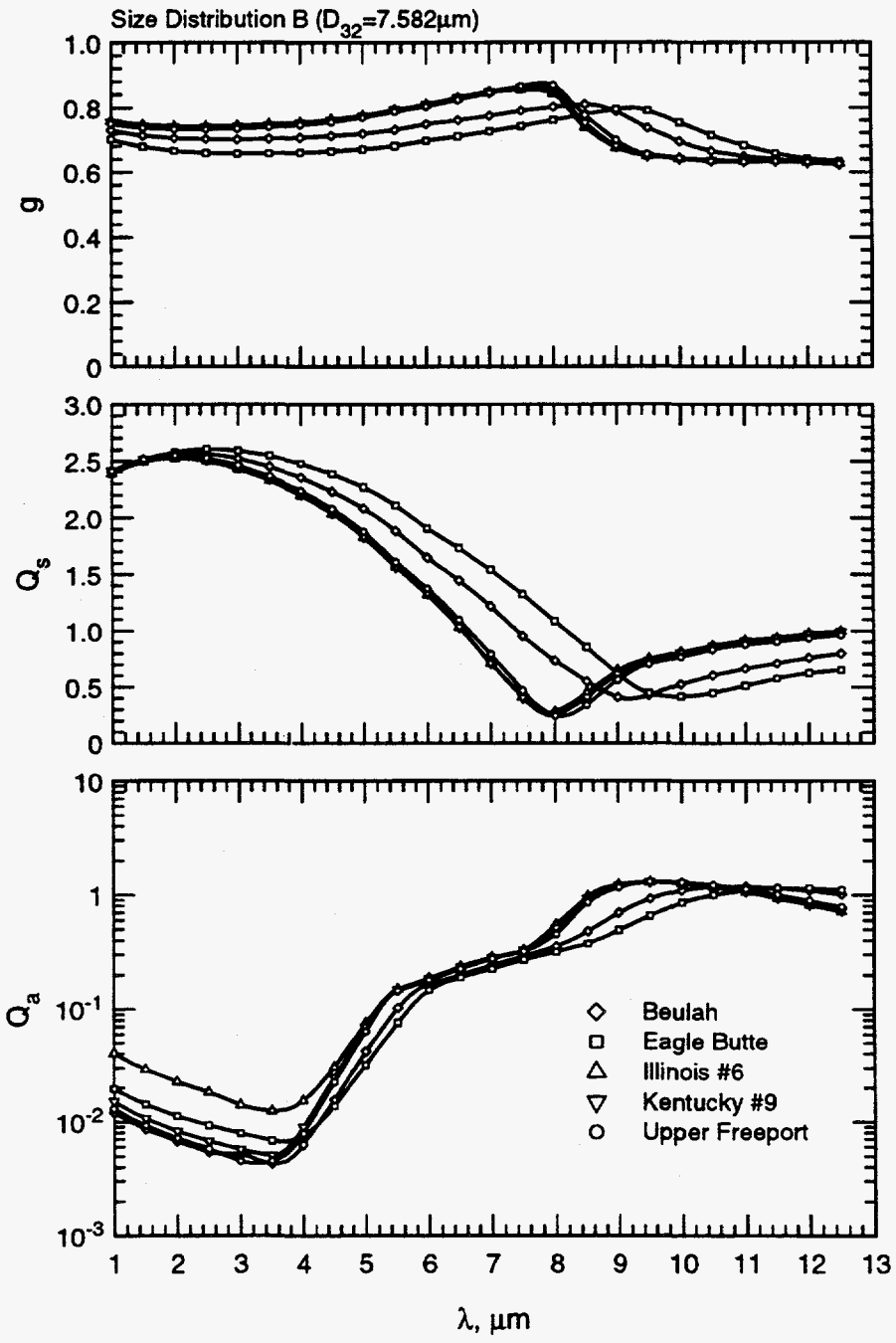

Figure V.27: The scattering properties of dispersions of different ash compositions, but all having size distribution B.

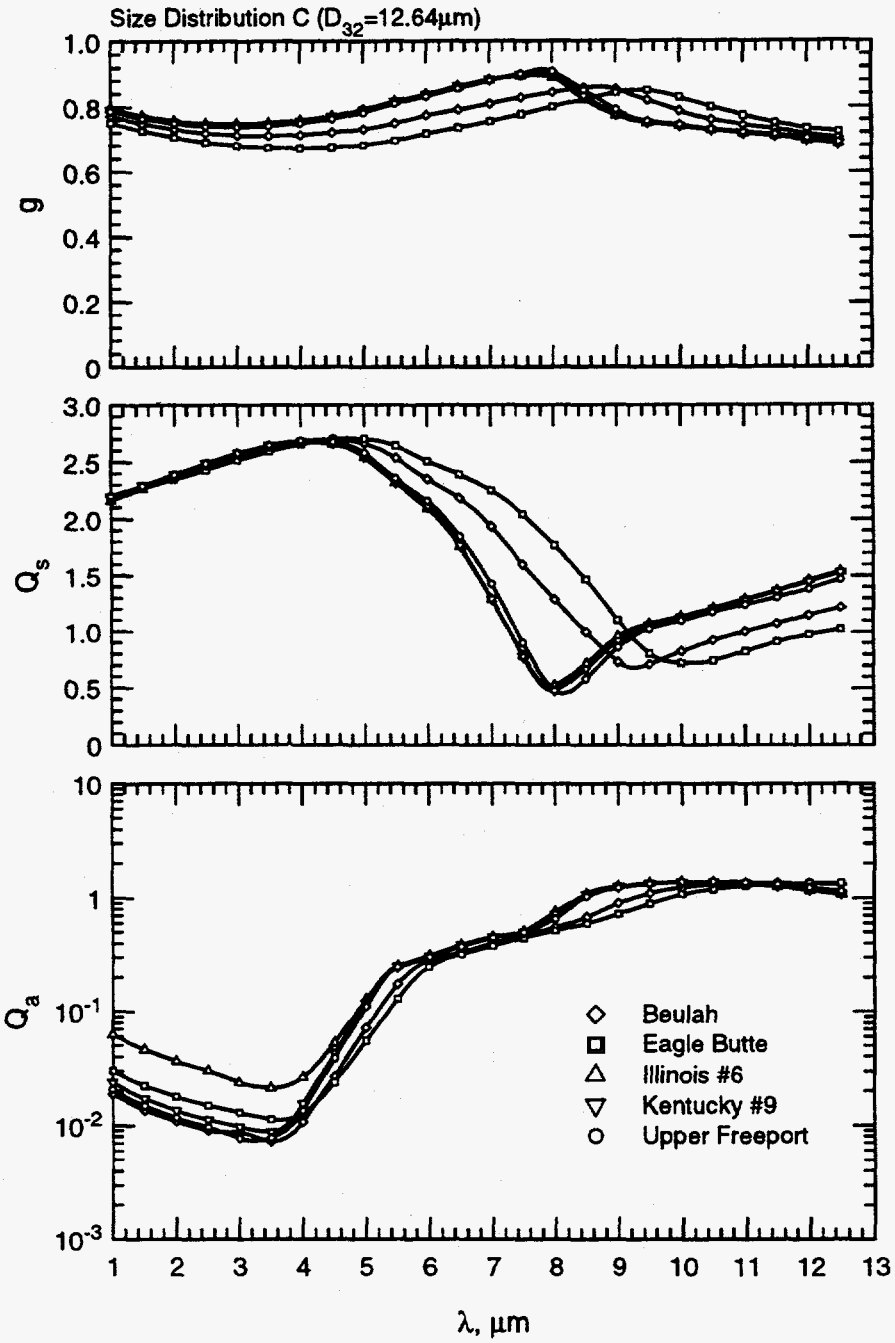

Figure V.28: The scattering properties of dispersions of different ash compositions, but all having size distribution C.

at each wavelength – a rather time-consuming computation. In general the average scattering properties of a dispersion with a distribution of compositions does not equal the scattering properties computed using the average of the distribution of compositions. In this section the error of using an average ash composition is evaluated.

It has been shown that at many wavelengths, particularly $\lambda < 4$ μm and $\lambda > 8$ μm, there is significant breadth in the distribution of optical constants. Large particle-to-particle variations in n and k are observed. To understand the effect of this composition distribution, radiative properties were computed using the single composition class defined by the average composition shown in Table V.2. This average composition is not exactly the same as the average composition of the whole ash, but, instead, is computed from the collection of particles which pass all the criteria recommended for the optical constants correlations in Chapter IV.

The comparison between the scattering properties of Upper Freeport ash allowing for particle-to-particle composition variations and an ash in which every particle has the *average* composition is shown in Fig. V.29. The agreement is quite close at all wavelengths. As shown in Fig. V.30, this close agreement is maintained for the larger size C distribution. These results are very encouraging, since they justify using the measured average composition of the ash to compute, to close approximation, the radiative properties of a polydispersion of composition (at least for fly ashes similar to those studied here).

To further investigate this matter, the effect of higher Fe_2O_3 content is illustrated by comparing the radiative properties of Illinois #6 ash with one of average composition (see Fig. V.31). Again, the agreement is quite close, but using the average composition tends to underpredict Q_a in the 1-4 μm range. An ash where some particles have higher iron content will have higher absorption efficiency than an ash where the iron content is dispersed uniformly among the particles. This seems to be particularly significant when the Fe_2O_3 content is high, as in Illinois #6. It should be noted, however, that this result depends significantly on the form of the correlation developed for k in the 1-4 μm region. Recall that it was assumed that a significant fraction of the total absorption by Fe_2O_3 in the slag was due to intervalence charge transfer; thus there would be a second order dependence of k on the iron content ($k \sim x^2_{Fe_2O_3}$). This dependence implies that a dispersion in which a few particles have higher iron content and the remainder have low iron content will absorb more

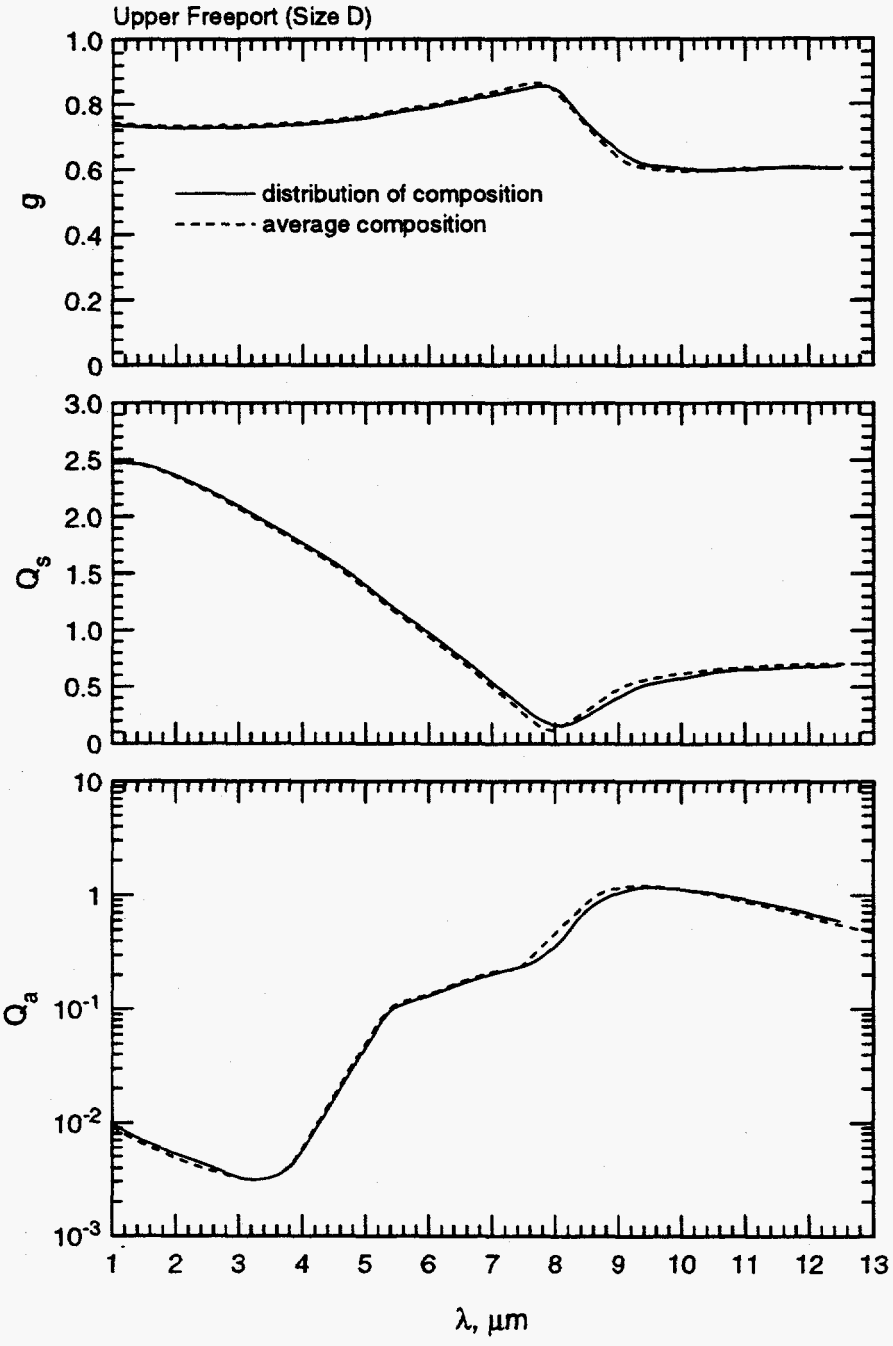

Figure V.29: Comparison between scattering properties of Upper Freeport ash and an ash in which every particle has the average composition.

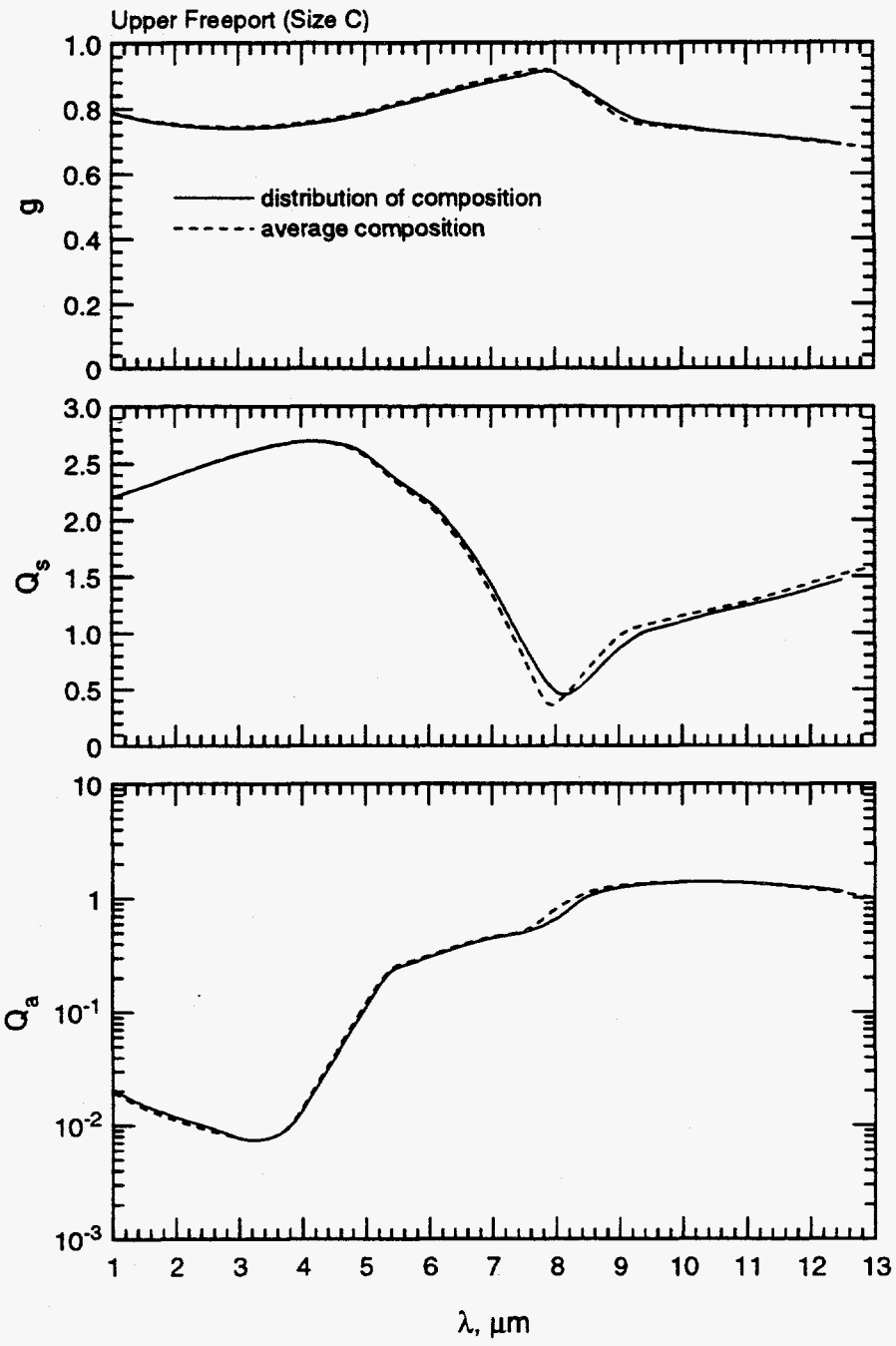

Figure V.30: Comparison between scattering properties of Upper Freeport ash with size distribution C and an ash in which every particle has the average composition.

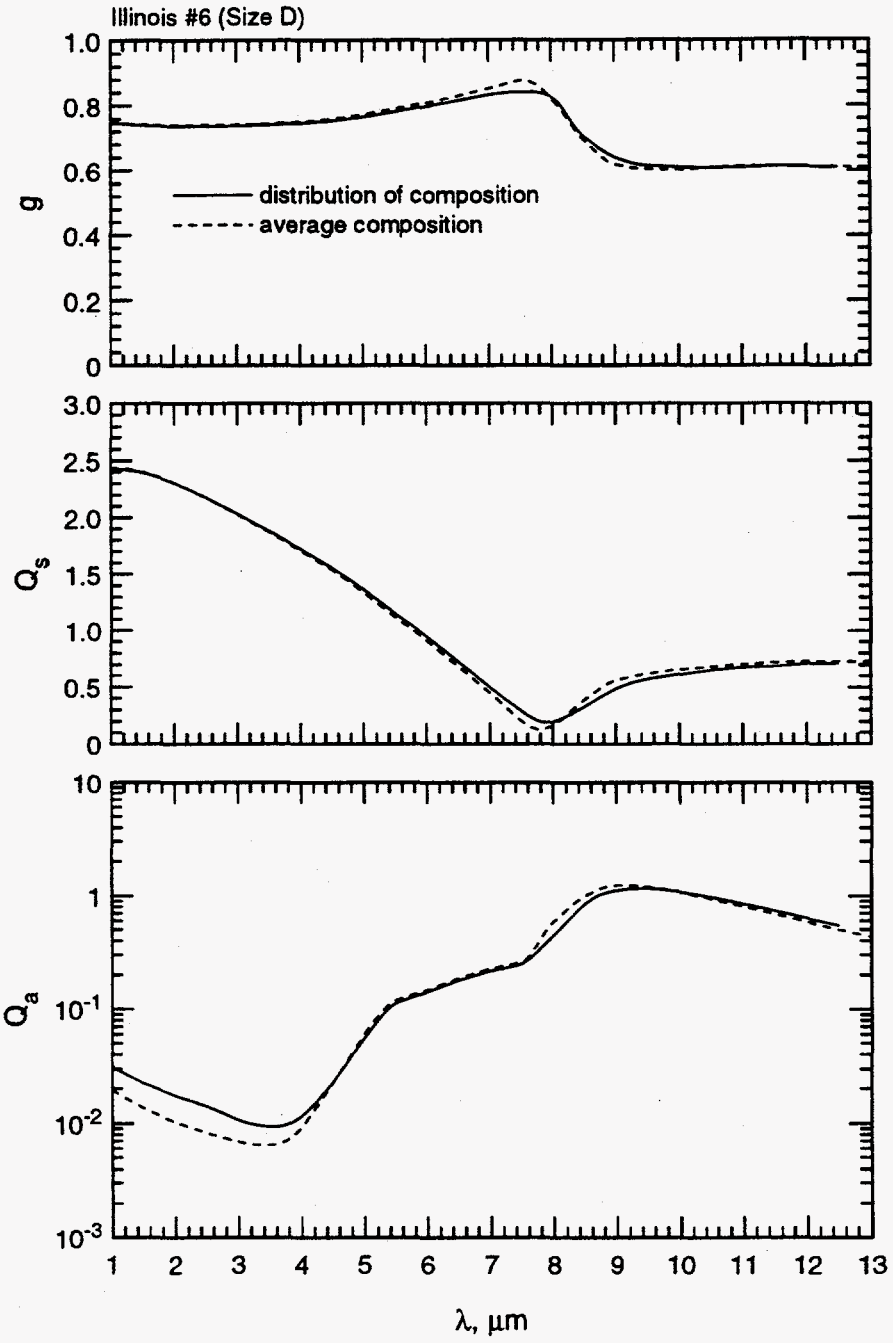

Figure V.31: Comparison between scattering properties of Illinois #6 ash and an ash in which every particle has the average composition.

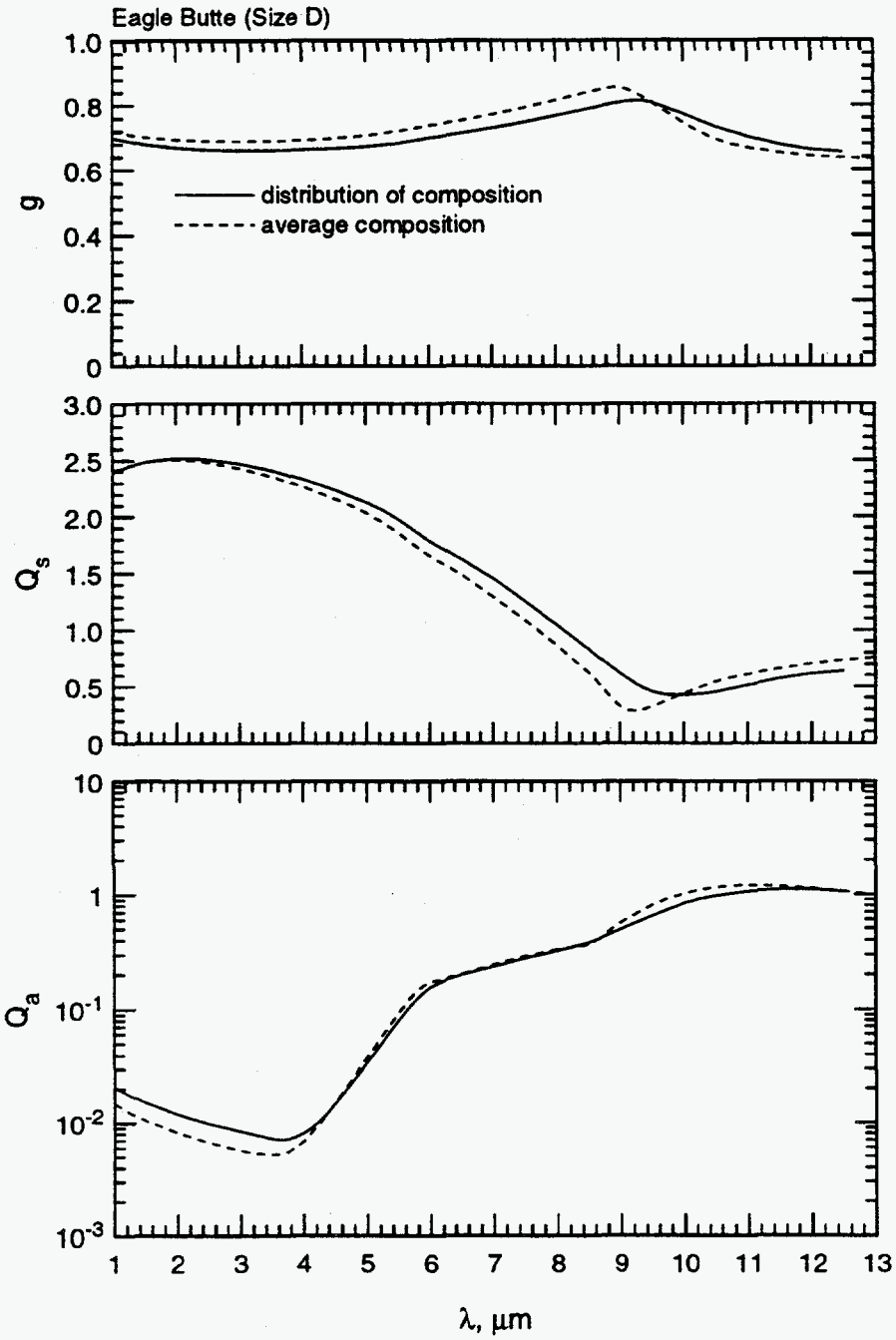

Figure V.32: Comparison between scattering properties of Eagle Butte ash and an ash in which every particle has the average composition.

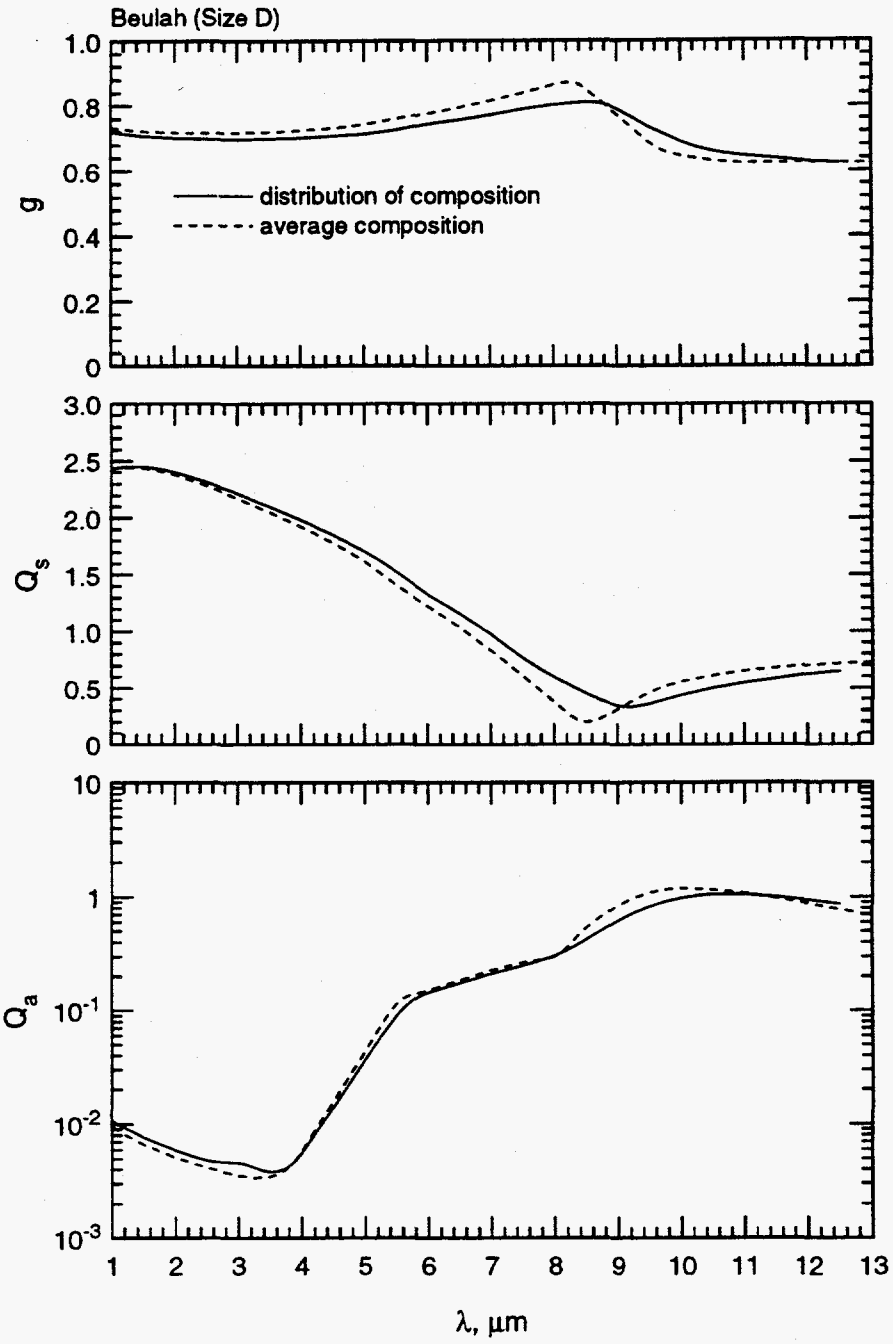

Figure V.33: Comparison between scattering properties of Beulah ash and an ash in which every particle has the average composition.

than a dispersion with the same overall Fe_2O_3 content distributed uniformly throughout. Ashes formed in reducing environments may have less absorption by intervalence charge transfer; thus the second order dependence of k on $x_{Fe_2O_3}$ may be reduced. This decreased second order dependence would lessen the errors associated with using an average composition.

Finally, the Upper Freeport ash has been shown to have a rather narrow composition distribution, while the Eagle Butte and Beulah ashes have much broader distributions. Thus the effect of using the average composition to compute radiative properties should produce the largest errors for the latter two ashes. As shown in Fig. V.32 and Fig. V.33, the errors introduced by assuming average composition are somewhat larger for these two ashes. Eagle Butte is a higher iron ash, hence using the average composition underpredicts Q_a in the 1-4 μm range as it did for the Illinois #6 ash. For both the Eagle Butte and Beulah ashes, the largest error in the scattering efficiencies occurs near its minimum, as expected. The minimum Q_s occurs at wavelengths where $n-1$ is small and is therefore sensitive to composition. A similar result was observed by Ghosal [17] in transmittance measurements of ashes in infrared transparent liquids.

Chapter VI.

Effect of Fly Ash on Radiative Heat Transfer

In this chapter the effect of fly ash on radiation heat transfer through a planar layer of hot CO_2 and H_2O is studied. There have been several studies of the effect of fly ash on radiation heat transfer in coal combustors [5,6,7,8,9,10,37-38] including work on radiative transfer in coal-fired MHD radiant boilers [39]. In the following sections the radiative properties derived in the previous chapter are used to estimate the effect of fly ash on radiative transfer through a planar layer of ash dispersed in infrared active combustion product gases (CO_2 and H_2O).

VI.1 The Radiative Transport Equation for a Planar Layer

The radiation transfer through a planar layer is governed by Eq. (V.1). If the radiation intensity is independent of azimuth then we can write Eq. (V.1) in the form [35]

$$\mu \frac{dI_\lambda(x,\mu)}{dx} + \beta_\lambda I_\lambda(x,\mu) = \alpha_\lambda I_{b\lambda}[T(x)] + \frac{\sigma_\lambda}{2}\int_{-1}^{1} I_\lambda(x,\mu')\Phi_\lambda(\mu,\mu')d\mu' \qquad (VI.1)$$

Here μ is the cosine of the angle of a ray with the normal to the layer, and x is the distance along the normal to the layer.

The scattering phase function for fly ash dispersions (and for most real scattering media) is not isotropic. Instead, it typically has a rather pronounced forward scattering lobe. A good approximation to the scattering phase function is constructed by assuming that the phase function consists of a delta function in the forward direction plus other angular contributions. For example, the scattering phase function can be expanded in a series of the form

$$\Phi_\lambda(\mu) = \sum_{i=0}^{\infty} A_i P_i(\mu) \qquad (VI.2)$$

where $P_i(\mu)$ are Legendre polynomials and A_i are the Legendre coefficients. The constants A_i can be computed using Mie theory as discussed in Appendix D. Extracting

a delta function in the forward direction and truncating the series after N terms produces [40]

$$\Phi_\lambda(\mu) = 2f\delta(1-\mu) + (1-f)\sum_{i=0}^{N} B_i P_i(\mu) \qquad (VI.3)$$

The constants f and B_i are related to the Legendre coefficients, A_i, by the relations

$$f = \frac{A_{N+1}}{2N+3} \quad \text{and} \quad B_i = \frac{A_i - (2i+1)f}{1-f} \qquad (VI.4)$$

The advantages of this approximation (which is exact when $N \rightarrow \infty$) are 1) it requires many fewer terms to produce a given accuracy and 2) it uses the Legendre coefficients which are readily computed from Mie scattering codes.

The accuracy of this $\delta - P_n$ approximation (Eq. (VI.3)) was evaluated by Gupta [8] for $N = 0$ and found to accurately model the hemispherical fluxes (to within two percent). If $N = 0$ then $f = A_1/3$, which is the asymmetry parameter g. The scattering phase function then becomes

$$\Phi_\lambda(\mu) \simeq (1-g) + 2g\delta(1-\mu) \qquad (VI.5)$$

This approximation is particularly convenient since the resulting scattering integral is independent of direction, μ. By substituting Eq. (VI.5) into the radiative transport equation and replacing the scattering coefficient with the effective scattering coefficient,

$$\sigma_{\lambda,\text{eff}} = (1-g)\sigma_\lambda, \qquad (VI.6)$$

the resulting equation has the form of the simpler radiative transport equation for a medium with isotropic scattering.

The largest errors introduced by this approximation are in the reflected and directional quantities at the layer boundaries. However, the errors are tolerable given the considerable simplification introduced by this approximation (See Appendix E for details of the errors introduced by this approximation).

In subsequent sections the scattering coefficient, σ_λ, will refer to the *effective* scattering coefficient defined by Eq. (VI.6) unless otherwise stated.

The scattering coefficient, σ_λ, and absorption coefficient, α_λ, for a dispersion of ash are

$$\sigma_\lambda = \frac{3}{2} C_v \frac{Q_s}{D_{32}} \qquad \text{and} \qquad \alpha_\lambda = \frac{3}{2} C_v \frac{Q_a}{D_{32}} \qquad (VI.7)$$

as discussed in Section V.1. The scattering and absorption efficiencies, Q_s and Q_a are averaged over composition and size as described previously. Since the Sauter mean diameter, D_{32} is known for a given size distribution (see Eq. (V.34)) the only remaining unknown is the volume fraction, C_v, of ash in the gaseous dispersion.

VI.2 Ash Loading in Pulverized Coal Combustors

In this section the ultimate (after complete combustion) value of the ash volume fraction, C_v, is estimated as a function of the mass fraction of incombustible mineral matter in the coal before combustion. Composition analyses are presented for a number of U.S. coals in Table VI.1. Unfortunately, ash mass fractions were not available for the ashes studied by Ghosal.

The ash loading in a coal combustor is dependent on a number of factors including the mineral content of the original coal, the fuel bound oxygen content, and the amount of excess air for combustion. Also, since the density of the gaseous products is proportional to the ratio of pressure to temperature, P/T, the average ash volume fraction is also proportional to P/T.

The partial pressures of CO_2, H_2O, and CO in the combustion products are also dependent on the original coal composition, and to a lesser extent on pressure and temperature through chemical equilibrium considerations.

For purposes of determining approximate average values of the ultimate ash volume fraction, C_v, and of the H_2O and CO_2 partial pressures in typical coal combustion products, the coal combustion reaction is assumed to be

$$(n_C C + n_H H + n_O O) + n_{air} f O_2 + n_{air}(1-f)N_2 \rightarrow n_{CO_2} CO_2 + n_{H_2O} H_2O + n_{air}(1-f)N_2 \qquad (VI.8)$$

where n_i is the number of moles of species i and f is the volume fraction of oxygen in the "air", typically 0.21. The elemental composition of coal varies somewhat with rank and seam, but is primarily carbon, hydrogen, oxygen, and ash (all the inert minerals in coal). Elemental analyses [41] of several coals is presented in Table VI.1. For purposes of establishing ash loading the sulfur content of the coal is ignored and the coal is assumed to be dry. The ash content varies from 5 to 20 percent for the coals listed. Also, since high levels of fuel bound oxygen decreases the air demand, the ash volume fraction may be slightly higher for coals with more oxygen.

Table VI.1: Coal composition analyses for several U.S. coals (Argonne premium coal samples)

			Elemental Weight Percent				
Seam	State	Rank	C	H	O	S	Ash
Upper Freeport	PA	Med. Vol. Bit.	86	4.7	8	2.3	13
Wyodak–Anderson	WY	Subbituminous	75	5.4	18	0.6	9
Illinois #6	IL	High Vol. Bit.	78	5.0	14	4.8	15
Pittsburgh #8	PA	High Vol. Bit.	83	5.3	9	2.2	9
Pocahontas #3	VA	Low Vol. Bit.	91	4.4	2	0.7	5
Blind Canyon	UT	High Vol. Bit.	81	5.8	12	0.6	5
Lewiston-Stockton	WV	High Vol. Bit.	83	5.3	10	0.7	20
Beulah-Zap	ND	Lignite	73	4.8	20	0.8	10

Notes:
C, H and O are on moisture and ash free bases
S and Ash are on dry bases

The mole fractions of the products in Eq. (VI.8) are found assuming $f = 0.21$ and 10% excess air. The density and mass of the resulting gaseous products (ρ_{gas} and x_{gas}) are computed assuming an ideal gas mixture. The ash volume fraction is computed using the relation

$$C_v \simeq \frac{x_{\text{ash}}/\rho_{\text{slag}}}{x_{\text{gas}}/\rho_{\text{gas}}} \qquad (VI.9)$$

where x_{ash} is the mass of ash (per unit mass of coal), ρ_{slag} is the density of the ash particles (assumed = 2.5 g/cm^3). It is also assumed that the slag density is much higher than the gas density.

Results of the calculations are shown in Fig. VI.1 for a temperature of 1500 K and total pressure of 1 atm. The volume fraction, C_v, is of the form

$$C_v \sim \frac{x_{\text{ash}}}{1 - x_{\text{ash}}} \frac{P}{T}. \qquad (VI.10)$$

The solid curve was computed for coal carbon, hydrogen, and oxygen weight percentages of 75, 5, and 10, respectively. The dotted curves show results for coal compositions from Table VI.1. In Fig. VI.1, the ash volume fraction, C_v, is approximately 2×10^{-6} for high ash coal ($x_{\text{ash}} \sim 20\%$). Lower ash coals, 5-8%, have $C_v \simeq 0.5 \times 10^{-6}$. It is important to keep in mind that C_v is proportional to P/T; thus, high pressure combustors (such a coal gasifiers) will have much larger C_v values. Also, if the ash follows the gas flow without significant redistribution, then cooler layers near the boundaries of the combustor will have a higher volume fraction of ash.

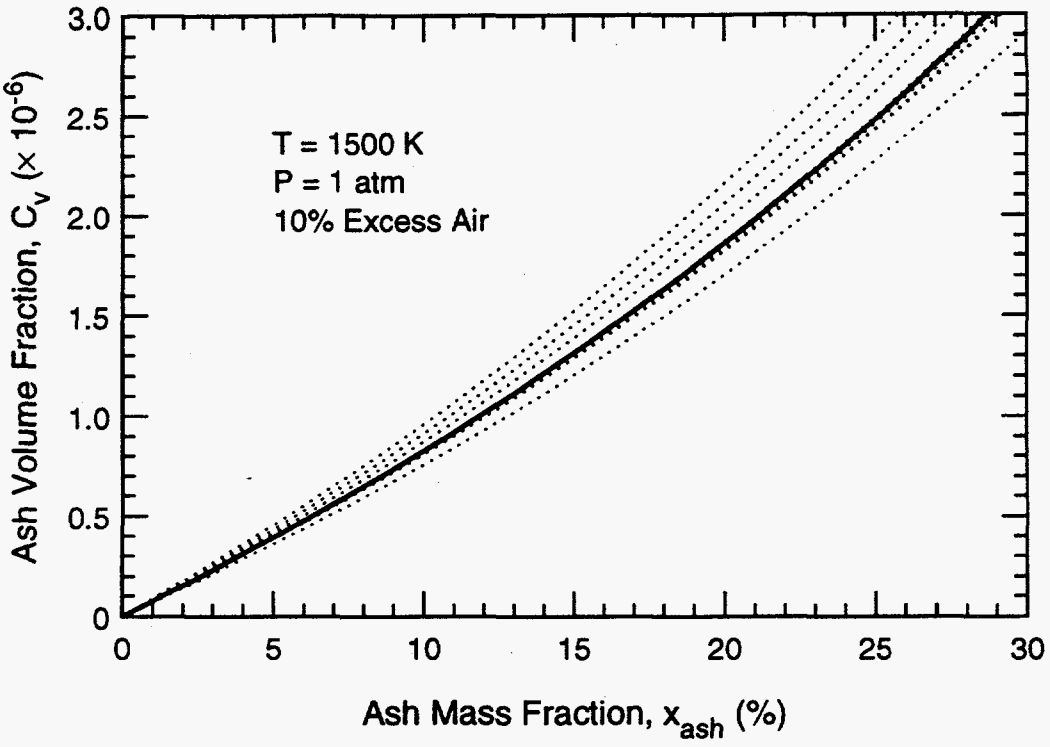

Figure VI.1: Ash volume fraction versus mass fraction of ash in the coal, x_{ash}, at T=1500K and P=1atm. The solid curve is for coal (C,H,O) mass fractions of (75,5,10) weight percent. The dashed curves are for coals in Table VI.1.

In addition to the ash volume fraction, the partial pressures of CO_2 and H_2O are obtained from this analysis. For the dry coals and 10% excess air studied here, the partial pressure of CO_2 is approximately $p_{CO_2} \simeq 0.16$ atm, and the partial pressure of H_2O is approximately $p_{H_2O} \simeq 0.06$ atm. If the coal were wet the partial pressure of H_2O would be higher.

An example illustrates the significance of the values presented here, and some typical values for optical depth resulting from these ash loading calculations. Consider the radiative properties of a uniform dispersion of ash at 1500K and 1 atm. The ultimate volume fraction for such a dispersion is approximately 2×10^{-6} for a coal ash content of approximately 20-25 wt.%. From the previous Chapter the scattering efficiency divided by D_{32} is approximately $0.4 \times 10^6 \mathrm{m}^{-1}$ at $\lambda \simeq 1$ μm. The asymmetry parameter $g \simeq 0.7$ so the effective scattering efficiency divided by D_{32} is approximately $Q_s(1-g)/D_{32} \simeq 0.12 \times 10^6 \mathrm{m}^{-1}$. The scattering coefficient

is approximately $\sigma_{\lambda\simeq 1} = (3/2)C_v Q_s(1-g)/D_{32} \simeq 0.36\text{m}^{-1}$. A 3-meter thick layer of uniformly dispersed ash would have a scattering optical depth, $\tau_s = \sigma_\lambda L \simeq 1.1$. The transmittance for such an optical depth, ignoring in–scatter, is approximately $e^{-1.1} = 0.33$. A layer 30-meter thick would be essentially opaque ($\tau \simeq 1.6 \times 10^{-5}$) due to scattering by the ash.

VI.3 Radiative Coefficients for Fly Ash Dispersions

The radiative coefficients, σ_λ and α_λ, for the Beulah, Eagle Butte, Illinois #6, Kentucky #9, and Upper Freeport ashes studied in Chapter V are presented in terms of the absorption coefficient, α_λ, and extinction coefficient, $\beta_\lambda = \sigma_\lambda + \alpha_\lambda$, in Fig. VI.2 and the scattering albedo, $\omega_\lambda \equiv \sigma_\lambda/\beta_\lambda$, in Fig. VI.3. Here we have used $C_v = 1 \times 10^{-6}$ to compute the coefficients, but one can easily scale the results for any ash loading using Eq. (VI.7).

The results indicate that the extinction coefficient is largest near the SiO_2 absorption band (8–12 μm) where absorption accounts for approximately 70-90% of the extinction. At shorter wavelengths the ash is a good scatterer, with $\omega_\lambda \simeq 0.95$ or larger. It is also evident from these figures that a band model with just a few bands would probably produce reasonably accurate radiation transfer calculations. Compared to the large and rapid spectral variations in the extinction for the infrared active gases, the ash is relatively gray. However, if one accounts for the exponential dependence of the transmittance, say, on β_λ, the spectral variation is markedly increased. There is approximately a factor of two decrease in β_λ over the wavelength range from $1 \leq \lambda \leq 7\mu$m. The scattering albedo is not at all gray, but probably could be approximated by a three band model ($\omega \simeq 0.975$ for $\lambda < 5\mu$m, $\omega \simeq 0.6$ for $5 < \lambda < 7.5\mu$m, and $\omega \simeq 0.2$ for $\lambda > 7.5\mu$m).

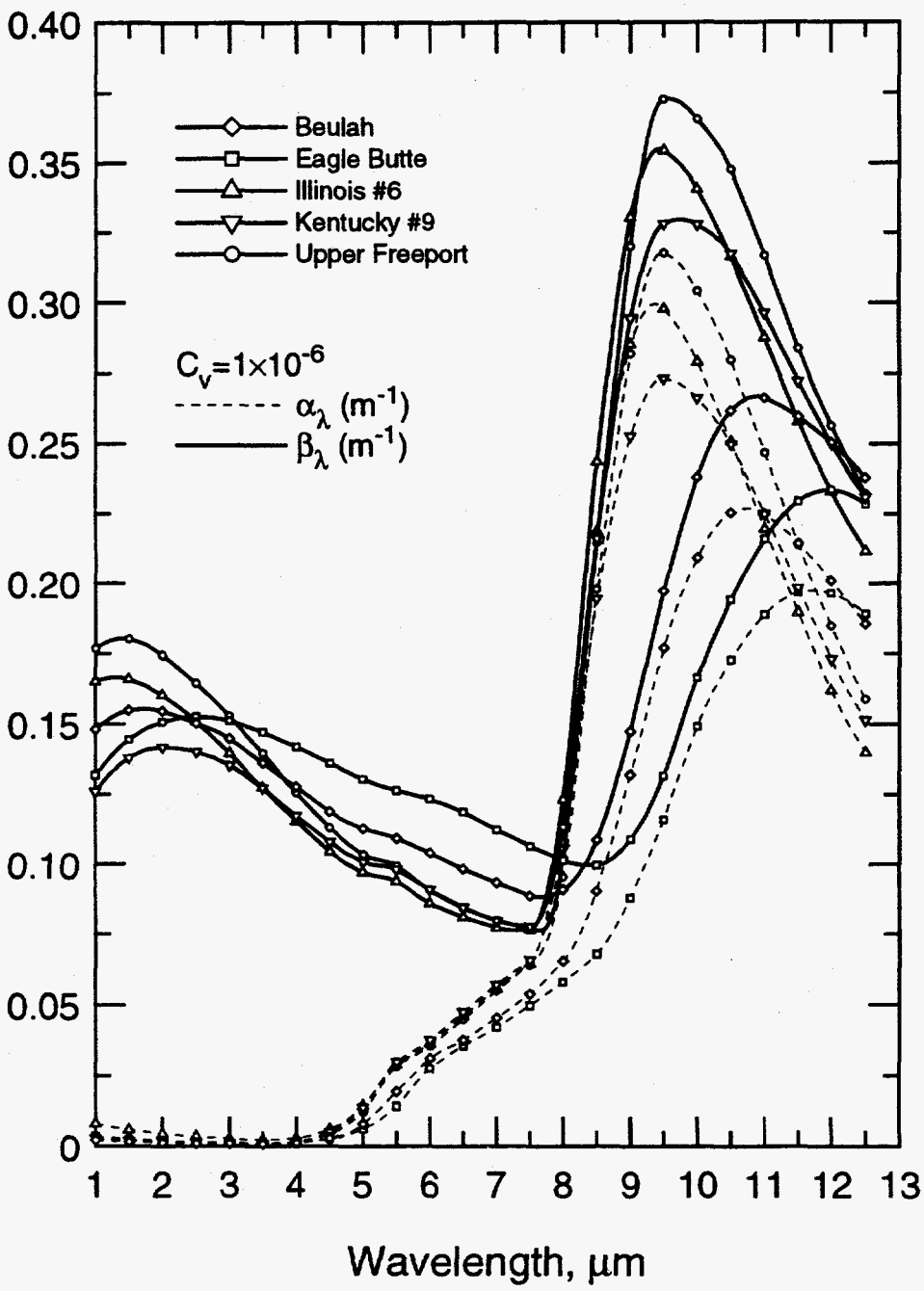

Figure VI.2: Extinction and absorption coefficients for the five fly ashes (here $C_v = 1 \times 10^{-6}$).

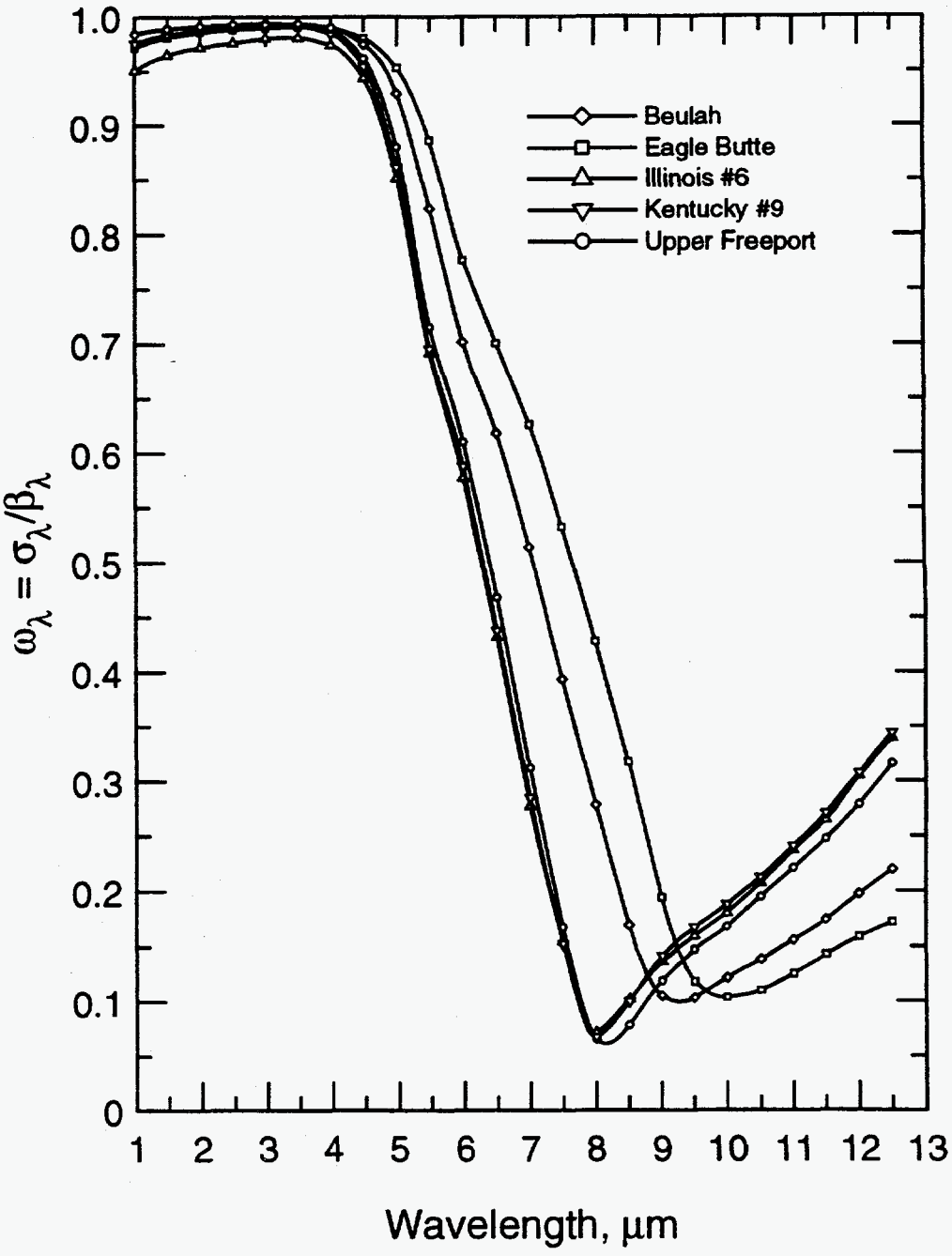

Figure VI.3: Scattering albedo for the five fly ashes.

VI.4 Wavelength-Integrated Properties of Ash Dispersions

Although the spectral extinction and absorption coefficients presented above provide all necessary information for computing radiative transfer through a medium,† it is sometime useful to express the radiative properties in terms of the Planck mean quantities. Specifically, the Planck mean absorption coefficient is defined as

$$\alpha_P(T) = \frac{\int_0^\infty \alpha_\lambda(T) I_{b\lambda}(T) d\lambda}{\int_0^\infty I_{b\lambda}(T) d\lambda} = \frac{\pi}{\sigma T^4} \int_0^\infty \alpha_\lambda(T) I_{b\lambda}(T) d\lambda. \qquad (VI.11)$$

Here $I_{b\lambda}(T)$ is the Planck blackbody function. The Planck mean extinction coefficient, $\beta_P(T)$ is defined similarly by replacing α_λ with β_λ in Eq. (VI.11).

The temperature dependence of α_P and β_P is due to both the temperature dependence of the radiative properties and the temperature dependence of the spectral distribution of blackbody radiation. In this analysis the radiative properties are assumed to be independent of temperature; thus the temperature dependence of α_P and β_P is due solely to the spectral variation of the radiative properties.

The Planck mean absorption and extinction coefficients were computed assuming negligible radiation outside the wavelength range of interest. That is, the results are normalized by the blackbody power fraction within the 1-13 μm wavelength range. The resulting mean quantities are illustrated in Fig. VI.4. Note that an ash volume fraction of $C_v = 1 \times 10^{-6}$ was used, but that the results scale as usual for any ash loading.

The Planck mean absorption coefficient in Fig. VI.4 is highest at the lowest temperature, 1000 K, and decreases with increasing temperature because at the lower temperature a larger fraction of the blackbody radiation lies at the longer wavelengths where the spectral absorption is greatest due to Si-O stretch vibrations. The three bituminous ashes (Upper Freeport, Illinois #6, and Kentucky #9) have a higher α_P than the lower SiO_2 ashes (Eagle Butte and Beulah). However, at the highest temperature (2000 K) α_P increases with the Fe_2O_3 content of the ashes, as expected.

The Planck mean extinction coefficient increases with temperature for the Beulah, Upper Freeport, and Illinois #6 ashes, but is approximately constant for the Eagle

† Recall that the scattering coefficient is scaled by $(1-g)$ to allow for non-isotropic scattering; thus, only two radiative properties are required.

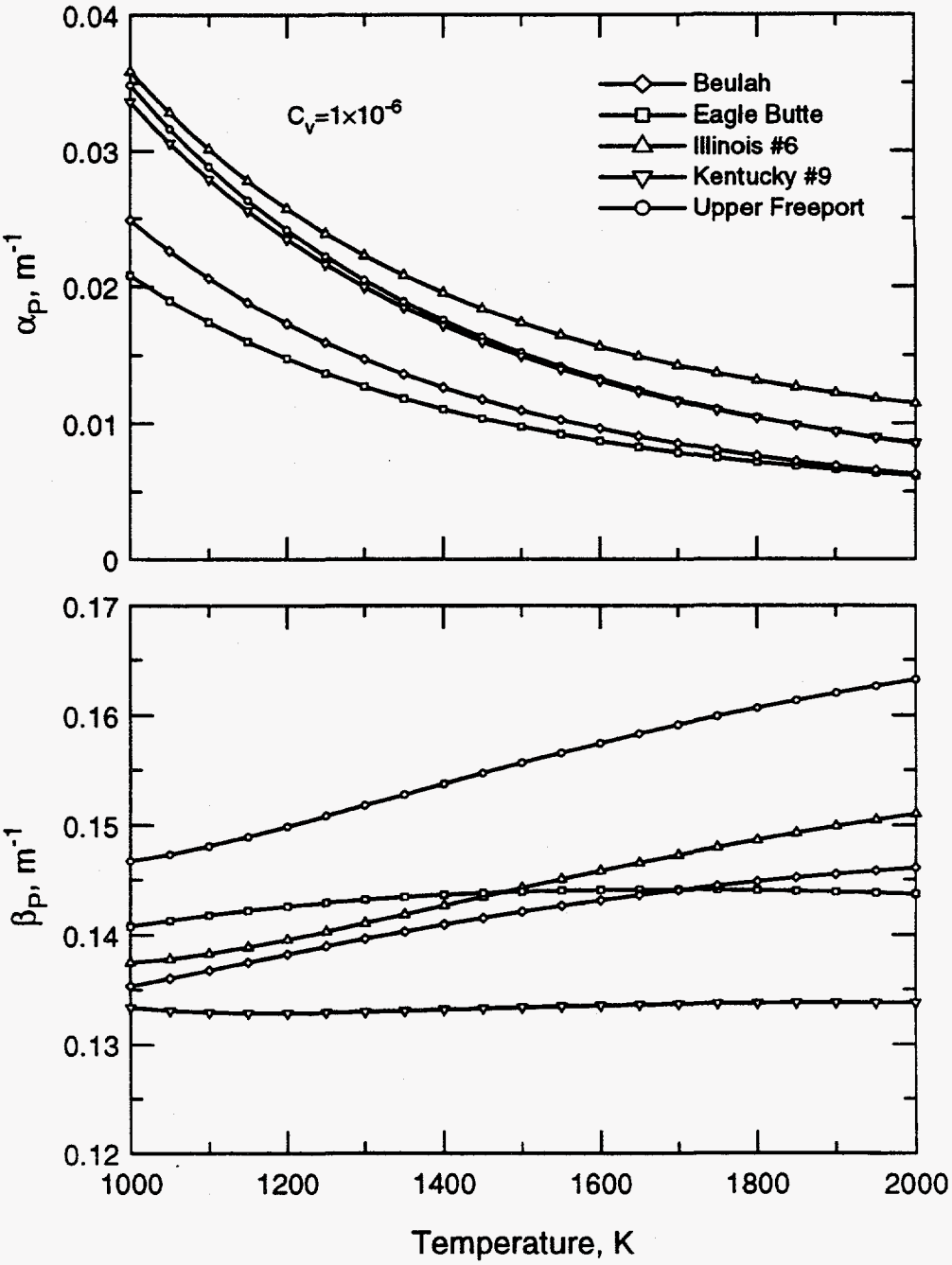

Figure VI.4: Planck mean absorption and extinction coefficients for five fly ashes.

Butte and Kentucky #9 ashes. In all cases the dependence of β_λ on temperature is fairly small, with typically less than a 10% change for $1000 \leq T \leq 2000$K. This weak temperature dependence is a result of the weak spectral variations in β. The increase in absorption coefficient at longer wavelengths is somewhat balanced by a decrease in the scattering coefficient, with the result being the relatively gray spectrum described earlier.

To determine how the various wavelength ranges contribute to the Planck mean quantities, a cumulative Planck absorption function is defined such that

$$\frac{\alpha_{P,0-\lambda}}{\alpha_P} = \frac{\int_0^\lambda \alpha_\lambda(T) I_{b\lambda(T)} d\lambda}{\int_0^\infty \alpha_\lambda(T) I_{b\lambda(T)} d\lambda} \qquad (VI.12)$$

A cumulative extinction function, $\beta_{P,0-\lambda}/\beta_P$ is likewise defined by replacing α with β in Eq. (VI.12). The resulting cumulative functions are illustrated for the Upper Freeport ash in Fig. VI.5 and for the Eagle Butte ash in Fig. VI.6. The functions are plotted for temperatures of 1000, 1500, and 2000 K. Overlaid on the graphs are light dashed lines showing the cumulative blackbody fraction, which corresponds to the expected result if the radiative properties were independent of wavelength (i.e., gray).

The results in Figures VI.5 and VI.6 show that the contribution to the Planck mean extinction coefficient is primarily due to radiative properties for $\lambda < 8\mu$m, particularly at the higher temperatures. As the gray properties curves (dashed lines) indicate, this is mostly due to the spectral distribution of the Planck blackbody radiation. The absorption coefficient is very small at short wavelengths thus most of the contribution to the Planck mean absorption coefficient is attributable to properties at longer wavelengths ($\lambda > 5\mu$m). Nevertheless, at 2000 K approximately 35% of the total Planck mean absorption coefficient for the higher iron Eagle Butte ash (Fig. VI.6) is due to absorption at $\lambda < 5\mu$m.

VI.5 Absorption Coefficients for Gaseous CO_2 and H_2O.

The gas for the following radiative heat transfer calculations is assumed to be at atmospheric pressure with CO_2 and H_2O partial pressures of $p_{CO_2} \simeq 0.16$ atm and $p_{H_2O} \simeq 0.06$ atm, respectively. The absorption coefficients of these infrared active gases show complex spectral structures. Generally the spectra consist of bands

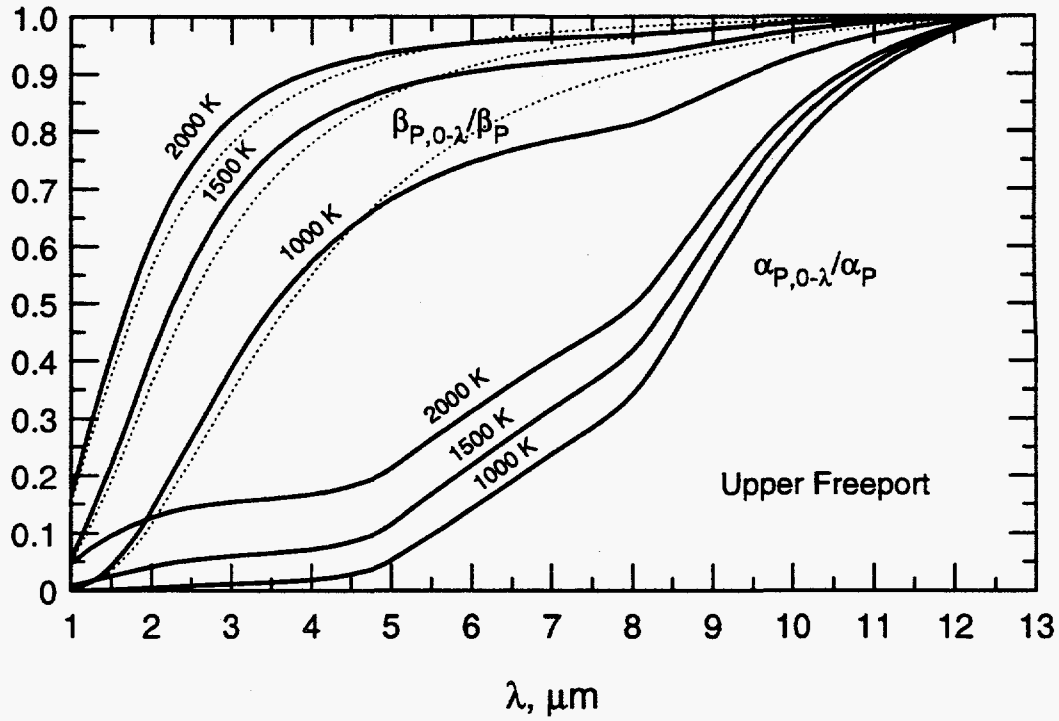

Figure VI.5: Cumulative Planck mean absorption and extinction coefficients for Upper Freeport ash. The light dashed lines are for gray properties.

consisting of many overlapping absorption lines. The line spacings are typically on the order of a few cm^{-1}; thus to resolve a spectrum one requires tabulation or computation at thousands of wavelengths. If such a tabulation or computation were possible, one would find that the absorption coefficient of the gas depends only on the temperature, total pressure, and partial pressures of the participating species† . Unfortunately, such an approach is not only very complicated but computationally impractical.

Instead, an approximate absorption coefficient is computed using narrow band models presented in Ludwig, et.al. [2]. In these models, tabulated average absorption coefficient and line density parameters allow calculation of an average absorption coefficient over relatively narrow wavelength ranges. However, since the formulation must account for overlapping lines, the resulting absorption coefficient is also a function of the pathlength.

---

† There will also be dependence on gas composition since collision broadening depends on the collision partners

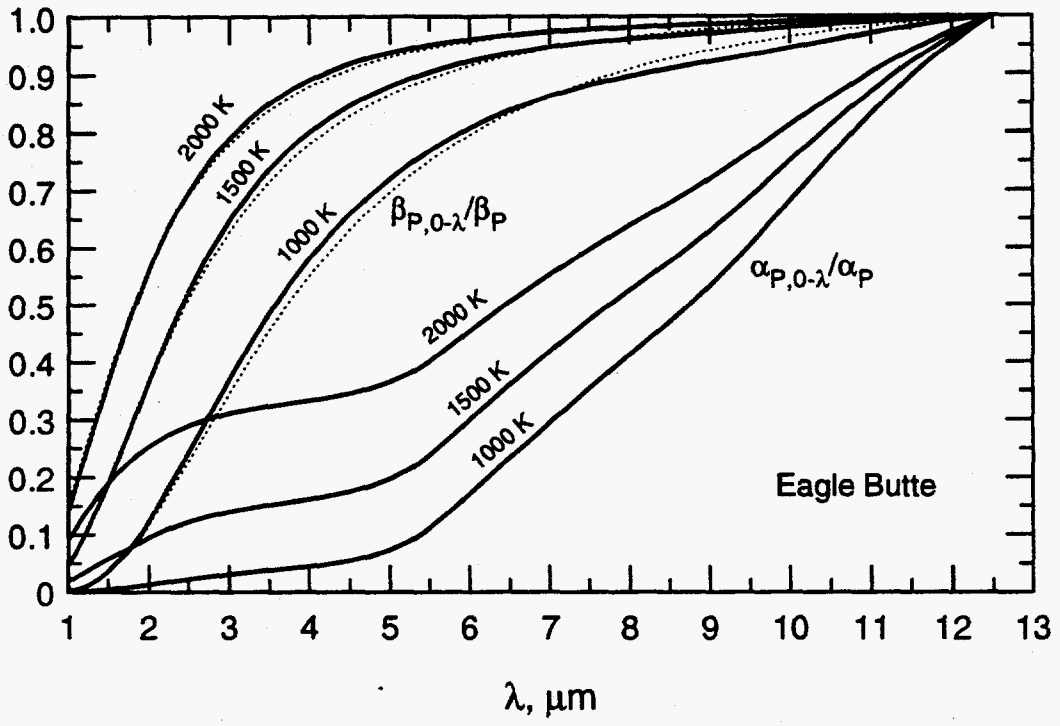

Figure VI.6: Cumulative Planck mean absorption and extinction coefficients for Eagle Butte ash. The light dashed lines are for gray properties.

The absorption coefficient versus wavelength was computed assuming a path-length L equal to the thickness of the layer. Typical results for $T = 1000$, 1500, and 2000 K are shown in Fig. VI.7 for $L = 3$m, a total pressure of 1 atm, and partial pressures of CO_2 and H_2O of 0.16 atm and 0.06 atm, respectively. As we see, the main absorption features are the 2.7 μm CO_2 and H_2O absorption bands, the 4.3 μm CO_2 absorption band, and the 6.4 μm H_2O band. The dots on the 1500 K curve show the 200 wavelength values at which the spectrum was computed. These 200 wavelength intervals are equally spaced in $\ln \lambda$ values.

VI.6 Emission, Transmission, and Reflection by an Isothermal Layer

Using the properties described above, the radiative transport equation, Eq. (VI.1) was solved using the discrete ordinates method (see Appendix E). For the calculation the $L = 3$m layer was divided into 20 equal layers, and the angular radiance was

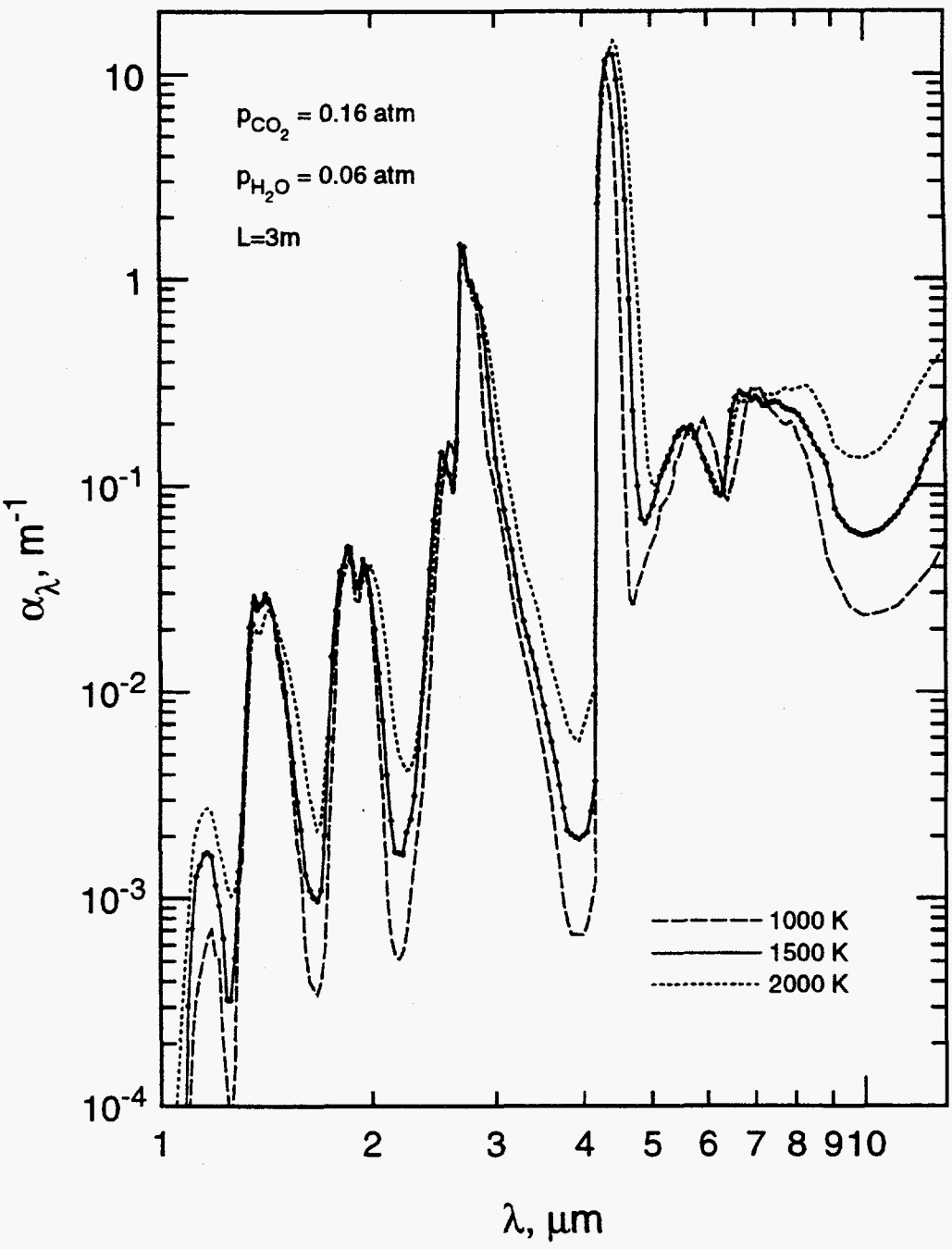

Figure VI.7: Absorption coefficient for 3-meter pathlength of CO_2 (0.16 atm) and H_2O (0.06 atm) at 1000, 1500, and 2000 K and a total pressure of 1 atm.

solved for 16 discrete directions ($-1 < \mu < 1$) with μ chosen for Gauss quadrature integration. The radiative properties were evaluated at 200 individual wavelengths, uniform in $\ln(\lambda)$ over the range $1 \leq \lambda \leq 13\mu$m. Two separate calculations were performed to obtain the hemispherical emittance, transmittance, and reflectance of the layer:

(a) The hemispherical emittance of the layer is obtained by letting the boundaries be non-emitting ($T = 0$) and non-reflecting ($\epsilon = 1$) and allowing only emission from the gas at a uniform temperature $T = 1500$ K. The spectral radiative heat flux, $q_\lambda(x)$ is computed for the layer and the hemispherical emittance is defined as

$$\epsilon_\lambda = \frac{q_\lambda(L)}{\pi I_{b\lambda}(T)}. \qquad (VI.13)$$

Here $q_\lambda(L)$ is defined as the spectral heat flux,

$$q_\lambda(x) = 2\pi \int_{-1}^{1} I_\lambda(x,\mu)\mu d\mu, \qquad (VI.14)$$

evaluated at $x = L$.

(b) The hemispherical transmittance and reflectance are obtained by letting the boundary at $x = 0$ emit at 1500 K but not reflect ($\epsilon = 1$) while the boundary at $x = L$ neither emits nor reflects ($T = 0, \epsilon = 1$). Since only the transmitted and reflected radiation are of interest here, the gas emittance is set to zero. This last point does not mean the gas does not absorb; instead the radiative properties of the medium are computed as if the gas were at 1500 K. Then the gas temperature is set to zero to prevent emission. For this calculation the spectral transmittance is

$$\tau_\lambda = \frac{q_\lambda(L)}{\pi I_{b\lambda}(T)}. \qquad (VI.15)$$

The spectral hemispherical reflectance is

$$\rho_\lambda = 1 - \frac{q_\lambda(0)}{\pi I_{b\lambda}(T)}. \qquad (VI.16)$$

The spectral emittance for several loadings (including no ash) of the Upper Freeport ash is shown in Fig. VI.8. The effect of ash loading on the emittance is a pronounced enhancement at longer wavelengths where the ash is a good emitter, but there are several interesting features at shorter wavelengths. First, near the peaks of the gas emission lines (e.g., 2.7 μm) the addition of ash reduces the emittance. This

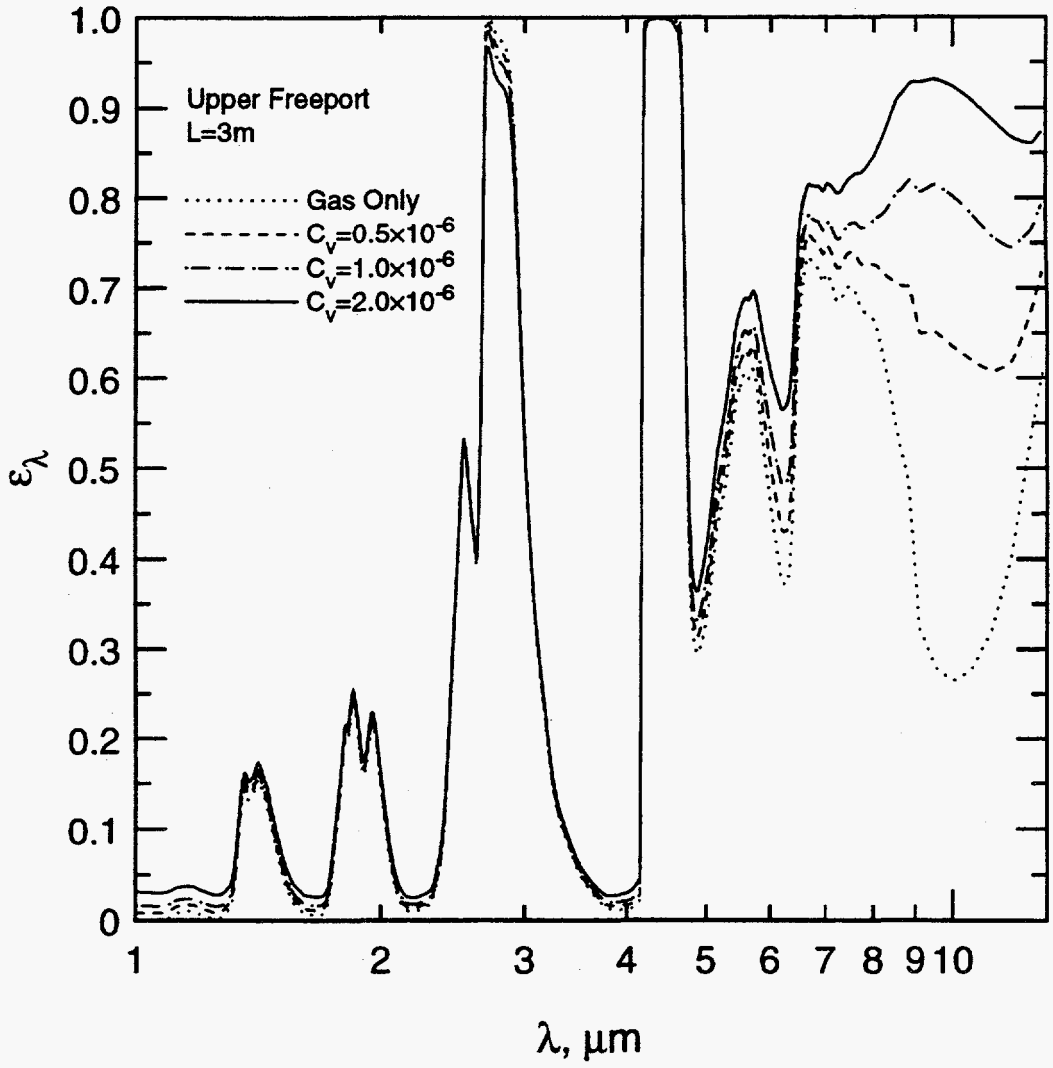

Figure VI.8: Spectral emittance of a planar layer of gas and Upper Freeport ash at 1500 K.

is in agreement with the expected trends [42]. Between the absorption bands the ash increases the emittance.

The transmittance for several loadings of the Upper Freeport ash is shown in Fig. VI.9. The effect of ash on the transmittance is very significant at all wavelengths. At long wavelengths the ash causes extinction by absorption, while at shorter wavelengths the attenuation is due to scattering.

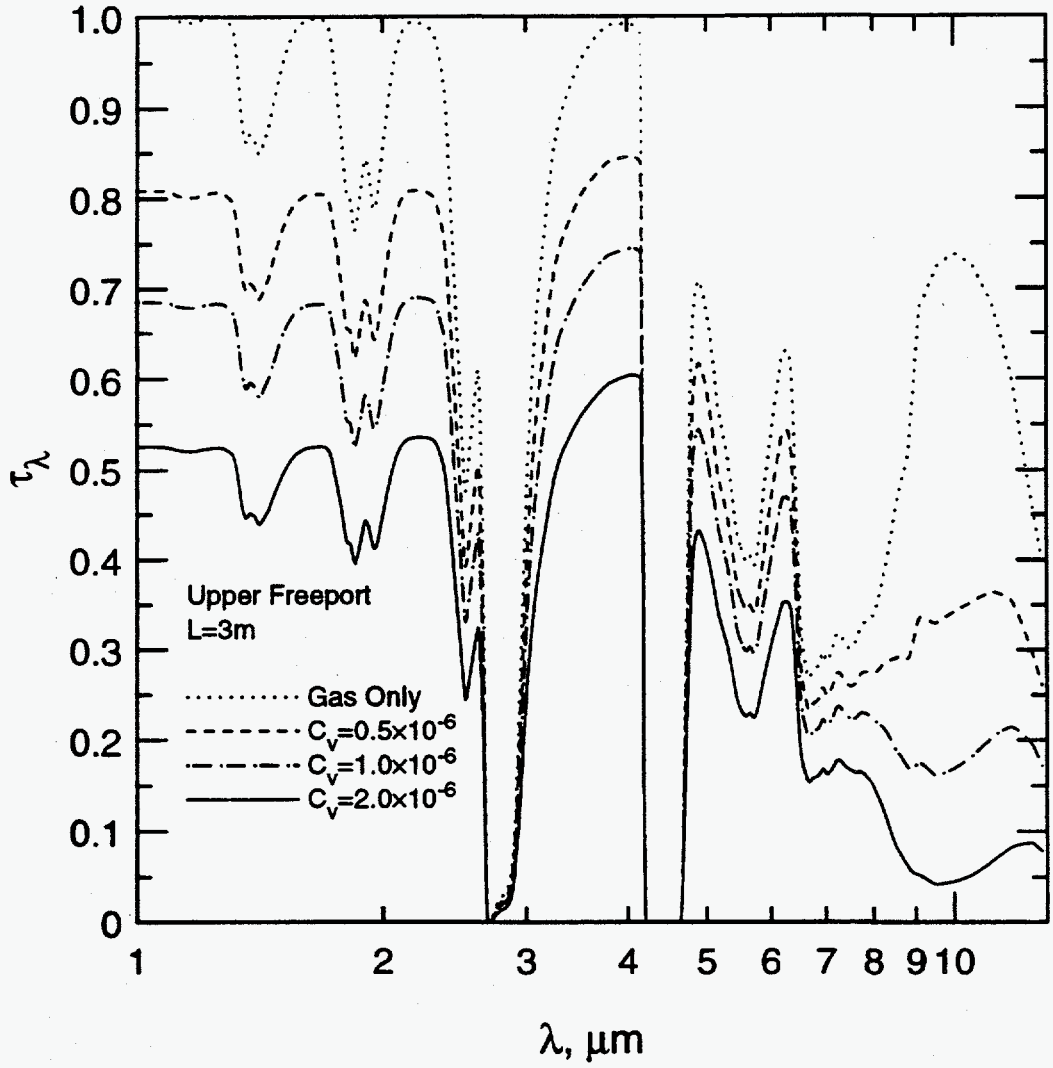

Figure VI.9: Spectral transmittance of a planar layer of gas and Upper Freeport ash at 1500 K.

The total hemispherical emittance, transmittance, and reflectance of the layer are computed by integrating over wavelength. For example,

$$\epsilon = \frac{\int_0^\infty q_\lambda d\lambda}{\sigma T^4} \qquad (VI.17)$$

In this calculation the wavelength ranges are truncated so the emittance is computed using

$$\epsilon \simeq \frac{\int_{\lambda_1}^{\lambda_2} q_\lambda d\lambda}{\int_{\lambda_1}^{\lambda_2} \pi I_{b\lambda}(T) d\lambda} \qquad (VI.18)$$

A similar integration is used to compute the total transmittance. The total reflectance is simply

$$\rho = 1 - \epsilon - \tau. \qquad (VI.19)$$

Note that the reflectance can also be computed by integrating the reflected spectral flux at $x = 0$ in case (b). Both methods were used and compared to check for accuracy, and good agreement was obtained in all cases.

The resulting total emittance, transmittance, and reflectance are summarized in Table VI.2 for several ash loadings and all five ashes. The first column shows the results for gas only ($\epsilon = 0.303$ and $\tau = 0.697$). This result agrees reasonably well with that of Goodwin [11]. As expected, adding ash to the gas causes an increase in the total emittance of the layer and a decrease in the total transmittance. A volume fraction of $C_v = 2 \times 10^{-6}$ causes a 10-20% increase in the emittance and a 42-47% decrease in the transmittance, depending on the ash. The higher iron Illinois #6 ash causes the largest increase in the emittance, with a low loading (0.5×10^{-6}) causing as much as a 7.5% increase in the emittance.

The ash-to-ash variations in total hemispherical quantities are typically only a few percent for a given ash loading, with the notable exception that high Fe_2O_3 ash causes a significant emittance increase. The emittance increases due to ash will not be significant in regions where there is soot, since the emissivity increase due to soot will overwhelm that from ash. The most significant effect of ash on the radiative transport through an isothermal layer is the increased extinction due to scattering. As suggested in the literature, e.g., Gupta, et al [8], a cold layer of ash between the walls and flames in a combustor may provide significant radiation shielding and hence a marked reduction in heat transfer between the hot core gas and the cooler walls.

VI.7 Heat Flux through a Layer in Radiative Equilibrium

In the previous section it was assumed that the medium was at a uniform temperature. No justification for this assumption was presented, but such a condition would occur in a well-stirred medium where convective and/or conductive heat transport are dominant, continually replenishing the radiative losses throughout the layer, particularly near the surfaces of the reactor where radiative losses are largest.

In this section the heat flux through a layer in radiative equilibrium is studied. Radiative equilibrium occurs when radiative transport through the medium dominates

Table VI.2: Total properties for a 3 m isothermal slab of ash and gas.

$L = 3$ m
$P = 1$ atm
$T = 1500$ K
$P_{CO_2} = 0.16$ atm
$P_{H_2O} = 0.06$ atm

Upper Freeport	$D_{32} = 5.579 \times 10^{-6}\mu$m						
$C_v(\times 10^6)$	0	0.5	1.0	2.0	0.5	1.0	2.0
$C_v L/D_{32}$	0	0.269	0.538	1.075			
ρ	0.000	0.108	0.183	0.282	% Change by adding Ash		
τ	0.697	0.571	0.486	0.373	-18.1%	-30.3%	-46.5%
ϵ	0.303	0.321	0.331	0.344	5.9%	9.2%	13.5%

Illinois #6	$D_{32} = 5.836 \times 10^{-6}\mu$m						
$C_v(\times 10^6)$	0	0.5	1.0	2.0	0.5	1.0	2.0
$C_v L/D_{32}$	0	0.257	0.514	1.028			
ρ	0.000	0.098	0.167	0.258	% Change by adding Ash		
τ	0.697	0.576	0.492	0.378	-17.4%	-29.4%	-45.8%
ϵ	0.303	0.326	0.341	0.364	7.6%	2.5%	20.1%

Beulah	$D_{32} = 6.991 \times 10^{-6}\mu$m						
$C_v(\times 10^6)$	0	0.5	1.0	2.0	0.5	1.0	2.0
$C_v L/D_{32}$	0	0.215	0.429	0.858			
ρ	0.000	0.101	0.173	0.271	% Change by adding Ash		
τ	0.697	0.582	0.501	0.391	-16.5%	-28.1%	-43.9%
ϵ	0.303	0.317	0.326	0.338	4.6%	7.6%	11.6%

Kentucky #9	$D_{32} = 7.244 \times 10^{-6}\mu$m						
$C_v(\times 10^6)$	0	0.5	1.0	2.0	0.5	1.0	2.0
$C_v L/D_{32}$	0	0.207	0.414	0.828			
ρ	0.000	0.093	0.160	0.253	% Change by adding Ash		
τ	0.697	0.586	0.508	0.400	-15.9%	-27.1%	-42.6%
ϵ	0.303	0.321	0.332	0.347	5.9%	9.6%	14.5%

Eagle Butte	$D_{32} = 8.405 \times 10^{-6}\mu$m						
$C_v(\times 10^6)$	0	0.5	1.0	2.0	0.5	1.0	2.0
$C_v L/D_{32}$	0	0.178	0.357	0.714			
ρ	0.000	0.101	0.174	0.272	% Change by adding Ash		
τ	0.697	0.581	0.500	0.388	-16.6%	-28.3%	-44.3%
ϵ	0.303	0.317	0.326	0.339	4.6%	7.6%	11.9%

convection and/or conduction. In this limit the temperature of the medium is dependent on the radiative flux and absorption coefficient of the medium. This limit is closer to the situation in the radiant boiler of a real combustor, where flows are predominantly parallel to the walls of the boiler and conduction through the gas is poor.

To construct a model for the following calculations, it is assumed that CO_2, H_2O, and fly ash are uniformly distributed between two black walls a distance L apart. Initially the walls are at 1500 K and the medium is likewise at a uniform temperature of 1500 K. This initial distribution defines the ash volume loading, $C_{v,1500}$, from which the mass loading of ash is approximately $\rho_{\mathbf{ash}} C_{v,1500}/\rho_{\mathbf{gas}}$, where $\rho_{\mathbf{ash}}$ is the average density of the fly ash particles ($\sim 2500 \mathrm{kg/m^3}$) and $\rho_{\mathbf{gas}}$ is the gas density. The temperatures of the walls at $x = 0$ and $x = L$ are now changed to 1000 K and 2000 K, respectively, while maintaining the same *mass* loading of ash relative to the mass of gas. The resulting radiative transfer causes the gas near the cooler wall at $x = L$ to become cooler and the gas near the hotter wall at $x = 0$ to become hotter than 1500 K. The ash mass loading remains fixed, but the volume loading decreases with increasing temperature since the volume of a unit mass of gas increases with temperature while the volume of a unit mass of ash remains relatively constant. Thus C_v depends on the gas temperature as described in Section VI.2 (Eq. (VI.10)).

The solution of the radiative transport equation for the planar layer, Eq. (VI.1), is now complicated by the fact that $T(x)$ is not constant, but instead depends on the radiative flux through the medium. To understand this dependence, consider the following analysis for the planar medium.

The radiative transport equation for the planar medium given in Eq. (VI.1) contains the unknown temperature, $T(x)$, explicitly. However, by integrating Eq. (VI.1) over $-1 \leq \mu \leq 1$ and multiplying by 2π, one obtains the equation

$$\frac{dq_\lambda}{dx} + \beta_\lambda g_\lambda = 4\pi\alpha_\lambda I_{b\lambda}[T(x)] + \sigma_\lambda g_\lambda. \qquad (VI.20)$$

Here we define the spectral heat flux, q_λ, as

$$q_\lambda(x) = 2\pi \int_{-1}^{1} I_\lambda(x,\mu)\mu d\mu \qquad (VI.21)$$

and the spectral incident radiation, g_λ as

$$g_\lambda(x) = 2\pi \int_{-1}^{1} I_\lambda(x,\mu) d\mu \qquad (VI.22)$$

Note that the identity $2\pi \int_{-1}^{1} \Phi_\lambda(\mu, \mu')d\mu' = 4\pi$ is used to eliminate the scattering phase function. The spectral extinction coefficient is $\beta_\lambda = \sigma_\lambda + \alpha_\lambda$, so that Eq. (VI.20) can be written as

$$\frac{dq_\lambda}{dx} + \alpha_\lambda g_\lambda = 4\pi \alpha_\lambda I_{b\lambda}[T(x)]. \qquad (VI.23)$$

Integrating Eq. (VI.23) over all wavelengths gives

$$\frac{dq}{dx} + \int_0^\infty \alpha_\lambda g_\lambda d\lambda = 4\pi \int_0^\infty \alpha_\lambda I_{b\lambda}[T(x)]d\lambda. \qquad (VI.24)$$

Here $q(x) = \int_0^\infty q_\lambda(x)d\lambda$ is the total radiant flux.

Since dq/dx in Eq. (VI.24) is the net heat flux into a control volume of differential width dx, a heat balance on the control volume specifies it explicitly. If there is no internal power generation and one ignores heat flux into the control volume by conduction or convection, then the net radiative flux is zero, i.e.,

$$\frac{dq}{dx} = 0, \qquad \text{(Radiative Equilibrium)}. \qquad (VI.25)$$

With this assumption about the sources of power in the medium, one can write

$$\int_0^\infty \alpha_\lambda g_\lambda(x)d\lambda = 4\pi \int_0^\infty \alpha_\lambda I_{b\lambda}[T(x)]d\lambda. \qquad (VI.26)$$

Suppose one defines a ratio, f_λ, such that

$$f_\lambda = \frac{I_{b\lambda}}{\hat{\sigma}T^4} \qquad (VI.27)$$

in a fashion similar to the "Picket Fence" analysis of Ozisik [35]. Here $\hat{\sigma} \simeq 5.67 \times 10^{-8} \mathrm{W/m^2K^4}$ is the Stefan-Boltzmann constant. Substituting Eq. (VI.27) into Eq. (VI.26) gives

$$\hat{\sigma}T^4 = \frac{\int_0^\infty \alpha_\lambda g_\lambda d\lambda}{4\pi \int_0^\infty \alpha_\lambda f_\lambda d\lambda}. \qquad (VI.28)$$

Combining Eq. (VI.1) with Eq. (VI.27) and Eq. (VI.28) gives

$$\mu \frac{dI_\lambda(x,\mu)}{dx} + \beta_\lambda I_\lambda(x,\mu) = \alpha_\lambda f_\lambda \left[\frac{\int_0^\infty \alpha_\lambda g_\lambda d\lambda}{4\pi \int_0^\infty \alpha_\lambda f_\lambda d\lambda}\right] + \frac{\sigma_\lambda}{2} \int_{-1}^{1} I_\lambda(x,\mu')\Phi_\lambda(\mu,\mu')d\mu' \qquad (VI.29)$$

This equation contains no explicit reference to temperature, although it does contain temperature implicitly through f_λ and through the dependence of the radiative properties on temperature. However, Eq. (VI.29) is suitable for iterative solution, where one initially assumes a temperature for the medium and computes $g_\lambda(x)$.

Using this result for $g_\lambda(x)$ one uses Eq. (VI.28) to compute an improved temperature which is subsequently used to compute $f_\lambda(x)$ and new radiative properties. Using these improved temperatures and properties an improved $g_\lambda(x)$ is obtained by re-solving Eq. (VI.29). This process is continued until the difference between two successive temperature calculations is less than some specified tolerance. Typically the convergence to within 0.1% is achieved after only a few iterations, but it does depend on the radiative properties, with solutions for optically thicker media requiring more iterations.

Note that in practice the spectral solution is obtain only at discrete wavelengths, and is commonly referred to as the "picket fence" model. In this model the spectral properties and blackbody function are assumed to be constant over a small wavelength interval, $\Delta\lambda$, and each spectral quantity is integrated over this interval. For example, the subscript λ in the formula above is replaced by integer subscript i, where for example

$$g_i = \int_{\lambda_i-\Delta\lambda}^{\lambda_i+\Delta\lambda} g_\lambda d\lambda. \qquad (VI.30)$$

Similar discretization of λ is effected for all spectral quantities, and Eq. (VI.29) becomes a system of integro-differential equations for the spectral radiance $I_i(x,\mu)$. Note that Ozisik [35](p.302) mistakenly suggests that this system of equations can be solved once for I_i and then Eq. (VI.28) can be used to find T. As shown here, f_i also depends on T and thus, in general, T is implicit in the system of equations.

Further simplification of Eq. (VI.29) is possible if one assumes that the scattering is isotropic, or that the scattering can be modeled as a combination of isotropic plus forward scattering. This latter approach requires replacing the radiative properties with effective radiative properties as discussed in Section VI.1, and is used throughout this analysis. For isotropic scattering one obtains

$$\mu\frac{dI_\lambda(x,\mu)}{dx} + \beta_\lambda I_\lambda(x,\mu) = \alpha_\lambda f_\lambda\left[\frac{\int_0^\infty \alpha_\lambda g_\lambda d\lambda}{4\pi\int_0^\infty \alpha_\lambda f_\lambda d\lambda}\right] + \frac{\sigma_\lambda}{4\pi} g_\lambda \qquad (VI.31)$$

This equation is readily solved using the discrete ordinates technique described in Appendix E.

Again, the gas for this analysis is assumed to be at atmospheric pressure with CO_2 and H_2O being the only radiatively active gases with partial pressures of 0.16 atm and 0.06 atm, respectively. The gas spectral properties are again taken from Ludwig, et.al. [2], and are computed at each position, x, in the layer using the local temperature

$T(x)$. Once again the wavelength space is divided into 200 equal intervals in $\log \lambda$ space but the range is extended through the visible and far infrared to include the range $0.1 \leq \lambda \leq 30\mu$m. Ash properties outside the measured range are extrapolated by assuming they are constant outside the range of measurement. This discretization of the broad wavelength range was found to provide ample resolution to model the narrow band results of Ludwig, et.al.

The extension of the wavelength range into the visible portion of the spectrum was found to be necessary for accurate calculation of the blackbody fraction at the higher temperatures (2000 K). While at 1500 K the blackbody fraction at wavelengths shorter than 1 μm is only 1.3%, at 2000 K approximately 6.7% of the total blackbody power is at wavelengths shorter than 1 μm. While this fraction is still small enough that uncertainties in the radiative properties at $\lambda < 1\mu$m do not significantly affect the total (wavelength integrated) results, neglecting this spectral range unnecessarily skewed the spectral heat flux. Extension of the spectral range from 13 μm to 30 μm has almost no effect on the results, since less than 0.7% of the blackbody power is at wavelengths longer than 1 μm at 2000 K, and less than 4.5% is at wavelengths longer than 13 μm at 1000 K. Nevertheless, the additional spectral range did not significantly reduce the spectral resolution since divisions were in equal increments of $\ln \lambda$ (only 29 of the 200 wavelength bands were at wavelengths longer than 13 μm).

As described in Section VI.4, the Upper Freeport and Kentucky #9 ashes have Planck mean extinction coefficients that span the range of values for all ashes studied here; therefore calculations are only presented for those two ashes.

The temperature distribution for a planar layer of gas and ash was computed for several loadings of ash. The results for a 10 m layer of gas plus Upper Freeport ash is illustrated in Fig. VI.10. As expected, the temperature gradient through the medium increases as the ash loading increases, but the effect is not particularly large. For example, the temperature distribution through the medium for a coal with 20% by mass of ash ($C_{v,1500} \sim 2 \times 10^{-6}$) will be within approximately ± 100 K of that for the same medium without ash. Of course, this calculation assumes the boundaries are maintained at the same temperatures (1000 K and 2000 K) independently of the heat flux across the layer.

The most significant effect of ash addition is to reduce the heat flux. Figure VI.11 shows the spectral heat flux through the planar layer with various loadings of Upper Freeport ash. Clearly, for the assumed boundary temperatures, most of the radiative

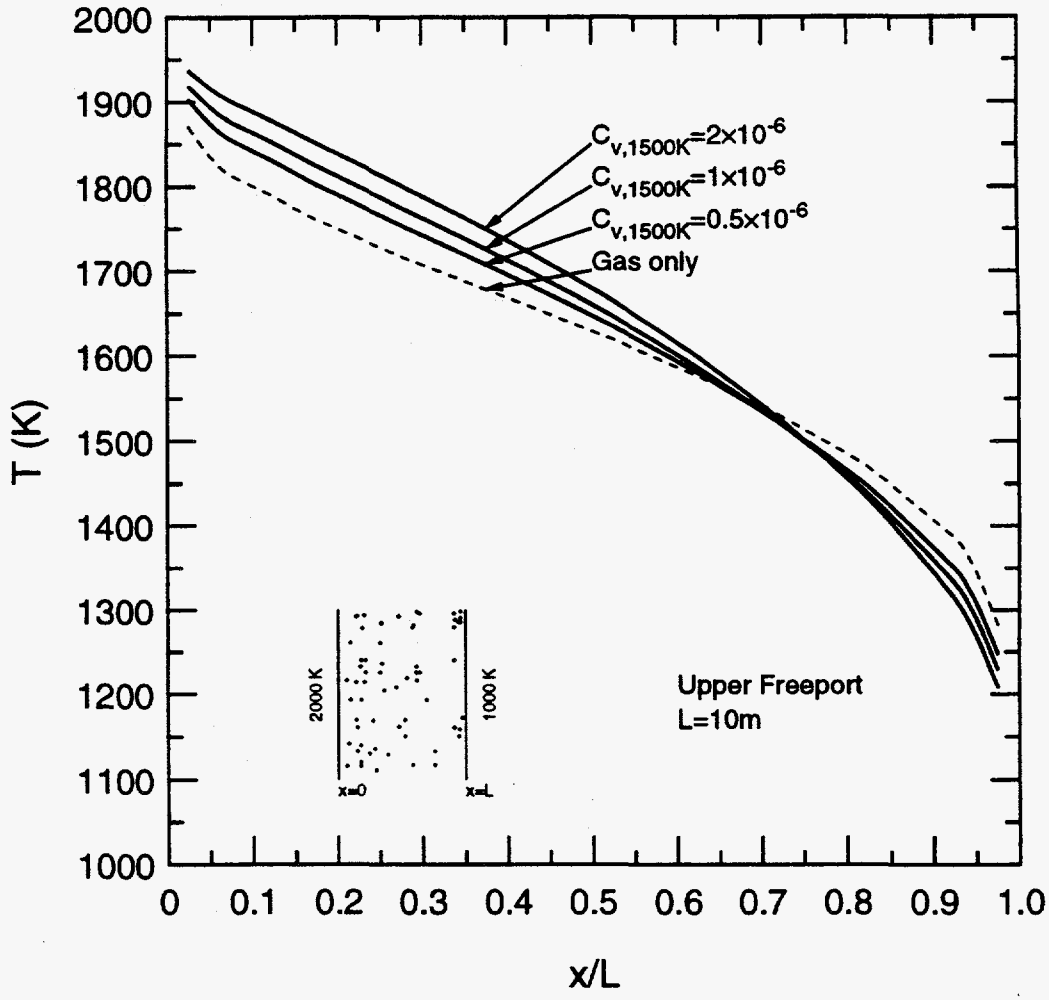

Figure VI.10: Effect of ash loading on the temperature distribution through a planar layer of ash plus CO_2 and H_2O.

flux is at wavelengths shorter than 4 μm and longer than 0.6 μm, while the peak spectral flux is at a wavelength of approximately 1.5 μm. In addition, the peak flux is decreased by a factor of almost four due to addition of 20% ash ($C_{v,1500} \sim 2 \times 10^{-6}$). The effect of this decrease in heat flux will be very significant in a real combustor with gas flow. The coal combustion products will cool nearly four times more slowly as a result of radiation screening due to scattering by the ash. This is the principal reason why, for the same heat release, pulverized coal combustors have to be much larger than those burning oil or gas.

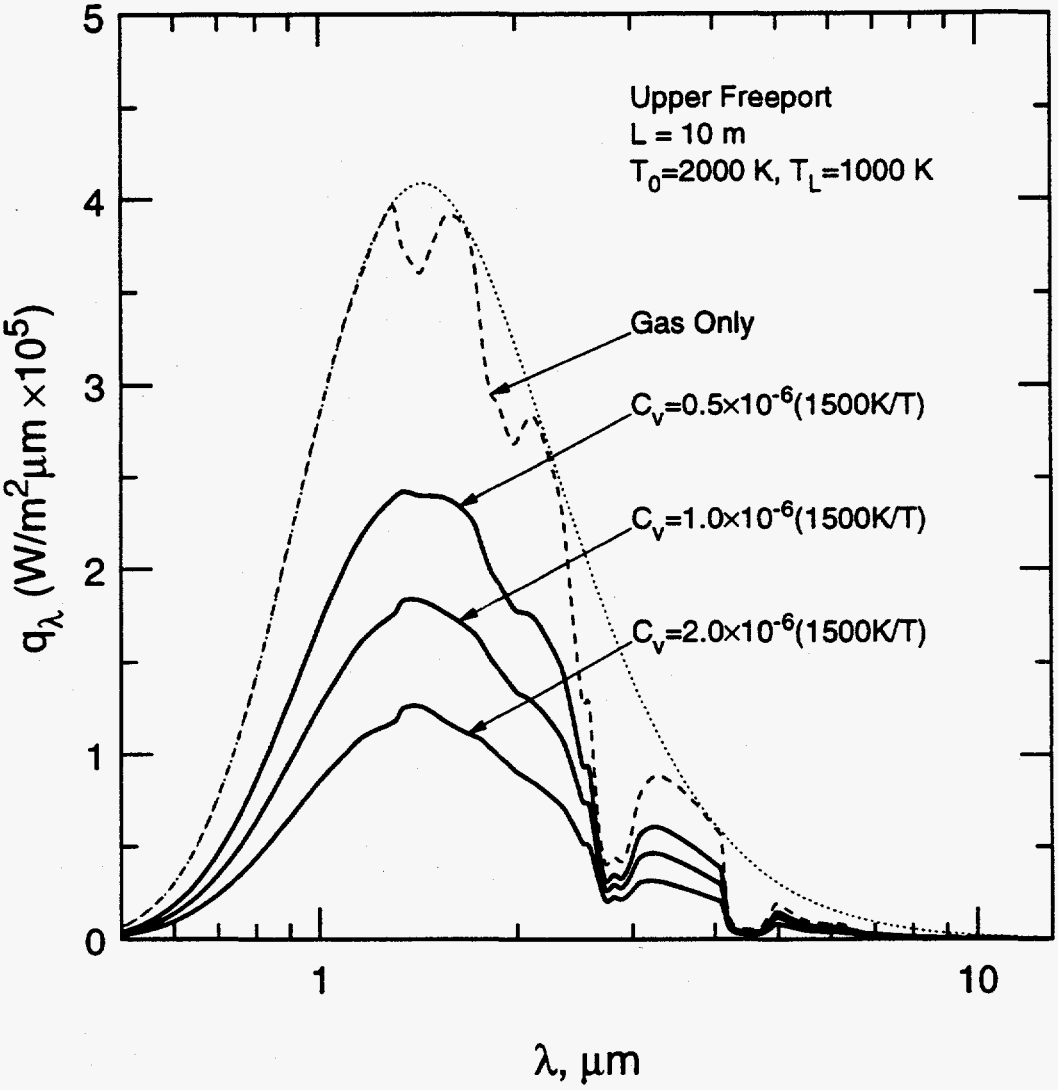

Figure VI.11: Effect of ash loading on the spectral heat flux distribution through a planar layer of ash plus CO_2 and H_2O.

The integrated total heat fluxes for two layer thicknesses and for two different ashes (Upper Freeport and Kentucky#9) are shown in Fig. VI.12. Here the dimensionless flux,

$$Q = \frac{q}{\hat{\sigma}(T_o^4 - T_1^4)} \qquad (VI.32)$$

is defined for black walls at temperature T_o and T_1. As expected, addition of ash decreases the total heat flux through the medium. Figure VI.12 also shows that the Upper Freeport ash consistently reduces the heat flux more than the Kentucky#9 ash.

This difference can be attributed to the larger scattering coefficient of the finer, more broadly distributed Upper Freeport ash. The effect is not substantially attributable to differences in Mie scattering (e.g., scattering efficiency), but simply that there are many more Upper Freeport particles per unit mass of ash than there are for Kentucky #9. Most ash particles have a scattering efficiency, Q_s, of approximately 2 or so in the 1-2 μm wavelength range, but the scattering coefficient is proportional to Q_s/D_{32}, and distributions with larger particles and/or broader size distributions (such as Upper Freeport) have larger D_{32} (e.g., See Eq. (V.34)).

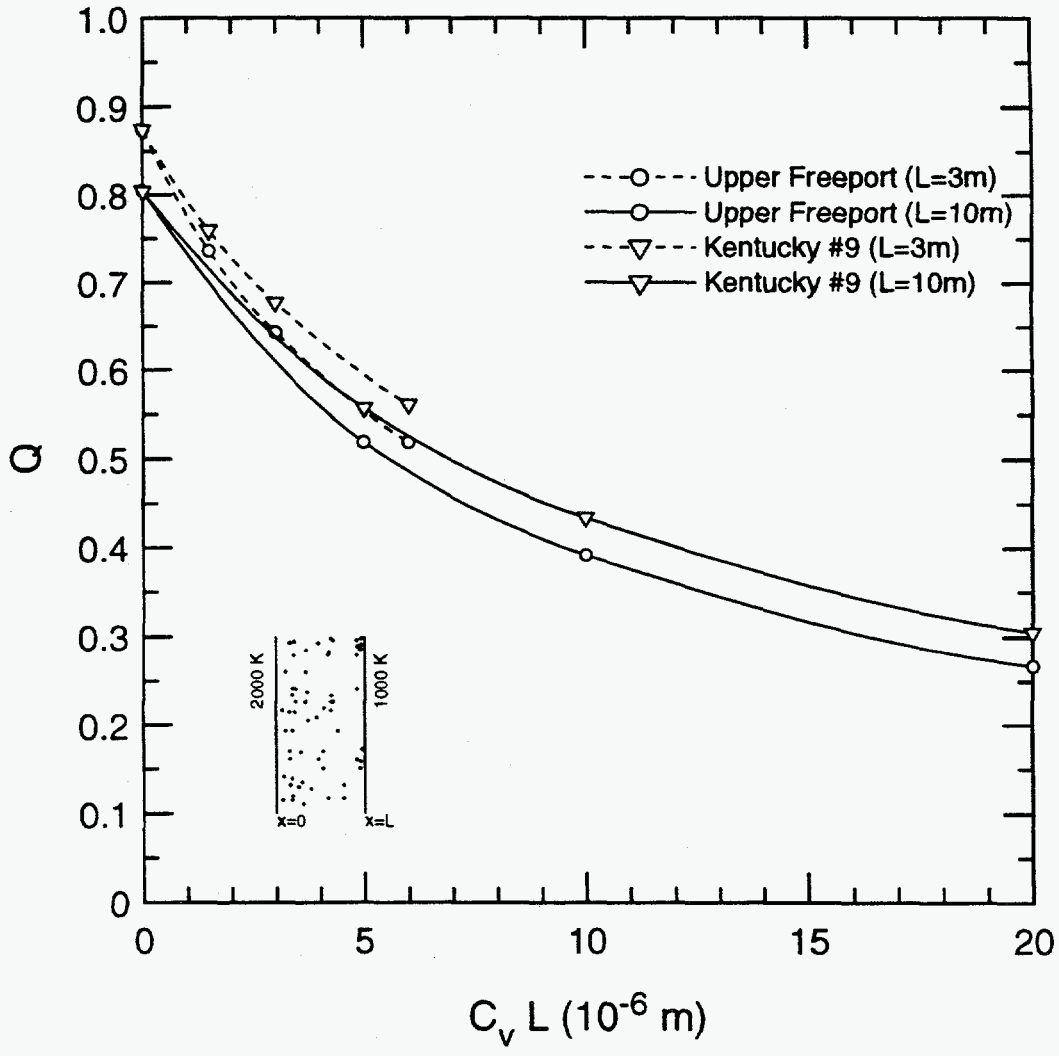

Figure VI.12: Effect of ash loading on the total radiative heat flux through a planar layer of ash plus CO_2 and H_2O.

The effect of ash loading on the heat flux is qualitatively similar to the effect of increasing the optical depth of a gray medium. In a gray medium the dimensionless heat flux, Q, between black walls at temperatures T_o and T_1 is approximately [35]

$$Q(\tau_0) \simeq \frac{4/3}{\gamma + \tau_0}, \quad (\tau_0 \to \infty) \tag{VI.33}$$

in the limit of large optical depth, $\tau_0 = \beta L \to \infty$. Here the constant $\gamma \simeq 1.42089$. An approximate empirical fit to the exact solution for $Q(\tau_0)$ for a gray medium is

$$Q(\tau_0) \simeq \frac{4/3}{\gamma + \tau_0} + 0.06162 \exp(-4\tau_0) \tag{VI.34}$$

Now one can calculate an effective optical depth, $\tau_{o,\mathrm{gas}}$, such that the dimensionless heat flux $Q(\tau_{0,\mathrm{gas}})$ equals the result from the spectral calculation for a medium with prescribed thickness with only the participating gas (no ash). For $L = 3$m we find $\tau_{0,\mathrm{gas}} \simeq 0.163$ and for $L = 10$m we find $\tau_{0,\mathrm{gas}} \simeq 0.280$. For purposes of this analysis, suppose the optical depth of the gas plus ash is

$$\tau_0 \simeq \tau_{0,\mathrm{gas}} + \beta_P L \tag{VI.35}$$

where β_P is the Planck mean extinction coefficient for the ash. The radiation being extinguished is predominantly that from the hot wall at 2000 K; thus β_P is evaluated at 2000 K. By contrast, the gas temperature is between 1000 and 2000 K across the layer; thus C_v will be evaluated at 1500 K, which is reasonably close to the average medium temperature. This distinction between the temperature of the incident radiation that is being scattered and absorbed by the medium and the average temperature which determines the volume fraction of particles is significant, and it is not clear that the best choices have been made here. However, for the purposes of this discussion, these choices are satisfactory.

For a given ash loading, one can compute the optical depth from Eq. (VI.35). Figure VI.13 compares Q from the full spectral calculation with that from this simplified model for the optical depth. The light dashed line shows the gray solution $Q(\tau_0)$ from Eq. (VI.34). The agreement is very good, confirming the notion that the primary effect of adding ash is fundamentally the same as increasing the optical depth of the layer.

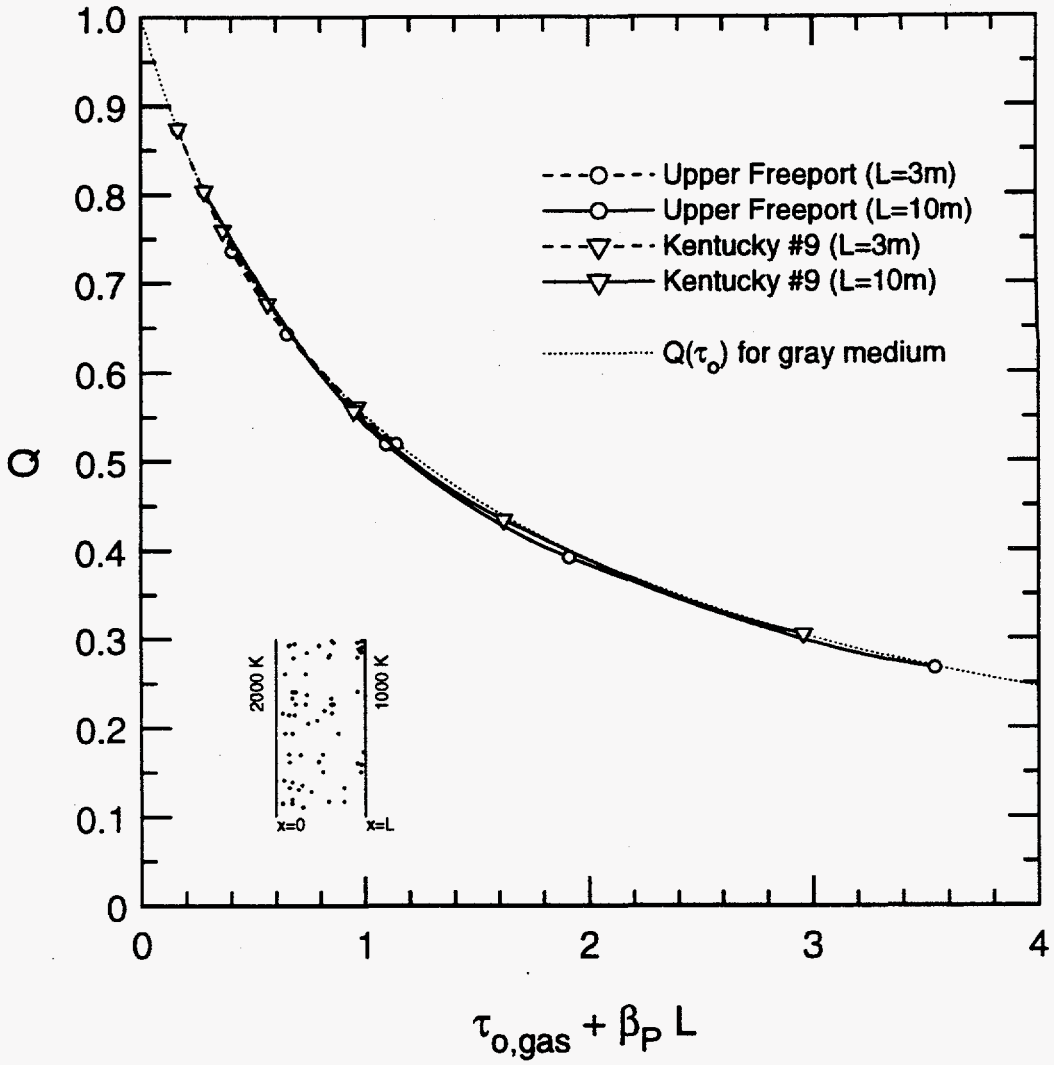

Figure VI.13: Effect of ash loading on the total radiative heat flux through a planar layer of ash plus CO_2 and H_2O versus the approximate optical depth of the layer.

Chapter VII.

Summary and Conclusions

An experimental study of the optical constants of molten coal slags has been presented. The principal purpose of this work was to improve and extend the database on optical constants of coal slags from which one can calculate the effects of fly ash on radiative heat transfer in pulverized coal combustors. The measurements quantify the effect of composition on the optical constants over a wavelength range from 1-13 μm. The range of compositions studied extend the available measurements [11] to include ash particles with much lower SiO_2 content. These measurements also extend the temperature range of Goodwin's [11] measurements to higher temperatures, where the slag is molten. Correlations for the complex refractive index, $m = n + ik$, were formulated and fitted to the measured optical constants. The correlations allow one to compute n and k for a range of typical ash compositions for the wavelength range from 1 13 μm and for temperatures to 1600°C. By combining these correlations with the size and composition distributions of fly ash samples from representative U.S. coals measured by Ghosal [17], the radiative properties of fly ash dispersions were computed using Mie theory. Finally, the effects of the fly ash on radiative heat transfer were computed for a planar layer of dispersed ash containing the infrared active gases CO_2 and H_2O for both isothermal conditions and for radiative equilibrium.

The basic approach of this work rests on the observation that the radiative properties of fly ash are dependent on the optical constants of the materials that constitute fly ash, and that these optical constants (n, k) are material properties that depend only on the composition and temperature of the material and on the wavelength of incident radiation. The optical constants do not depend on the size or shape of fly ash particles.

Another important observation that justifies the approach adopted here in practice is that the vast majority of fly ash particles are closely spherical and glassy (i.e., homogeneous and isotropic) because they are formed by the quenching of liquid slag droplets. Therefore, it is valid to use standard Mie theory to calculate the radiative properties of dispersions of such particles from measurements of the size and composition distributions for the fly ash in question. It should also be pointed out that even for particles that are not spherical and homogeneous (e.g., cenospheres), it is

necessary to know the optical constants to estimate the scattering properties of such particles.

To study the effect of composition on the optical constants, synthetic slags were produced in a furnace at approximately 1600°C. The technique consisted of mixing pure oxides (SiO_2, Al_2O_3, CaO, and Fe_2O_3) in precise amounts and melting them in the furnace. Electron microprobe measurements were made to quantify the resulting slag compositions.

Once a slag of known composition was produced, it was remelted in the furnace and its optical constants were measured. An infrared imaging and detection system was developed that allowed measurement of either the transmittance or the near-normal reflectance of the molten slag. At wavelengths shorter than approximately 5 μm the slags are relatively transparent ($k \leq 10^{-3}$) and a transmittance technique was used to measure the absorption index, k. In this technique a platinum mirror was submerged below the molten surface of the slag inside the electric furnace. The absorption index, k, was determined directly from double pass transmission measurements while precisely varying the depth of slag above the mirror. At longer wavelengths the absorption of slag is very high and the submerged reflector technique described above is unable to produce films thin enough to allow transmittance measurements. Therefore, near-normal reflectance measurements were made and the Kramers-Kronig relations were used to determine n and k.

The results were generally as expected from the earlier work of Goodwin. In the wavelength range below 4 μm the absorption index, k, depends on the Fe_2O_3 content of the slag. Increasing the Fe_2O_3 content generally increases k. The temperature dependence of k in this wavelength range generally agrees with the trends found in Goodwin's [11] measurements of k at lower temperatures. For slag produced in an oxidizing environment (e.g., air), k increases with increasing temperature in the 1-4 μm range.

At wavelengths in the range from 7-10 μm the absorption index is predominantly determined by the concentration of SiO_2 in the slag, and is attributable to Si–O–Si vibrational absorption. Compared to the SiO_2 absorption band seen in lower temperature slags and SiO_2 glasses, this absorption band for molten slag was broadened and shifted to somewhat longer wavelengths. A single damped harmonic oscillator (Lorentz oscillator) fitted the data reasonably well with errors $n - n_{\text{fit}}$ and $k - k_{\text{fit}}$ typically within ± 0.1.

In the wavelength range from approximately 5-8 μm the absorption index was not measured in this study. In this range k is too large to measure using the transmittance apparatus, and too small to compute from the Kramers-Kronig analysis of reflectance measurements. However, an empirical fit based on a two–phonon model of the absorption index was developed using data from Goodwin's lower temperature measurements of transmittance of thin wafers. This correlation matched the transmittance results at shorter wavelengths very well.

The real refractive index was typical of alumino-silicate glasses, with $n \sim 1.6$ at 1 μm and decreasing with increasing wavelength until reaching a minimum near 7-9 μm, where $n-1$ was typically small or negative. This region of normal dispersion was fitted very well by a mixture rule that used the composition and density of the material to predict n. In the 8-13 μm region the Lorentz oscillator model for the optical constants fitted the measured values as discussed above.

Once correlations for the optical constants were formulated, a computer code was developed to compute the optical constants over the wavelength range from 1-13 μm for a broad range of compositions. Composition distributions for five real ashes [17] were used to compute these optical constants distributions. The resulting n and k distributions were combined with size distribution data for these ashes and Mie theory was used to compute the scattering and absorption properties for dispersions of the various ashes in a transparent gas. These results were combined with estimates of typical ash loadings in coal combustors and radiative properties were computed. Specifically, the spectral scattering coefficient, σ_λ, absorption coefficient, α_λ, and scattering phase function,Φ_λ, for typical ash dispersions were computed. A simplified scattering phase function consisting of isotropic plus forward scattered components was used to simplify the subsequent radiative transfer calculations.

The radiative properties of several fly ash distributions were computed. In the wavelength range from 1-4 μm the ash dispersion behaves predominantly as a scattering medium, with scattering albedo $\omega_\lambda = \sigma_\lambda/(\sigma_\lambda + \alpha_\lambda) \geq 0.95$. In the wavelength range from 8-13 μm the ash is a good absorber, with $\omega_\lambda < 0.4$. For ashes with similar compositions and the same volumetric loading, the extinction coefficient, $\beta_\lambda = \alpha_\lambda + \sigma_\lambda$, is larger for dispersions with smaller particles and/or a broader distribution of sizes† . This increase in β_λ is primarily due to the fact that

† Note that Ghosal found that ashes with smaller area median diameters typically also had broader size distributions.

for typical ash particle sizes of interest the particle size parameter, $x = \pi D/\lambda$, is of order unity or larger; thus the scattering efficiency, Q_s, for such particles typically varies slowly with x about the value $Q_s \sim 2$. Therefore, the scattered power for a uniform incident power flux (power/area) is roughly proportional to the surface area of all the particles ($\sim D^2$). An ash dispersion with a broader range of particle sizes or with a smaller mean size has a larger total surface area per unit volume of ash (i.e., smaller D_{32}), hence a larger scattering coefficient ($\sigma_\lambda \sim Q_s/D_{32}$). At the long wavelengths where absorption is strong ($kx > 1$) the absorption by a particle is also roughly proportional to its surface area. At shorter wavelengths where kx is small, the absorption coefficient is proportional to the volume of the particles, but this absorption contributes only a small part to the total extinction.

The effects of particle-to-particle composition variations on the radiative properties of an ash dispersion were also studied. It was found that only small errors were introduced by neglecting such composition variations and instead using mean ash compositions to estimate the optical constants. However, for ashes with higher Fe_2O_3 content, neglect of the particle to particle variations in Fe_2O_3 content causes slight underprediction of the absorption efficiency (Q_a) in the 1-4 μm wavelength range. Most of this effect is attributable to the approximately second order dependence of k on the iron content (Fe_2O_3) of the slag.

Representative radiative transfer calculations were made for dispersions of ash in a combustion products gas mixture containing CO_2 and H_2O for both an isothermal medium and for one in radiative equilibrium. The geometry was limited to a one-dimensional planar layer for simplicity. For an isothermal medium the fly ash increases the total emittance of the slab and decreases the total transmittance as compared to the same slab without the ash. The increase in emittance was primarily due to emission by the ash in the 1-5 μm wavelength range. In this range the emission by the ash increases with increasing Fe_2O_3 content. The decrease in transmittance due to scattering by added fly ash was significantly larger than the corresponding increase in emittance. For high ash loadings the transmittance of a 3 m slab of gas and ash could be as low as 40%, compared to approximately 70% for the same slab without ash.

A second radiation transfer calculation was made to study the effect of ash on heat transfer between black boundaries at fixed temperatures. In this calculation the ash temperature was computed by assuming that the medium was in radiative equilibrium. That is, the only mode of heat transfer through the medium is *via*

radiative transfer. The results showed that high ash loadings decrease the heat transfer between the walls by as much as a factor of 2-3, and that even moderate levels of ash loading significantly reduced the heat transfer.

The measurements and calculations presented in this study provide a basis for a more detailed and accurate understanding of radiative heat transfer in coal combustors. It has been demonstrated that the effects of particle composition, size distribution, and loading can be computed. Other applications, including development of improved diagnostics for gas temperature, ash loading, or particle size distribution may also benefit from this work.

There are several issues which remain unresolved and could benefit from additional research. Perhaps the most serious uncertainty in the procedures outlined here for computing the radiative properties of ash dispersions from optical constant is the presence of cenospheric particles. Ghosal [17] has deduced from density classification the fraction of non-solid particles in fly ash samples from six U.S. coals. Some samples (e.g., San Miguel ash) contain a very large mass fraction (97%) of particles with density less than $2.2 g/cm^3$, indicating that such particles had internal voids. Ashes with large fractions of such particles also tend to have very large particle sizes, with volume median diameters in the range from 20 to 40 μm common [17]. Further study of the effect of these non-solid particles on the radiative properties of ash dispersions is warranted.

Direct measurement of the radiative properties under well controlled laboratory condictions to confirm the calculations presented here would also be desirable; however, an issue that remains unresolved is how one can produce a suitably uniform dispersion of unagglomerated ash particles in a hot gaseous medium which is transparent to infrared radiation. During combustion the ash loading is low enough that particles do not significantly agglomerate; however, once the particles are collected (e.g., in a baghouse) the smaller ones tend to stick to the larger ones. When the particles are subsequently dispersed through sonic nozzles or other techniques it is found that one cannot completely separate the particles – small particles continue to stick to larger ones. Ghosal [17] overcame this problem by dispersing ashes in a liquid and providing continuous aggitation, but then one measures the refractive index relative to the liquid and at low temperature. The agglomeration problem can be overcome by performing direct measurements in a coal combustor [14], but complications due to radiation from the infrared active gases, soot, and char, and the scattered emission from hot regions of the furnace, along with many other practical

difficulties of making precise optical measurements in such a hostile environment, make such measurments very difficult and subject to great uncertainties.

Finally, while this work has presented some representative thermal radiation transfer calculations for an ideal geometry and conditions, the correlations and radiative properties given here should allow one to extend these calculations to more specific three dimensional geometries of interest to designers of coal combustors, taking account of heat release, flow, and other real factors such as slag and ash coated walls. In connection with such slag coatings, it should be noted that insofar as they are compacted solid (or liquid) slag layers (and not loosely compacted fly ash), the optical constants data represented here are of direct value in calculating radiant transfer through the layers.

Appendix A.

Tabulated Optical Properties of Molten Coal Slags

This appendix contains tables of results for the transmittance measurements, reflectance measurements and the computed real and imaginary refractive indices (n and k) for the nine slags studied in this work. The first three tables (A.1–A.3) contain the results of transmittance measurements. The last nine tables (A.4-A.12) contain the results of near normal reflectance measurements and the resulting n and k found through the Kramers–Kronig analysis presented in Chapter II, Section II.2.2.

Table A.1: Absorption index of molten slag SA01.

$\lambda(\mu m)$	k	$\lambda(\mu m)$	k
1.0	4.50×10^{-5}	2.3	3.98×10^{-5}
1.1	4.11×10^{-5}	2.4	3.88×10^{-5}
1.2	4.83×10^{-5}	2.6	3.76×10^{-5}
1.3	4.44×10^{-5}	2.8	6.40×10^{-5}
1.4	4.08×10^{-5}	3.0	6.27×10^{-5}
1.5	3.99×10^{-5}	3.2	6.32×10^{-5}
1.6	3.97×10^{-5}	3.4	6.88×10^{-5}
1.7	3.96×10^{-5}	3.6	9.44×10^{-5}
1.8	4.09×10^{-5}	3.8	1.44×10^{-4}
1.9	3.91×10^{-5}	4.0	2.04×10^{-4}
2.0	4.13×10^{-5}	4.2	3.51×10^{-4}
2.1	3.83×10^{-5}	4.6	1.05×10^{-3}
2.2	3.62×10^{-5}		

Table A.2: Absorption index of molten slag SA05.

$\lambda(\mu m)$	k	$\lambda(\mu m)$	k
1.0	3.09×10^{-4}	2.6	3.16×10^{-4}
1.1	3.15×10^{-4}	2.8	3.51×10^{-4}
1.2	3.63×10^{-4}	3.0	3.31×10^{-4}
1.3	3.42×10^{-4}	3.2	3.32×10^{-4}
1.4	3.46×10^{-4}	3.4	3.28×10^{-4}
1.5	3.51×10^{-4}	3.6	3.48×10^{-4}
1.6	3.17×10^{-4}	3.8	3.88×10^{-4}
1.7	2.88×10^{-4}	4.0	4.89×10^{-4}
1.8	3.25×10^{-4}	4.2	6.09×10^{-4}
1.9	3.07×10^{-4}	4.4	8.39×10^{-4}
2.0	3.23×10^{-4}	4.6	1.29×10^{-3}
2.2	3.30×10^{-4}	4.8	1.72×10^{-3}
2.4	3.29×10^{-4}	5.0	2.72×10^{-3}

Table A.3: Absorption index of molten slag SA4S.

$\lambda(\mu m)$	k	$\lambda(\mu m)$	k
1.0	1.50×10^{-4}	3.2	1.41×10^{-4}
1.1	1.46×10^{-4}	3.3	1.41×10^{-4}
1.2	1.42×10^{-4}	3.4	1.48×10^{-4}
1.3	1.38×10^{-4}	3.5	1.54×10^{-4}
1.4	1.29×10^{-4}	3.6	1.59×10^{-4}
1.5	1.28×10^{-4}	3.7	1.71×10^{-4}
1.6	1.19×10^{-4}	3.8	1.85×10^{-4}
1.7	1.20×10^{-4}	3.9	1.92×10^{-4}
1.8	1.17×10^{-4}	4.0	2.03×10^{-4}
1.9	1.22×10^{-4}	4.1	2.33×10^{-4}
2.0	1.17×10^{-4}	4.2	2.66×10^{-4}
2.1	1.17×10^{-4}	4.4	3.89×10^{-4}
2.2	1.14×10^{-4}	4.5	4.51×10^{-4}
2.3	1.15×10^{-4}	4.6	6.17×10^{-4}
2.4	1.16×10^{-4}	4.7	8.01×10^{-4}
2.5	1.24×10^{-4}	4.8	1.04×10^{-3}
2.6	1.25×10^{-4}	4.9	1.39×10^{-3}
2.7	1.22×10^{-4}	5.0	1.83×10^{-3}
2.8	1.36×10^{-4}	5.1	2.14×10^{-3}
2.9	1.43×10^{-4}	5.2	2.68×10^{-3}
3.0	1.40×10^{-4}	5.3	3.41×10^{-3}
3.1	1.41×10^{-4}		

Table A.4: Molten slag SA00

$\lambda(\mu m)$	R	n	k	$\lambda(\mu m)$	R	n	k
1.10	4.207×10^{-2}	1.52	–	7.80	5.940×10^{-3}	1.16	–
1.20	4.203×10^{-2}	1.52	–	7.90	4.754×10^{-3}	1.14	–
1.30	4.212×10^{-2}	1.52	–	8.00	3.738×10^{-3}	1.11	–
1.40	4.165×10^{-2}	1.51	–	8.10	3.158×10^{-3}	1.08	–
1.50	4.124×10^{-2}	1.51	–	8.20	3.403×10^{-3}	1.05	1.09×10^{-1}
1.60	4.155×10^{-2}	1.51	–	8.30	5.070×10^{-3}	1.02	1.43×10^{-1}
1.80	4.079×10^{-2}	1.51	–	8.40	8.852×10^{-3}	0.99	1.87×10^{-1}
2.00	4.043×10^{-2}	1.50	–	8.50	1.578×10^{-2}	0.96	2.44×10^{-1}
2.20	4.015×10^{-2}	1.50	–	8.60	2.568×10^{-2}	0.94	3.10×10^{-1}
2.40	4.014×10^{-2}	1.50	–	8.70	3.784×10^{-2}	0.94	3.80×10^{-1}
2.60	3.987×10^{-2}	1.50	–	8.80	5.155×10^{-2}	0.95	4.53×10^{-1}
2.80	3.888×10^{-2}	1.49	–	8.90	6.471×10^{-2}	0.98	5.20×10^{-1}
3.00	3.853×10^{-2}	1.49	–	9.00	7.648×10^{-2}	1.01	5.79×10^{-1}
3.20	3.851×10^{-2}	1.49	–	9.10	8.738×10^{-2}	1.05	6.33×10^{-1}
3.40	3.795×10^{-2}	1.48	–	9.20	9.684×10^{-2}	1.10	6.79×10^{-1}
3.60	3.741×10^{-2}	1.48	–	9.30	1.064×10^{-1}	1.15	7.24×10^{-1}
3.80	3.677×10^{-2}	1.47	–	9.40	1.140×10^{-1}	1.20	7.60×10^{-1}
4.00	3.589×10^{-2}	1.47	–	9.50	1.211×10^{-1}	1.26	7.92×10^{-1}
4.20	3.463×10^{-2}	1.46	–	9.60	1.271×10^{-1}	1.33	8.16×10^{-1}
4.40	3.321×10^{-2}	1.44	–	9.70	1.316×10^{-1}	1.39	8.31×10^{-1}
4.60	3.298×10^{-2}	1.44	–	9.80	1.346×10^{-1}	1.46	8.35×10^{-1}
4.80	3.208×10^{-2}	1.43	–	9.90	1.368×10^{-1}	1.52	8.32×10^{-1}
5.00	3.091×10^{-2}	1.43	–	10.00	1.384×10^{-1}	1.59	8.21×10^{-1}
5.20	2.967×10^{-2}	1.41	–	10.20	1.374×10^{-1}	1.70	7.68×10^{-1}
5.40	2.868×10^{-2}	1.41	–	10.40	1.334×10^{-1}	1.79	6.94×10^{-1}
5.60	2.719×10^{-2}	1.39	–	10.60	1.298×10^{-1}	1.84	6.22×10^{-1}
5.80	2.589×10^{-2}	1.38	–	10.80	1.252×10^{-1}	1.88	5.44×10^{-1}
6.00	2.515×10^{-2}	1.38	–	11.00	1.194×10^{-1}	1.90	4.69×10^{-1}
6.20	2.341×10^{-2}	1.36	–	11.20	1.142×10^{-1}	1.90	4.05×10^{-1}
6.40	2.217×10^{-2}	1.35	–	11.40	1.096×10^{-1}	1.90	3.46×10^{-1}
6.60	1.995×10^{-2}	1.33	–	11.60	1.032×10^{-1}	1.89	2.86×10^{-1}
6.80	1.813×10^{-2}	1.31	–	11.80	9.589×10^{-2}	1.85	2.44×10^{-1}
7.00	1.608×10^{-2}	1.29	–	12.00	9.038×10^{-2}	1.82	2.21×10^{-1}
7.20	1.371×10^{-2}	1.27	–	12.20	8.542×10^{-2}	1.79	2.07×10^{-1}
7.40	1.131×10^{-2}	1.24	–	12.40	8.164×10^{-2}	1.77	2.02×10^{-1}
7.60	8.622×10^{-3}	1.20	–	12.60	7.905×10^{-2}	1.75	2.04×10^{-1}
7.70	7.385×10^{-3}	1.19	–				

Table A.5: Molten slag SA01

$\lambda(\mu m)$	R	n	k	$\lambda(\mu m)$	R	n	k
1.10	4.333×10^{-2}	1.53	–	7.80	6.737×10^{-3}	1.17	–
1.20	4.318×10^{-2}	1.52	–	7.90	5.404×10^{-3}	1.15	–
1.30	4.287×10^{-2}	1.52	–	8.00	4.300×10^{-3}	1.13	–
1.40	4.331×10^{-2}	1.53	–	8.10	3.527×10^{-3}	1.10	–
1.50	4.299×10^{-2}	1.52	–	8.20	3.425×10^{-3}	1.06	1.03×10^{-1}
1.60	4.384×10^{-2}	1.53	–	8.30	4.696×10^{-3}	1.03	1.36×10^{-1}
1.80	4.328×10^{-2}	1.52	–	8.40	7.775×10^{-3}	1.00	1.77×10^{-1}
2.00	4.245×10^{-2}	1.52	–	8.50	1.379×10^{-2}	0.97	2.31×10^{-1}
2.20	4.191×10^{-2}	1.51	–	8.60	2.264×10^{-2}	0.95	2.94×10^{-1}
2.40	4.151×10^{-2}	1.51	–	8.70	3.430×10^{-2}	0.95	3.63×10^{-1}
2.60	4.077×10^{-2}	1.50	–	8.80	4.724×10^{-2}	0.96	4.33×10^{-1}
2.80	3.964×10^{-2}	1.50	–	8.90	6.056×10^{-2}	0.98	5.01×10^{-1}
3.00	3.972×10^{-2}	1.50	–	9.00	7.234×10^{-2}	1.01	5.61×10^{-1}
3.20	3.930×10^{-2}	1.49	–	9.10	8.353×10^{-2}	1.05	6.16×10^{-1}
3.40	3.871×10^{-2}	1.49	–	9.20	9.356×10^{-2}	1.09	6.64×10^{-1}
3.60	3.804×10^{-2}	1.48	–	9.30	1.032×10^{-1}	1.14	7.10×10^{-1}
3.80	3.742×10^{-2}	1.48	–	9.40	1.105×10^{-1}	1.19	7.45×10^{-1}
4.00	3.706×10^{-2}	1.48	–	9.50	1.180×10^{-1}	1.24	7.79×10^{-1}
4.20	3.564×10^{-2}	1.46	–	9.60	1.247×10^{-1}	1.30	8.07×10^{-1}
4.40	3.430×10^{-2}	1.45	–	9.70	1.301×10^{-1}	1.36	8.27×10^{-1}
4.60	3.412×10^{-2}	1.45	–	9.80	1.332×10^{-1}	1.43	8.34×10^{-1}
4.80	3.319×10^{-2}	1.44	–	9.90	1.365×10^{-1}	1.49	8.38×10^{-1}
5.00	3.195×10^{-2}	1.43	–	10.00	1.378×10^{-1}	1.56	8.28×10^{-1}
5.20	3.068×10^{-2}	1.42	–	10.20	1.384×10^{-1}	1.67	7.91×10^{-1}
5.40	2.988×10^{-2}	1.42	–	10.40	1.360×10^{-1}	1.75	7.32×10^{-1}
5.60	2.871×10^{-2}	1.41	–	10.60	1.336×10^{-1}	1.82	6.70×10^{-1}
5.80	2.751×10^{-2}	1.40	–	10.80	1.309×10^{-1}	1.88	6.01×10^{-1}
6.00	2.659×10^{-2}	1.39	–	11.00	1.255×10^{-1}	1.91	5.23×10^{-1}
6.20	2.511×10^{-2}	1.38	–	11.20	1.207×10^{-1}	1.92	4.55×10^{-1}
6.40	2.288×10^{-2}	1.36	–	11.40	1.156×10^{-1}	1.92	3.89×10^{-1}
6.60	2.125×10^{-2}	1.34	–	11.60	1.093×10^{-1}	1.91	3.29×10^{-1}
6.80	1.922×10^{-2}	1.32	–	11.80	1.029×10^{-1}	1.89	2.82×10^{-1}
7.00	1.738×10^{-2}	1.30	–	12.00	9.704×10^{-2}	1.86	2.49×10^{-1}
7.20	1.485×10^{-2}	1.28	–	12.20	9.177×10^{-2}	1.83	2.27×10^{-1}
7.40	1.234×10^{-2}	1.25	–	12.40	8.713×10^{-2}	1.80	2.15×10^{-1}
7.60	9.494×10^{-3}	1.21	–	12.60	8.369×10^{-2}	1.78	2.12×10^{-1}
7.70	8.109×10^{-3}	1.20	–				

Table A.6: Molten slag SA05

$\lambda(\mu m)$	R	n	k	$\lambda(\mu m)$	R	n	k
1.10	4.356×10^{-2}	1.53	–	7.80	7.826×10^{-3}	1.19	–
1.20	4.359×10^{-2}	1.53	–	7.90	6.527×10^{-3}	1.17	–
1.30	4.359×10^{-2}	1.53	–	8.00	5.214×10^{-3}	1.15	–
1.40	4.327×10^{-2}	1.53	–	8.10	4.233×10^{-3}	1.12	–
1.50	4.258×10^{-2}	1.52	–	8.20	3.649×10^{-3}	1.09	9.18×10^{-2}
1.60	4.265×10^{-2}	1.52	–	8.30	4.214×10^{-3}	1.06	1.22×10^{-1}
1.80	4.267×10^{-2}	1.52	–	8.40	6.353×10^{-3}	1.02	1.60×10^{-1}
2.00	4.223×10^{-2}	1.52	–	8.50	1.085×10^{-2}	1.00	2.09×10^{-1}
2.20	4.203×10^{-2}	1.52	–	8.60	1.850×10^{-2}	0.97	2.70×10^{-1}
2.40	4.195×10^{-2}	1.51	–	8.70	2.826×10^{-2}	0.97	3.34×10^{-1}
2.60	4.207×10^{-2}	1.52	–	8.80	4.065×10^{-2}	0.97	4.05×10^{-1}
2.80	4.086×10^{-2}	1.51	–	8.90	5.280×10^{-2}	0.99	4.70×10^{-1}
3.00	4.068×10^{-2}	1.50	–	9.00	6.479×10^{-2}	1.02	5.31×10^{-1}
3.20	3.993×10^{-2}	1.50	–	9.10	7.529×10^{-2}	1.05	5.83×10^{-1}
3.40	3.966×10^{-2}	1.50	–	9.20	8.558×10^{-2}	1.09	6.33×10^{-1}
3.60	3.947×10^{-2}	1.50	–	9.30	9.450×10^{-2}	1.14	6.75×10^{-1}
3.80	3.853×10^{-2}	1.49	–	9.40	1.031×10^{-1}	1.19	7.15×10^{-1}
4.00	3.813×10^{-2}	1.48	–	9.50	1.093×10^{-1}	1.24	7.42×10^{-1}
4.20	3.716×10^{-2}	1.48	–	9.60	1.170×10^{-1}	1.30	7.74×10^{-1}
4.40	3.510×10^{-2}	1.46	–	9.70	1.219×10^{-1}	1.36	7.91×10^{-1}
4.60	3.499×10^{-2}	1.46	–	9.80	1.261×10^{-1}	1.42	8.02×10^{-1}
4.80	3.422×10^{-2}	1.45	–	9.90	1.282×10^{-1}	1.48	8.01×10^{-1}
5.00	3.302×10^{-2}	1.44	–	10.00	1.316×10^{-1}	1.54	8.03×10^{-1}
5.20	3.192×10^{-2}	1.43	–	10.20	1.326×10^{-1}	1.65	7.67×10^{-1}
5.40	3.078×10^{-2}	1.42	–	10.40	1.310×10^{-1}	1.73	7.14×10^{-1}
5.60	2.936×10^{-2}	1.41	–	10.60	1.291×10^{-1}	1.80	6.57×10^{-1}
5.80	2.838×10^{-2}	1.40	–	10.80	1.273×10^{-1}	1.85	5.94×10^{-1}
6.00	2.700×10^{-2}	1.39	–	11.00	1.222×10^{-1}	1.88	5.21×10^{-1}
6.20	2.623×10^{-2}	1.39	–	11.20	1.197×10^{-1}	1.91	4.63×10^{-1}
6.40	2.426×10^{-2}	1.37	–	11.40	1.148×10^{-1}	1.92	3.92×10^{-1}
6.60	2.222×10^{-2}	1.35	–	11.60	1.087×10^{-1}	1.91	3.28×10^{-1}
6.80	2.057×10^{-2}	1.33	–	11.80	1.014×10^{-1}	1.88	2.79×10^{-1}
7.00	1.847×10^{-2}	1.31	–	12.00	9.640×10^{-2}	1.85	2.47×10^{-1}
7.20	1.601×10^{-2}	1.29	–	12.20	9.024×10^{-2}	1.82	2.23×10^{-1}
7.40	1.342×10^{-2}	1.26	–	12.40	8.604×10^{-2}	1.79	2.14×10^{-1}
7.60	1.084×10^{-2}	1.23	–	12.60	8.253×10^{-2}	1.77	2.12×10^{-1}
7.70	9.441×10^{-3}	1.21	–				

Table A.7: Molten slag SA10

$\lambda(\mu m)$	R	n	k	$\lambda(\mu m)$	R	n	k
1.10	4.806×10^{-2}	1.56	–	7.80	9.909×10^{-3}	1.22	–
1.20	4.830×10^{-2}	1.56	–	7.90	8.211×10^{-3}	1.20	–
1.30	4.802×10^{-2}	1.56	–	8.00	6.890×10^{-3}	1.17	–
1.40	4.760×10^{-2}	1.56	–	8.10	5.502×10^{-3}	1.15	–
1.50	4.753×10^{-2}	1.56	–	8.20	4.658×10^{-3}	1.12	–
1.60	4.737×10^{-2}	1.56	–	8.30	4.495×10^{-3}	1.09	1.10×10^{-1}
1.80	4.649×10^{-2}	1.55	–	8.40	5.659×10^{-3}	1.06	1.45×10^{-1}
2.00	4.615×10^{-2}	1.55	–	8.50	9.024×10^{-3}	1.03	1.91×10^{-1}
2.20	4.558×10^{-2}	1.54	–	8.60	1.482×10^{-2}	1.01	2.46×10^{-1}
2.40	4.542×10^{-2}	1.54	–	8.70	2.349×10^{-2}	0.99	3.09×10^{-1}
2.60	4.498×10^{-2}	1.54	–	8.80	3.408×10^{-2}	1.00	3.75×10^{-1}
2.80	4.384×10^{-2}	1.53	–	8.90	4.585×10^{-2}	1.01	4.41×10^{-1}
3.00	4.344×10^{-2}	1.53	–	9.00	5.756×10^{-2}	1.04	5.02×10^{-1}
3.20	4.336×10^{-2}	1.53	–	9.10	6.706×10^{-2}	1.07	5.51×10^{-1}
3.40	4.253×10^{-2}	1.52	–	9.20	7.733×10^{-2}	1.11	6.00×10^{-1}
3.60	4.232×10^{-2}	1.52	–	9.30	8.650×10^{-2}	1.15	6.43×10^{-1}
3.80	4.166×10^{-2}	1.51	–	9.40	9.437×10^{-2}	1.20	6.78×10^{-1}
4.00	4.119×10^{-2}	1.51	–	9.50	1.012×10^{-1}	1.24	7.07×10^{-1}
4.20	3.961×10^{-2}	1.50	–	9.60	1.089×10^{-1}	1.30	7.39×10^{-1}
4.40	3.846×10^{-2}	1.49	–	9.70	1.124×10^{-1}	1.35	7.49×10^{-1}
4.60	3.838×10^{-2}	1.49	–	9.80	1.180×10^{-1}	1.41	7.66×10^{-1}
4.80	3.734×10^{-2}	1.48	–	9.90	1.189×10^{-1}	1.46	7.60×10^{-1}
5.00	3.622×10^{-2}	1.47	–	10.00	1.235×10^{-1}	1.51	7.69×10^{-1}
5.20	3.474×10^{-2}	1.46	–	10.20	1.258×10^{-1}	1.61	7.45×10^{-1}
5.40	3.357×10^{-2}	1.45	–	10.40	1.259×10^{-1}	1.69	7.05×10^{-1}
5.60	3.248×10^{-2}	1.44	–	10.60	1.258×10^{-1}	1.76	6.62×10^{-1}
5.80	3.120×10^{-2}	1.43	–	10.80	1.242×10^{-1}	1.81	6.08×10^{-1}
6.00	3.014×10^{-2}	1.42	–	11.00	1.221×10^{-1}	1.85	5.52×10^{-1}
6.20	2.870×10^{-2}	1.41	–	11.20	1.189×10^{-1}	1.88	4.93×10^{-1}
6.40	2.675×10^{-2}	1.39	–	11.40	1.153×10^{-1}	1.89	4.34×10^{-1}
6.60	2.500×10^{-2}	1.37	–	11.60	1.100×10^{-1}	1.89	3.78×10^{-1}
6.80	2.276×10^{-2}	1.35	–	11.80	1.051×10^{-1}	1.88	3.34×10^{-1}
7.00	2.107×10^{-2}	1.34	–	12.00	1.004×10^{-1}	1.86	2.97×10^{-1}
7.20	1.836×10^{-2}	1.31	–	12.20	9.510×10^{-2}	1.84	2.71×10^{-1}
7.40	1.584×10^{-2}	1.29	–	12.40	9.169×10^{-2}	1.82	2.58×10^{-1}
7.60	1.283×10^{-2}	1.26	–	12.60	8.799×10^{-2}	1.79	2.49×10^{-1}
7.70	1.134×10^{-2}	1.24	–				

Table A.8: Molten slag SA20

$\lambda(\mu m)$	R	n	k	$\lambda(\mu m)$	R	n	k
1.10	5.055×10^{-2}	1.58	–	7.80	1.436×10^{-2}	1.27	–
1.20	5.051×10^{-2}	1.58	–	7.90	1.278×10^{-2}	1.25	–
1.30	5.096×10^{-2}	1.58	–	8.00	1.118×10^{-2}	1.23	–
1.40	5.001×10^{-2}	1.58	–	8.10	9.531×10^{-3}	1.21	–
1.50	4.971×10^{-2}	1.57	–	8.20	7.993×10^{-3}	1.19	–
1.60	5.015×10^{-2}	1.58	–	8.30	6.823×10^{-3}	1.16	–
1.80	5.014×10^{-2}	1.58	–	8.40	6.341×10^{-3}	1.13	1.10×10^{-1}
2.00	4.945×10^{-2}	1.57	–	8.50	7.052×10^{-3}	1.10	1.45×10^{-1}
2.20	4.893×10^{-2}	1.57	–	8.60	9.540×10^{-3}	1.08	1.88×10^{-1}
2.40	4.862×10^{-2}	1.57	–	8.70	1.413×10^{-2}	1.06	2.39×10^{-1}
2.60	4.870×10^{-2}	1.57	–	8.80	2.182×10^{-2}	1.05	3.02×10^{-1}
2.80	4.721×10^{-2}	1.55	–	8.90	2.967×10^{-2}	1.06	3.55×10^{-1}
3.00	4.765×10^{-2}	1.56	–	9.00	3.917×10^{-2}	1.07	4.12×10^{-1}
3.20	4.677×10^{-2}	1.55	–	9.10	4.814×10^{-2}	1.09	4.61×10^{-1}
3.40	4.623×10^{-2}	1.55	–	9.20	5.918×10^{-2}	1.12	5.17×10^{-1}
3.60	4.580×10^{-2}	1.54	–	9.30	6.582×10^{-2}	1.16	5.49×10^{-1}
3.80	4.535×10^{-2}	1.54	–	9.40	7.507×10^{-2}	1.20	5.91×10^{-1}
4.00	4.514×10^{-2}	1.54	–	9.50	8.049×10^{-2}	1.24	6.14×10^{-1}
4.20	4.383×10^{-2}	1.53	–	9.60	8.917×10^{-2}	1.28	6.50×10^{-1}
4.40	4.241×10^{-2}	1.52	–	9.70	9.272×10^{-2}	1.32	6.61×10^{-1}
4.60	4.247×10^{-2}	1.52	–	9.80	9.876×10^{-2}	1.37	6.81×10^{-1}
4.80	4.163×10^{-2}	1.51	–	9.90	1.011×10^{-1}	1.41	6.84×10^{-1}
5.00	4.030×10^{-2}	1.50	–	10.00	1.074×10^{-1}	1.45	7.04×10^{-1}
5.20	3.916×10^{-2}	1.49	–	10.20	1.114×10^{-1}	1.54	6.94×10^{-1}
5.40	3.792×10^{-2}	1.48	–	10.40	1.149×10^{-1}	1.61	6.80×10^{-1}
5.60	3.692×10^{-2}	1.47	–	10.60	1.168×10^{-1}	1.68	6.52×10^{-1}
5.80	3.513×10^{-2}	1.46	–	10.80	1.172×10^{-1}	1.74	6.15×10^{-1}
6.00	3.449×10^{-2}	1.46	–	11.00	1.161×10^{-1}	1.78	5.74×10^{-1}
6.20	3.278×10^{-2}	1.44	–	11.20	1.163×10^{-1}	1.82	5.37×10^{-1}
6.40	3.096×10^{-2}	1.43	–	11.40	1.142×10^{-1}	1.85	4.86×10^{-1}
6.60	2.908×10^{-2}	1.41	–	11.60	1.115×10^{-1}	1.86	4.37×10^{-1}
6.80	2.745×10^{-2}	1.40	–	11.80	1.067×10^{-1}	1.86	3.87×10^{-1}
7.00	2.530×10^{-2}	1.38	–	12.00	1.022×10^{-1}	1.85	3.52×10^{-1}
7.20	2.291×10^{-2}	1.36	–	12.20	9.876×10^{-2}	1.83	3.27×10^{-1}
7.40	2.019×10^{-2}	1.33	–	12.40	9.525×10^{-2}	1.82	3.09×10^{-1}
7.60	1.750×10^{-2}	1.30	–	12.60	9.272×10^{-2}	1.80	3.00×10^{-1}
7.70	1.601×10^{-2}	1.29	–				

Table A.9: Molten slag SA4S

$\lambda(\mu m)$	R	n	k	$\lambda(\mu m)$	R	n	k
1.10	5.037×10^{-2}	1.58	–	6.80	2.928×10^{-2}	1.41	–
1.20	5.013×10^{-2}	1.58	–	7.00	2.767×10^{-2}	1.40	–
1.30	5.060×10^{-2}	1.58	–	7.20	2.572×10^{-2}	1.38	–
1.40	5.012×10^{-2}	1.58	–	7.40	2.352×10^{-2}	1.36	–
1.50	4.972×10^{-2}	1.57	–	7.60	2.124×10^{-2}	1.34	–
1.60	4.985×10^{-2}	1.57	–	7.80	1.876×10^{-2}	1.32	–
1.80	4.947×10^{-2}	1.57	–	8.00	1.617×10^{-2}	1.29	–
2.00	4.946×10^{-2}	1.57	–	8.20	1.324×10^{-2}	1.26	–
2.20	4.900×10^{-2}	1.57	–	8.40	1.025×10^{-2}	1.22	–
2.40	4.874×10^{-2}	1.57	–	8.60	7.603×10^{-3}	1.18	–
2.60	4.955×10^{-2}	1.57	–	8.80	6.284×10^{-3}	1.13	1.10×10^{-1}
2.80	4.761×10^{-2}	1.56	–	9.00	8.450×10^{-3}	1.09	1.72×10^{-1}
3.00	4.763×10^{-2}	1.56	–	9.20	1.626×10^{-2}	1.05	2.58×10^{-1}
3.20	4.748×10^{-2}	1.56	–	9.40	2.995×10^{-2}	1.04	3.56×10^{-1}
3.40	4.652×10^{-2}	1.55	–	9.60	4.837×10^{-2}	1.07	4.61×10^{-1}
3.60	4.614×10^{-2}	1.55	–	9.80	6.689×10^{-2}	1.11	5.54×10^{-1}
3.80	4.558×10^{-2}	1.54	–	10.00	8.392×10^{-2}	1.18	6.32×10^{-1}
4.00	4.481×10^{-2}	1.54	–	10.20	9.762×10^{-2}	1.27	6.91×10^{-1}
4.20	4.330×10^{-2}	1.52	–	10.40	1.080×10^{-1}	1.36	7.28×10^{-1}
4.40	4.149×10^{-2}	1.51	–	10.60	1.146×10^{-1}	1.45	7.41×10^{-1}
4.60	4.218×10^{-2}	1.52	–	10.80	1.190×10^{-1}	1.53	7.37×10^{-1}
4.80	4.127×10^{-2}	1.51	–	11.00	1.212×10^{-1}	1.61	7.19×10^{-1}
5.00	4.037×10^{-2}	1.50	–	11.20	1.233×10^{-1}	1.68	6.96×10^{-1}
5.20	3.913×10^{-2}	1.49	–	11.40	1.230×10^{-1}	1.74	6.55×10^{-1}
5.40	3.823×10^{-2}	1.49	–	11.60	1.211×10^{-1}	1.78	6.08×10^{-1}
5.60	3.728×10^{-2}	1.48	–	11.80	1.181×10^{-1}	1.81	5.59×10^{-1}
5.80	3.641×10^{-2}	1.47	–	12.00	1.160×10^{-1}	1.84	5.14×10^{-1}
6.00	3.526×10^{-2}	1.46	–	12.20	1.118×10^{-1}	1.85	4.62×10^{-1}
6.20	3.417×10^{-2}	1.45	–	12.40	1.059×10^{-1}	1.83	4.17×10^{-1}
6.40	3.314×10^{-2}	1.44	–	12.60	1.019×10^{-1}	1.82	3.90×10^{-1}
6.60	3.128×10^{-2}	1.43	–				

Table A.10: Molten slag SA2S

$\lambda(\mu m)$	R	n	k	$\lambda(\mu m)$	R	n	k
1.10	5.405×10^{-2}	1.61	–	6.80	3.246×10^{-2}	1.44	–
1.20	5.340×10^{-2}	1.60	–	7.00	3.098×10^{-2}	1.43	–
1.30	5.387×10^{-2}	1.60	–	7.20	2.980×10^{-2}	1.42	–
1.40	5.293×10^{-2}	1.60	–	7.40	2.796×10^{-2}	1.40	–
1.50	5.267×10^{-2}	1.60	–	7.60	2.581×10^{-2}	1.38	–
1.60	5.270×10^{-2}	1.60	–	7.80	2.418×10^{-2}	1.37	–
1.80	5.188×10^{-2}	1.59	–	8.00	2.222×10^{-2}	1.35	–
2.00	5.165×10^{-2}	1.59	–	8.20	1.972×10^{-2}	1.33	–
2.20	5.138×10^{-2}	1.59	–	8.40	1.731×10^{-2}	1.30	–
2.40	5.093×10^{-2}	1.58	–	8.60	1.476×10^{-2}	1.28	–
2.60	5.051×10^{-2}	1.58	–	8.80	1.193×10^{-2}	1.24	–
2.80	4.972×10^{-2}	1.57	–	9.00	9.527×10^{-3}	1.20	–
3.00	4.946×10^{-2}	1.57	–	9.20	8.618×10^{-3}	1.17	1.10×10^{-1}
3.20	4.929×10^{-2}	1.57	–	9.40	1.020×10^{-2}	1.14	1.65×10^{-1}
3.40	4.894×10^{-2}	1.57	–	9.60	1.535×10^{-2}	1.13	2.33×10^{-1}
3.60	4.848×10^{-2}	1.56	–	9.80	2.391×10^{-2}	1.13	3.07×10^{-1}
3.80	4.823×10^{-2}	1.56	–	10.00	3.426×10^{-2}	1.15	3.75×10^{-1}
4.00	4.792×10^{-2}	1.56	–	10.20	4.505×10^{-2}	1.19	4.35×10^{-1}
4.20	4.648×10^{-2}	1.55	–	10.40	5.398×10^{-2}	1.23	4.77×10^{-1}
4.40	4.496×10^{-2}	1.54	–	10.60	6.210×10^{-2}	1.28	5.11×10^{-1}
4.60	4.573×10^{-2}	1.54	–	10.80	6.877×10^{-2}	1.32	5.35×10^{-1}
4.80	4.463×10^{-2}	1.53	–	11.00	7.369×10^{-2}	1.36	5.49×10^{-1}
5.00	4.377×10^{-2}	1.53	–	11.20	7.962×10^{-2}	1.40	5.68×10^{-1}
5.20	4.245×10^{-2}	1.52	–	11.40	8.401×10^{-2}	1.45	5.76×10^{-1}
5.40	4.149×10^{-2}	1.51	–	11.60	8.733×10^{-2}	1.48	5.78×10^{-1}
5.60	4.049×10^{-2}	1.50	–	11.80	9.076×10^{-2}	1.52	5.82×10^{-1}
5.80	3.944×10^{-2}	1.49	–	12.00	9.477×10^{-2}	1.56	5.85×10^{-1}
6.00	3.871×10^{-2}	1.49	–	12.20	9.700×10^{-2}	1.59	5.77×10^{-1}
6.20	3.750×10^{-2}	1.48	–	12.40	9.847×10^{-2}	1.62	5.67×10^{-1}
6.40	3.666×10^{-2}	1.47	–	12.60	1.002×10^{-1}	1.65	5.58×10^{-1}
6.60	3.398×10^{-2}	1.45	–				

Table A.11: Molten slag SA1S

$\lambda(\mu m)$	R	n	k	$\lambda(\mu m)$	R	n	k
1.10	5.414×10^{-2}	1.61	–	6.80	3.604×10^{-2}	1.47	–
1.20	5.432×10^{-2}	1.61	–	7.00	3.456×10^{-2}	1.46	–
1.30	5.418×10^{-2}	1.61	–	7.20	3.349×10^{-2}	1.45	–
1.40	5.413×10^{-2}	1.61	–	7.40	3.171×10^{-2}	1.43	–
1.50	5.391×10^{-2}	1.60	–	7.60	3.016×10^{-2}	1.42	–
1.60	5.329×10^{-2}	1.60	–	7.80	2.835×10^{-2}	1.40	–
1.80	5.325×10^{-2}	1.60	–	8.00	2.711×10^{-2}	1.39	–
2.00	5.238×10^{-2}	1.59	–	8.20	2.484×10^{-2}	1.37	–
2.20	5.203×10^{-2}	1.59	–	8.40	2.308×10^{-2}	1.36	–
2.40	5.238×10^{-2}	1.59	–	8.60	2.094×10^{-2}	1.34	–
2.60	5.216×10^{-2}	1.59	–	8.80	1.855×10^{-2}	1.32	–
2.80	5.091×10^{-2}	1.58	–	9.00	1.573×10^{-2}	1.29	–
3.00	5.130×10^{-2}	1.59	–	9.20	1.343×10^{-2}	1.26	–
3.20	5.062×10^{-2}	1.58	–	9.40	1.100×10^{-2}	1.23	–
3.40	5.031×10^{-2}	1.58	–	9.60	9.460×10^{-3}	1.19	9.64×10^{-2}
3.60	4.970×10^{-2}	1.57	–	9.80	1.007×10^{-2}	1.16	1.42×10^{-1}
3.80	4.980×10^{-2}	1.57	–	10.00	1.298×10^{-2}	1.15	1.95×10^{-1}
4.00	4.909×10^{-2}	1.57	–	10.20	1.806×10^{-2}	1.15	2.51×10^{-1}
4.20	4.860×10^{-2}	1.56	–	10.40	2.432×10^{-2}	1.15	3.03×10^{-1}
4.40	4.630×10^{-2}	1.55	–	10.60	3.091×10^{-2}	1.16	3.49×10^{-1}
4.60	4.699×10^{-2}	1.55	–	10.80	3.774×10^{-2}	1.18	3.91×10^{-1}
4.80	4.673×10^{-2}	1.55	–	11.00	4.403×10^{-2}	1.19	4.27×10^{-1}
5.00	4.538×10^{-2}	1.54	–	11.20	5.203×10^{-2}	1.21	4.71×10^{-1}
5.20	4.427×10^{-2}	1.53	–	11.40	6.012×10^{-2}	1.23	5.11×10^{-1}
5.40	4.353×10^{-2}	1.53	–	11.60	6.848×10^{-2}	1.26	5.51×10^{-1}
5.60	4.231×10^{-2}	1.52	–	11.80	7.783×10^{-2}	1.29	5.93×10^{-1}
5.80	4.139×10^{-2}	1.51	–	12.00	8.738×10^{-2}	1.33	6.33×10^{-1}
6.00	4.088×10^{-2}	1.51	–	12.20	9.568×10^{-2}	1.38	6.63×10^{-1}
6.20	3.966×10^{-2}	1.50	–	12.40	1.020×10^{-1}	1.43	6.81×10^{-1}
6.40	3.979×10^{-2}	1.50	–	12.60	1.088×10^{-1}	1.49	6.99×10^{-1}
6.60	3.715×10^{-2}	1.48	–				

Table A.12: Molten slag NAEB

$\lambda(\mu m)$	R	n	k	$\lambda(\mu m)$	R	n	k
1.10	5.687×10^{-2}	1.63	–	6.80	3.685×10^{-2}	1.47	–
1.20	5.697×10^{-2}	1.63	–	7.00	3.511×10^{-2}	1.46	–
1.30	5.707×10^{-2}	1.63	–	7.20	3.395×10^{-2}	1.45	–
1.40	5.649×10^{-2}	1.62	–	7.40	3.147×10^{-2}	1.43	–
1.50	5.633×10^{-2}	1.62	–	7.60	2.957×10^{-2}	1.41	–
1.60	5.581×10^{-2}	1.62	–	7.80	2.754×10^{-2}	1.40	–
1.80	5.527×10^{-2}	1.61	–	8.00	2.541×10^{-2}	1.38	–
2.00	5.460×10^{-2}	1.61	–	8.20	2.262×10^{-2}	1.35	–
2.20	5.433×10^{-2}	1.61	–	8.40	2.002×10^{-2}	1.33	–
2.40	5.432×10^{-2}	1.61	–	8.60	1.709×10^{-2}	1.30	–
2.60	5.437×10^{-2}	1.61	–	8.80	1.375×10^{-2}	1.26	–
2.80	5.330×10^{-2}	1.60	–	9.00	1.074×10^{-2}	1.22	–
3.00	5.275×10^{-2}	1.60	–	9.20	8.769×10^{-3}	1.18	1.01×10^{-1}
3.20	5.269×10^{-2}	1.59	–	9.40	9.673×10^{-3}	1.14	1.60×10^{-1}
3.40	5.234×10^{-2}	1.59	–	9.60	1.588×10^{-2}	1.11	2.44×10^{-1}
3.60	5.183×10^{-2}	1.59	–	9.80	2.827×10^{-2}	1.11	3.43×10^{-1}
3.80	5.141×10^{-2}	1.59	–	10.00	4.437×10^{-2}	1.13	4.39×10^{-1}
4.00	5.093×10^{-2}	1.58	–	10.20	6.156×10^{-2}	1.19	5.26×10^{-1}
4.20	4.982×10^{-2}	1.57	–	10.40	7.682×10^{-2}	1.26	5.93×10^{-1}
4.40	4.799×10^{-2}	1.56	–	10.60	8.856×10^{-2}	1.35	6.35×10^{-1}
4.60	4.862×10^{-2}	1.56	–	10.80	9.687×10^{-2}	1.43	6.53×10^{-1}
4.80	4.794×10^{-2}	1.56	–	11.00	1.019×10^{-1}	1.51	6.51×10^{-1}
5.00	4.689×10^{-2}	1.55	–	11.20	1.055×10^{-1}	1.58	6.37×10^{-1}
5.20	4.570×10^{-2}	1.54	–	11.40	1.064×10^{-1}	1.64	6.09×10^{-1}
5.40	4.502×10^{-2}	1.54	–	11.60	1.071×10^{-1}	1.69	5.80×10^{-1}
5.60	4.390×10^{-2}	1.53	–	11.80	1.058×10^{-1}	1.72	5.43×10^{-1}
5.80	4.337×10^{-2}	1.52	–	12.00	1.052×10^{-1}	1.75	5.15×10^{-1}
6.00	4.255×10^{-2}	1.52	–	12.20	1.048×10^{-1}	1.77	4.84×10^{-1}
6.20	4.154×10^{-2}	1.51	–	12.40	1.019×10^{-1}	1.78	4.47×10^{-1}
6.40	4.141×10^{-2}	1.51	–	12.60	1.002×10^{-1}	1.79	4.21×10^{-1}
6.60	3.766×10^{-2}	1.48	–				

Appendix B.

Composition Analysis by Electron Microprobe

Results of composition analysis for slag SA05 are presented in this appendix. The composition was measured at several positions through the depth of the solid slag sample and across the free surface using an electron microprobe. The variation in slag composition was found to be small across the horizontal section of the slag but significant along the vertical cross section. Estimates of the errors and uncertainties in the microprobe analyses are discussed and a summary of the results is presented.

B.1 Sample Preparation

The slag SA05 was prepared as discussed in Chapter 3 to produce a dark glassy solid. A cylindrical sample, approximately 13 mm diameter and 10 mm long, was extracted from the solid slag using a diamond tipped core drill. One end of the cylindrical sample was the free slag surface and the other end was parallel to the bottom of the alumina crucible. The cylinder was cut vertically along its centerline to yield two half-cylinders. The two pieces were arranged in a single epoxy mount, one half exposing the vertical cross-section and the other half exposing the free slag surface, as illustrated in Figure B.1.

The sample was prepared for analysis at the Center for Materials Research (CMR) polishing laboratory at Stanford University. The sample was polished using 6 μm diamond grit until a smooth flat surface was attained. Care was taken to not remove more slag than necessary so that the new surface would be very close to the original unpolished slag surface. Once a suitable smooth surface was produced, a thin conductive layer of carbon was sputtered onto the sample which was fixed in a brass mount. A small dab of carbon paint was used to ensure good electrical contact between the sample and the brass mount.

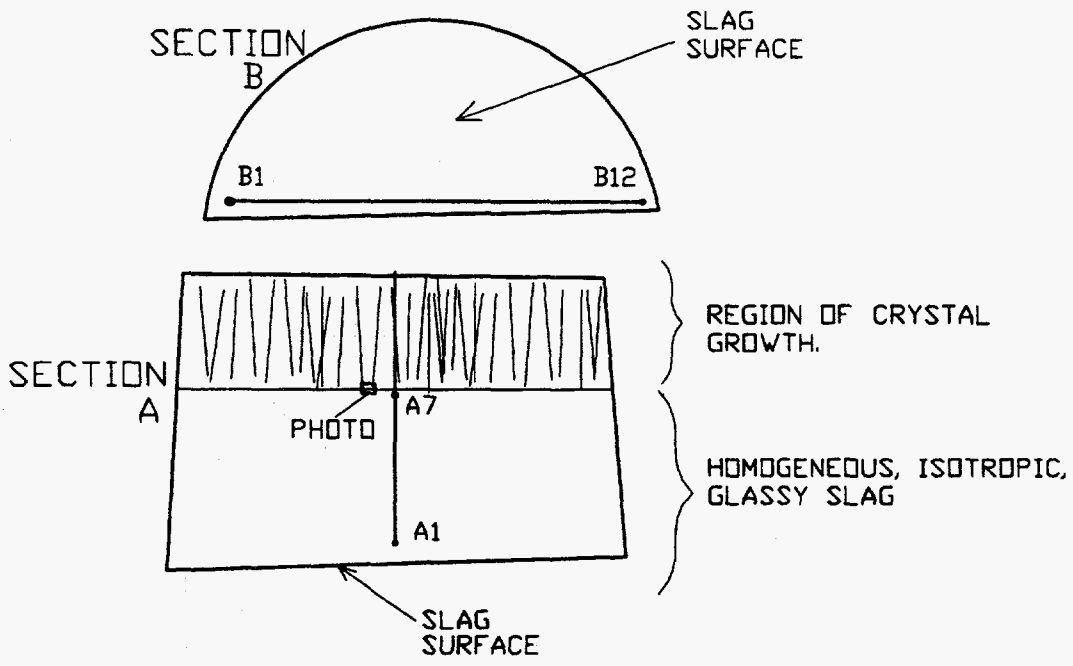

Figure B.1: Arrangement of the SA05 slag samples. Section A exposes the vertical cross section of the sample and Section B exposes the top slag surface.

B.2 Electron Microprobe Setup

The JOEL 733 electron microprobe, in the CMR microprobe lab, was used for this analysis. It is equipped with a standard wavelength dispersive X-ray spectrometer having three diffraction crystals (PET, LiF, and TAP) for analysis over a broad range of X-ray wavelengths. The sample platform is equipped with computer-controlled X-Y-Z translation capabilities. The positions on the sample at which the composition is analyzed are programmed into the system by the user and, apart from occasional manual focusing, the operation is reasonably automated.

For this analysis, two data lines were selected. The first data line, on sample Section A, is from a point near the surface of the slag to a point near the bottom of the slag. In all, there are seven positions along this line that lie in the glassy portion of the slag (line A1-A7). These seven positions are equally spaced between A1 and A7 (see Fig. B.1). A similar data line with 12 positions was selected on sample Section B, equally spaced between points B1 and B12.

Four elements, Si, Al, Fe, and Ca, were analyzed in this study. Element standards provided at CMR were used to quantify the elemental compositions. The accuracy of the stated compositions of these standards was not verified; however, staff at CMR were confident that the standards were suitable for this application.

For all measurements presented in this study, the electron beam was maintained at a current of approximately 10.0 nA and an accelerating potential of 15kV. The electron beam, at the sample position, was focused to a diameter of approximately 10 μm. The sample period, i.e., the duration of X-ray sampling at each sample position, was 30 sec. The uncertainty due to X–ray counting statistics is generally proportional to $\sqrt{N}/N$, and since the count, N, is proportional to the beam current and sampling duration product, these settings were chosen to give an acceptably low uncertainty level. An additional restriction is that the beam current be small so that the sample and standards are not evaporated (volatilized) . These settings met this criterion.

B.3 Results of Microprobe Analysis in the Two–Phase Region

As illustrated in Fig. B.1, the vertical section of the sample has two distinct regions, a region of glassy slag (bottom of Fig. B.1) and a region containing crystalline structures. The glassy region is featureless with no noticeable variations in color. However, in the crystalline region there are thin vertical structures which appear to be surrounded by an amorphous glass. The crystals appear to originate near the bottom of the slag, where it was in contact with the alumina crucible † .

Before performing composition analysis along the "data–lines", the composition was measured at selected locations to help explain the crystalline structure near the bottom of the slag (near top of Section A in Fig. B.1). A backscatter electron image (Fig. B.2) was taken for a small region, measuring approximately 280 μm by 220 μm, near the interface between the amorphous region and two-phase region (see Fig. B.1). This image aids in visualizing the structure of the two–phase region and in explaining the positions chosen for this first set of analyses.

---

† This crystal formation, with apparent growth emanating from the alumina/slag boundaries into the amorphous glass was seen in many slag samples.

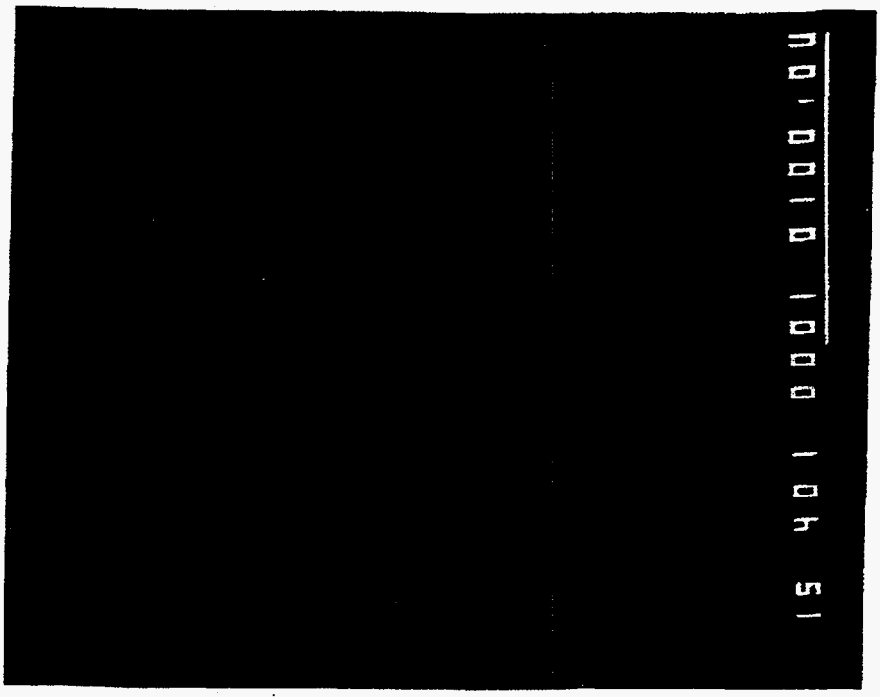

Figure B.2: Backscatter electron image of a small area near the interface of the two–phase region in Section A. Magnification is 400 times and the image is oriented to correspond to the PHOTO label in Fig.(B.1)

The photo in Fig. B.2 shows the structure of the two phase region. A backscatter electron image (BSI) shows variations in composition in the slag, or rather, variations in the local average atomic number. Compositions with higher average atomic number appear brighter than less dense compositions. From Fig. B.2 it appears that long thin crystals have grown though an otherwise homogeneous medium.

The compositions at two nearby points in the two–phase region of Section A were measured, and results are shown in Table B.1. The "Bright Region" refers to a region between two dark structures, but still within the two–phase region. This region appears, in the backscatter image, to be similar in brightness to the bulk slag composition, and the results in Table B.1 confirm that the composition is very similar to that of the bulk slag.

The "Dark Region" referred to in Table B.1 corresponds to the dark structures shown in Fig. B.2. The composition of these dark structures is quite different than that of the surrounding slag. Specifically, the crystals are very high in Al_2O_3, with approximately twice the content of the bulk slag. The chemical composition of the dark crystalline region is approximately $Al_2O_3 \cdot SiO_2$, with traces of Fe_2O_3 and CaO. The molar ratio Al/Si is approximately 2.04. This nearly exactly integral molar ratio, not found in the bulk slag, is good evidence that the dark structures are crystalline.

Table B.1: Compositions at two adjacent points in the two–phase region of Section A, wt.%

Oxide	Bright Region	Dark Region
SiO_2	53.6	35.4
Al_2O_3	29.9	61.3
CaO	11.7	1.7
Fe_2O_3	4.7	2.1

It is important to understand the possible limitations of these results. Although the data presented in Table B.1 are probably accurate, it is difficult to be certain. The region in which these data were obtained is inhomogeneous, with obvious small scale structure. The microprobe collects X–rays from a finite volume and records an average composition. The BSI also results from an average over a finite sample volume, but this volume is smaller, in general, than that sampled during conventional microprobe analysis. Therefore, even if the BSI shows no structure, there could be structure just below the sampling volume(s). It is apparent from the BSI that the dark structure is three dimensional, and that only a cross section of a more complicated structure is visible. From these arguments it is difficult to know whether the dark crystalline structure actually has 2.1 wt.% Fe_2O_3 or if some of this iron is due to material either just above or just below the crystal. Therefore, the results presented in Table B.1 should probably be regarded as semi–quantitative; however they may be quite accurate.

B.4 Homogeneity of the Glassy Slag

Away from the two–phase region the slag appears, in all backscatter images and under an optical microscope, to be homogeneous and isotropic. The microprobe analyses along the data lines on the two slag sections more accurately quantify the homogeneity of the slag. In this section the results of these microprobe analyses are presented.

Table B.2: Composition across slag surface (in wt.%).

Pt.#	x, mm	CaO	Fe_2O_3	SiO_2	Al_2O_3
B1	8.93	10.81	4.69	56.99	27.51
B2	10.03	10.59	4.64	56.87	27.90
B3	11.13	10.86	4.89	56.69	27.56
B4	12.23	10.66	4.94	56.60	27.80
B5	13.33	10.84	4.82	56.79	27.54
B6	14.43	10.99	4.66	56.73	27.62
B7	15.53	10.83	4.73	56.92	27.52
B8	16.63	10.82	4.68	56.88	27.62
B9	17.73	10.69	4.56	57.16	27.60
B10	18.83	10.96	4.75	56.89	27.40
B11	19.93	10.65	4.64	56.79	27.93
B12	21.03	10.68	4.87	56.63	27.81
Mean, $\bar{x}$		10.78	4.74	56.83	27.65
$2\sigma/\bar{x}$, %		2.26	4.74	0.53	1.16
Uncertainty below based on X-ray counts for sample and standard Uncertainty less than this is not significant.					
$2\sigma/\bar{x}$, %		2.91	5.60	0.96	1.34

The electron microprobe is capable of automatically moving the sample to a number of predesignated locations – measuring the composition at each location. Using this feature, the composition along the two data–lines (A1–A7 and B1–B12) was measured. Table B.2 shows the variation of composition along the surface on the slag (Section B) and Table B.3 shows the vertical variation of composition (Section A). These data apply only to the *visibly* homogeneous regions of the slag.

In addition to the composition, the microprobe analysis provides the X-ray count from which one can estimate a limiting uncertainty level. For example, the number

of counts, N, for the Si–K_α absorption line peak was measured as 120360 (in 30 sec at beam current of 10 nA). The standard deviation, σ, associated with this finite count is approximately $\sqrt{N}/N$, or 0.288%. For 95% confidence, the uncertainties are approximately 2σ, or 0.58%. This calculation is repeated for the standard sample and combined to give a total minimum uncertainty of approximately 0.96% (with 95% confidence) for SiO_2. This calculation was repeated for each of the four elements (Al, Si, Ca, and Fe) and the approximate limiting uncertainty is presented at the bottom of Table B.2. Since this uncertainty is unavoidable with such X–ray counting measurements[†] , any smaller variations are, to within 95% confidence, not significant.

From Table B.2, is it apparent that the slag composition does not vary significantly across the horizontal slag surface. The largest variation is in Fe_2O_3, with a 2σ variation of 4.75%. This variation is still below the fundamental uncertainty of the measurement for Fe_2O_3 (5.60%). Therefore, based on the information presented here we cannot determine whether the measured horizontal composition variation is systematic.

Table B.3: Vertical variation of composition for SA05

Pt.#	y, mm	CaO	Fe_2O_3	SiO_2	Al_2O_3
A1	25.00	10.61	4.84	56.82	27.73
A2	25.72	10.87	5.17	56.29	27.67
A3	26.45	11.03	5.08	56.29	27.60
A4	27.17	11.33	5.27	54.62	28.78
A5	27.89	11.22	5.61	54.24	28.93
A6	28.62	11.05	5.47	54.44	29.04
A7	29.34	11.11	5.38	54.35	29.16
Mean,$\bar{x}$		11.03	5.26	55.29	28.42
$2\sigma/\bar{x}$,%		3.96	9.04	3.74	4.63

The vertical variation of composition is presented in Table B.3. This composition variation is significant for all four oxides, with 2σ being well beyond the fundamental 2σ limits presented in Table B.2 for each oxide. Figure B.3 illustrates this vertical variation of composition, where the oxide compositions (in wt.%) are normalized

† Significant gains in precision are possible by increasing the sampling time. However, since the uncertainty is proportional to the square root of the sampling time, such gains are expensive.

by the value of each at point A1 (see Fig. B.1) . Increasing vertical position value corresponds to increasing depth into the slag.

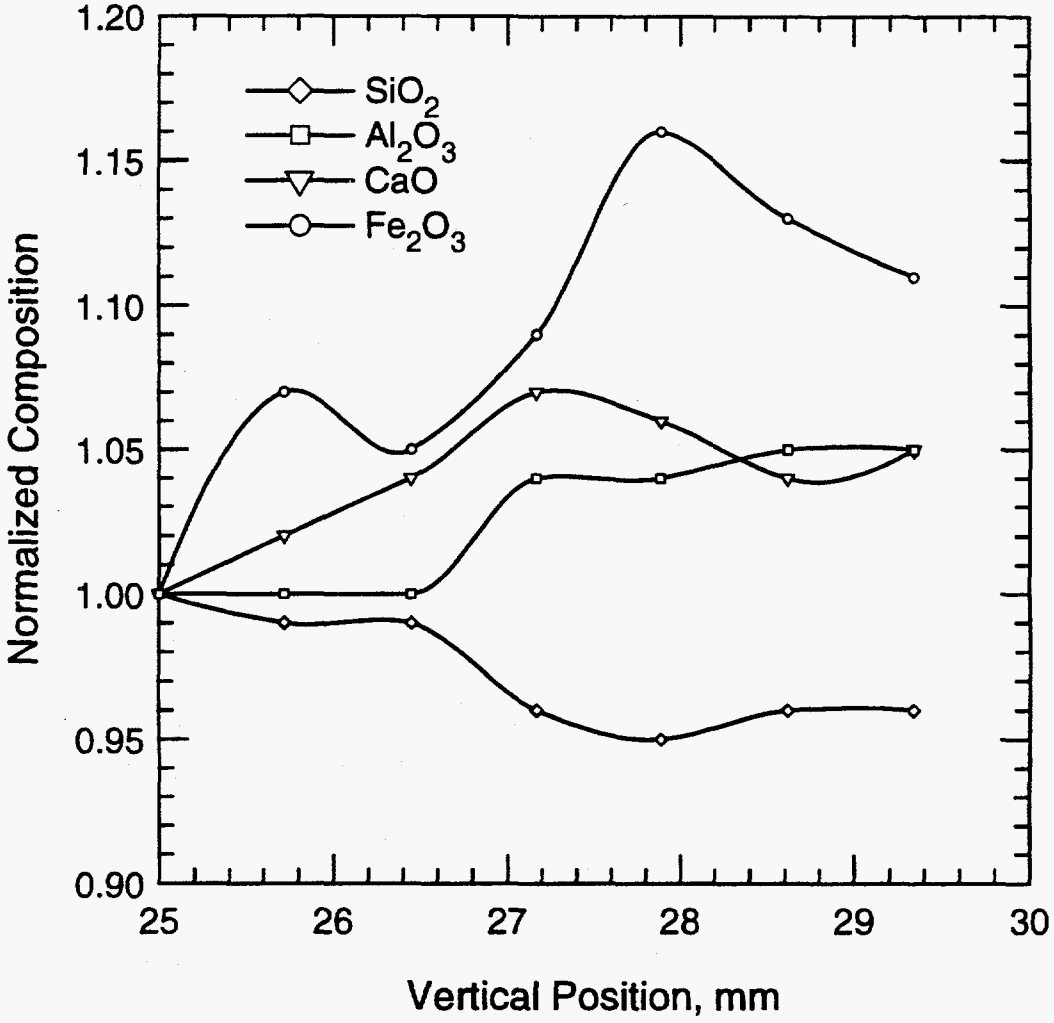

Figure B.3: Vertical variation of the slag SA05 composition. Increasing vertical position is further from the slag free surface.

As shown in Fig. B.3, the Fe_2O_3 and CaO concentrations increase with increasing depth into the slag. Over the 5 mm depth the Fe_2O_3 content increases by as much as 10–15%. The fact that Fe_2O_3 is the heaviest (or densest) constituent in the slag probably explains this trend. The CaO content changes much less, with approximately a 5% increase across the same 5 mm. The Al_2O_3 content also increases with increasing depth into the slag, but this change is also moderate (~5%), and is probably due to

diffusion of Al_2O_3 from the crucible. It is useful to note however, that the overall Al_2O_3 content is not substantially increased by dissolution of the alumina crucible. The SiO_2 content decreases slightly with increasing depth into the slag, and is the only ingredient showing this behavior.

Finally, in addition to the statistical uncertainty associated with a finite count, as discussed above, there are several possible sources of error in these measurements, and care was taken to avoid them where possible. First, it is known that some elements are volatilized, or evaporated, when an excessively powerful electron beam is focused on the sample or standard. Of the elements studied in this work, Ca is the most susceptible to such effects. To ensure that Ca, or other elements, were not volatilized, measurements were repeated at one location, leaving the beam on that location for an extended period of time. The results of this test showed that the 10nA beam had no noticeable effect on the sample composition.

Another source of error in these measurements is drift in the position of the diffraction crystals. In normal operation, the diffraction crystals are moved along the Rowland circle, causing a shift in the detected wavelength. By slowly scanning in wavelength, one finds the peak of a desired absorption line. This crystal position is recorded and used for measurements at all of the sample positions along the data lines. However, if the crystal becomes slightly misaligned during the course of the measurements, and is not realigned, the count rates will fall since the detected wavelength is shifted away from the peak of the absorption curve. The alternative to this procedure is to scan in wavelength at every sample and standard position, a process that is very time consuming. Fortunately, since the sample and standard count rates are measured at each position, this misalignment is easily noticed since the resulting sum of weight percent compositions will likely change, usually falling below 100%. For the data presented here, it is clear that there was some minor drift in the crystal alignment but it was never large. The smallest total weight percentage obtained in any of these measurements was approximately 97%, and more frequently was 98% or more.

The effect of this diffraction crystal drift was studied for one sample position on Section B, and the results are presented in Table B.4. These data were taken after the initial peak search and after all the data presented above were taken. Therefore, it represents the worst case if, as expected, the diffraction crystal drift accumulated over the course of the measurements.

Table B.4: Effect of peak absorption search in microprobe analysis.

	Composition (wt.%)				Relative Error,%	
	Without peak search		With peak search		$\frac{(x_{w/o}-x_w)}{x_w} \times 100\%$	
Compound	Raw	Normal	Raw	Normal	Raw	Normal
SiO_2	55.17	57.12	56.43	55.73	- 2.23	2.48
Al_2O_3	26.57	27.51	29.64	29.27	-10.36	-6.03
CaO	10.21	10.57	10.42	10.29	- 2.02	2.71
Fe_2O_3	4.64	4.80	4.76	4.70	- 2.52	2.18
Total, %	96.59	100	101.25	100	—	—

Referring to Table B.4, the first column of data, labeled "Without peak search", was obtained immediately after measuring the composition along the data–lines. The total weight percent for this data is only 96.6%, indicating that some shift in the peak positions had probably occurred. The second column is simply the first column normalized to give a total weight of 100%.

After recording the data without a peak search, a peak search was made to correct the misalignment of the diffraction crystals. The third column of Table B.4 shows the results of this trial. The total weight changed to 101.25%, which is much closer to the expected value. Also, the Al_2O_3 content increased substantially due to correction of the peak wavelength value. The other compounds show less than a 2.52% increase from the previous measurements.

From the results presented above it is evident that some small error was introduced by failing to do a wavelength scan at each sample position. The errors in the SiO_2, Al_2O_3 and CaO compositions are significant, since they are above the statistical uncertainty presented in Table B.2. Nevertheless, it is also evident that the errors are within acceptable limits for the purpose of this study, and that the homogeneity of the slag sample is well characterized by these data.

B.5 Summary

A number of interesting results were obtained from this study of the composition distribution in the synthetic slag SA05. The concentrations of four elemental constituents (Al, Si, Fe, and Ca) were measured at several locations across the surface of the slag and through a vertical cross section, leading to the following conclusions:

1. The slag sample was not homogeneous throughout, but had a region near the bottom of the crucible containing Al_2O_3 rich crystals. Outside of this non-homogeneous region the slag was reasonably homogeneous with no visible structure, that is, it was an amorphous glass.

2. The composition across the surface of the slag is constant, to within the uncertainty limits of this study. This result is expected for a frozen liquid surface.

3. There is a significant change in the composition of the slag along a vertical cross section. The largest relative variation is that of Fe_2O_3, which increases by 10-15% with increasing depth in the slag, up to a maximum measured depth of 5 mm. The variation of the other three constituents is less than 5–10%.

4. While it is relatively easy to analyse the composition of the synthetic slags to within an accuracy of a few percent using the JOEL 733 electron microprobe, there are a number of critical sources of error that make analysis to very high accuracy or precision difficult. The tendency to use four digit precision (0.01%) in quoting composition analyses is probably not justified unless extreme care is taken to demonstrate that degree of precision.

Appendix C.

Optical Constants of Water and CCl_4.

Detailed measurements of the optical constants of liquids over the wavelength range from 1–13 μm are surprisingly sparse in the literature; however, considerable data for liquid water are available. In particular, data from two reviews of the optical properties of water, by Hale and Querry [43] and by Irvine and Pollack [44], are compared with measured data. In addition, the real refractive index, n, of carbon tetrachloride (CCl_4) is available over the wavelength range from the visible to approximately 9 μm [45].

Transmittance and reflectance measurements of water, and reflectance measurements of CCl_4 were made using the apparatus described in Chapter III and compared to published data. The goal of these experiments was to provide an estimate of the accuracy of the techniques used for measuring the optical constants of molten slags. The primary difference between the molten slag measurements and those described here is that these measurements were made at room temperature, and the slag measurements were made at 1600°C. Nevertheless, these results provide an approximate measure of the accuracy one should expect from the techniques used for molten slags, and also provide a good test of the application of the Kramers–Kronig procedure.

C.1 Reflectance Measurements

The near normal reflectance and transmittance of liquid water was measured using the apparatus described in Chapter III – the same apparatus used to measure the optical properties of molten slag. Approximately 30 mℓ of bottled distilled water was added to an alumina crucible and placed inside the furnace (the furnace power remained off during these experiments). The nitrogen purge hood was in place and the system was purged with nitrogen at a volume flow rate of approximately 45 scfh (ft^3/hr at STP). The system was allowed to equilibrate for a period of approximately 1 hour while minor optical adjustments were made. The water reached a steady temperature of approximately 16°C while the surrounding room temperature was approximately 25°C. The lower water temperature was attributed to evaporation.

The reflectance of the water was measured over the wavelength range from 1 to 13 μm. The results of this measurement are shown in Fig. C.1, along with previously published data. The reflectance is obtained from the ratio

$$R = R_{\text{ref}} \frac{I_{\text{sample}}}{I_{\text{ref}}} \tag{C.1}$$

where I_{sample} is the signal reflected from the water surface and I_{ref} is the signal reflected from the reference surface. In these experiments the reference is a gold mirror with an assumed reflectance, R_{ref}, of 0.992, as discussed in Chapter III.

The measured reflectance in Fig. C.1 is compared with values calculated using the Fresnel relation

$$R = \frac{(n-1)^2 + k^2}{(n+1)^2 + k^2} \tag{C.2}$$

where the optical constants, n and k, are taken from published reviews [43,44]. The agreement with published data is good over the entire wavelength range, with the largest difference being near the peaks of the absorption bands and at wavelengths longer than approximately 11 μm. The two sets of published data also show the largest disagreement in these same spectral regions.

Once the reflectance is measured over a broad range of wavelengths the real refractive index, n, is computed using the Kramers–Kronig (KK) technique, as discussed in Chapter II. The results of this analysis are shown in Fig. C.2. The comparison with published data is very good; however, the measured values overpredict the refractive index in the wavelength range from 11 to 13 μm. Note that the disagreement between the measured values and the published values is of the same order of magnitude as the disagreement between the two sets of published data, but does not lie within the expected uncertainty of the experimental data. The source of this disagreement can be understood by considering the imaginary refractive index.

The KK analysis allows the absorption index, k, to be computed if k is large enough (> 0.1 or so) and if the reflectance is known over a wavelength range that spans all major absorption features near the wavelength of interest. For example, the KK technique predicts the absorption index, k, in the wavelength range from 2.8 to 3.2 μm very well, as shown in Fig. C.3. The value of k predicted by KK analysis of the measured reflectance is in good agreement with data from Hale and Querry [43]. At most other wavelengths k is less than 0.1 and the KK technique cannot determine k; however, in the wavelength range from 11 to 13 μm the absorption index is large

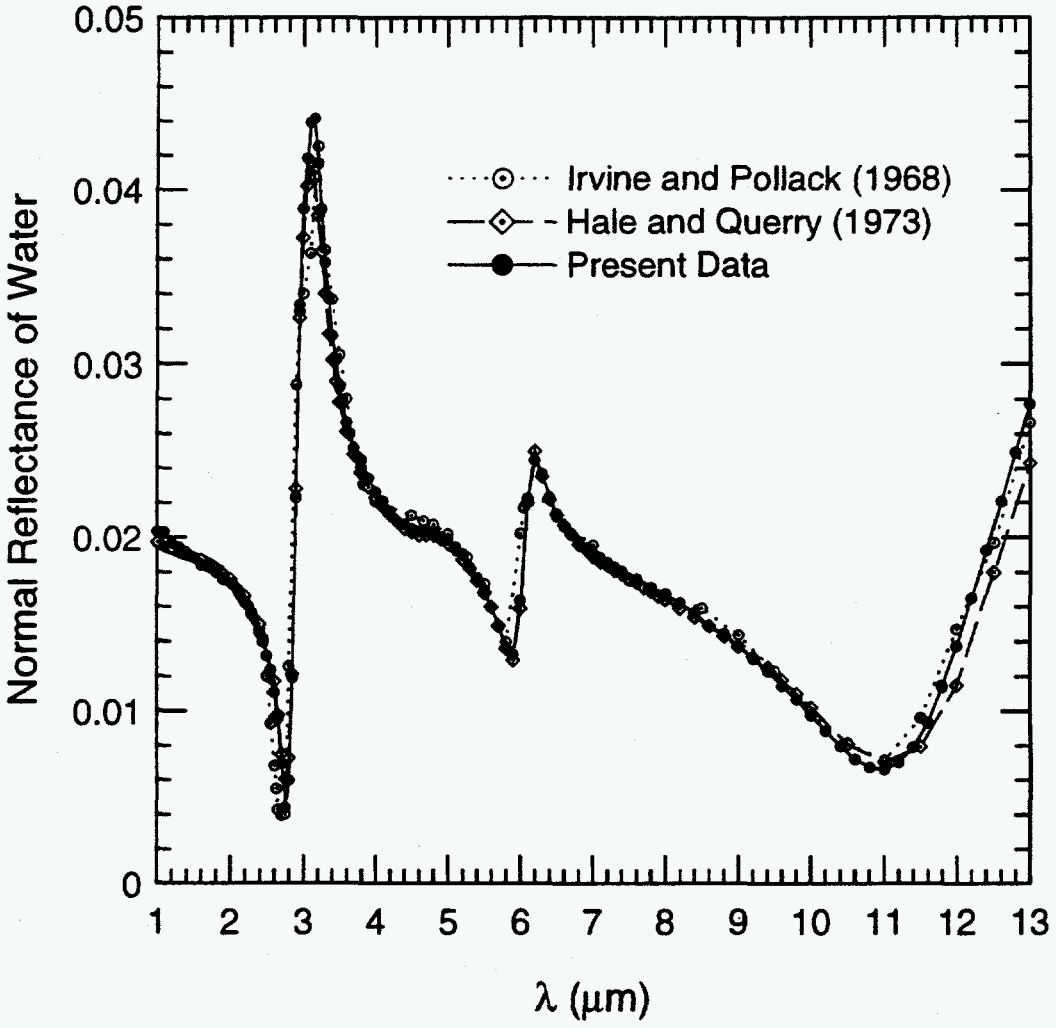

Figure C.1: The near normal reflectance of liquid water, compared with published data.

and increasing with increasing wavelength. In this spectral range the first criterion, $k > 0.1$, for using the KK analysis is satisfied; however, the absorption features at wavelengths longer than 13 μm are not negligible. Since the reflectance was not measured at wavelengths longer than 13 μm, the KK technique underpredicts k, as shown in Fig. C.4. Since k is underpredicted, it follows that n must be overpredicted to produce the correct normal reflectance.

It should be noted that despite the fact that the absorption features at longer wavelengths are ignored, the KK method is well-behaved. That is, it does predict the correct order of magnitude for k, and even predicts the increase in k with wavelength

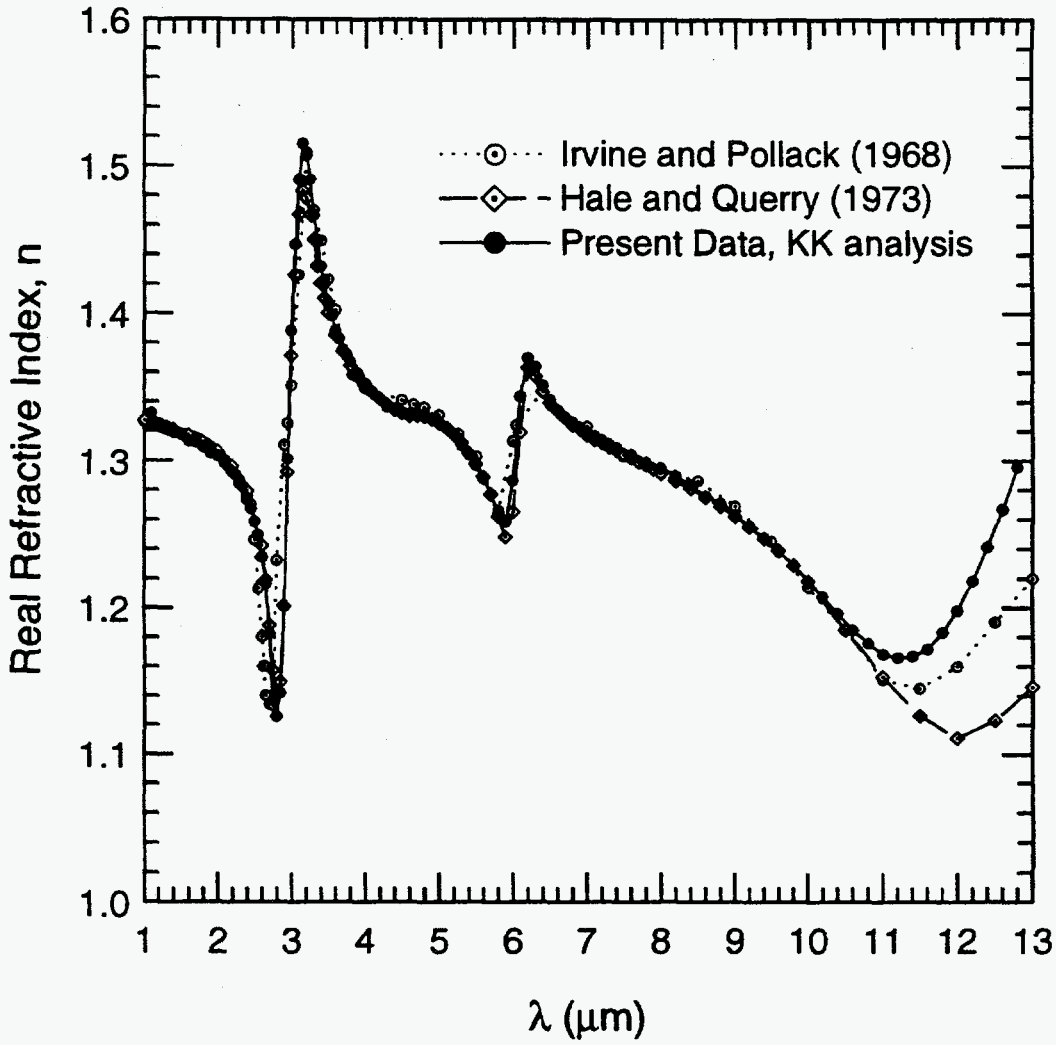

Figure C.2: The real refractive index of water computed using the Kramers–Kronig analysis of measured data, compared with published data.

in the 11 to 13 μm wavelength range. The difference between the published value of k and the result of the KK method at 12.8 μm is approximately 25%.

As another test of the experimental technique, the reflectance of CCl_4 was also measured. The absorption index of CCl_4 is very small over the wavelength range from 1 to 9 μm, apart from several rather narrow absorption lines. Therefore, the refractive index of CCl_4 predominantly shows normal dispersion, with n decreasing with increasing wavelength. Also, since k is small, the reflectance measurement is a

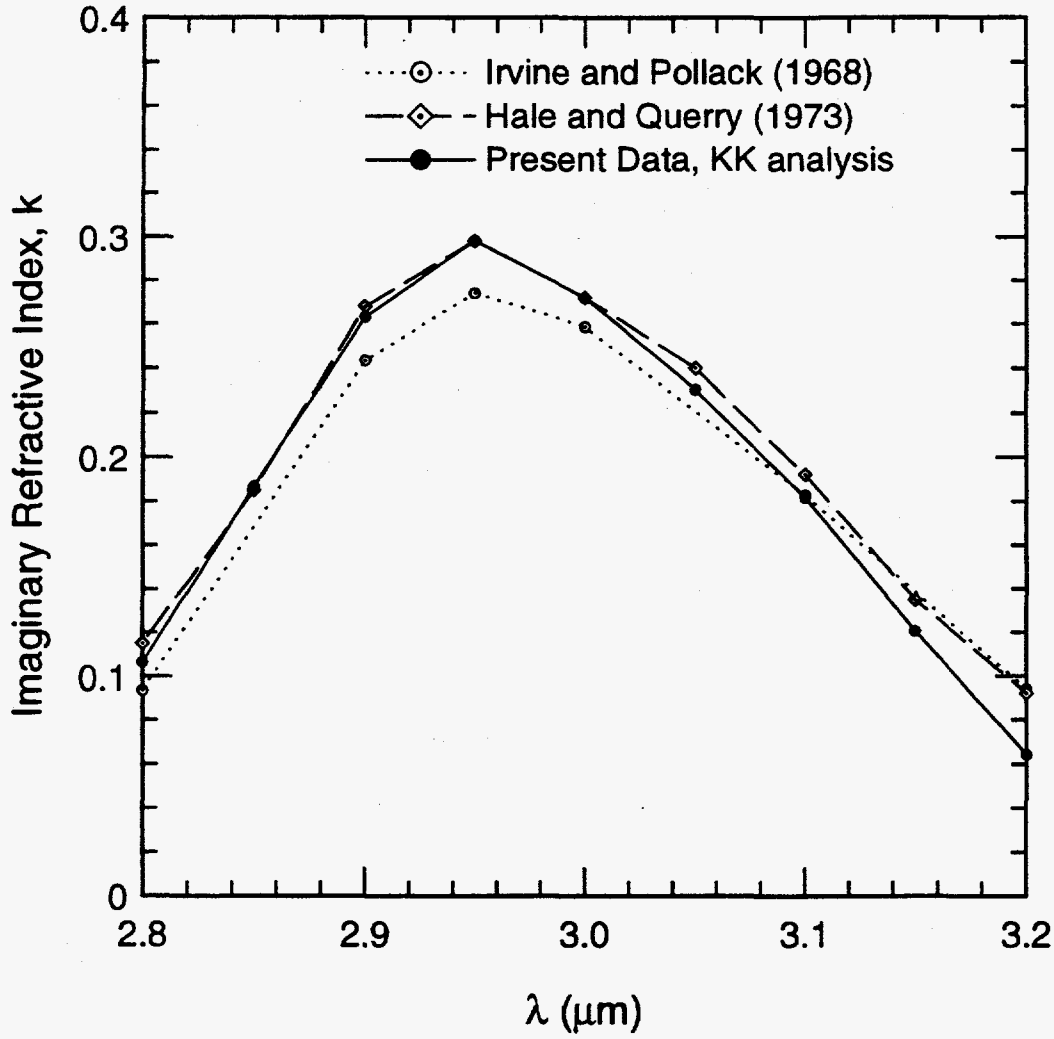

Figure C.3: The absorption index, k, of water in the wavelength range from 2.8 to 3.2 μm compared to published values.

good test for possible problems due to reflected light from the bottom of the alumina crucible containing the liquid.

Since k is small, the Fresnel relation for normal reflectance becomes

$$R = \frac{(n-1)^2 + k^2}{(n+1)^2 + k^2} \simeq \frac{(n-1)^2}{(n+1)^2}. \tag{C.3}$$

This can be rearranged to give n as a function of R, such that

$$n \simeq \frac{1+\sqrt{R}}{1-\sqrt{R}}; \qquad k^2 << (n-1)^2. \tag{C.4}$$

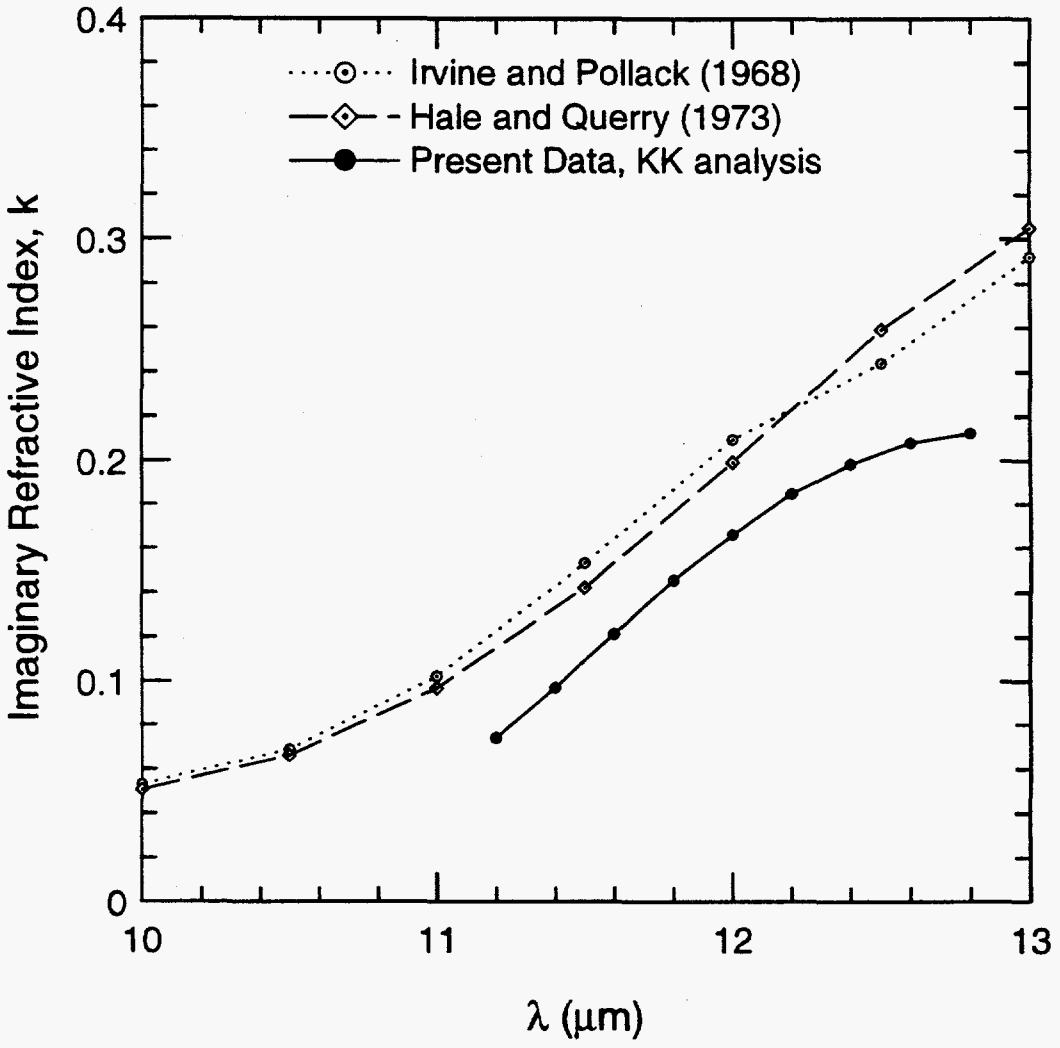

Figure C.4: The calculated absorption index, k, of water in the wavelength range from 11 to 13 μm compared to published values.

Thus, one can compute n directly from R. The results of this calculation are shown in Fig. C.5, along with the published data of Pfund [45]. The figure also shows two dashed lines for +1.0% and +0.5% of Pfund's data. The agreement between the current measurements and those of Pfund are very good, with the difference being less than 0.5% for most data points. It is interesting to note that Pfund's measurements were not made using reflectance, but by refraction through a hollow prism filled with CCl_4. Thus these measurements provide an independent verification of Pfund's results.

As a further check of the KK technique, the reflectance data for CCl_4 were reduced using the same procedure as that used to reduce the water reflectance measurements above. This procedure involves averaging multiple measurements at identical wavelengths to produce a single-valued set of $R(\lambda)$ data, which is subsequently corrected for the reflectance of the gold reference mirror by multiplying by 0.992. The resulting set of reflectance data are analyzed using the KK relations presented in Chapter II. The results of this analysis yield $n(\lambda)$.

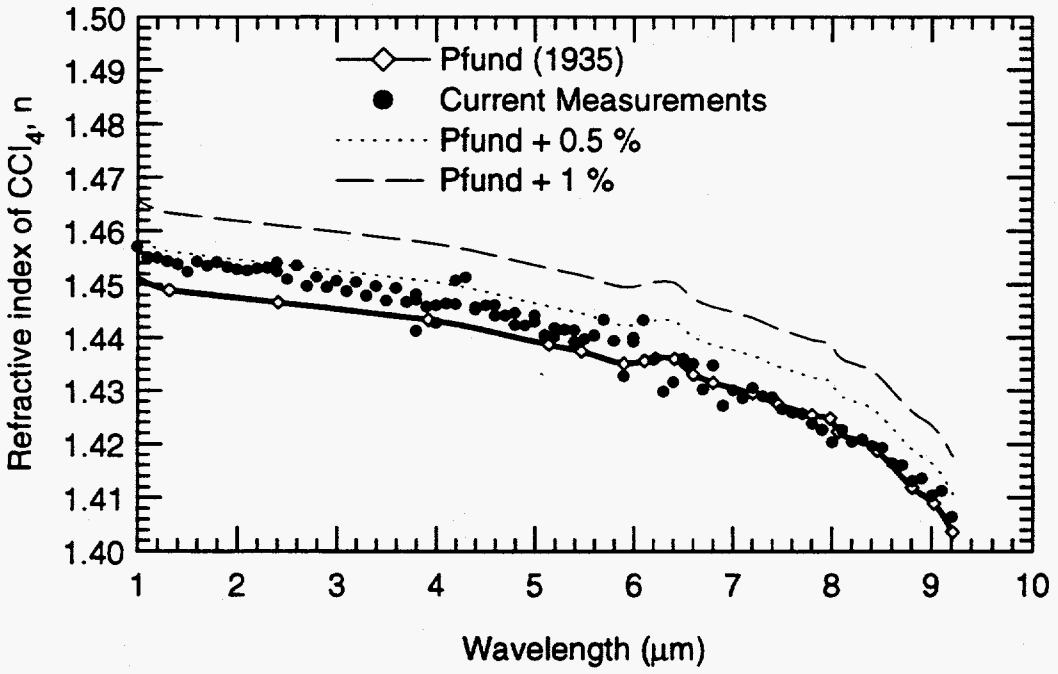

Figure C.5: The refractive index of CCl_4 calculated using the measured reflectance and the approximate Fresnel relation, $n \simeq (1+\sqrt{R})/(1-\sqrt{R})$, compared to published data.

The results of the KK analysis are shown in Fig. C.6, along with the data from Pfund. The results are once again in good agreement with the published data. This analysis demonstrates that the "noise" in the reflectance data does not adversely affect the KK data reduction procedure. This is expected, in view of the integral nature of the KK relations.

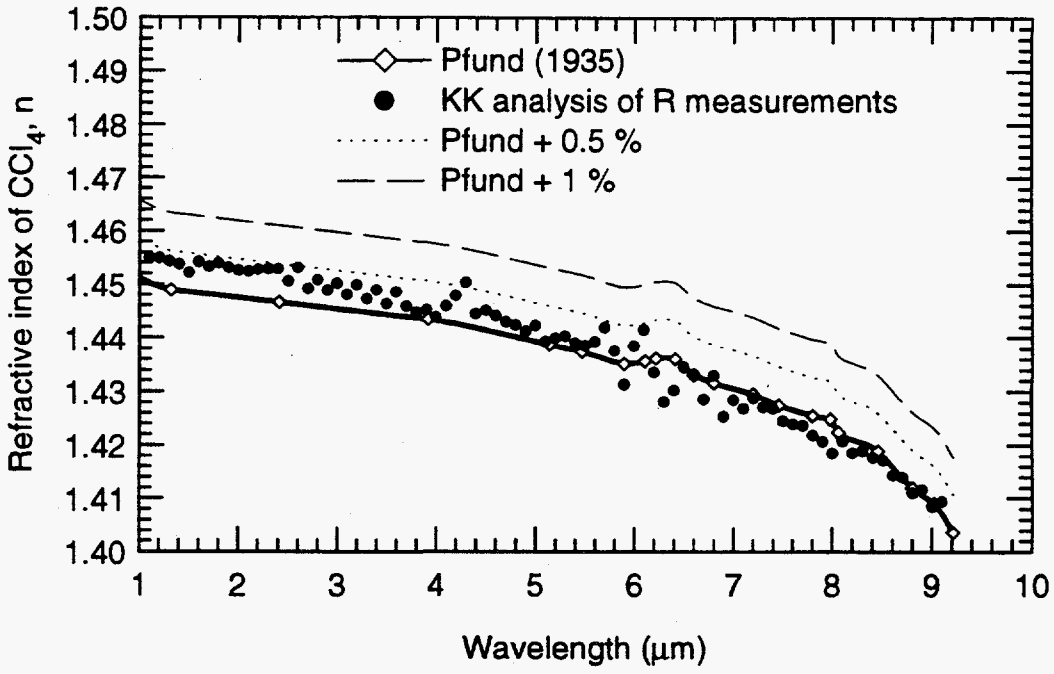

Figure C.6: The refractive index of CCl_4 calculated using the Kramers–Kronig data reduction procedure compared to published data.

C.2 Transmittance Measurements

The transmittance technique described in Chapter III was used to measure the transmittance of liquid water in the wavelength range from approximately 1.0 to 2.5 μm. In this wavelength range the absorption index of water varies from approximately 10^{-6} to over 10^{-3}. Note that for $k = 10^{-3}$ at $\lambda = 2.5$ μm, the absorption coefficient, $\alpha \equiv 4\pi k/\lambda$, is approximately 5 mm^{-1}, and the attenuation through a 1 mm thick layer of water is approximately $e^{-5} \simeq 0.6\%$. For layer thicknesses used in this transmittance apparatus ($\sim$ 0.2–0.5 mm) a k of 10^{-3} is large, and signals become exponentially small for increases in k or thickness† .

† In fact, at wavelengths where k is as large as 10^{-3} or so, the evaporation rate of the water is measurable, and constantly observed since the layer thickness is constantly changing. This effect was minimized by preforming the experiments as quickly as possible and by alternating the order in which the signals at the two depths were obtained. Of course, this adds somewhat to the noise in the measurements since it is possible that in some instances sufficient time was not allowed for the liquid surface to settle completely.

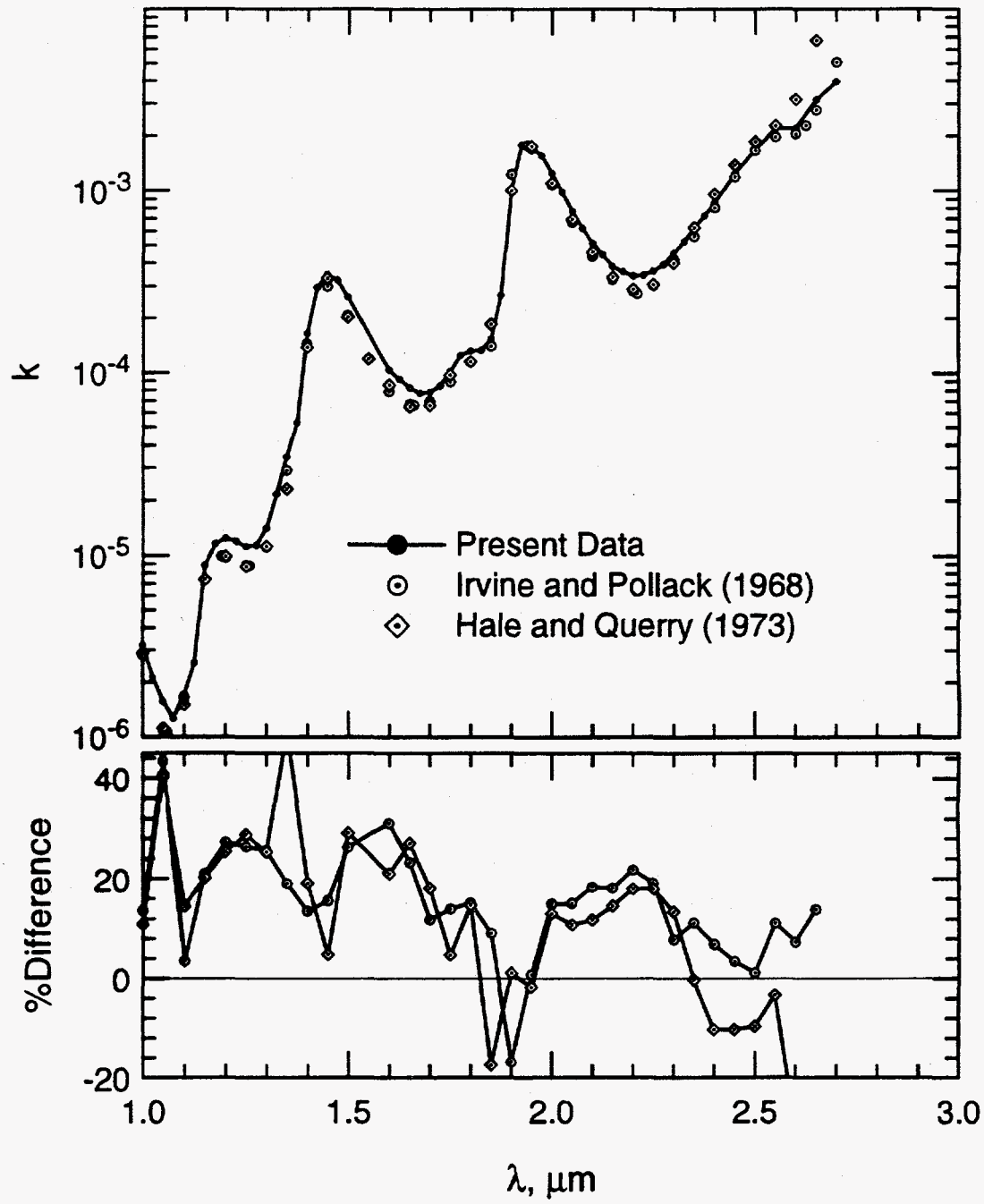

Figure C.7: The absorption index of water obtained from transmittance measurements, compared to published data.

The measured transmittance is shown in Fig. C.7, along with the difference between measured values and published values [43,44]. The agreement with published data is good. On average, the difference between the published data and the measured values is approximately 20%, with the largest differences being for small k. At larger k, the agreement is somewhat better.

It should be recognized that the published data used here are from reviews of existing literature, and not independent experimental investigations. The two published data sets use many of the same references to infer the "best" value for the absorption index. The agreement between the most reliable published experimental results in the 1–2.5 μm range was generally within 10%–20%, but the agreement was regarded as quite good when values from two independent investigations were within 20% of one another. Therefore, it is reasonable to conclude that the measured values above are in disagreement by as much as 20% with the best available data, but that the error may be somewhat smaller.

Limited attempts were made to improve the measured values. It was suspected that the purity of the water used here may have caused the high k values, particularly since the errors are largest for small k, where impurities would have the largest effect. To see if this may have been a large factor, the measurements were repeated using ordinary tap water, and with alternative sources of bottled distilled water, but the results were not significantly changed. Another possible source of error was that air bubbles or particles were present in the water. However, no bubbles or particles were apparent either visibly or when the water was illuminated with a HeNe laser. Nevertheless, this may have been a problem, since the alumina crucible can out-gas to the water and possibly cause bubble formation, and since the nitrogen flow through the furnace can carry particles from under the purge hood into the water. Since such particles would burn and dissolved in the slag when the furnace is at 1600°C, a redesign to test this effect was not deemed necessary.

Appendix D.

Radiative Properties of Particle Dispersions

The radiative properties of dispersions of particles can be calculated from more fundamental properties of the dispersion, such as the optical constants and size of the individual particles. In this Appendix the procedure for computing the radiative properties of a polydispersion of particles is presented.

D.1 The Radiative Transport Equation

The basis for computing the radiative transfer through an absorbing, emitting, and scattering medium is the radiative transport equation [20,35]

$$\nabla\cdot[\hat{\Omega}I_\lambda(\mathbf{r},\hat{\Omega})]+(\alpha_\lambda+\sigma_\lambda)I_\lambda(\mathbf{r},\hat{\Omega}) = \alpha_\lambda I_{b\lambda}(T)+\frac{\sigma_\lambda}{4\pi}\int_{4\pi}\Phi_\lambda(\hat{\Omega}\cdot\hat{\Omega}')I_\lambda(\mathbf{r},\hat{\Omega}')d\Omega'. \quad \text{(D.1)}$$

Here $I_\lambda(\mathbf{r},\hat{\Omega})$ is the spectral radiance at position $\mathbf{r}$ in direction $\hat{\Omega}$ at wavelength λ. The spectral absorption coefficient, α_λ, spectral scattering coefficient, σ_λ, and scattering phase function, $\Phi_\lambda(\hat{\Omega},\hat{\Omega}')$ are generally functions of position, $\mathbf{r}$, and are most often strong functions of wavelength† . Solution of the transport equation, Eq. (D.1), requires knowledge of the scattering coefficient, the absorption coefficient, and the scattering phase function. For a polydispersion of particles, such as fly ash, these radiative properties can be calculated from more fundamental data.

---

† Radiative properties of real materials always vary strongly with wavelength if one considers a wide enough wavelength range. However, if the significant radiant energy is confined to a narrow wavelength range where the radiative properties are approximately constant, then the wavelength dependence may be negligible — the so-called "gray" model. This gray model is not generally applicable to fly ash or infrared active gases at typical combustion temperatures.

D.2 Size-Averaged Radiative Properties

Most aerosols, including fly ash dispersions, are polydisperse, i.e. composed of particles with a wide range of sizes. For fly ash dispersions, particle diameters range from below 1 μm to a few with diameters over 100 μm. In such cases, the scattering and absorption properties found from Mie theory, for example, must be integrated over the broad range of particle sizes.

Scattering and absorption properties of a single particle are described by the scattering efficiency, Q_{sca}, the absorption efficiency, Q_{abs}, and the scattering phase function, Φ, which describes the angular distribution of scattered light. The scattering efficiency is defined as the ratio of the power scattered by the particle to the power incident on its projected area ($\pi D^2/4$ for a sphere). Similarly, the absorption efficiency is defined as the ratio of the power absorbed by the particle to the power incident on its projected area.

A particle illuminated by monochromatic light of wavelength λ has scattering and absorption properties that depend on the geometry and optical constants, $m = n+ik$, of the particle. If the particle is a homogeneous sphere of isotropic material with diameter D, then the scattering and absorption properties are functions only of m and the size parameter $x = \pi D/\lambda$. If the particle is not homogeneous, isotropic, or spherical, its scattering and absorption properties are still described by Q_{sca}, Q_{abs}, and Φ, but they generally depend on the particle shape and its orientation with respect to the incident light.

We assume that the size of the particle can be described by a single variable, D, and that the distribution of particle sizes can be described by a scalar size distribution function $f(D)$. More precisely, let the function $f(D)$ be defined such that $f(D)\,dD$ is the fraction of particles with size between D and $D+dD$. If the optical constants of all the particles are the same, then for a given wavelength the scattering characteristics for particles of size D can be expressed as $Q_{\text{sca}}(D)$, $Q_{\text{abs}}(D)$, and $\Phi(D)$. Of course, $\Phi(D)$ also depends on the scattering angle θ measured from the forward direction.

Now consider the transport equation, Eq. (D.1). The scattering coefficient of the medium is defined as the fraction of the power incident at position $\mathbf{r}$ that is scattered out of the direction $\hat{\mathbf{\Omega}}$ in traversing distance ds into the direction $\hat{\mathbf{\Omega}}$. If the particle number density in a differential volume is N, then the number of particles with size D

is $Nf(D)\,dDdAds$, where the differential cross sectional area is dA. If power incident on the particles with cross sectional area A_p is $I(s)\,A_p$, then the power scattered by particles of size D is the product

$$Nf(D)\,dDdAdsA_p(D)\,Q_{\text{sca}}(D)\,I(s) = NQ_{\text{sca}}(D)\,A_p(D)\,f(D)\,I(s)\,dAds.$$

The power incident on the volume is $I(s)\,dA$, and the power at $s+ds$ is $I(s+ds)\,dA$, thus the change in radiance along distance ds owing to scattering by particles of size D is

$$\frac{dI}{ds} = NQ_{\text{sca}}(D)\,A_p(D)\,f(D)\,dDI.$$

The contribution by particles of all sizes is obtained by integrating over all particle sizes, thus the resulting scattering coefficient is

$$\sigma_\lambda = \int_0^\infty NQ_{\text{sca}}(D)\,A_p(D)\,f(D)\,dD \tag{D.2}$$

The volume fraction of particles, i.e., the particle volume per unit volume, is

$$C_v = N\int_0^\infty V_p(D)\,f(D)\,dD \tag{D.3}$$

where $V_p(D)$ is the volume of a particle of size D. The Sauter mean diameter,D_{32}, is defined as

$$D_{32} = \frac{\int_0^\infty D^3 f(D)\,dD}{\int_0^\infty D^2 f(D)\,dD}. \tag{D.4}$$

The Sauter mean diameter is equal to the particle diameter for a monodispersion of particles, and typically increases (compared to the median size) for increasing breadth of particle sizes. Combining Eq. (D.2) with Eq. (D.3) and Eq. (D.4) one obtains the formula

$$\sigma_\lambda = \frac{3}{2}\frac{C_v}{D_{32}}\frac{\int_0^\infty Q_{\text{sca}}(D)\,A_p(D)\,f(D)\,dD}{4\pi\int_0^\infty D^2 f(D)\,dD}\frac{\pi/6\int_0^\infty D^3 f(D)\,dD}{\int_0^\infty V_p(D)\,f(D)\,dD}. \tag{D.5}$$

If the particles are spherical, this equation simplifies to

$$\sigma_\lambda = \frac{3}{2}\frac{C_v}{D_{32}}\frac{\int_0^\infty Q_{\text{sca}}(D)\,D^2 f(D)\,dD}{\int_0^\infty D^2 f(D)\,dD}. \quad \text{(sphere)} \tag{D.6}$$

Using analysis similar to that above, the absorption efficiency for a sphere can be expressed as

$$\alpha_\lambda = \frac{3}{2}\frac{C_v}{D_{32}}\frac{\int_0^\infty Q_{\text{abs}}(D)\,D^2 f(D)\,dD}{\int_0^\infty D^2 f(D)\,dD}. \quad \text{(sphere)} \tag{D.7}$$

The mean absorption, scattering, or extinction efficiencies for a polydispersion of spherical particles can be written in the form

$$\overline{Q} = \frac{\int_0^\infty Q(D)\, D^2 f(D)\, dD}{\int_0^\infty D^2 f(D)\, dD}. \quad \text{(sphere)} \tag{D.8}$$

The scattering phase function for a polydispersion of particles is found from an analysis similar to that above. For example, for spherical particles one finds

$$\overline{\Phi} = \frac{1}{\overline{Q_{\text{sca}}}} \frac{\int_0^\infty Q_{\text{sca}}(D)\, \Phi(D)\, D^2 f(D)\, dD}{\int_0^\infty D^2 f(D)\, dD}. \quad \text{(sphere)} \tag{D.9}$$

Several interesting results can be deduced from the form of the scattering and absorption coefficients above. Suppose the scattering and absorption efficiency are constant, independent of the particle size. Such a limit is approximated by very large particles ($x \gg 1$) where $Q_{\text{ext}} \to 2$. If the particles are solid spheres, then the volume fraction, C_v, is proportional to the mass fraction, and the scattering and absorption coefficient will be proportional to the inverse of D_{32}, or proportional to the cross sectional area of the particles per unit volume. For a fixed mass fraction of particles, the optical depth of a medium decreases with increasing particle diameters. In the (Rayleigh) limit of very small particles ($x \ll 1$) the scattering efficiency is proportional to D^4, and the absorption efficiency is proportional to D. Therefore, the scattering coefficient is typically very small, and is dominated by scattering from the largest particles in the dispersion. In contrast, the absorption efficiency is independent of size of the particles, with $\alpha_\lambda \propto C_v$.

D.3 Averaging with General Distribution Functions

In general, the optical constants of a material depend on the composition, temperature, and wavelength, and a polydispersion of fly ash particles will have a distribution sizes. Therefore, since the scattering properties depend on the optical constants, the fly ash dispersion will have a distribution of size, composition, and temperature at a given wavelength. In addition, the size of a particle could be generalized to include the geometry of the particles, so that non–spherical or otherwise complicated particles are included. In this section this general formulation of the average radiative properties is presented.

In general, a distribution function could be defined such that $f(D,C,T)\,dDdCdT$ is the fraction of particles with size (or geometry) D within dD, composition C within dC, and with temperature T within dT. The scattering efficiency would be $Q_{\text{sca}} = Q_{\text{sca}}(D,m)$, where the complex refractive index, $m = n + ik = m(C,T)$. The derivation of average radiative properties would follow in a fashion similar to the derivation presented above for distribution function $f(D)$. For example, the scattering coefficient would become

$$\sigma_\lambda = \int_0^\infty \int_C \int_T N Q_{\text{sca}}[D, m(C,T)]\, A_p(D)\, f(D,C,T)\, dDdCdT \qquad \text{(D.10)}$$

Alternatively, a distribution function could be defined such that $f(D,n,k)\,dDdndk$ is the fraction of particles with size D within dD, refractive index n within dn, and absorption index k within dk. This model is likely to be less complicated since it more directly represents the important variables – the scattering properties do not directly depend on composition, but rather depend on the optical constants which in turn depend on the composition. Particles with very different composition may have similar optical constants. Unfortunately, the high level of detailed knowledge required to determine $f(D,C,T)$ or $f(D,n,k)$ for most real dispersion, and specifically for fly ash, is not available. Therefore, such a detailed formulation is currently of little practical use.

As a final alternative, the polydispersion can be approximated as a combination of classes of particles, where each class has similar optical constants. In this formulation it is assumed that each class of particles has size distribution $f(D)$, and that particles within each class have identical optical constants. If we assume that the particles are spherical then the scattering coefficient is

$$\sigma_\lambda = \frac{3}{2} \sum_i \frac{C_{v,i}\overline{Q_{\text{sca},i}}}{D_{32,i}}. \qquad \text{(D.11)}$$

Here $C_{v,i}$, $\overline{Q_{\text{sca},i}}$, and $D_{32,i}$ are the volume fraction, average scattering efficiency, and Sauter mean diameter for particles in class i. Similarly, the absorption coefficient becomes

$$\alpha_\lambda = \frac{3}{2} \sum_i \frac{C_{v,i}\overline{Q_{\text{abs},i}}}{D_{32,i}}. \qquad \text{(D.12)}$$

Finally, the scattering phase function is

$$\Phi_\lambda = \frac{3}{2\sigma_\lambda} \sum_i \frac{C_{v,i}\overline{Q_{\text{sca},i}}}{D_{32,i}} \overline{\Phi_{\lambda,i}}. \qquad \text{(D.13)}$$

Here $\overline{Q_{\text{abs},i}}$ and $\overline{\Phi_{\lambda,i}}$ are the average absorption efficiency and average scattering phase function for particles in class i.

D.4 Mie Scattering

The scattering and absorption of a plane electromagnetic wave by a single spherical, isotropic, and homogeneous particle can be calculated using Mie theory [18]. The scattering efficiency, Q_{sca}, and absorption efficiency, Q_{abs} of a single particle are defined as the power that is scattered and absorbed, respectively, normalized by the power incident on the particle's projected area. To compute these quantities, as well as other scattering properties of a spherical particle, one must know the refractive index, $m = n + ik$, of the particle relative to the surrounding medium, and the particle size parameter, $x \equiv \pi D/\lambda$. If the surrounding medium has refractive index n_∞, and the particle has refractive index $m_p = n_p + ik_p$, then $m = n_p/n_\infty + ik_p/n_\infty$. For most gases the refractive index n_∞ is approximately unity. The size parameter, x, is the size of the particle relative to the wavelength of the incident monochromatic light, that is, the particle size parameter, $x = \pi D/\lambda$. Here D is the particle diameter and λ is the wavelength of light in the surrounding medium. If the wavelength in vacuum is λ_o, then $\lambda = \lambda_o/n_\infty$, and the size parameter is

$$x = \frac{\pi D n_\infty}{\lambda_o} \tag{D.14}$$

From Bohren and Huffman [18], the scattering efficiency is given by the infinite series

$$Q_{\text{sca}} = \frac{2}{x^2} \sum_{n=1}^{\infty} (2n+1) \left(|a_n(x,m)|^2 + |b_n(x,m)|^2 \right) \tag{D.15}$$

and the extinction efficiency is given by the series

$$Q_{\text{ext}} = \frac{2}{x^2} \sum_{n=1}^{\infty} (2n+1) \, \text{Re}\{a_n(x,m) + b_n(x,m)\}. \tag{D.16}$$

The absorption efficiency is simply

$$Q_{\text{abs}} = Q_{\text{ext}} - Q_{\text{sca}}. \tag{D.17}$$

In addition, the asymmetry parameter, g, is given by the series

$$g = \frac{4}{x^2 Q_{\text{sca}}} \left[\sum_{n=1}^{\infty} \frac{n(n+2)}{n+1} \text{Re}\{a_n a_{n+1}^* + b_n b_{n+1}^*\} + \sum_{n=1}^{\infty} \frac{2n+1}{n(n+1)} \text{Re}\{a_n b_n^*\} \right]. \tag{D.18}$$

Here $a_n = a_n(x,m)$ and $b_n = b_n(x,m)$ and the superscript $()^*$ denotes complex conjugate. The asymmetry parameter describes the asymmetry of the scattering,

with g ranging from $g = 1$ for completely forward scattering to $g = -1$ for completely backward scattering. For symmetric forward and backbard scattering, including isotropic scattering, $g = 0$. Very large dielectric particles have $g \sim 1$ while very small particles (Rayleigh scattering) have $g \simeq 0$.

The complex Mie amplitudes $a_n(x,m)$ and $b_n(x,m)$ can be computed from the relations

$$\begin{aligned} a_n(x,m) &= \frac{[D_n(mx)/m + n/x]\,\psi_n(x) - \psi_{n-1}(x)}{[D_n(mx)/m + n/x]\,\xi_n(x) - \xi_{n-1}(x)} \\ b_n(x,m) &= \frac{[mD_n(mx) + n/x]\,\psi_n(x) - \psi_{n-1}(x)}{[mD_n(mx) + n/x]\,\xi_n(x) - \xi_{n-1}(x)} \end{aligned} \tag{D.19}$$

where the functions $D_n(\rho)$ satisfies the recurrence relation

$$D_{n-1}(\rho) = \frac{n}{\rho} - \frac{1}{D_n(\rho) + n/\rho}. \tag{D.20}$$

The functions $\psi_n(x)$ and $\xi_n(x)$ are the Riccati-Bessel functions and are both computed by the upward recurrence relation

$$\psi_{n+1}(x) = \frac{2n+1}{x}\psi_n(x) - \psi_{n-1}(x) \tag{D.21}$$

where $\xi_n(x) = \psi_n(x) - i\chi_n(x)$. Note $\chi_n(x)$ also obeys the recurrence relation in Eq. (D.21). The starting conditions for the upward recurrence are

$$\begin{aligned} \psi_{-1}(x) &= \cos x, & \psi_0(x) &= \sin x, \\ \chi_{-1}(x) &= -\sin x, & \chi_0(x) &= \cos x. \end{aligned} \tag{D.22}$$

A critical aspect of the Mie calculation is truncation of the series after a finite number of terms. Bohren and Huffman [18] indicate that approximately $N \simeq x + 4x^{1/3} + 2$ terms are required to accurately compute Q_{ext} and Q_{sca}, where N is the integer nearest to the real value of $x + 4x^{1/3} + 2$. Also, since ψ_n and ξ_n are computed by upward recurrence, as described above, only N values must be computed. This estimate of N is in close agreement to that of Wiscombe [46] where the required number of terms, N, was carefully examined. Wiscombe found that

$$N = \begin{cases} x + 4x^{1/3} + 1 & ; \quad 0.02 \le x \le 8 \\ x + 4.05x^{1/3} + 2 & ; \quad 8 < x < 4200 \\ x + 4x^{1/3} + 2 & ; \quad 4200 \le x \le 20{,}000 \end{cases} \tag{D.23}$$

very accurately predicted the required number of terms. Wiscombe's choice of N, Eq. (D.23), is adopted in this work.

The function $D_n(mx)$ is computed by downward recurrence, where $D_{\text{N}_\text{D}}(mx)$ is assumed to be $0 + i0$ for some large value of $n = \text{N}_\text{D}$, and $D_n(mx)$ for smaller n is

computed from the relation Eq. (D.20). As was stated above, the number of terms in the series for Q_{sca} and Q_{ext} is N, thus at least the lowest N values of D_n must be accurate. Therefore, N_D must be sufficiently greater than N so that the value of $D_N(mx)$ is independent of the initial choice $D_{\text{N}_\text{D}}(mx)$, and of course accurate. Bohren and Huffman suggest using

$$\text{N}_\text{D} = \begin{cases} N + 15 & ; N > |mx| \\ |mx| + 15 & ; N < |mx| \end{cases} \tag{D.24}$$

where again N_D is the integer value nearest the real value. Upon careful examination, one finds that using Eq. (D.24) leads to significant errors in $D_N(mx)$ when x is large (>100), but choosing N_D approximately 10% larger provides accurate results. Therefore, we choose N_D as

$$\text{N}_\text{D} = \begin{cases} 1.1\,(N + 15) & ; N > |mx| \\ 1.1\,(|mx| + 15) & ; N < |mx|. \end{cases} \tag{D.25}$$

The formulae presented above can be used to compute the complex Mie amplitudes, $a_n(x, m)$ and $b_n(x, m)$, and the efficiencies Q_{ext} and Q_{sca}. From these values one can compute the absorption efficiency from $Q_{\text{abs}} = Q_{\text{ext}} - Q_{\text{sca}}$, which leads to calculations of the spectral scattering and absorption coefficients (σ_λ and α_λ), as will be shown.

The remaining calculation of the spectral scattering scattering phase function, Φ_λ, is facilitated by expressing Φ_λ as a series of Legendre polynomials, i.e.

$$\Phi_\lambda(\mu) = \sum_{k=0}^{\infty} A_k P_k(\mu); \qquad A_0 = 1 \tag{D.26}$$

The Legendre coefficients, A_k, are calculated directly using the values of $a_n(x, m)$ and $b_n(x, m)$ above. The procedure for computing A_k is taken directly from Dave [47] and is presented here without derivation. Only those formulae required for calculation of the Legendre coefficients, A_k, are presented.

The Legendre coefficients A_k are for randomly polarized incident monochromatic light, and are the average of the parallel and perpendicular polarizations of the scattered light, i.e.,

$$A_{k-1} = \frac{1}{2}\left(\frac{4}{x^2 Q_{\text{sca}}}\right)\left(L_k^{(1)} + L_k^{(2)}\right); \qquad k = 1, 2, 3, \ldots. \tag{D.27}$$

Here ${L_k}^{(1)}$ and ${L_k}^{(2)}$ are real values obtained from the series

$$ {L_k}^{(1)} = (k-\tfrac{1}{2}) \sum_{j=k'}^{\infty} {a_j}^{(k-1)} \sum_{i=0}^{k'} {b_i}^{(k-1)} \Delta_{i,k} \mathrm{Re}\left[D_p(x,m)\, D_q^*(x,m) \right] \qquad \text{(D.28)} $$

and

$$ {L_k}^{(2)} = (k-\tfrac{1}{2}) \sum_{j=k'}^{\infty} {a_j}^{(k-1)} \sum_{i=0}^{k'} {b_i}^{(k-1)} \Delta_{i,k} \mathrm{Re}\left[C_p(x,m)\, C_q^*(x,m) \right] \qquad \text{(D.29)} $$

The superscript (*) denotes complex conjugate and Re[ ] denotes the real part of a complex quantity. The integer k' and $\Delta_{i,k}$ are defined as

$$ k' \equiv \begin{cases} \frac{k-1}{2} & ; \quad \text{odd } k \\ \\ \frac{k-2}{2} & ; \quad \text{even } k \end{cases} \qquad \text{and} \qquad \Delta_{i,k} \equiv \begin{cases} 1 & i = 0, \text{ odd } k \\ 2 & i > 0, \text{ odd } k \\ 2 & i \geq 0, \text{ even } k \end{cases} , \qquad \text{(D.30)} $$

respectively. Thus $k' = (0,0,1,1,2,2,\ldots)$ for $k = (1,2,3,4,5,6,\ldots)$, respectively. The subscripts p and q are defined as

$$ p = j - i + 1 \quad \text{and} \quad q = j + i + 1 + \delta \qquad \text{(D.31)} $$

where $\delta = 0$ for odd k and $\delta = 1$ for even k.

The coefficients ${a_j}^{(k-1)}$ and ${b_i}^{(k-1)}$ are real constants – unrelated to the complex Mie amplitudes $a_n(x,m)$ and $b_n(x,m)$. For a fixed value of k, the series of values of ${a_j}^{(k-1)}$ and ${b_i}^{(k-1)}$ are determined from the recurrence relations

$$ {a_j}^{(k-1)} = \frac{(2j-k)(2j+k-1)}{(2j+k)(2j-k+1)} {a_{j-1}}^{(k-1)} \quad (\text{odd } k \text{ and } j > k') \qquad \text{(D.32}a\text{)} $$

and

$$ {b_i}^{(k-1)} = \frac{(k-2i+1)(k+2i-2)}{(k-2i)(k+2i-1)} {b_{i-1}}^{(k-1)} \quad (\text{odd } k \text{ and } i > 0) . \qquad \text{(D.32}b\text{)} $$

The starting values of ${a_j}^{(k-1)}$ and ${b_i}^{(k-1)}$ for $j = k' = (k-1)/2$ and $i = 0$, respectively, are also given by recurrence relations, but with recurrence on the superscript $(k-1)$, not the subscript. For odd k (where $k' = (k-1)/2$) these starting values for the sums over j and i are given as

$$ {a_{(k-1)/2}}^{(k-1)} = \begin{cases} 2 & ; k = 1 \\ \\ \frac{4(k-1)(k-2)}{(2k-1)(2k-3)} {a_{(k-3)/2}}^{(k-3)} & ; k = 3,5,7,\ldots \end{cases} \qquad \text{(D.33}a\text{)} $$

and

$$b_0{}^{(k-1)} = \begin{cases} 1 & ; k = 1 \\ \left(\frac{k-2}{k-1}\right)^2 b_0{}^{(k-3)} & ; k = 3,5,7,\ldots \end{cases} \tag{D.33b}$$

For even values of k, the recurrence relations analogous to Eq. (D.32) are

$$a_j{}^{(k-1)} = \frac{(2j-k+1)(2j+k)}{(2j+k+1)(2j-k+2)} a_{j-1}{}^{(k-1)} \quad \text{(even } k \text{ and } j > k'\text{)} \tag{D.34a}$$

and

$$b_i{}^{(k-1)} = \frac{(2i+k+1)(2i-k)}{(2i-k+1)(2i+k)} b_{i-1}{}^{(k-1)} \quad \text{(even } k \text{ and } i > 0\text{)}. \tag{D.34b}$$

The starting values for these two recurrence relations, i.e., for $j = k' = (k-2)/2$ and $i = 0$, respectively, are given by the recurrence relations

$$a_{(k-2)/2}{}^{(k-1)} = \begin{cases} \frac{4}{3} & ; k = 2 \\ \frac{4(k-1)(k-2)}{(2k-1)(2k-3)} a_{(k-4)/2}{}^{(k-3)} & ; k = 4,6,8,\ldots \end{cases} \tag{D.35a}$$

and

$$b_0{}^{(k-1)} = \begin{cases} \frac{1}{2} & ; k = 2 \\ \left(\frac{k-2}{k-1}\right)^2 b_0{}^{(k-3)} & ; k = 4,6,8,\ldots \end{cases} \tag{D.35b}$$

The complex functions $C_\ell(x,m)$ and $D_\ell(x,m)$, where ℓ is either p or q in Eq. (D.28) or Eq. (D.29), are determined from sums over the complex Mie amplitudes $a_n(x,m)$ and $b_n(x,m)$. Again, from Dave [47],

$$C_\ell(x,m) = \frac{1}{\ell}(2\ell-1)(\ell-1) b_{\ell-1}(x,m) + (2\ell-1)\sum_{i=1}^{\infty}\left[\left(\frac{1}{n}+\frac{1}{n+1}\right) a_n(x,m) - \left(\frac{1}{n+1}+\frac{1}{n+2}\right) b_{n+1}(x,m)\right] \tag{D.36a}$$

and

$$D_\ell(x,m) = \frac{1}{\ell}(2\ell-1)(\ell-1) a_{\ell-1}(x,m) + (2\ell-1)\sum_{i=1}^{\infty}\left[\left(\frac{1}{n}+\frac{1}{n+1}\right) b_n(x,m) - \left(\frac{1}{n+1}+\frac{1}{n+2}\right) a_{n+1}(x,m)\right] \tag{D.36b}$$

Here $n = \ell + 2i - 2$ in Eq. (D.36). Note here that $n \geq 1$.

Finally, the infinite series in Eq. (D.28), Eq. (D.29), and Eq. (D.36) are truncated after N terms as prescribed by Eq. (D.23). Dave [47] shows that for a size parameter x the series in Eq. (D.26) can be truncated after approximately $2x+10$ terms. However, if one is interested in radiative heat transfer, it is possible to obtain accurate results with far fewer terms (see Appendix E).

Appendix E.

Solution of the Radiative Transport Equation

This appendix describes the formulation and solution of the radiative transport equation for a planar medium using the discrete ordinates method. The discrete ordinates method is relatively simple to program and easily extensible to multi-dimensional domains in which radiative properties depend on position and/or temperature. The technique for a one-dimensional participating medium is described here.

E.1 The Radiative Transport Equation For a Planar Layer

The radiative transport equation for a one dimensional planar medium is [35]

$$\mu \frac{dI(x,\mu)}{dx} = -[\sigma(x)+\alpha(x)]\, I(x,\mu) + \alpha(x)\, I_b[T(x)] + \frac{\sigma(x)}{4\pi}\int_0^{2\pi}\int_{-1}^{1} \Phi(\mu_0)\, I(x,\mu')\, d\mu' d\phi \qquad \text{(E.1)}$$

where x is the coordinate normal to the infinite planar layer, μ is the cosine of the angle measured from the positive x-direction, and $T(x)$ is the temperature distribution in the medium. The radiance, $I(x,\mu)$, and all the radiative properties are spectral quantities but the subscript λ is dropped for brevity. The scattering phase function, $\Phi(\mu_0)$ depends only on the angle between incident and scattered radiation which is given by

$$\mu_0 = \Omega \cdot \Omega' = \mu\mu' - \sqrt{1-\mu'^2}\sqrt{1-\mu^2}\cos(\phi-\phi'), \qquad \text{(E.2)}$$

where the azimuthal angle ϕ lies in the range $0 \le \phi \le 2\pi$.

It is convenient to introduce the dimensionless optical depth, τ,

$$\tau \equiv \int_0^x (\alpha+\sigma)\, dx' \qquad \text{(E.3)}$$

as the new independent space variable and the dimensionless scattering albedo

$$\omega(\tau) \equiv \frac{\sigma(\tau)}{\alpha(\tau)+\sigma(\tau)}. \qquad \text{(E.4)}$$

For a layer with thickness ℓ the total optical depth is simply $\tau = \int_0^\ell (\alpha + \sigma)\, dx$. With this change of variables the radiation transport equation,Eq. (E.1), becomes

$$\mu \frac{\partial I(\tau,\mu)}{\partial \tau} = -I(\tau,\mu) + S(\tau,\mu) \tag{E.5a}$$

$$S(\tau,\mu) \equiv [1-\omega(\tau)]\, I_b[T(\tau)] + \frac{\omega(\tau)}{4\pi} \int_0^{2\pi} \int_{-1}^{1} \Phi(\mu_0)\, I(\tau,\mu')\, d\mu' d\phi \tag{E.5b}$$

Solutions of equation (E.5) are obtained using the *discrete ordinates method* [48-49]. In that method, Eq. (E.5) is approximated by evaluation of the direction cosine, μ, at a finite number of discrete directions, μ_m, and integrals over μ become finite summations. For example, an integral is approximated by the *quadrature formula*

$$\int_{-1}^{1} f(\mu)\, d\mu = \sum_{m=1}^{M} f(\mu_m)\, w_m$$

where the ordinate, μ, has been divided into M discrete values μ_m with w_m being the weight associated with μ_m.

E.2 Quadrature Formula

An important aspect of the *discrete ordinates method* is selection of the directions,μ_m. It is useful to understand quadrature formulae so that "good" choices for μ_m are made.

Following the development from Chandrasekhar [48], consider the general integral

$$I = \int_a^b f(x)\, w(x)\, dx \tag{E.6}$$

where $f(x)$ is some general function and $w(x)$ is a weight function. The goal is to construct a suitable quadrature formula (approximate summation) which closely approximates I using a finite number, M, of discrete abscissas, x_j.

Letting x_j be one of the set $(x_1, x_2, \ldots, x_M)$, where $a \le x_j \le b$, we construct a polynomial using Lagrange's formula

$$\phi(x) = \sum_{j=1}^{M} f(x_j)\, \frac{F(x)}{(x-x_j)\, F'(x_j)} \tag{E.7a}$$

where

$$F(x) = \prod_{j=1}^{M} (x - x_j) \quad \text{and} \quad F'(x_j) = \prod_{\substack{i=1 \\ i \neq j}}^{M} (x_j - x_i) \tag{E.7b}$$

From this formula it is clear that $\phi(x) = f(x)$ at the quadrature points x_j. Moreover, if $f(x)$ is a polynomial of order $M-1$ or less, $\phi(x)$ is exactly equal to $f(x)$ for all x.

Substituting the polynomial approximation, $\phi(x)$, for the function $f(x)$ in the integral I gives

$$I \simeq \int_a^b \phi(x)\, w(x)\, dx = \sum_{j=1}^{M} \frac{f(x_j)}{F'(x_j)} \int_a^b \frac{F(x)\, w(x)}{(x - x_j)} dx$$

or, by defining a_j as

$$a_j \equiv \frac{1}{F'(x_j)} \int_a^b \frac{F(x)\, w(x)}{x - x_j} dx, \tag{E.8}$$

we obtain

$$I \simeq \sum_{j=1}^{M} a_j f(x_j). \tag{E.9}$$

The error introduced by approximating Eq. (E.6) with Eq. (E.9) is

$$\epsilon_M = I - \sum_{j=1}^{M} a_j f(x_j). \tag{E.10}$$

Since $\phi(x)$ was an M^{th} order polynomial passing exactly through M points of the function $f(x)$, the error, ϵ_M, vanishes if $f(x)$ is a polynomial of order $M-1$ or less; so long as the M x_j's are unique, any x_j's will do. The question arises: can the x_j be chosen in a "smart" way to make the error vanish for cases when $f(x)$ is a polynomial of order higher than $M-1$? Carl Friedrich Gauss showed that x_j *can* be chosen in such a way.

Consider the case when $f(x)$ is a polynomial of order $2M-1$. Define the moments of the weight function $w(x)$ as

$$\alpha_\ell = \int_a^b x^\ell w(x)\, dx. \quad ; \quad (\ell = 0, 1, \ldots, 2M-1) \tag{E.11}$$

For the approximate quadrature formula to be exact, the moments must satisfy the equations

$$\alpha_\ell = \sum_{j=1}^{M} a_j x_j^\ell \quad ; \quad (\ell = 0, 1, \ldots, 2M-1) \tag{E.12}$$

which gives $2M$ equations for the $2M$ unknowns $(a_1, \ldots, a_M)$ and $(x_1, \ldots, x_M)$.

Chandrasekhar [48] carefully outlines a method for finding the a_j and x_j using Eq. (E.12), thus demonstrating that one can construct an M point quadrature formula that will exactly evaluate integrals of weighted polynomials of order $2M-1$. This result is very important and not at all intuitive *a priori*.

Now that it is established that there are "good" choices for x_j, reconsider the original approximating polynomial, $\phi(x)$, which is a polynomial of order M. Recall that $\phi(x)$ is equal to $f(x)$ at the x–values $(x_1, \ldots, x_M)$ and the function $F(x) = \prod_{j=1}^{M}(x - x_j)$ is also a polynomial of order M. If $f(x)$ is a polynomial of order $2M-1$ it can be written as

$$f(x) = \phi(x) + F(x) \sum_{\ell=0}^{M-1} q_\ell x^\ell \tag{E.13}$$

where q_ℓ are known constants for a given polynomial $f(x)$. Using this expression for $f(x)$ the error, Eq. (E.10), of the quadrature formula is

$$\begin{aligned} \epsilon_M &= \int_a^b f(x)\, w(x)\, dx - \sum_{j=1}^{M} a_j f(x_j) \\ &= \int_a^b \phi(x)\, w(x)\, dx + \int_a^b F(x) \left(\sum_{\ell=0}^{M-1} q_\ell x^\ell \right) w(x)\, dx \\ &\quad - \int_a^b \phi(x)\, w(x)\, dx \\ &= \sum_{\ell=0}^{M-1} q_\ell \int_a^b F(x)\, w(x)\, x^\ell dx \end{aligned} \tag{E.14}$$

Since all the q_ℓ are not necessarily zero, the error, ϵ_M, vanishes only if

$$\int_a^b F(x)\, w(x)\, x^\ell = 0 \qquad , \qquad (\ell = 0, \ldots, M-1)\,. \tag{E.15}$$

This condition determines $F(x)$ and the ordinates x_j, which are simply found from $F(x_j) = 0$. Once x_j are known, the weights, a_j are determined from Eq. (E.8).

Consider the special case of $w = 1$ and the limits $a = -1$, $b = 1$. For this special case the integral, I, is defined as

$$I \equiv \int_{-1}^{1} f(\mu)\, d\mu$$

and the condition determining the function $F(\mu)$ becomes

$$\int_{-1}^{1} F(\mu)\,\mu^{\ell} = 0 \qquad , \qquad (\ell = 0, \ldots, M-1)\,. \tag{E.16}$$

A function $F(\mu)$ which satisfies Eq. (E.16) for all $\ell < M$ is the Legendre polynomial $P_M(\mu)$. Therefore, the choice of μ_j as the roots of the Legendre polynomial $P_M(\mu) = 0$ yields a quadrature formula with M terms that is capable of exactly evaluating integrals of polynomials of order $2M-1$. The weight factors w_j (previously termed a_j) are determined from Eq. (E.8) to be

$$w_j = \frac{1}{P'_M(\mu_j)} \int_{-1}^{1} \frac{P_M(\mu)}{\mu - \mu_j} d\mu. \tag{E.17}$$

This choice of μ_j and w_j is known as the Gauss quadrature and the "Gauss quadrature formula" is simply

$$\int_{-1}^{1} f(\mu)\,d\mu \simeq \sum_{j=1}^{M} f(\mu_j)\,w_j \tag{E.18}$$

Press, et. al. [50] discusses algorithms that quickly compute μ_j and w_j for a given order M.

E.3 The Discrete Ordinates Method

The Gauss quadrature formula developed in the previous section is used to approximate the radiative transport equation, Eq. (E.5), as M equations for the "discrete ordinate" directions $(\mu_1, \ldots, \mu_M)$. Integrals in μ are replaced by quadrature summations and the resulting system of equations is

$$\mu_m \frac{dI^m}{d\tau} + I^m = S^m \qquad (m = 1, 2, \ldots, M) \tag{E.19a}$$

where

$$S^m \equiv S(\tau, \mu_m) \simeq (1-\omega)\,I_b + \frac{\omega}{2} \sum_{j=1}^{M} \Phi(\mu_m, \mu_j)\,I^j w_j \tag{E.19b}$$

and

$$\Phi(\mu_m, \mu_j) \equiv \frac{1}{2\pi} \int_0^{2\pi} \Phi(\mu_0)\,d\phi. \tag{E.19c}$$

The scattering albedo, ω, and Plank blackbody function, I_b, are both general functions of position τ, as could also be the scattering phase function $\Phi(\mu_m, \mu_j)$.

The scattering phase function, $\Phi(\mu_m, \mu_j)$, is evaluated by expanding $\Phi(\mu_0)$ as a series of Legendre polynomials,

$$\Phi(\mu_0) = \sum_{i=0}^{\infty} A_i P_i(\mu_0), \qquad A_0 = 1 \tag{E.20}$$

where μ is in the range $-1 \leq \mu \leq 1$. Using the orthogonality relation for $P_m(\mu)$

$$\int_{-1}^{1} P_i(\mu) P_j(\mu) \, d\mu = \frac{2}{2j+1} \delta_{ij}$$

where $\delta_{ij} = 0$ if $i \neq j$ and 1 if $i = j$, one can determine the expansion coefficients, A_j, from the relation

$$A_j = \frac{2j+1}{2} \int_{-1}^{1} \Phi(\mu) P_j(\mu) \, d\mu. \tag{E.21}$$

Once the A_j are determined for a given $\Phi(\mu)$, it remains to compute $\Phi(\mu, \mu')$ from Eq. (E.19c). In practice the infinite Legendre series expansion is truncated after a finite number of terms, N, so that

$$\Phi(\mu_m, \mu_j) \simeq \sum_{n=0}^{N} A_n P_n(\mu_m) P_n(\mu_j). \tag{E.22}$$

Mie calculations indicate that for large particles, choosing N as approximately twice the particle size parameter, x, is sufficient to resolve the phase function with adequate accuracy. The Legendre polynomials are computed using upward recurrence from the relation

$$P_n(\mu) = \frac{(2n-1)\mu P_{n-1} - (n-1) P_{n-2}}{n}; \qquad P_1(\mu) = \mu; \qquad P_0(\mu) = 1.$$

The next step in the discrete ordinates method is to finite difference the spatial derivative using a non-uniform grid in τ. Dividing the layer into L planar layers with $L+1$ surfaces at $(\tau_0, \tau_1, \ldots, \tau_L)$, and using central differences (2^{nd} order accurate) about $(i + \frac{1}{2})$, one can approximate Eq. (E.19a) as

$$\mu_m \left(\frac{I^m_{i+1} - I^m_i}{\Delta \tau_i} \right) + I^m_{i+\frac{1}{2}} = S^m_{i+\frac{1}{2}} \tag{E.23}$$

where

$$\Delta \tau_i \equiv \tau_{i+1} - \tau_i \qquad \text{and} \qquad I^m_i \equiv I(\tau_i, \mu_m).$$

The values at half intervals $(i + \frac{1}{2})$ are evaluated by averaging on the two interfaces bounding the interval, i.e.,

$$I^m_{i+\frac{1}{2}} = \frac{1}{2}\left(I^m_{i+1} + I^m_i\right) \qquad S^m_{i+\frac{1}{2}} = \frac{1}{2}\left(S^m_{i+1} + S^m_i\right). \tag{E.24}$$

Finally, rearranging terms in Eq. (E.23) and substituting Eq. (E.24), the difference formula is written as

$$I_{i+1}^m = \left(\frac{\frac{\mu_m}{\Delta\tau_i} - \frac{1}{2}}{\frac{\mu_m}{\Delta\tau_i} + \frac{1}{2}} \right) I_i^m + \frac{\frac{1}{2}\left(S_{i+1}^m + S_i^m\right)}{\frac{\mu_m}{\Delta\tau_i} + \frac{1}{2}} \qquad (\mu_m > 0) \qquad \text{(E.25}a\text{)}$$

This difference equation is evaluated only in the forward direction, $(\mu_m > 0)$, by starting with boundary values at $\tau = \tau_0$ and stepping forward in τ. A similar equation is formulated for stepping in the backward direction, $\mu_m < 0$. Following a procedure similar to that above, one can write

$$I_{i-1}^m = \left(\frac{\frac{\mu_m}{\Delta\tau_{i-1}} + \frac{1}{2}}{\frac{\mu_m}{\Delta\tau_{i-1}} - \frac{1}{2}} \right) I_i^m - \frac{\frac{1}{2}\left(S_i^m + S_{i-1}^m\right)}{\frac{\mu_m}{\Delta\tau_{i-1}} - \frac{1}{2}}. \qquad (\mu_m < 0) \qquad \text{(E.25}b\text{)}$$

Note that S_i^m depends on the radiance, I_i^j at τ_i in all directions μ_j $(j = 1, \ldots, M)$ through Eq. (E.19b). However, one can overcome this complication by using iteration. That is, we assume initially that the S_i^m are known for all m and i, then compute the radiance I_j^m using Eq. (E.25). Next, we recompute S_j^m using the newly acquired radiance, I_j^m. This iteration is repeated until subsequent calculations of I_j^m produce negligible change.

E.3.1 Boundary Conditions

For unique solutions to exist, one must specify the boundary conditions at $\tau = 0$ and $\tau = \tau_0$. Since the analysis thus far has been restricted to azimuthally symmetric radiation in a plane layer (1-D), azimuthally symmetric boundary conditions are also used. Consider the boundaries to be diffusely emitting, partially diffuse reflecting, and partially specular reflecting. Thus

$$I\left(0, \mu\right) = \epsilon_0 I_b\left(T_0\right) - 2\rho_0^d \int_{-1}^{0} I\left(0, \mu'\right) \mu' d\mu' + \rho_0^s I\left(0, -\mu\right); \qquad (\mu > 0) \qquad \text{(E.26}a\text{)}$$

$$I\left(\tau_0, \mu\right) = \epsilon_L I_b\left(T_1\right) + 2\rho_L^d \int_{0}^{1} I\left(\tau_0, \mu'\right) \mu' d\mu' + \rho_L^s I\left(\tau_0, -\mu\right); \qquad (\mu < 0) \qquad \text{(E.26}b\text{)}$$

where ϵ is the diffuse emissivity, ρ^d is the diffuse reflectivity, ρ^s is the specular reflectivity, and subscripts "0" and "L" denote the boundaries at $\tau = 0$ and $\tau = \tau_0$ respectively.

The integrals in the boundary conditions are replaced with Gauss quadrature formulas to give

$$I_0^m = \epsilon_0 I_{b0} - 2\rho_0^d \sum_{\substack{j \\ \mu_j<0}} I_0^j \mu_j w_j + \rho_0^s I_0(-\mu_m) \qquad (\mu_m > 0) \tag{E.27a}$$

$$I_L^m = \epsilon_L I_{bL} - 2\rho_L^d \sum_{\substack{j \\ \mu_j>0}} I_L^j \mu_j w_j + \rho_L^s I_L(-\mu_m) \qquad (\mu_m < 0) \tag{E.27b}$$

Note that the radiation incident on the layer boundaries is coupled to the emergent radiance if the boundaries are reflecting. However, by iterating as described for S_i^m, the solution can be obtained without solving any time-consuming matrix equations for the boundary intensities.

E.3.2 Convergence Criterion

Iteration is used as discussed above to avoid the implicit dependence of the source function S_i^m and the boundary conditions on the radiance, I_i^m. Convergence of the iterative process is presumed when the heat flux at each optical depth, τ_i, changes from one iteration to the next by less than some prescribed small amount. The heat flux through the layer can be computed at each optical depth, τ_i, and for each iteration using the quadrature approximation

$$Q_i \simeq 2\pi \sum_{m=0}^{M} I_i^m \mu_m w_m. \tag{E.28}$$

E.3.3 Solution Procedure

The formulation presented above was implemented in a computer program. The algorithm is relatively simple, since all equations are solved explicitly and iteration is used to find the solution. The following summary outlines the necessary steps of the computation:

1. Input layer thickness and number of divisions L, number of ordinates M, absorption coefficient $\alpha(x)$, scattering coefficient $\sigma(x)$, temperature distribution $T(x)$, Legendre coefficients $(A_0, \ldots, A_N)$, and boundary conditions.

2. Compute optical depths $(\tau_0, \ldots, \tau_L)$, albedo $(\omega_0, \ldots, \omega_L)$, ordinates $(\mu_1, \ldots, \mu_M)$ and weights $(w_1, \ldots, w_M)$, and scattering phase function $\Phi(\mu_i, \mu_j)$.

3. Set initial values for I_i^m, S_i^m, and Q_i^m.

4. Compute I_i^m from Eq. (E.25).

5. Using new I_i^m from step **4**, compute S_i^m from Eq. (E.19b).

6. Compute boundary intensities from Eq. (E.27).

7. Compute Q_i at all τ_i and compare with previous Q_i. If change is greater than some error, ϵ, repeat steps **4–7**.

8. Print results.

E.4 Results and Code Evaluation

A number of computations were made to check the validity and accuracy of the codes. In all cases the codes produced the expected results when compared to exact calculations [35] for isotropic and anisotropic scattering. No significant accuracy or convergence problems were encountered.

All the calculations presented here are for monodispersions of single–composition particles at a single wavelength. We assume that the medium is composed of single–sized spheres with complex refractive index, $m = 1.5 + i10^{-4}$. The size of the spheres, the layer thickness or particle number density, and the absorption coefficient of the surrounding medium is varied to allow investigation of the effect of anisotropic scattering, optical depth, and scattering albedo on the heat flux and emergent radiance.

j	A_j			j	A_j	j	A_j
	$x = 0.5$	$x = 9$	$x = 36$	$x = 36$ cont...			
0	1.00000	1.00000	1.00000	28	17.92965	56	7.37375
1	0.14660	1.94672	2.43076	29	17.83307	57	7.65716
2	0.50398	2.99090	3.64363	30	17.84446	58	7.43930
3	0.02760	2.95185	4.09975	31	17.74673	59	7.40488
4	0.00064	3.72708	5.11313	32	17.61028	60	6.67121
5		3.73798	5.56431	33	17.54370	61	6.03762
6		4.23106	6.59476	34	17.23547	62	4.60609
7		4.07042	7.26245	35	17.17773	63	3.68276
8		3.91514	8.26331	36	16.71310	64	2.99628
9		3.59674	8.97579	37	16.62407	65	2.96285
10		2.93476	9.65623	38	16.07435	66	2.91504
11		2.43094	10.32124	39	15.90400	67	2.47309
12		1.76028	10.92715	40	15.34633	68	2.28324
13		1.24217	11.54660	41	15.06051	69	1.60334
14		1.08177	12.12031	42	14.46099	70	1.44967
15		0.92934	12.76528	43	14.01492	71	0.44679
16		1.19935	13.45026	44	13.28404	72	0.30244
17		0.91896	14.04943	45	12.69559	73	-0.02195
18		1.13655	14.76339	46	11.81117	74	0.25306
19		0.21873	15.28887	47	11.20362	75	0.07880
20		0.82504	15.92009	48	10.29457	76	0.05265
21		-0.00477	16.33683	49	9.78790	77	-0.07277
22		0.00940	16.84643	50	8.93928	78	0.02366
23		0.00228	17.11450	51	8.47910	79	0.00478
24		0.00042	17.48682	52	7.81775	80	0.00333
25			17.59325	53	7.55318	81	-0.00447
26			17.83077	54	7.26440	82	0.00107
27			17.80505	55	7.43740	83	0.00013

E.4.1 The Scattering Phase Function

The scattering phase function was computed for particles sizes ranging from $x = 0.5$ to $x = 100$. The Legendre expansion coefficients, A_j, were computed using Eq. (E.21) and Mie scattering theory to determine $\Phi(\mu)$. Table E.1 shows some typical sets of expansion coefficients for particle size parameters $x = 0.5$, $x = 9$, and $x = 36$. The series was truncated when the coefficients became smaller than 10^{-3}, which generally corresponded to two or three times x for large x.

When x is large, the scattering phase function is very complicated with approximately x scattering lobes. Therefore, many terms in a Legendre expansion are required to accurately fit the phase function. Moreover, if the scattering phase function

requires N terms to be accurately modeled, then the discrete ordinates method will require at least $M = (N+1)/2$ ordinates (directions) if accurate integrations of the phase function are to be performed (recall that the Gauss quadrature integration rule can exactly integrate polynomials of order $2M-1$ using only M abscissas). If scattering is very important ($\omega \rightarrow 1$), as it is in fly ash dispersions, then this problem is considerably more troublesome.

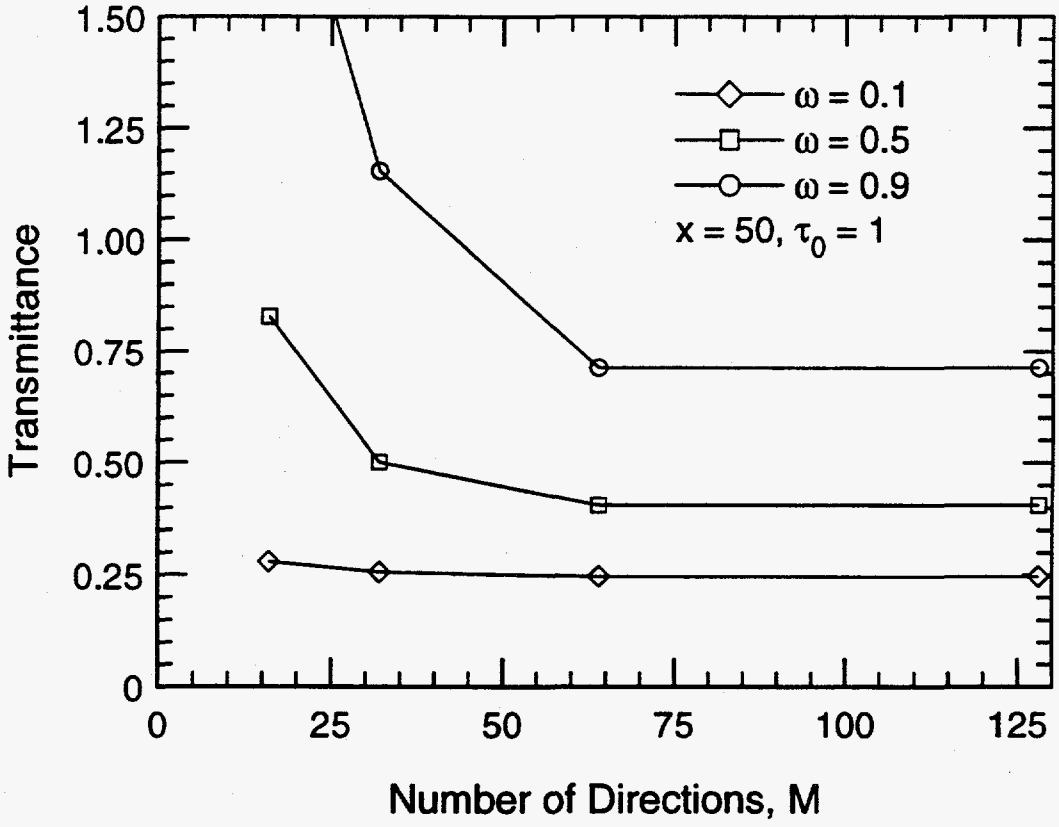

Figure E.1: The transmittance of a scattering layer versus the number of ordinates.

Figure E.1 shows the effect of choosing too few ordinate directions on the transmittance, $0 \leq T \leq 1$, of a plane layer of particles of size $x = 50$. The limiting value at large M is correct, but when scattering is important ($\omega = 0.9$) the results are only reasonable for the two points $M = 64$ and $M = 128$. Figure E.1 also shows that if scattering is not very important ($\omega = 0.1$) then an M as small as 16 gives reasonably accurate results.

E.4.2 Scaling Anisotropic Scattering

It is now evident why an alternative to solving the anisotropic equations is desirable. Even though it is plausible to use very large M values in the one–dimensional radiative transport problem, solutions for two or three dimensional geometries and at many discrete wavelengths would require tremendous amounts of computer memory and time. One solution is to model the scattering phase function as partially isotropically scattering with the remaining scattered radiation in a forward–directed delta function, i.e.,

$$\Phi(\mu) \simeq (1-g) + 2g\delta(\mu - 1) \tag{E.29}$$

where g is the asymmetry parameter, the ratio of the forward scattered light to the backward scattered light.

By substituting Eq. (E.29) into the radiative transport equation, the forward directed portion of the scattering phase function vanishes and we are left with an isotropically scattering problem with an *effective* scattering coefficient

$$\sigma' = (1-g)\,\sigma,$$

which translates into an effective optical depth, τ_0', and effective scattering albedo, ω', given by

$$\tau_0' = (1 - g\omega)\,\tau_0$$

$$\omega' = (1-g)\,\omega/(1-g\omega)\,.$$

The asymmetry parameter, g, is unity for purely forward scattering, zero for symmetric scattering (e.g. Rayleigh scattering), and -1 for purely backward scattering. For compositions similar to most fly ash particles, the asymmetry parameter is generally greater than zero, i.e., the scattering is predominantly forward. The asymmetry parameter is defined as the first moment of the scattering phase functions and is therefore related to the Legendre expansion coefficient A_1 by

$$g = \frac{1}{3}A_1$$

Lee and Buckius [51] and Gupta et al. [8] have shown that scaling anisotropic scattering using this model scattering phase function leads to good accuracy for

x	g	x	g
0.5	0.0489	16.0	0.7452
1.0	0.1990	18.0	0.7890
1.5	0.4998	20.0	0.7123
2.0	0.6260	24.0	0.7795
3.0	0.7344	28.0	0.7762
4.0	0.7503	32.0	0.7732
5.0	0.7076	36.0	0.8103
6.0	0.6445	40.0	0.7880
7.0	0.5196	50.0	0.8016
8.0	0.4539	60.0	0.8045
9.0	0.6489	70.0	0.8082
10.0	0.7435	80.0	0.8196
12.0	0.7886	90.0	0.8088
14.0	0.7081	100.0	0.8224

hemispherical quantities such as heat flux. To verify this scaling rule and also to check the correctness of the computer code, the hemispherical transmittance and reflectance was computed for a range of particle sizes, x, with complex refractive index $m = 1.5 + i10^{-4}$.

Table E.2 shows the x-values for which calculations were performed and their corresponding asymmetry parameters, g. Notice that the asymmetry parameter increases from approximately 0.05 at $x = 0.5$ to a maximum value of 0.82 at $x = 100$. The general trend is for g to increase with increasing x as the forward scattered lobe associated with diffraction becomes more pronounced. However, owing to the complicated nature of Mie scattering, the function $g(x)$ is not strictly monotonic. It is beyond the scope of this discussion to fully explain this phenomenon, but in large particles it can be explained by considering the interference between the forward *diffracted* light and the forward *refracted* light (the light transmitted through the particle). Small particles require a more complicated explanation since refraction is not very meaningful for small x.

Figures E.2 – E.4 show the hemispherical emittance versus particle size, x, for various optical depths, τ_0, and scattering albedos, ω. The results for anisotropic scattering, with $M = 128$, show excellent agreement with the results using "scaled" isotropic scattering, with the largest discrepancy occurring for $\omega = 0.9$ and $\tau_0 = 5.0$ in the range $1 < x < 5$. As expected, when the influence of multiple scattering is low ($\tau_0\omega << 1$) the scaled isotropic results are very accurate, but it is also evident that even when there are significant levels of multiple scattering ($\tau = 10, \omega = 0.9$) the scaled isotropic model predicts the hemispherical emittance very well.

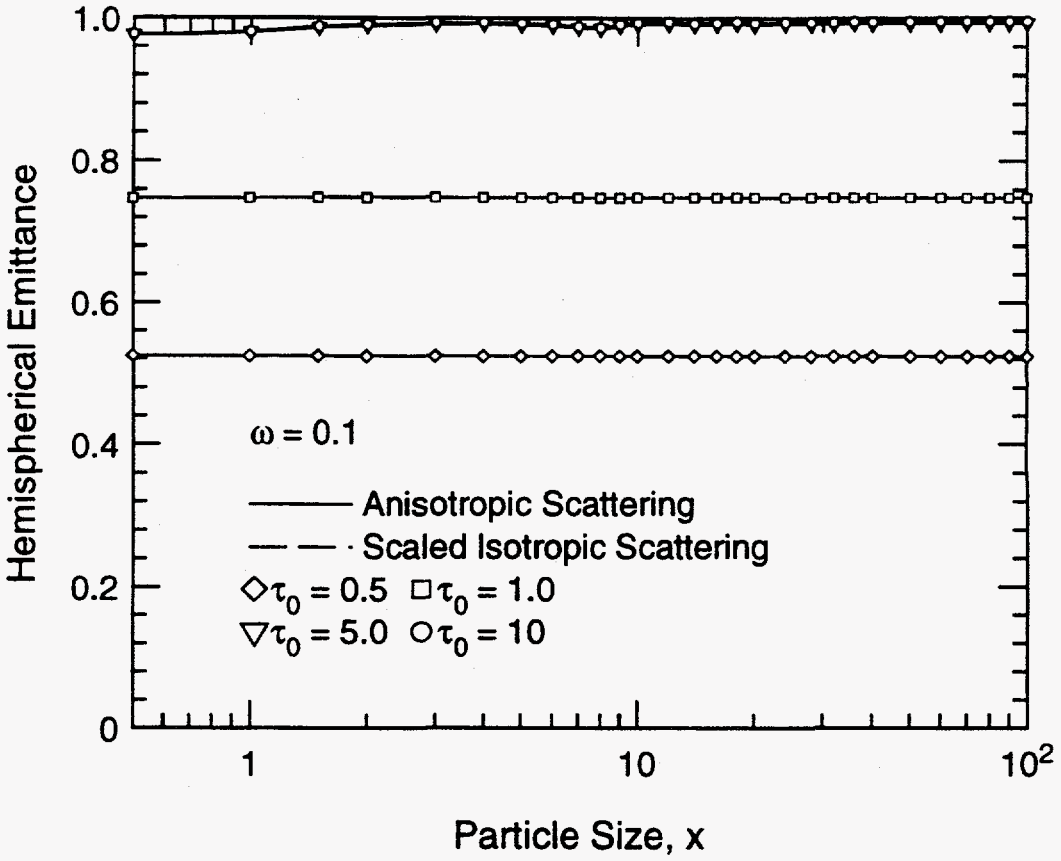

Figure E.2: The hemispherical emittance versus particle size for scattering albedo, $\omega = 0.1$, and various optical depths, τ_0

Figure E.5 shows the computed hemispherical reflectance for $\omega = 0.9$. The scaled isotropic model does not predict reflectance quite as accurately as it predicts emittance, with errors on the order of 5-8% for $\tau_0 = 0.5$ and less than approximately 1% for $\tau_0 = 10$. This small error is acceptable in most engineering situations.

The scaled isotropic model predicts hemispherical quantities very accurately, but does not predict directional emergent radiances as accurately. Figure E.6 shows the directional reflectance for three different particle sizes. The scaled isotropic solution predicts the directional reflectance very accurately for $x = 0.5$, which is to be expected since the scattering phase function is very symmetric and is closely represented by isotropic scattering. However, for larger x, the model phase function does not approximate the real phase function so well, and higher order models are

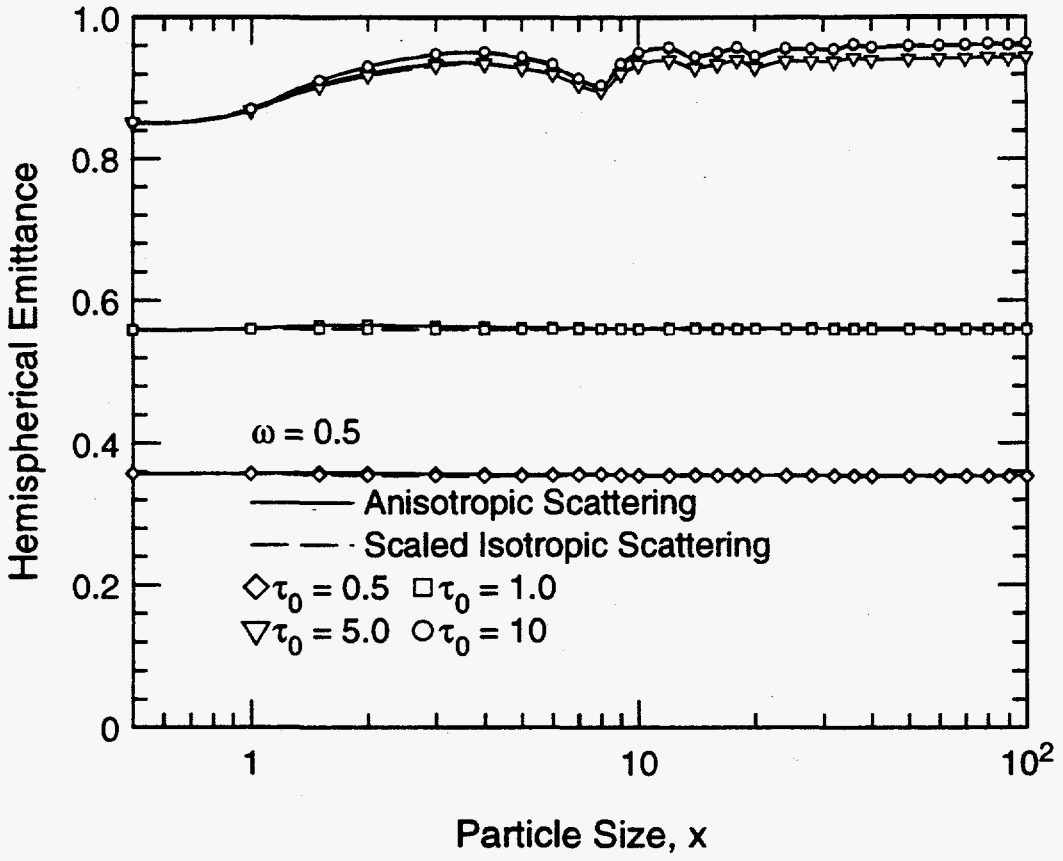

Figure E.3: The hemispherical emittance versus particle size for scattering albedo, $\omega = 0.5$, and various optical depths, τ_0

required. The model phase function (isotropic plus a delta function) causes under-prediction of the reflectance at angles far from the normal and over-prediction near the normal ($\theta = 0$). Similar trends (not presented) are seen for directional emittance and transmittance.

E.5 The $\delta - P_N$ approximation

The simple scattering phase function model presented in the previous section can be generalized to give improved accuracy. As discussed in the previous section, the phase function can be expressed as a series of Legendre polynomials where the

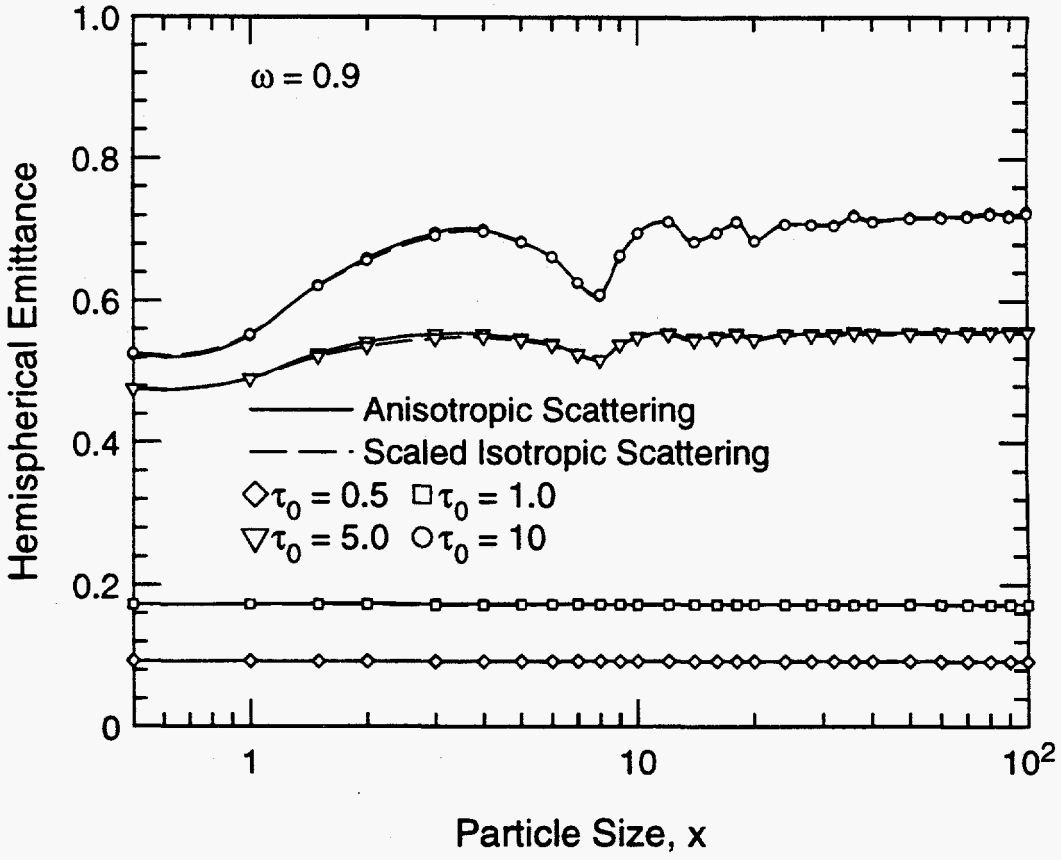

Figure E.4: The hemispherical emittance versus particle size for scattering albedo, $\omega = 0.9$, and various optical depths, τ_0

Legendre coefficients, A_j, become small for large j. For a spherical particle with size parameter x, the number of terms required to model the phase function using Eq. (E.20) is approximately $2x + 10$ [47].

For the following calculations the average scattering properties for a dispersion of particles is studied. To narrow the scope of this calculation, only radiation at 4μm is considered and the optical constants are assumed to be $m = 1.49 + i1.95 \times 10^{-4}$ (similar to slag SA05). The distribution of particles is assumed to be log-normal with volume median diameter of $\overline{D_3} = 9\mu$m and geometric standard deviation $\sigma_g = 2.0$. See Chapter V for a description of how the average properties are computed.

As discussed in the previous sections, the scattering phase function for a single particle is characterized by a large forward directed lobe (if the particle is moderately large) and a number (approximately = x) of smaller lobes spread approximately

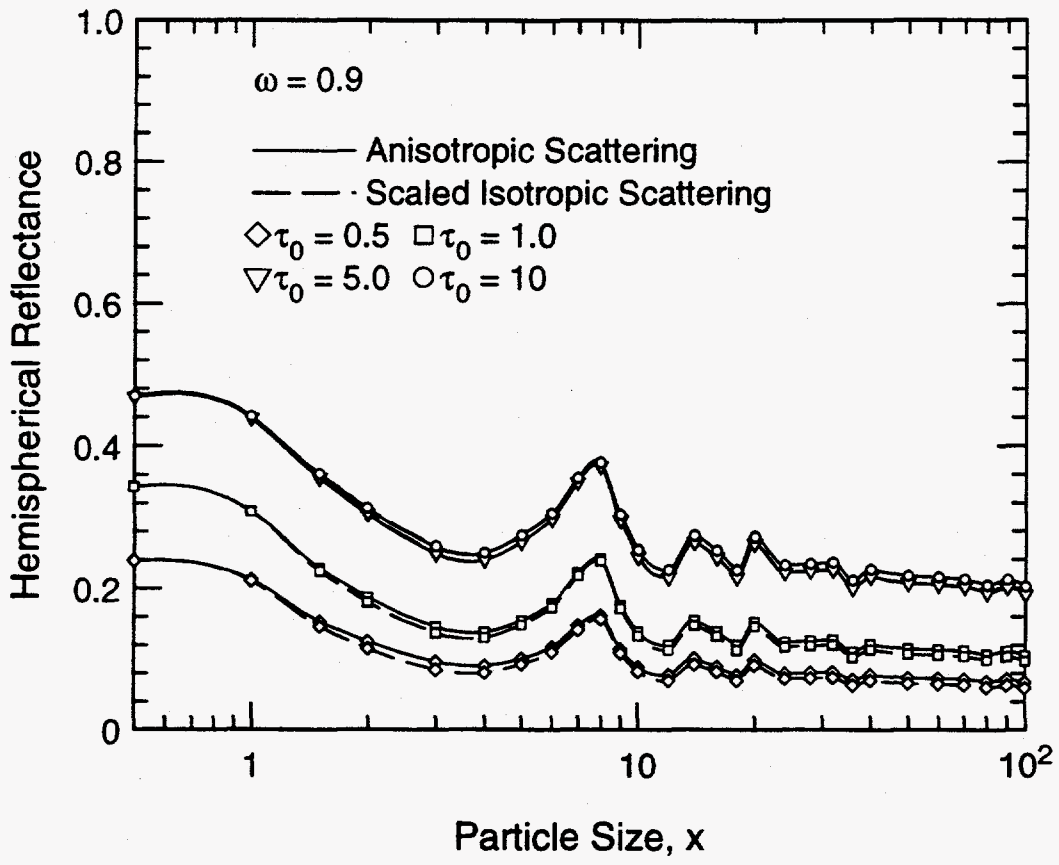

Figure E.5: The hemispherical reflectance versus particle size for scattering albedo, $\omega = 0.9$, and various optical depths, τ_0

uniformly in θ. As x is increased the number of lobes increases and more terms in the Legendre series are required to describe the additional complexity. However, when the scattering is averaged over many particle sizes, as is the case for radiation heat transfer in an ash dispersion, the lobes average out, and $\Phi(\theta)$ becomes a relatively smooth function in θ. A plot of $\Phi(\theta)$ is shown in Fig. E.7 for the model dispersion described above.

Although the complicated lobe structure in $\Phi(\theta)$ is removed by averaging over a distribution of particle sizes, the Legendre series still retains many significant terms. The averaged scattering phase function still has a strong forward scattering lobe that is not accurately modeled with a few orders of Legendre polynomials. However, if the forward lobe is modeled as a delta function then the remaining portion of the

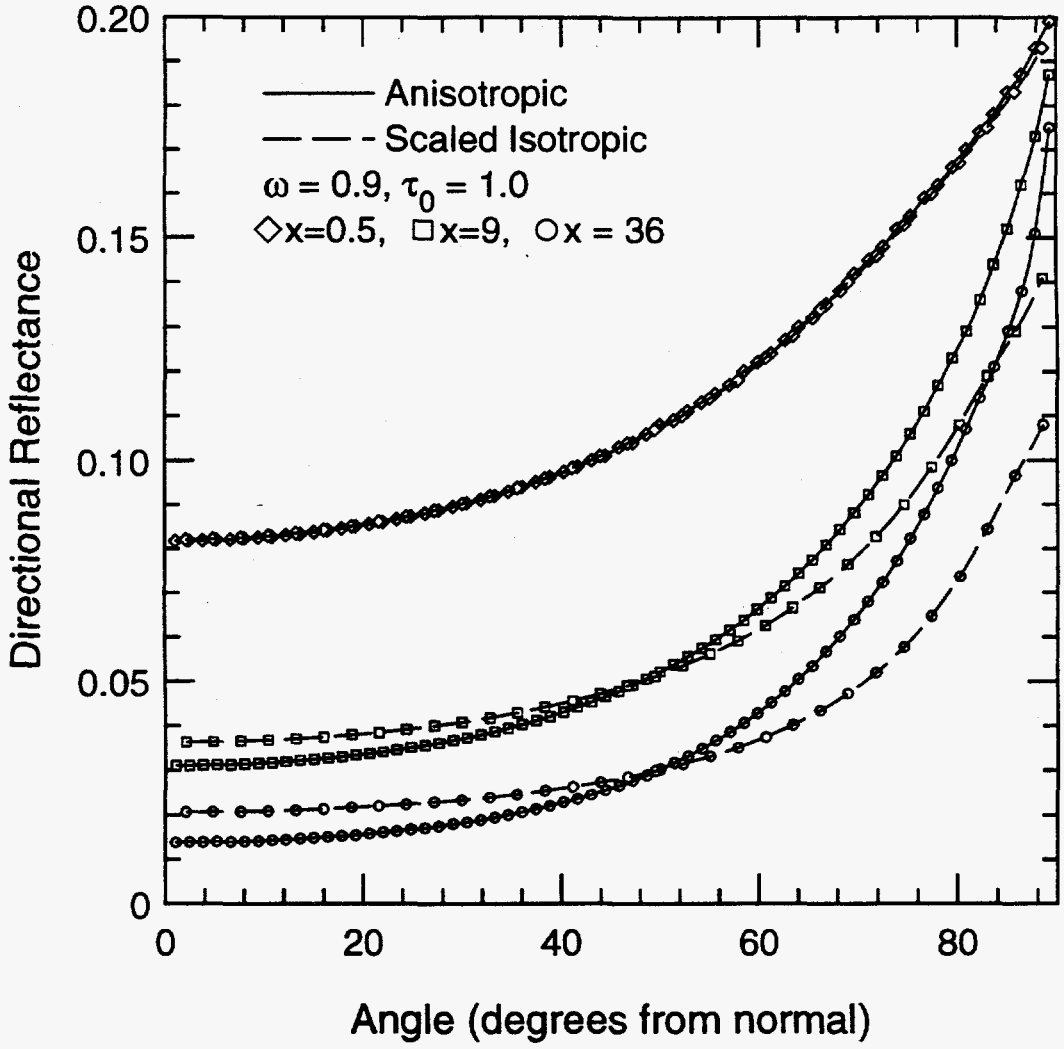

Figure E.6: The directional reflectance for $\omega = 0.9$, $\tau_0 = 1$, and $x = 0.5,\ 9,$ and 36

curve is reasonably modeled by only a few orders of Legendre polynomials. This approximation is the basis for the $\delta - P_N$ model.

Consider the phase function expansion [40]

$$\Phi(\mu) = 2f\delta(1-\mu) + (1-f)\sum_{j=0}^{N} B_j P_j(\mu) \tag{E.30}$$

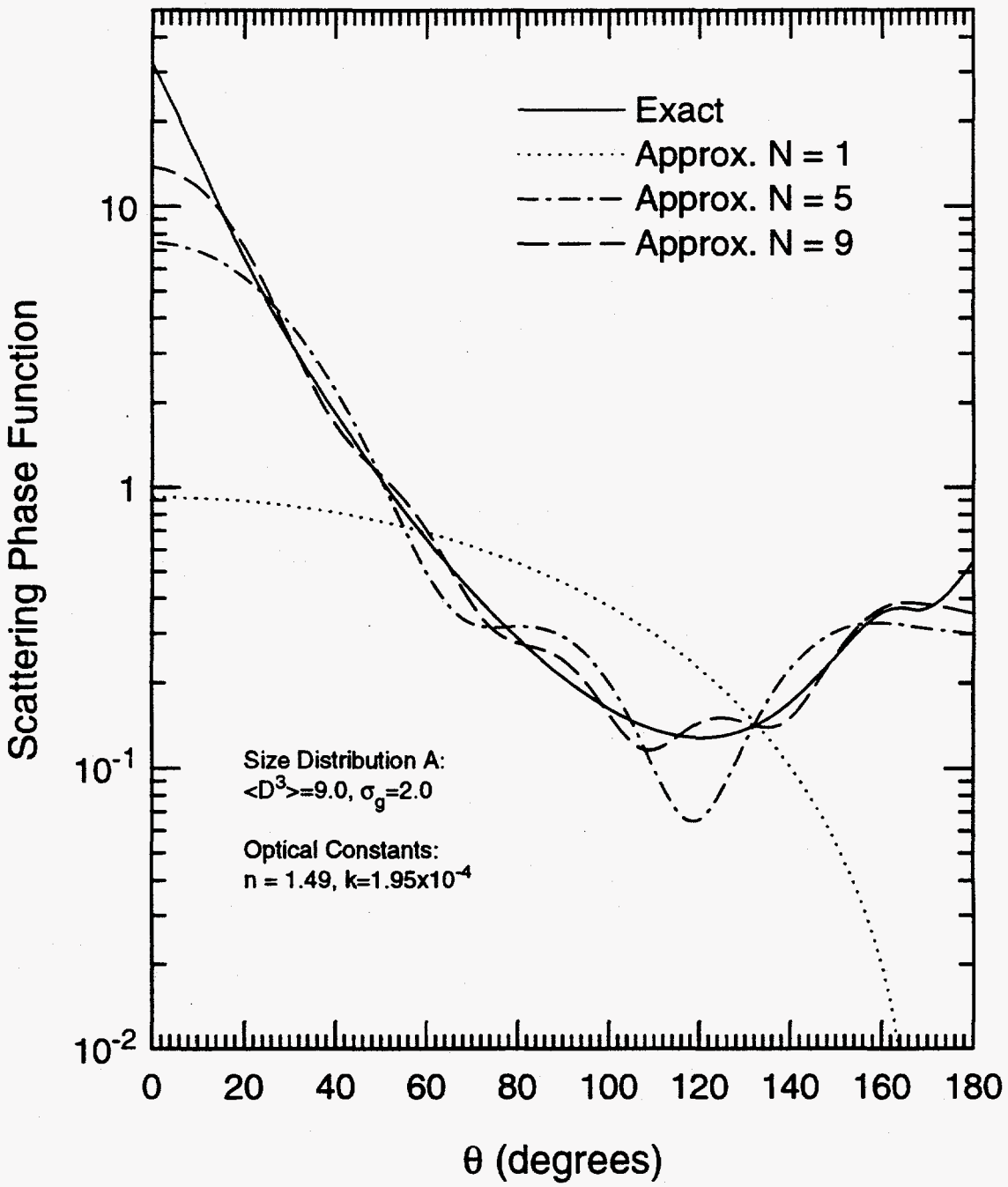

Figure E.7: Average scattering phase function, $\Phi(\theta)$ for a log-normal polydispersion of particles with $\overline{D_3} = 9\mu$m and $\sigma_g = 2$ and optical constants $m = 1.49 + i1.95 \times 10^{-4}$ at a wavelength of 4μm.

where f and B_i are constants. As N approaches infinity $f \to 0$ and Eq. (E.30) is equivalent to Eq. (E.20). Using Eq. (E.20) and the orthogonality relation

$$\int_{-1}^{1} P_j(\mu) P_i(\mu) \, d\mu = \begin{cases} 0, & \text{if } i \neq j; \\ \frac{2}{2j+1}, & \text{if } i = j. \end{cases} \tag{E.31}$$

the constants in Eq. (E.30) are determined in terms of the A_j in Eq. (E.20), i.e.,

$$f = \frac{A_{N+1}}{2N+3} \quad \text{and} \quad B_j = \frac{A_j - (2j+1) f}{1 - f}. \tag{E.32}$$

The approximate scattering phase function, Eq. (E.30), is shown in Fig. E.7 for $N = 1$, $N = 5$, and $N = 9$. The high accuracy of this $\delta - P_N$ model is evident for even relatively small N.

E.5.1 Evaluation of $\delta - P_N$ model for a planar layer

The $\delta - P_N$ model for $\Phi(\theta)$ was evaluated using a computer code developed for computing the radiative transfer through a planar layer. The layer is assumed to have the particle size distribution and optical properties described previously. The scattering albedo, $\omega \equiv \sigma/(\sigma + \alpha) = 0.9979$, was computed from the size-averaged scattering and absorption efficiencies.

The reflected and transmitted directional radiance is shown in Figs.E.8 and E.9 for various optical depths, $\tau_o = \alpha L$, where the layer thickness is L and the absorption coefficient is α. The angle, θ, on both plots is measured from the outward normal. We see that the error in the small N approximations to $\Phi(\theta)$ is largest when τ_o is small. However, for $N = 5$ or $N = 9$ the error is very small for all τ_o shown.

The hemispherical transmittance, T, and reflectance, R, are shown in Table E.3, along with the associated error for each phase function model. The results are consistent with Fig. E.8 and Fig. E.9 in that the error is largest for small τ_o. However, it is significant that except when either T or R is small, even the $N = 0$ solution is reasonably accurate. Furthermore, for $N = 5$ the error is less than 0.55% for all the cases shown. Using $N = 9$ gives essentially exact solutions for the hemispherical transmittance and reflectance.

From this analysis, it is evident that using the $\delta - P_N$ model for the scattering phase function is quite accurate for $N > 5$. If errors on the order of a few percent can be tolerated, $N = 2$ or less can be used. Also, if only the hemispherical fluxes are of interest, the $N = 0$ solution is probably adequate.

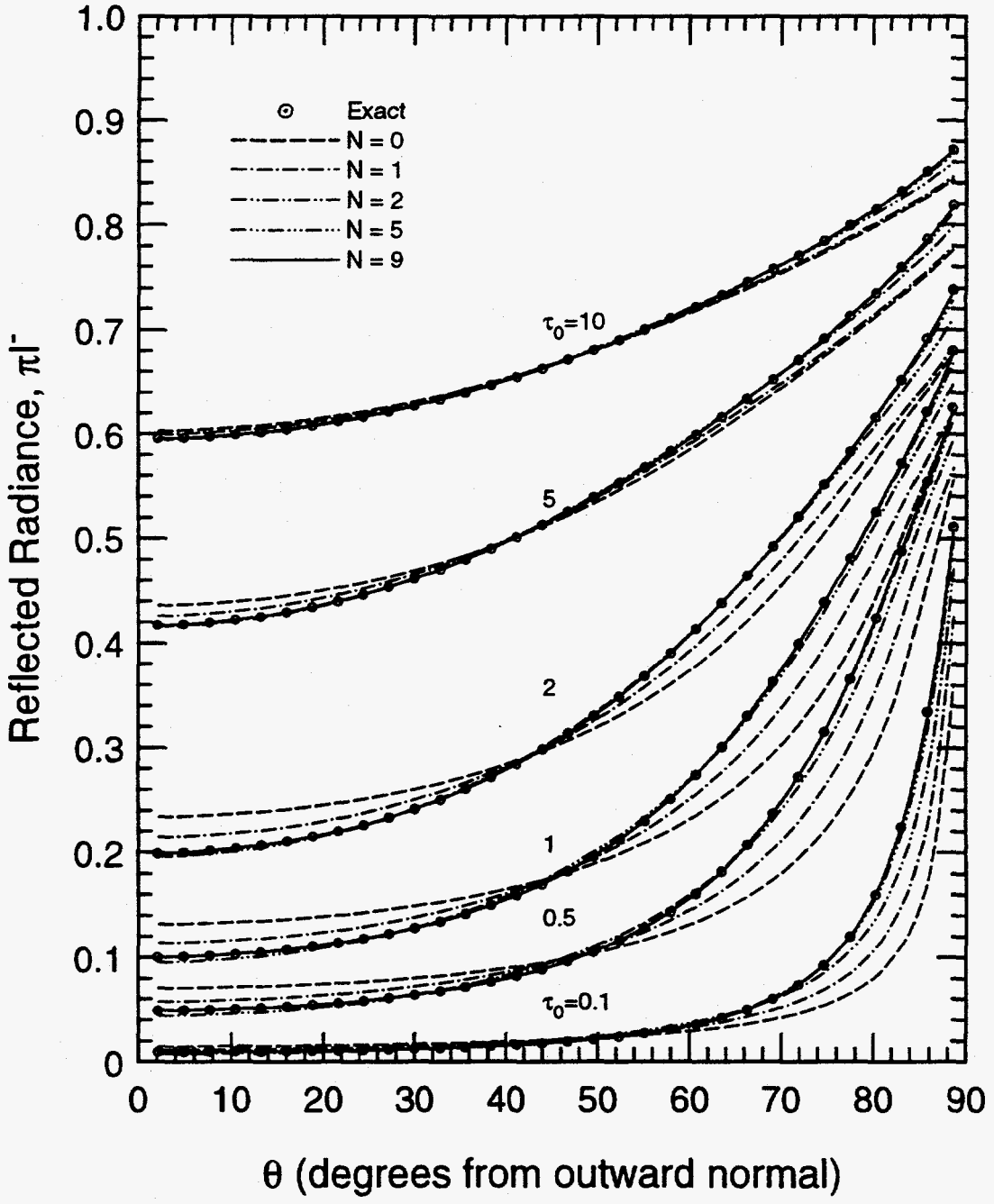

Figure E.8: Reflected radiance versus direction for a planar polydispersion of particles with various optical depths and a $\delta - P_N$ model of $\Phi(\theta)$ with $N = 0, 1, 2, 5, 9$ and ∞.

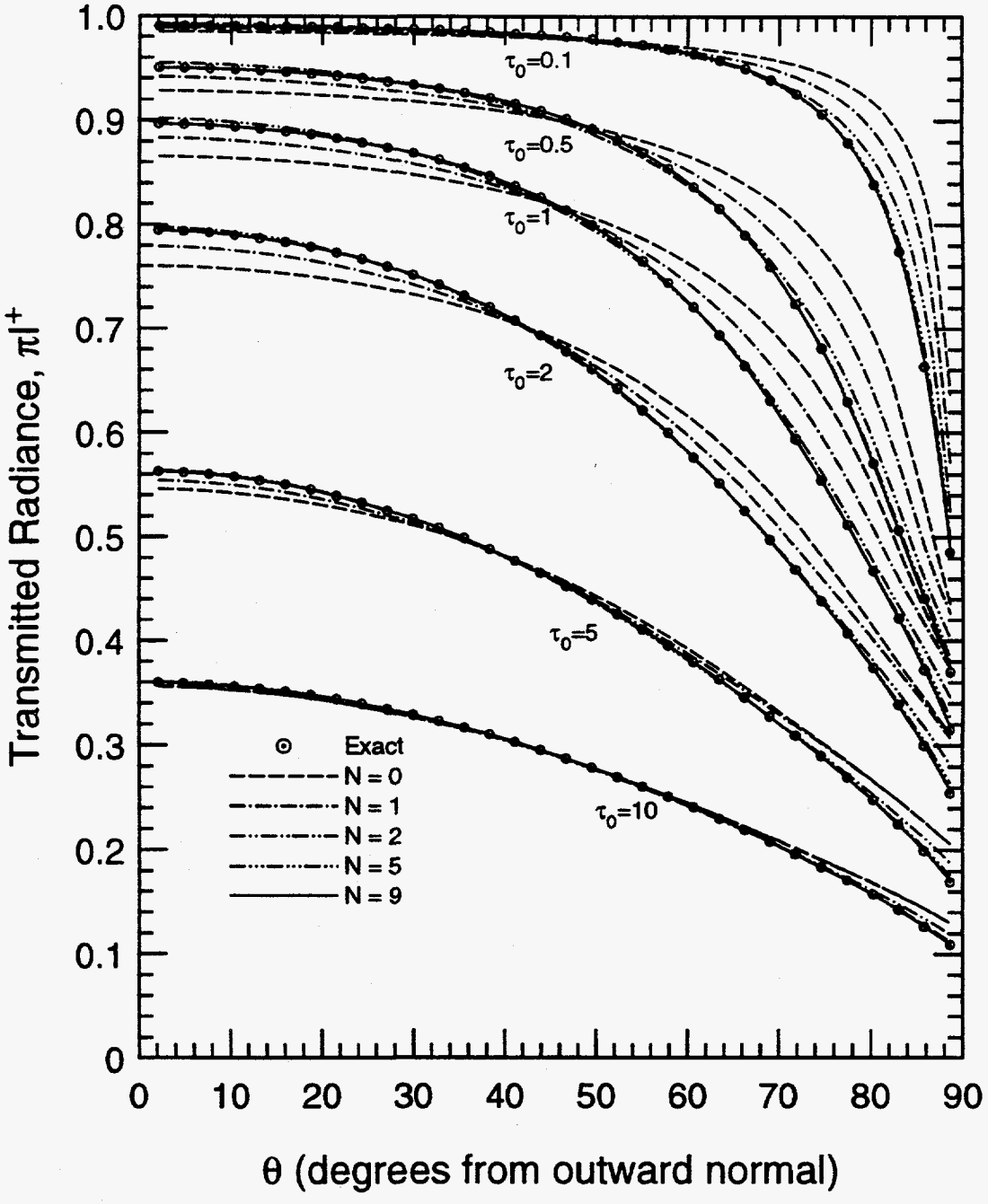

Figure E.9: Transmitted radiance versus direction for planar polydispersion of particles with various optical depths and $\delta - P_N$ model of $\Phi(\theta)$ with $N = 0, 1, 2, 5, 9$ and ∞.

	$\tau_o = 0.1$		Percent Error	
Order	R	T	R	T
Exact	0.03460	0.96499	—	—
0	0.02810	0.97148	-18.78	0.67
1	0.03069	0.96889	-11.29	0.40
2	0.03337	0.96621	-3.54	0.13
5	0.03441	0.96518	-0.55	0.02
9	0.03457	0.96501	-0.07	0.00

	$\tau_o = 0.5$		Percent Error	
Order	R	T	R	T
Exact	0.13094	0.86699	—	—
0	0.11943	0.87849	-8.79	1.33
1	0.12484	0.87308	-4.66	0.70
2	0.12993	0.86799	-0.77	0.12
5	0.13085	0.86707	-0.07	0.01
9	0.13093	0.86700	-0.01	0.00

	$\tau_o = 1$		Percent Error	
Order	R	T	R	T
Exact	0.21657	0.77928	—	—
0	0.20633	0.78952	-4.73	1.31
1	0.21136	0.78449	-2.41	0.67
2	0.21601	0.77984	-0.26	0.07
5	0.21653	0.77933	-0.02	0.01
9	0.21657	0.77929	-0.00	0.00

Table E.3: continued...

	$\tau_o = 2$		Percent Error	
Order	R	T	R	T
Exact	0.33752	0.65422	—	—
0	0.33114	0.66060	-1.89	0.97
1	0.33420	0.65754	-0.99	0.51
2	0.33725	0.65449	-0.08	0.04
5	0.33749	0.65424	-0.01	0.00
9	0.33752	0.65422	-0.00	0.00

	$\tau_o = 5$		Percent Error	
Order	R	T	R	T
Exact	0.53624	0.44332	—	—
0	0.53451	0.44505	-0.32	0.39
1	0.53507	0.44448	-0.22	0.26
2	0.53612	0.44344	-0.02	0.03
5	0.53622	0.44333	-0.00	0.00
9	0.53623	0.44332	-0.00	-0.00

	$\tau_o = 10$		Percent Error	
Order	R	T	R	T
Exact	0.67825	0.28181	—	—
0	0.67769	0.28236	-0.08	0.20
1	0.67776	0.28224	-0.07	0.15
2	0.67819	0.28185	-0.01	0.01
5	0.67823	0.28180	-0.00	-0.00
9	0.67824	0.28179	-0.00	-0.01

E.6 Summary

The discrete ordinates method for calculating radiative transport through a planar layer with scattering and absorption has been presented. Considerable attention was given to the effect of anisotopic scattering on the accuracy of the solution. Using the full Legendre series expansion for the scattering phase function was shown to be very expensive in computation time. A simple approximation in which the scattering phase function was assumed to be a delta function plus isotropic scattering was shown to give accurate estimates for total hemispherical quantities, but the error in directional quantities was significant. A generalized form of this simple approximation to the scattering phase function, the $\delta - P_n$ model, was found to be suitable for accurately computing both hemispherical and directional quantities while only using a few terms (≤ 5) for the phase function series.

Appendix F.

Glass Structure and Optical Properties

A large fraction of the fly ash produced in a coal combustor is in the form of glassy particles [52] produced by rapid cooling of molten droplets of inorganic oxides (clays). Based on Raman studies of melts of aluminosilicate glasses, it is expected that the structure of these molten droplets is closely related to the structure of the quickly cooled glassy particles [53-54], and that this structure will affect the optical properties of both the molten droplets and the solid glassy particles in very similar ways. To understand optical absorption by SiO_2 glasses it is necessary to understand the structure of the glass.

The most commonly accepted model for the structure of the glass is the *random network model* first developed by Zachariasen [55] and is discussed in introductory texts (e.g., Holloway [25]) on glass. The most common glasses are based on silica (SiO_2) with varying amounts of metal oxides such as Al_2O_3, CaO, MgO, Na_2O, and Fe_2O_3, to name a few. The random network model assumes each Si^{4+} ion is surrounded by four O^{2-} anions in a tetrahedral arrangement about the Si^{4+} cation. In pure SiO_2 these tetrahedral units are bound at the vertices to form a three dimensional network of Si-O-Si chains, or polymers. The O in this bond is called a *bridging* oxygen. In crystalline quartz the arrangement of the tetrahedral units is regular, producing long range order throughout the material. However, in glass the angle of the Si-O-Si bonds and the azimuthal angle between two neighboring tetrahedral units varies. Thus, the glass has short range order, within the range of the tetrahedral unit, that is similar to that of quartz, but the bond angles between tetrahedral units is not regular. There is a distribution of bond angles and bond strengths associated with the disorder of the glass. Figures F.1 and F.2 illustrate the structure of silica glasses.

Consider the tetrahedral structure of the basic silica glass. For pure SiO_2 the chemical arrangement for a pair of Si atoms is

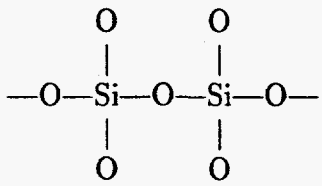

where the central oxygen is the bridging oxygen. Here the bond angles are not shown since the true structure is 3-dimensional. A more realistic geometrical illustration

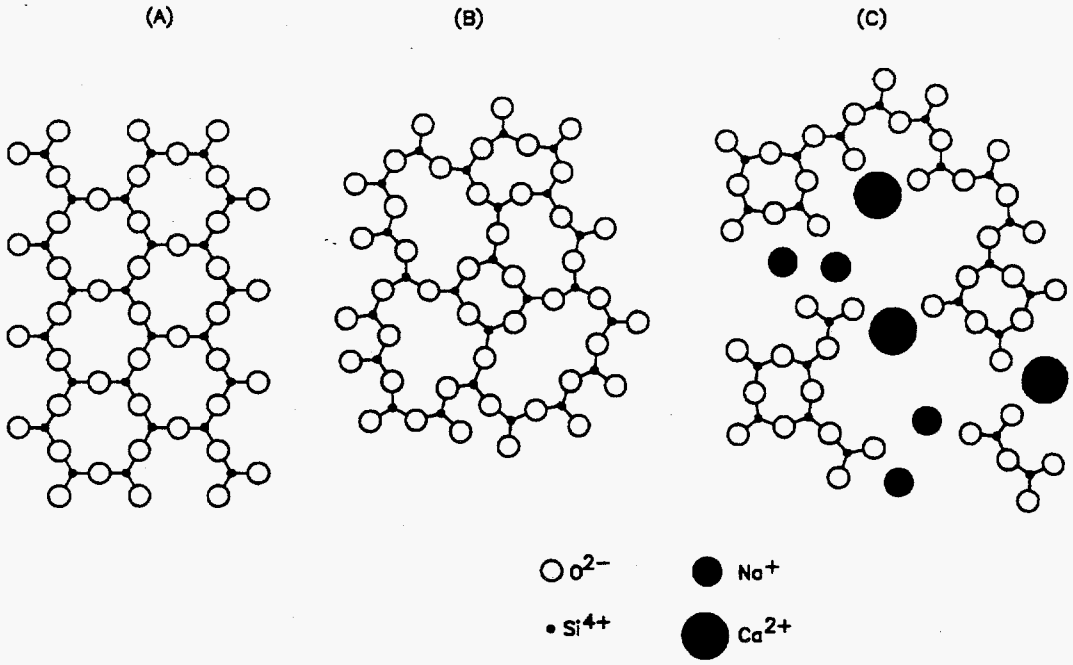

Figure F.1: Two dimensional representation of silica network for (a) crystalline silica, (b) glassy silica, and (c) silica network modified by calcium and sodium.

is presented in Fig. F.1 and Fig. F.2. The absorption of photons incident on such an atomic structure depends on the bond strengths and angles of the Si_2O_4 network structure.

The addition of metal oxides to silica glass causes structural changes which affect the optical properties of the glass. The most significant effect of the addition of other oxides is on the bonds between adjacent tetrahedral units. Since these bonds are responsible for the optical properties at the restrahlen wavelengths ($\lambda > 8\mu$m) the addition of oxides mostly affects these longer wavelength optical properties.

Some oxides introduce cations that are capable of replacing a silicon ion in the network, and are called *network formers*. For example, Al_2O_3, introduces an Al^{3+} cation that can replace a silicon cation to form a chain, for example, Si-O-Al-O-. However, to achieve local charge neutrality it is necessary to have an additional cation (e.g., $0.5Ca^{2+}$ or Na^{+}) in the vicinity of the Al^{3+} cation. Note that these lower valence cations, Ca^{2+} or Na^{+}, have coordinations ≥ 6.

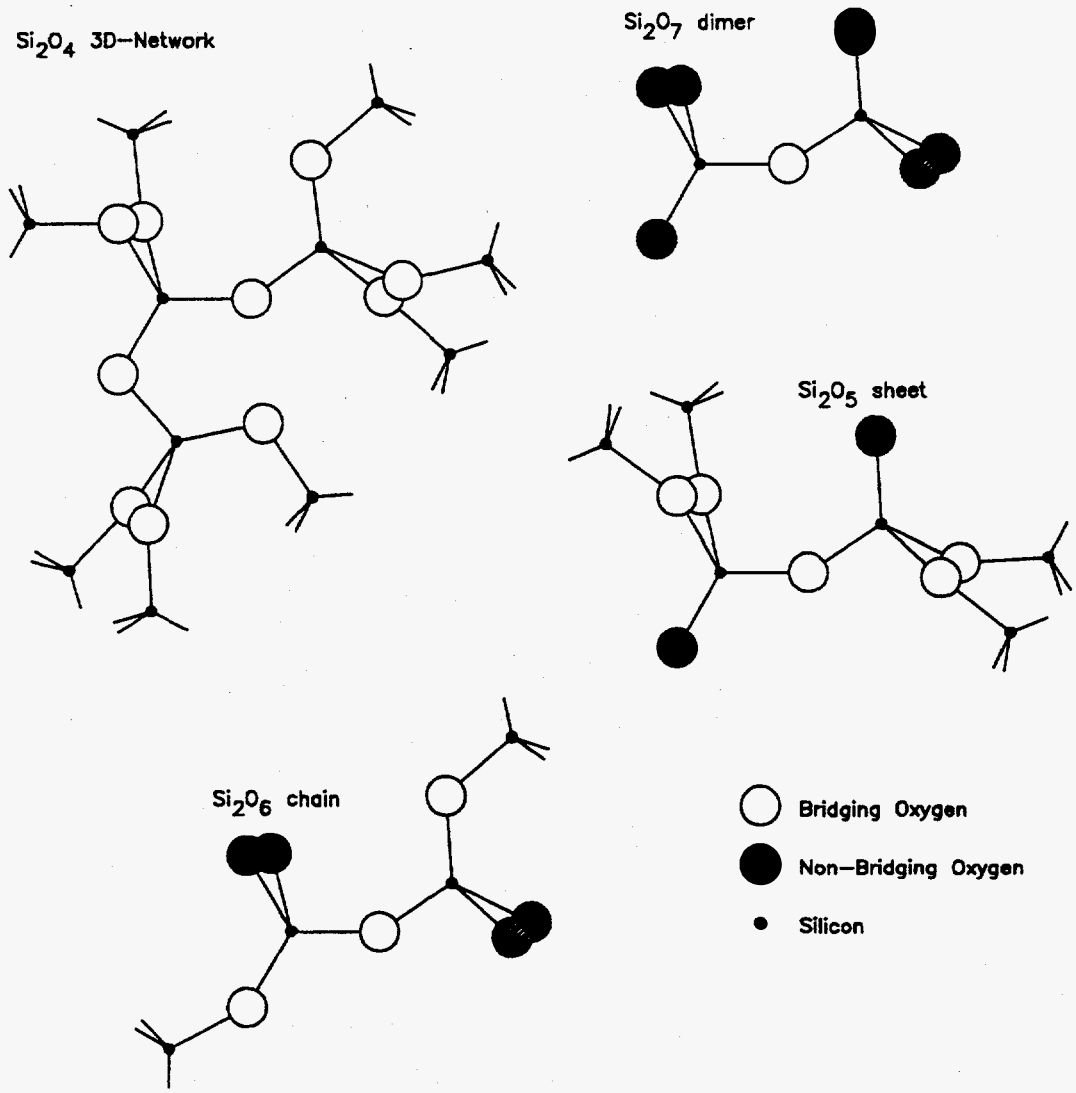

Figure F.2: Examples of silica random network model structures for glasses.

Some oxides introduce cations that do not form networks, but instead balance the charges of the vertices of would-be tetrahedral units, thus breaking the bridging oxygen bonds. Examples of such ions are Ca^{2+} and Na^{+}. The addition of these *network breaking* ions causes an increase in the number of *non-bridging oxygens*, or NBO's. If sufficient quantities of network-breaking ions are added, the glass becomes depolymerized so that the predominant silicon bond is $Si-O^{-}$.

For example, Ca and Na cations are bond breakers. Their presence reduces the number of bridging oxygens. If one adds such network breaking metal cations, (Ca^{2+} or Na^{+}) then the network is modified to the forms

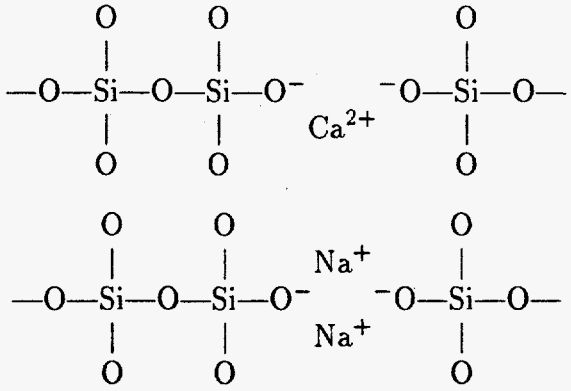

Here we represent the three–dimensional network as a two–dimensional form; thus bond angles are not correctly represented.

Network forming metal cations (i.e., those which allow tetrahedral coordination) such as Al^{3+} and Fe^{3+} can replace silicon ions in the network, provided there are available metal cations (M^{+}) to charge balance the tetrahedral site. For example, in the schematic below two tetrahedrally coordinated Al atoms are charge balanced by a single nearby Ca^{2+} cation.

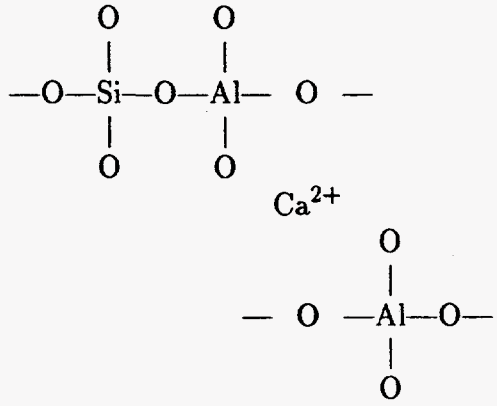

Here the bridging oxygens above and below the Ca^{2+} cation are connected to a continuing network of Si–O–Si. Alternatively, Hemmings and Berry [52] suggest that while aluminum can replace a silicon atom in tetrahedral coordination, the result is a non-bridging oxygen that is then charge balanced by a metal cation, such as

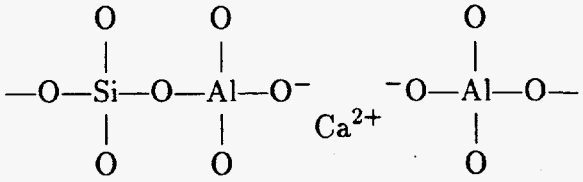

The difference between these two alternative models is notable, and perhaps both situations occur in real glasses. Finally, if there are insufficient available charge balancing metal cations to allow Al to be tetrahedrally coordinated, then Al may also act as a network breaker, such as

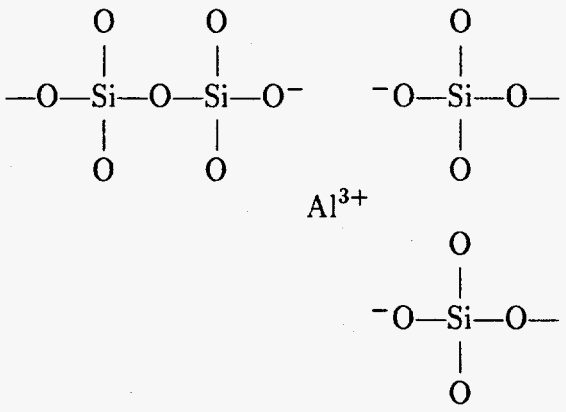

From this model we can qualitatively understand the effect of silica content and temperature on the strong absorption band of silica glasses. Sweet and White [56] and Crozier and Douglas [57] studied sodium silicate glasses with varying concentrations of SiO_2 and Na_2O. As mentioned above, the Na metal cation is a network breaker in silica glasses, thus the studies provide an estimate of the frequency for the bridging Si-O-Si bond and the non-bridging Si-O^- bond. Both studies find that the bridging bond for room temperature sodium silica glass produces a peak absorption at a frequency of approximately 1100 cm^{-1} and a peak absorption for non–bridging Si-O near 950 cm^{-1}. Another absorption peak near 760 cm^{-1}, weak in high silica glasses, but becoming stronger as more sodium is added is not explained by Sweet and White [56] or Crozier and Douglas [57], but Simon [34] suggests that it may be due to ring groups in the glass. Simon admits that this explanation is not rigorously substantiated but it is known that the occurrence of this absorption band is highly structure-sensitive.

Finally, Sweet and White [56] made reflectance measurements on the glasses at molten temperatures (900–980°C). The effect of temperature was to shift the absorption peaks to lower frequencies (longer wavelength). This shift was attributed to the increased bond length associated with thermal expansion of the glass. This result is quite significant since it implies that there is no significant structural difference between the cold solid glass and hot liquid glass. Simon [34] suggests that the broadening and shift to lower frequencies associated with increased temperature is explainable in terms of the level of disorder in the glass structure. Increasing the temperature of the glass causes the bond structures to be less regular, with a broader

distribution of bond angles and distances. The result is similar to that of adding cations (either network formers of network breakers) to the silica glass.

From the above discussion it is clear that the structure of glass is complex. There is a considerable body of literature on the subject, but recent work by Hemmings and Berry [52] provides a good discussion of the subject as it relates to glassy fly-ash particles.

Bibliography

1. D. K. Edwards, "Molecular gas band radiation", in T.F.Irvine, Jr., and J.P.Hartnett (eds.), *Advances in Heat Transfer*, 5, pp.253-324, Academic Press, New York, 1976.

2. C. B. Ludwig, W. Malkmus, J. E. Reardon, and J. A. L. Thomson, *Handbook of Infrared Radiation from Combustion Gases*, NASA SP-3080, National Aeronautics and Space Administration, Washington, D.C., 1973.

3. M. Q. Brewster and T. Kunitomo, "The optical constants of coal, char, and limestone", Journal of Heat Transfer, 106, pp.678-683, 1984.

4. S. C. Lee and C. L. Tien, "Optical constants of soot in hydrocarbon flames", *Eighteenth Symposium (International) on Combustion*, The Combustion Institute, Pittsburgh, Pa., pp.1159-1166, 1981.

5. A. F. Sarofim, "Flame emissivities: alternate fuels", in C. T. Bowman and J. Birkeland (Eds.)*Combustion and Chemical Kinetics*, , 62 of *Progress in Aeronautics and Astronautics*, American Institute of Aeronautics and Astronautics, New York, 1978..

6. A. Lowe, T. F. Wall, and I. McC. Stewart, "Combustion kinetics in the modeling of large, pulverized fuel furnaces: a numerical experiment in sensitivity", A.I.Ch.E. Journal, 23, pp.440-448, 1977.

7. R. Viskanta, A. Ungan, and M. P. Mengüc, "Predictions of radiative properties of pulverized coal and fly–ash polydispersions", ASME paper 81-HT-24, presented at 20th Joint ASME/AIChE National Heat Transfer Conference, 1981.

8. R. P. Gupta, T. F. Wall, and J. S. Truelove, "Radiative scatter by fly ash in pulverized–coal–fired furnaces: application of the Monte Carlo method to anisotropic scatter", International Journal of Heat and Mass Transfer, 26, pp.1649-1660, 1983.

9. S. A. Boothroyd and A. R. Jones, "Radiative transfer scattering data relevant to fly ash", Journal of Physics D: Applied Physics, 17, 1107-1114, 1984.

10. Mengüc, M. P. and Viskanta, R. "Effect of fly-ash particles on spectral and total radiation blockage", Combustion Science and Technology, 60, pp.97-115, 1988.

11. D. G. Goodwin, "Infrared optical constants of coal slag", PhD Dissertation, HTGL Topical Report No. T-255, Stanford University, July, 1986.

12. C. Willis, "The complex refractive index of particles in a flame", Journal of Physics D: Applied Physics, 3, 1944-1556, 1970.

13. F. E. Volz, "Infrared optical constants of ammonium sulfate, sahara dust, volcanic pumice, and flyash", Applied Optics, 12, pp.564-568, 1973.

14. A. Lowe, I. McC. Stewart, and T. F. Wall, "The measurement and interpretation of radiation from fly ash particles in large pulverized coal flames", *Seventeenth Symposium (International) on Combustion*, The Combustion Institute, Pittsburgh, PA, pp.105-112, 1979.

15. P. J. Wyatt, "Some chemical, physical, and optical properties of fly ash particles", Applied Optics, 19, pp.975-983, 1980.

16. R. P. Gupta and T. F. Wall, "The optical properties of fly ash in coal fired furnaces", Combustion and Flame, 61, pp.145-151, 1985.

17. S. Ghosal, "Optical characterization of coal fly ashes and infrared extinction measurements on ash suspensions", Ph.D. Dissertation, Stanford University, 1993..

18. C. F. Bohren and D. R. Huffman,*Absorption and Scattering of Light by Small Particles*, John Wiley & Sons, 1983.

19. J. D. Jackson, *Classical Electrodynamics*, John Wiley & Sons, 1975.

20. R. Siegel and J. R. Howell, *Thermal Radiation Heat Transfer*, Hemisphere Publishing, Washington, 1981.

21. L. D. Landau, E. M. Lifshitz, and L. P. Pitaevskiĭ, *Electrodynamics of Continuous Media*, Landau and Lifshitz Course on Theoretical Physics, 8, Pergamon Press, 1984.

22. E. M. Levin, C. R. Robins, and H. F. McMurdie, *Phase Diagrams for Ceramists*, The American Ceramic Society, Inc., Columbus, Ohio, 1964..

23. M. Coenen, "Durchstrahlung des Glasbades bei Farbglasern," Glastechnische Berichte, 41, pp.1-10, 1968.

24. M. B. Volf, "Mathematical Approach to Glass", Glass Science and Technology, 9, Elsevier, 1988.

25. D. G. Holloway, *The Physical Properties of Glass*, Wykeham Publications (London) Ltd, 1973..

26. M. Born, and E. Wolf, *Principles of Optics*, (sixth edition), Pergamon Press, Oxford, 1980..

27. I. H. Malitson, "Interspecimen comparison of the refractive index of fused silica", Journal of the Optical Society of America, 55, pp.1205-1209, 1965.

28. I. H. Malitson, "Refraction and dispersion of synthetic sapphire", Journal of the Optical Society of America, 52, pp.1377-1379, 1962.

29. J. L. Jacobson and E. R. Nixon, "Infrared dielectric response and lattice vibrations of calcium and strontium oxides", Journal of Chemistry and Physics of Solids, 29, pp.967-976, 1968..

30. P. C. Bailey, "Absorption and reflectivity measurements on some rare earth iron garnets and α-Fe_2O_3", Journal of Applied Physics, 31, pp.395-405, 1960..

31. J. R. DeVore, "Refractive indices of rutile and sphalerite", Journal of the Optical Society of America, 41, pp.417-419, 1951..

32. R. E. Stephens and I. H. Malitson, National Bureau of Standards Journal of Research, 49, pp.249-252, 1952..

33. S. S. Mitra, "Optical Properties of Non-Metallic Solids for Photon Energies below the Fundamental Band Gap", in E. D. Palik (ed.) *Handbook of Optical Constants of Solids*, pp.213–270, Academic Press, 1985..

34. I. Simon, "Infrared studies of glasses", in J. D. MacKenzie (ed.) *Modern Aspects of the Vitreous State*, Butterworths, Washington, 1960..

35. M. N. Ozisik, *Radiative Transfer and Interactions with Conduction and Convection*, John Wiley and Sons, New York, 1973.

36. S. Ghosal, J.L. Ebert, and S. A. Self, "Fly ash size distributions: use of Coulter multisizer and fitting to truncated lognormal distributions", Particle and Particle Systems Charactization 10, pp.11-18, 1993..

37. D. G. Goodwin and M. Mitchner, "Flyash radiative properties and effects on radiative heat transfer in coal-fired systems", International Journal of Heat and Mass Transfer, 26, no. 4, pp.627-638, 1989..

38. J. L. Ebert and S. A. Self, "Radiation heat transfer in a dispersion of flyash", in R.W. Bryers and K.S. Vorres (eds), Engineering Foundation Conference on Mineral Matter and Ash Deposition from Coal, Santa Barbara, CA, Feb 22–26, pp.599-611, 1988..

39. K. H. Im and R.K. Ahluwalia, "Convective and radiative heat transfer in MHD radiant boilers", Journal of Energy, **5**, no.5, pp.308-314, 1981.

40. W. J. Wiscombe, "The delta-M method. Rapid yet accurate radiative flux calculations for strongly asymmetric phase functions." Journal of Atmospheric Sciences, **33**, pp.2452–2459, 1976.

41. Users Handbook for the Argonne Premium Coal Sample Program, Argonne National Laboratory, Argonne, Illinois, October (1989).

42. D.G. Goodwin and J.L. Ebert, "Rigorous bounds on the radiative interaction between real gases and scattering particles", Journal of Quantitative Spectroscopy and Radiative Transfer, 37, no. 5, pp.501-508, 1987.

43. G. M. Hale and M. R. Querry, "Optical constants of water in the 200–nm to 200– μm wavelength region", Applied Optics, 12, No.3, pp.555–563, 1973..

44. W. M. Irvine and J.B. Pollack, "Infrared optical properties of water and ice spheres", Icarus, 8, pp.324–360, 1968..

45. A. H. Pfund, "The dispersion of CS_2 and CCl_4 in the infrared", Journal of Optical Society of America, 25, No.11, pp.351–354, 1935..

46. W.J. Wiscombe, "Improved Mie scattering algorithms", Applied Optics, 19, no. 9, pp.1505–1509, 1980.

47. J. V. Dave, "Coefficients of the Legendre and Fourier series for the scattering functions of spherical particles", Applied Optics, 9, No. 8, pp.1888–1896, 1970.

48. S. Chandrasekhar, *Radiative Transfer*, Dover 1960.

49. W. A. Fiveland, "Discrete–ordinates solutions of the radiative transport equation for rectangular enclosures", Journal of Heat Transfer 106, pp.699-706, 1984.

50. W. H. Press, B. P. Flannery, S. A. Teukolsky, and W. T. Vettering, *Numerical Recipes - The Art of Scientific Computing*, Cambridge University Press, 1986.

51. H. Lee and R. O. Buckius, "Scaling anisotropic scattering in radiation heat transfer for a planar medium", Journal of Heat Transfer, 104C, pp.68-75, 1982.

52. R.T. Hemmings and E.E. Berry, "On the glass in coal fly ashes: recent advances", Fly Ash and Coal Conversion By–Products: Characterization, Utilization and Disposal IV, Materials Research Society Symposium Proceedings, Dec.1-3, 1987, Boston, MA..

53. B.O. Mysen, D. Virgo, and F.A. Seifert, "Relationships between properties and structure of aluminosilicate melts", American Mineralogist, 70, pp.88-105, 1985..

54. F. Seifert, B.O. Mysen, and D. Virgo, "Three–dimensional network structure of quenched melts (glass) in the systems SiO_2–$NaAlO_2$, SiO_2–$CaAl_2O_4$ and SiO_2–$MgAl_2\ O_4$", American Mineralogist, 67, pp.696-717, 1982..

55. R. Zachariasen, "Atomic arrangement in glass", Journal of the American Chemical Society, 54, pp.3841, 1932.

56. J.R. Sweet, and W.B. White, "Study of sodium silicate glasses and liquids by infrared reflectance spectroscopy", Physics and Chemistry of Glasses, 10, no.6, pp.246–251, 1969..

57. D. Crozier and R.W. Douglas "Study of sodium silicate glasses in the infra–red by means of thin films", Physics and Chemistry of Glasses, 6, no.6, pp.240–245, 1965..